# Probing strongly correlated 4f orbital symmetry of Ce, Sm and Yb compounds by linear dichroism in *angle − resolved* core-level photoemission

A dissertation submitted to
THE GRADUATE SCHOOL OF ENGINEERING SCIENCE
OSAKA UNIVERSITY
in partial fulfillment of the requirements for the degree of
DOCTOR OF PHILOSOPHY IN ENGINEERING

BY

YUINA KANAI

MARCH 2019

# Abstract

Strongly correlated rare-earth-based electron systems show various interesting behavior such as unconventional superconductivity, multipolar ordering, formation of heavy fermionic states, nontrivial (Kondo) semiconducting behavior, and quantum criticality at low temperatures. Ground-state $4f$-orbital symmetry determined by crystalline electric field (CEF) splitting is very basic information on realistic strongly correlated electron systems. In contrast to the case of transition-metal oxides in which electron correlations work among $d$-orbital electrons, the $4f$ ground-state symmetry is not straightforwardly revealed since it is unclear which sites act as effective ligands for $f$ sites. Therefore, the determination of the $4f$ orbital symmetry in a realistic system itself is the important problem.
Recently we have reported the determination of $4f$ CEF ground-state symmetry by linear dichroism (LD) in hard x-ray photoemission spectroscopy. The $4f$-orbital symmetry is reflected in the LD in core-level photoemission spectra owing to the selection rules in the photoemission process. In this thesis, we show the polarization-dependent hard x-ray photoemission studies of cubic $YbB_{12}$, $CeB_6$, $CeAl_2$, and tetragonal $SmCu_2Si_2$. We have also perfomed the ion-model calculations including the full multiplet theory and the local CEF splitting for rare-earth core-level photoemission spectra, using the XTLS 9.0 program. The observed LD as well as the polarization-dependent spectra in two different photoelectron directions for $YbB_{12}$ are quantitatively reproduced by the theoretical simulations for the $\Gamma_8$ $4f$-ground-state symmetry. The LD for $CeB_6$ and that for $CeAl_2$ have different features where the former indicates the $\Gamma_8$ ground-state symmetry and the latter is well explained by the simulations for the $\Gamma_7$ ground state. In addition, the contributions from $4f^2$ final state for LDs in the Ce core-level photoemission spectra are almost negligible for the discussions of the ground-state symmetry for Ce compounds in the cubic systems. The experimental LDs of $SmCu_2Si_2$ at two significantly different photoelectron directions far from the c axis are well reproduced by the simulations for the $\Gamma_7^1$ symmetry.
Since LD in valence-band $4f$ photoemission spectra have also been expected by the ion-model spectral calculations, we have tried to observe $4f$ ground-state symmetry by the LD in valence-band $4f$ photoemission spectra of Yb and Sm compounds. The observed LDs in the $4f$ valence-band PES spectra of Yb compounds are smaller than that predicted from the calculations even in the tetragonal symmetry for Yb compounds. LD in $4f$ valence-band PES spectra of a Sm compound in tetragonal symmetry is found to be negligible, which suggests that the polarization-dependent core d-level excitations are much more useful and reliable for revealing the local $4f$-orbital symmetry than the $4f$ excitations.

# Contents

# Chapter 1

# Introduction

Ground- and excited-state orbital symmetry in strongly correlated electron systems play crucial rules in their functional properties. For example, the highly two-dimensional characteristics of the conducting carriers in high-temperature superconducting cuprates are due to their Cu $3d_{x^2-y^2}$ orbital symmetry in the $CuO_2$ planes. Strongly correlated rare-earth-based electron systems show various interesting behavior such as unconventional superconductivity [1, 2], multipolar ordering, formation of heavy fermionic states [3, 4, 5], nontrivial (Kondo) semiconducting behavior [6, 7, 8], and quantum criticality [9] at low temperatures. Ground-state $4f$-orbital symmetry determined by a crystalline-electric-field (CEF) splitting is very basic information on realistic strongly correlated electron systems. In contrast to the case of transition-metal oxides in which electron correlations work among $d$-orbital electrons, the $4f$ ground-state symmetry is not straightforwardly revealed since it is unclear which sites act as effective ligands for $f$ sites. Therefore, the determination of the $4f$ orbital symmetry in the realistic systems itself is the important problem.

A standard experimental technique for determining $4f$ levels with their symmetry is to analyze inelastic neutron scattering spectra and anisotropy in the magnetic susceptibility of single crystals. However, magnetic $4f$-$4f$ excitations are often hampered by the phonon excitations with a comparable energy scale for the former method, and for the latter, it is difficult to uniquely determine the symmetry due to the many free parameters for a unique description of the CEF potential. Recently reported determination of $4f$ ground-state symmetry for tetragonal Ce compounds by linear dichroism in Ce $3d-4f$ x-ray absorption spectroscopy [10, 11, 12, 13] is a powerful method for tetragonal compounds. However, it cannot be applicable for cubic crystal because there is no anisotropic axis. In addition, the rotational symmetry in $4f$ orbital around $z(c)$ axis cannot be distinguished in tetragonal systems.

Recently, we have reported that the determination of $4f$ CEF ground-state symmetry can be feasible by linear dichroism in hard x-ray photoemission spectroscopy [14, 15, 16, 17]. Since the selection rules work in photoemission, the $4f$-orbital symmetry is reflected in linear dichroism in core-level photoemission spectra. The controllable measurement parameter called the photoelectron detection direction enable to determine the $4f$ charge distribution even for cubic crystals and the rotational $4f$ orbital symmetry around $z(c)$ axis in tetragonal systems.

In this thesis we show polarization-dependent hard x-ray photoemission studies of cubic $YbB_{12}$, $CeB_6$, $CeAl_2$, and tetragonal $SmCu_2Si_2$. We have also performed the ion-model calculations including the full multiplet theory [18] and the local CEF splitting for rare-earth

core-level photoemission spectra using the XTLS 9.0 program [19]. The observed linear dichroism in $Yb^{3+}$ $3d$ core-level photoemission spectra of cubic $YbB_{12}$ are quantitatively reproduced by the ion-model calculations assuming the $\Gamma_8$ CEF-split ground state [15]. The experimental linear dichroism in Ce and $Sm^{3+}$ $3d$ core-level photoemission spectra of $CeB_6$,$CeAl_2$, $SmCu_2Si_2$ also can be analyzed by the ion-model calculations, and we have successfully determined the CEF-split $4f$ ground-state symmetry of these rare-earth compounds.
In addition, since linear dichroism in valence-band $4f$ photoemission spectra have also been expected by the ion-model spectral calculations, we have tried to observe $4f$ ground-state symmmetry by linear dichroism in valence-band $4f$ photoemission spectra of Yb and Sm compounds [20].

This thesis is organized in nine chapters as follows:
Chapter 1 is this introduction.
In Chapter 2, the strongly correlated $4f$ electronic states in rare-earth compounds are reviewed. The electronic features of the rare-earth compounds and the calculations of CEF Hamiltonians are also explained.
In this Chapter 3, theory of photoemission spectroscopy is explained in detail.
Chapter 4 is our experimental system and technique such as instrumental information for machines at BL19LXU in SPring-8 where we performed this study and the polarization-switching technique are introduced.
In Chapters 5, 6, and 7, the linear dichroism in rare-earth core-level photoemission studies of $YbB_{12}$, the cubic Ce compounds, and $SmCu_2Si_2$ are shown. We discuss the $4f$-orbital symmetry from our experimental results and simulations for each compounds.
Our obtained linear dichroism in valence-band $4f$ photoemission is referred in Chapter 8. The experimental linear dichroisms in 4f photoemission spectra measured at BL27SU in SPring-8 are shown.
Finally, we summarize the studies in Chapter 9.

# Chapter 2

# Strongly correlated $4f$ electronic structures in the rare-earth compounds

## 2.1 Characteristic behavior of rare-earth compounds

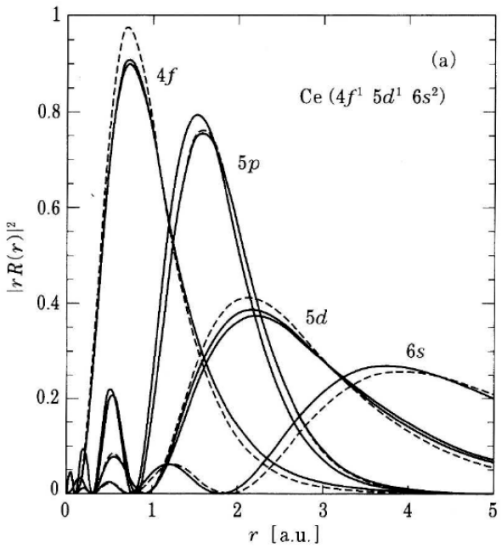


Figure 2.1: The radial distributions for the wave functions in Ce atoms [21]

Rare-earth ions have $4f^n5d6s^2(n$ = 0-14) electron configurations, in which the $4f$ electrons are spatially localized in rare-earth compounds. The $4f$-orbital radial distributions are nearer to the nuclear than those of the $5p$ core-level orbitals. Therefore, an ionic picture is a good starting point for describing their electronic structure as well as the origins of various phenomena in crystalline solids, where the strong Coulomb repulsion $U$ works between $4f$ electrons in rare-earth sites. The rare-earth $4f^n$ energy levels are split by spin-orbit coupling $\Delta_{so}$, and further split by a crystalline electric field (CEF) $\Delta_{CEF}$ in solids, by which the outer $4f$ charge distributions are deviated from spherical symmetry. In most rare-earth ions, $\Delta_{CEF} \ll \Delta_{so} \ll U$ as mentioned later.

In general, since several eV of Coulomb and exchange interactions and spin-orbit interactions of $10^{-1}$-$10^{0}$eV work in rare-earth compounds, the ground-state of $4f$ electrons are expressed by total angular momentum $J$ following the Hund's rules. In the case of rare-earth atoms, since the perturbation potential by neighboring atoms is orders of magnitude smaller than the split width between different $J$ multiplets (except for $Eu^{3+}$), the lowest $J$ multiplets are considered as the ground state in general. In this thesis CEF potentials have been treated mainly. The $2J$+1-fold degenerated lowest multiplet following the Hund's rules is split by CEF.

Though the interactions worked to $4f$ orbital for rare-earth ions are almost nothing due to the narrower radial distribution of the $4f$ orbital as above, the localized $4f$ orbital electrons

interact with the neighboring conducting electrons each other. So that the indirect interactions through conducting electrons work between localized moment in rare-earth compounds. The hybridization between conducting electrons and $4f$ electrons are called $cf$ hybridization and expressed as $J_{cf}$. The relations between the behavior in rare-earth compounds and the intensity of $cf$ hybridization $J_{cf}$ at low temperature is shown in Fig 2.2 called Doniach phase diagram. Rare-earth compounds which have $4f$ electrons show the various interesting phenomena such as unconventional and/or high-temperature superconductivity, spin and charge ordering, formation of heavy fermionic states, nontrivial (Kondo) semiconducting behavior, and quantum criticality. Ground-state 4f-orbital symmetry determined by CEF splitting is very basic information to reveal the origin of phenomena in these strongly correlated rare-earth.

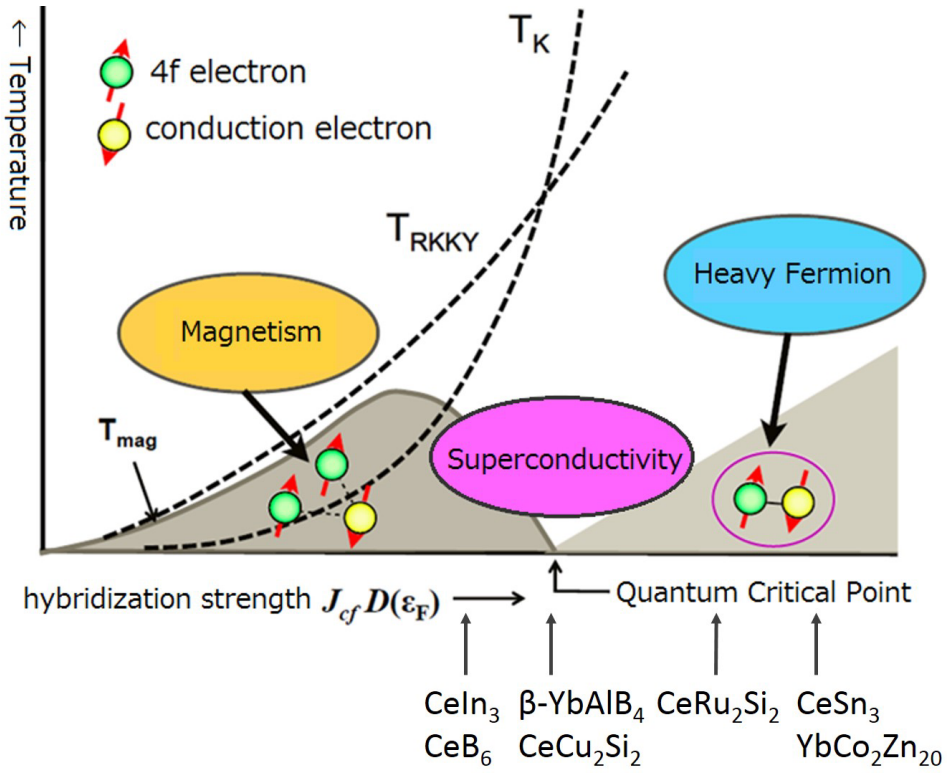


Figure 2.2: Doniach phase diagram[21]

## 2.2 Multiplet structures in multielectron system

The Hamiltonian when there are Z electrons in an ion/atom is expressed as:

$$\mathcal{H}_e = \sum_i^Z (-\frac{\hbar^2}{2m}\nabla_i^2 - \frac{Ze^2}{r_i}) + \underbrace{\sum_{i<j}^Z \frac{e^2}{r_{ij}}}_{\textit{Coulomb interaction between electrons}} \qquad (r_{ij} = |r_i - r_j|). \quad (2.1)$$

In general, where the Slater determinant $\Phi' \neq \Phi$, $\langle\Phi'|e^2/r_{ij}|\Phi\rangle \neq 0$. The multielectron configurations expressed by the Slater determinant cannot be the eigenstate for Hamiltonian

$\mathcal{H}_e$, due to the Coulomb interaction between electrons $\sum e^2/r_{ij}$. Since the Coulomb and exchange interactions between electrons originate from the orbital dependence, the multiplet structures appear in photoemission spectra for the core-level site in which the incomplete shell with strong localization exist.

We consider the simplest $(1s)^2(2s)^2(2p)^2$ electron configuration for the multiplet structures as an example from here. Since $L$ and $S$ are good quantum numbers, eigenstates can be specified by $L$ ,$S$. The configurations of electrons and multiplets for $(2p)^2$ are shown in Fig. 2.3.

The notation of multiplet is denoted by ${}^{2S+1}L_J$. Considering the multiplet ${}^1D$($L$=2, $S$=0),

| | $M_L$ | $M_S$ | L | S | | |
|---|---|---|---|---|---|---|
|  | 2 | 0 | 2 | 0 | $\Phi_1$ | |
|  | 1 | 1 | 1 | 1 | $\Phi_2$ | |
|  | 1 | 0 | 1, 2 | 0 | $\Phi_3$ | ${}^1$D(L=2, S=0) degeneracy:5 |
|  | 1 | 0 | 1, 2 | 0 | $\Phi_4$ | $\Phi_1, \Phi_{15}$, |
|  | 1 | -1 | 1 | 1 | $\Phi_5$ | $(1/\sqrt{2})(\Phi_3 - \Phi_4)$, |
|  | 0 | 1 | 1 | 1 | $\Phi_6$ | $(1/\sqrt{2})(\Phi_{12} - \Phi_{13})$, |
|  | 0 | 0 | 0, 1, 2 | 0, 1 | $\Phi_7$ | $(1/\sqrt{6})(-\Phi_7 - \Phi_8 + 2\Phi_9)$ |
|  | 0 | 0 | 0, 1, 2 | 0, 1 | $\Phi_8$ | ${}^1$S(L=0, S=0) degeneracy:1 |
|  | 0 | 0 | 0, 2 | 0 | $\Phi_9$ | $(1/\sqrt{3})(-\Phi_7 + \Phi_8 + \Phi_9)$ |
|  | 0 | -1 | 1 | 1 | $\Phi_{10}$ | ${}^3$P(L=1, S=1) degeneracy:9 |
|  | -1 | 0 | 1 | 1 | $\Phi_{11}$ | $\Phi_2, \Phi_5, \Phi_6, \Phi_{10}, \Phi_{11}, \Phi_{14}$, |
|  | -1 | 0 | 1, 2 | 0 | $\Phi_{12}$ | $(1/\sqrt{2})(\Phi_3 + \Phi_4)$, |
|  | -1 | 0 | 1, 2 | 0 | $\Phi_{13}$ | $(1/\sqrt{2})(\Phi_{12} + \Phi_{13})$, |
|  | -1 | -1 | 1 | 1 | $\Phi_{14}$ | $(1/\sqrt{2})(\Phi_7 + \Phi_8)$ |
|  | -2 | 0 | 2 | 0 | $\Phi_{15}$ | |

Figure 2.3: Configurations of electrons and multiplets for $(2p)^2$

$^1D$ has the degeneracy factor $(2L+1)(2S+1)=5$, and $\Phi_1$,$\Phi_5$ are corresponding in Fig. 2.3. To find the remaining three components of $^1D$, we use one-electron raising and lowering operator $l_\pm \equiv l_x \pm i l_y$. By the operator, the following relations come into existence.

$$l_+ l_- = (l_x + i l_y)(l_x - i l_y) = \hat{l}^2 - l_z^2 + l_z \tag{2.2}$$

$$l_+ l_- |lm\rangle = l(l+1) - m(m-1)|lm\rangle \tag{2.3}$$

Also the relations are established.

$$[l_z, l_-] = -l_- \tag{2.4}$$

$$\begin{aligned} l_z l_- |lm\rangle &= (-l_- + l_- l_z |lm\rangle \\ &= (m-1)(l_-|lm\rangle) \propto |l, m-1\rangle \end{aligned} \tag{2.5}$$

From Eqs. 2.3, 2.5, the following relation can be obtained.

$$l_-|lm\rangle = \sqrt{l(l+1) - m(m-1)}|l, m-1\rangle \tag{2.6}$$

Where $L_- \equiv l_{1-} + l_{2-}$,

$$\begin{aligned} L_-\Phi(L=2, M_L=2) &= L_-\Phi_1 = 2\Phi(L=2, M_L=1) && (2.7)\\ &= (l_{1-} + l_{2-})|1\frac{1}{2}\rangle|1-\frac{1}{2}\rangle \\ &= \sqrt{2}|1\frac{1}{2}\rangle|0-\frac{1}{2}\rangle - |1-\frac{1}{2}\rangle|0\frac{1}{2}\rangle \\ &= \sqrt{2}(\Phi_3 - \Phi_4). && (2.8) \end{aligned}$$

Therefore, the following solution can be obtained.

$$\Phi(L=2, M_L=1) = (1/\sqrt{2})(\Phi_3 - \Phi_4) \tag{2.9}$$

Approaching similarly, from the following formula as:

$$\begin{aligned} L_-\Phi(L=2, M_L=1) &= \sqrt{6}\Phi(L=2, M_L=0) && (2.10)\\ &= (1/\sqrt{2})(l_{1-} + l_{2-}(\Phi_3 - \Phi_4) \\ &= \frac{1}{\sqrt{2}}(l_{1-} + l_{2-})(|1\frac{1}{2}\rangle|0-\frac{1}{2}\rangle - |1-\frac{1}{2}\rangle|0\frac{1}{2}\rangle) \\ &= |1\frac{1}{2}\rangle|-1-\frac{1}{2}\rangle - |1-\frac{1}{2}\rangle|-1\frac{1}{2}\rangle + |0\frac{1}{2}\rangle|0-\frac{1}{2}\rangle \\ &= \Phi_7 - \Phi_8 + 2\Phi_9, && (2.11) \end{aligned}$$

the following solution can be also obtained.

$$\Phi(L=2, M_L=0) = (1/\sqrt{6})(\Phi_7 - \Phi_8 + 2\Phi_9) \tag{2.12}$$

In addition, the results also shown below.

$$\begin{aligned} L_{-}\Phi(L=2,M_L=0) &= \sqrt{6}\Phi(L=2,M_L=-1) \qquad (2.13)\\ &= (1/\sqrt{6})(l_{1-}+l_{2-})(\Phi_7-\Phi_8+2\Phi_9)\\ &= \frac{1}{\sqrt{6}}(l_{1-}+l_{2-})(|1\frac{1}{2}\rangle|-1-\frac{1}{2}\rangle-|1-\frac{1}{2}\rangle|-1\frac{1}{2}\rangle\\ &\quad +2|0\frac{1}{2}\rangle|0-\frac{1}{2}\rangle)\\ &= \frac{1}{\sqrt{3}}(3|0\frac{1}{2}\rangle|-1-\frac{1}{2}\rangle-3|0-\frac{1}{2}\rangle|-1\frac{1}{2}\rangle)\\ &= \sqrt{3}(\Phi_{12}-\Phi_{13}) \qquad (2.14) \end{aligned}$$

$$\Phi(L=2,M_L=-1)=(1/\sqrt{2})(\Phi_{12}-\Phi_{13}). \qquad (2.15)$$

Therefore, the electron configuration for multiplet ${}^1D(L=2,S=0)$ is corresponding to $\Phi_1$,$\Phi_{15}$,$1/\sqrt{2}(\Phi_3-\Phi_4)$,$1/\sqrt{2}(\Phi_{12}-\Phi_{13})$,$1/\sqrt{6}(\Phi_7-\Phi_8+2\Phi_9)$. Considering ${}^1S(L=0,S=0)$ multiplet, the electron configuration for multiplet ${}^1S$ is corresponding to $1/\sqrt{3}(-\Phi_7+\Phi_8+\Phi_9)$.

$$\Phi_7 \;:\; \frac{1}{\sqrt{2}}R_{2p}(r_1)R_{2p}(r_2)[Y_1^1(\theta_1,\phi_1)\alpha(\zeta_1)Y_1^{-1}(\theta_2,\phi_2)\beta(\zeta_2)-Y_1^1(\theta_2,\phi_2)\alpha(\zeta_2)Y_1^{-1}(\theta_1,\phi_1)\beta(\zeta_1)] \qquad (2.16)$$

$$\Phi_8 \;:\; \frac{1}{\sqrt{2}}R_{2p}(r_1)R_{2p}(r_2)[Y_1^1(\theta_1,\phi_1)\beta(\zeta_1)Y_1^{-1}(\theta_2,\phi_2)\alpha(\zeta_2)-Y_1^1(\theta_2,\phi_2)\beta(\zeta_2)Y_1^{-1}(\theta_1,\phi_1)\alpha(\zeta_1)] \qquad (2.17)$$

$$\Phi_9 \;:\; \frac{1}{\sqrt{2}}R_{2p}(r_1)R_{2p}(r_2)Y_1^0(\theta_1,\phi_1)Y_1^0(\theta_2,\phi_2)[\alpha(\zeta_1\beta_2-\alpha_2\beta_1] \qquad (2.18)$$

$Y_k^m(\theta,\phi)$ denote spherical surface harmonics. Where the energy level for $2p$ with $2p^1$ configuration is defined as $2h(2p)$, $Q(i,j)$ and $J(i,j)$ are written as:

$$Q(i,j) = \int\int |R_{2p}(r_1)|^2|R_{2p}(r_2)|^2(e^2/r_{12})|Y_1^i(\theta_1,\phi_1)|^2|Y_1^j(\theta_2,\phi_2)|^2 d\boldsymbol{r_1}d\boldsymbol{r_2} \qquad (2.19)$$

$$J(i,j) = \int\int |R_{2p}(r_1)|^2|R_{2p}(r_2)|^2(e^2/r_{12})Y_1^{j*}(\theta_1,\phi_1)Y_1^{i*}(\theta_2,\phi_2)Y_1^i(\theta_1,\phi_1)Y_1^j(\theta_2,\phi_2)d\boldsymbol{r_1}d\boldsymbol{r_2} \qquad (2.20)$$

,

the Hamiltonian is given by:

$$\mathcal{H}_{789} = = \begin{pmatrix} 2h(2p)+Q(1,1) & -J(1,1) & -J(1,0)\\ -J(1,1) & 2h(2p)+Q(1,1) & J(1,0)\\ -J(1,0) & J(1,0) & 2h(2p)+Q(0,0) \end{pmatrix}. \qquad (2.21)$$

By diagonalizing this matrix, we can obtain the eigenenergies $E({}^3P)$,$E({}^1D)$,$E({}^1S)$.
Here we expand the terms of $e^2/r_{ij}$. From the relation as follows:

$$\phi_{n_il_im_i}(\boldsymbol{r}_j)=R_{n_il_i}(r_j)Y_{l_im_i}(\theta_j,\phi_j), \qquad (2.22)$$

the expansion of the terms of $e^2/r_{ij}$ is given by:

$$\begin{aligned}
&\langle\phi_{n_2l_2m_2}\phi_{n_1l_1m_1}|e^2/r^{12}|\phi_{n_3l_3m_3}\phi_{n_4l_4m_4}\rangle \\
\equiv\ & \int\int\int d\boldsymbol{r}_1 \int\int\int d\boldsymbol{r}_2 \phi^*_{n_1l_1m_1}(\boldsymbol{r}_1)\phi^*_{n_2l_2m_2}(\boldsymbol{r}_2)\frac{e^2}{|\boldsymbol{r}_1-\boldsymbol{r}_2|}\phi_{n_3l_3m_3}((r)_1)\phi_{n_4l_4m_4}(\boldsymbol{r}_2)
\end{aligned} \tag{2.23}$$

.

The term of $\frac{1}{|\boldsymbol{r}_1-\boldsymbol{r}_2|}$ can be written as:

$$\begin{aligned}
\frac{1}{|\boldsymbol{r}_1-\boldsymbol{r}_2|} &= \{r_1^2+r_2^2-2r_1r_2\cos\theta\}^{-1/2} \\
&= \frac{1}{r_>}\{1-2\frac{r_<}{r_>}\cos(\theta)+(\frac{r_<}{r_>})^2\}^{-1/2} \\
&= \sum_{k=0}^{\infty}\frac{r_<^k}{r_>^{k+1}}P_k(\cos\theta)
\end{aligned} \tag{2.24}$$

where $r_> \equiv max(r_1,r_2)$,$r_< \equiv min(r_1,r_2)$, and $P_k(\cos\theta)$is a Legendre polynomial expressed as follows:

$$\begin{aligned}
P_k(\cos\theta) &= \frac{4\pi}{2k+1}\sum_{m=-k}^{k}Y_k^m(\theta_1,\phi_1)Y_k^{m*}(\theta_2,\phi_2) \\
&= \frac{4\pi}{2k+1}\sum_{m=-k}^{k}(-1)^m Y_k^m(\theta_1,\phi_1)Y_k^{-m}(\theta_2,\phi_2) \\
&= \sum_{m=-k}^{k}(-1)^m C_k^m(\theta_1,\phi_1)C_k^{-m}(\theta_2,\phi_2).
\end{aligned} \tag{2.25}$$

$C_m^k$ are areal harmonics and can be represented by

$$C_k^m(\theta,\phi) \equiv \sqrt{\frac{4\pi}{2k+1}}Y_k^m(\theta,\phi) \tag{2.26}$$

as with the Eq. 2.43. Therefore,

$$\frac{1}{|\boldsymbol{r}_1-\boldsymbol{r}_2|} = \sum_{k=0}^{\infty}\frac{r_<^k}{r_>^{k+1}}\{\sum_{q=-k}^{k}(-1)^q C_k^q(\theta_1,\phi_1)C_k^{-q}(\theta_2,\phi_2)\}. \tag{2.27}$$

. Substituting this to Eq. 2.23, the following formula can be obtained.

$$
\begin{aligned}
& \langle \phi_{n_2 l_2 m_2} \phi_{n_1 l_1 m_1} | e^2 / r^{12} | \phi_{n_3 l_3 m_3} \phi_{n_4 l_4 m_4} \rangle \\
= \; & e^2 \int_0^\infty r_1^2 dr_1 \int_0^\pi \sin_{\theta_1} d\theta_1 \int_0^{2\pi} d\phi_1 \int_0^\infty r_2^2 dr_2 \int_0^\pi \sin\theta_2 d\theta_2 \int_0^{2\pi} d\phi_2 \times \\
& R^*_{n_1 l_1}(r_1) Y^{m_1 *}_{l_1}(\theta_1, \phi_1) R^*_{n_2 l_2}(r_2) Y^{m_2 *}_{l_2}(\theta_2, \phi_2) \times \\
& \sum_{k=0}^{\infty} \frac{r_<^k}{r_>^{k+1}} \{ \sum_{q=-k}^{k} (-1)^q C^{(k)}_q(\theta_1, \phi_1) C^{(k)}_{-q}(\theta_2, \phi_2) \times \\
& R_{n_3 l_3}(r_1) Y^{m_3}_{l_3}(\theta_1, \phi_1) R_{n_4 l_4}(r_2) Y^{m_4}_{l_4}(\theta_2, \phi_2) \\
= \; & \sum_{k=0}^{\infty} [ e^2 \int_0^\infty \int_0^\infty R_{n_1 l_1}(r_1) R_{n_2 l_2}(r_2) \frac{r_<^k}{r_>^{k+1}} R_{n_3 l_3}(r_1 R_{n_4 l_4}(r_2) r_1^2 r_2^2 dr_1 dr_2 \times \\
& \sum_{q=-k}^{k} (-1)^q \{ \int_0^\pi \int_0^{2\pi} Y^{m_1 *}_{l_1}(\theta_1, \phi_1) C^{(k)}_q(\theta_1, \phi_1) Y^{m_3}_{l_3}(\theta_1, \phi_1) \sin\theta_1 d\theta_1 d\phi_1 \times \\
& \int_0^\pi \int_0^{2\pi} Y^{m_2 *}_{l_2}(\theta_2, \phi_2) C^{(k)}_{-q}(\theta_2, \phi_2) Y^{m_4}_{l_4}(\theta_2, \phi_2) \sin\theta_2 d\theta_2 d\phi_2 \} ]
\end{aligned} \tag{2.28}
$$

When we define the following terms as:

$$
\int_0^\pi \int_0^{2\pi} Y^{m_1 *}_{l_1}(\theta_1, \phi_1) C^{(k)}_q(\theta_1, \phi_1) Y^{m_3}_{l_3}(\theta_1, \phi_1) \sin\theta_1 d\theta_1 d\phi_1 \equiv c^k(l_1 m_1, l_3 m_3) \delta_{q, m_1 - m_3} \tag{2.29}
$$

$$
\int_0^\pi \int_0^{2\pi} Y^{m_2 *}_{l_2}(\theta_2, \phi_1) C^{(k)}_q(\theta_2, \phi_2) Y^{m_4}_{l_4}(\theta_2, \phi_2) \sin\theta_2 d\theta_2 d\phi_2 \equiv c^k(l_2 m_2, l_4 m_4) \delta_{-q, m_2 - m_4}, \tag{2.30}
$$

the relation written as:

$$
\begin{aligned}
c^k(lm, l'm') &= \int_0^\pi \int_0^{2\pi} Y^{m *}_l(\theta, \phi) C^{(k)}_{m-m'}(\theta, \phi) Y^{m'}_{l'}(\theta, \phi) \sin\theta d\theta d\phi \\
&= \sqrt{\frac{4\pi}{2k+1}} \int_0^\pi \int_0^{2\pi} Y^{m *}_l(\theta, \phi) Y^{m-m'}_k(\theta, \phi) Y^{m'}_{l'}(\theta, \phi) \sin\theta d\theta d\phi
\end{aligned} \tag{2.31}
$$

can be obtained. When it has a finite value, $|l - l'| \leq k \leq l + l'$. The following term in Eq. 2.28 is written as:

$$
\begin{aligned}
& \sum_{q=-k}^{k} (-1)^q \{ \int_0^\pi \int_0^{2\pi} Y^{m_1 *}_{l_1}(\theta_1, \phi_1) C^{(k)}_q(\theta_1, \phi_1) Y^{m_3}_{l_3}(\theta_1, \phi_1) \sin\theta_1 d\theta_1 d\phi_1 \times \\
& \int_0^\pi \int_0^{2\pi} Y^{m_2 *}_{l_2}(\theta_2, \phi_2) C^{(k)}_{-q}(\theta_2, \phi_2) Y^{m_4}_{l_4}(\theta_2, \phi_2) \sin\theta_2 d\theta_2 d\phi_2 \} \\
= \; & (-1)^{m_1 - m_3} c^k(l_1 m_1, l_3 m_3) c^k(l_2 m_2, l_4 m_4) \delta_{m_1 + m_2 + m_3 + m_4}.
\end{aligned} \tag{2.32}
$$

Therefore,

$$\begin{aligned}
&\langle\phi_{n_2l_2m_2}\phi_{n_1l_1m_1}|e^2/r^{12}|\phi_{n_3l_3m_3}\phi_{n_4l_4m_4}\rangle \\
= \;& e^2\int_0^\infty r_1^2dr_1\int_0^\pi \sin_{\theta_1}d\theta_1\int_0^{2\pi}d\phi_1\int_0^\infty r_2^2dr_2\int_0^\pi \sin\theta_2 d\theta_2\int_0^{2\pi}d\phi_2\times \\
& \sum_{k=0}^{\infty}(-1)^{m_1-m_3}c^k(l_1m_1,l_3m_3)c^k(l_2m_2,l_4m_4)V^k(n_1l_1,n_2l_2;n_3l_3,n_4l_4)\times\delta_{m_1+m_2,m_3+m_4} \qquad (2.33)\\
& V^k(n_1l_1,n_2l_2;n_3l_3,n_4l_4) \\
= \;& e^2\int_0^\infty\int_0^\infty R^*_{n_1l_1}(r_1)R^*_{n_2l_2}(r_2)\frac{r_<^k}{r_>^{k+1}}R_{n_3l_3}(r_1)R_{n_4l_4}(r_2)r_1^2r_2^2dr_1dr_2. \qquad (2.34)
\end{aligned}$$

Where $n_1l_1 = n_3l_3$,$n_2l_2 = n_3l_3$,

$$\begin{aligned}
& V^k(n_1l_1,n_2l_2;n_3l_3,n_4l_4) \\
= \;& \int_0^\infty\int_0^\infty |R_{n_1l_1}(r_1)|^2|R_{n_2l_2}(r_2)|^2\frac{e^2}{r_>}(\frac{r_<}{r_>})^k r_1^2r_2^2dr_1dr_2 \\
\equiv \;& F^k(n_1l_1,n_2l_2). \qquad (2.35)
\end{aligned}$$

Where $n_1l_1 = n_4l_4$,$n_2l_2 = n_3l_3$,

$$\begin{aligned}
& V^k(n_1l_1,n_2l_2;n_3l_3,n_4l_4) \\
= \;& \int_0^\infty\int_0^\infty R_{n_1l_1}(r_1)R_{n_2l_2}(r_2)\frac{e^2}{r_>}(\frac{r_<}{r_>})^k R_{n_2l_2}(r_1)R_{n_1l_1}(r_2)r_1^2r_2^2dr_1dr_2 \\
\equiv \;& G^k(n_1l_1,n_2l_2). \qquad (2.36)
\end{aligned}$$

In addition, where $n_1l_1 = n_2l_2 = nl$, $G^k(nl,nl) = F^k(nl,nl)$. $F^k(n_1l_1,n_2l_2)$ and $G^k(n_1l_1,n_2l_2)$ are called Slater integrals. By Slater integral $F^k(2p,2p) \equiv F^k$, $\mathcal{H}_{789}$ is expressed as:

$$\begin{aligned}
\mathcal{H}_{789} = \;& \begin{pmatrix} 2h(2p)+F^0+\frac{1}{25}F^2 & -\frac{6}{25}F^2 & -\frac{3}{25}F^2 \\ -\frac{6}{25}F^2 & 2h(2p)+F^0+\frac{1}{25}F^2 & \frac{3}{25}F^2 \\ -\frac{3}{25}F^2 & \frac{3}{25} & 2h(2p)+F^0+\frac{4}{25}F^2 \end{pmatrix} \\
= \;& (2h(2p)+F^0+\frac{1}{25}F^2)\begin{pmatrix} 1&0&0\\0&1&0\\0&0&1\end{pmatrix}+\frac{F^2}{25}\begin{pmatrix} 0&-6&-3\\-6&0&3\\-3&3&3\end{pmatrix}. \qquad (2.37)
\end{aligned}$$

The corresponding eigenstates are given by:

$$^1S\begin{pmatrix} -1/\sqrt{3}\\1/\sqrt{3}\\1/\sqrt{3}\end{pmatrix},\;\; ^1D\begin{pmatrix} 1/\sqrt{6}\\-1/\sqrt{6}\\2/\sqrt{6}\end{pmatrix},\;\; ^3P\begin{pmatrix} 1/\sqrt{2}\\1/\sqrt{2}\\0\end{pmatrix}. \qquad (2.38)$$

Therefore, the multiplet energy splitting for $2p$ orbital becomes as shown in Fig. 2.4.

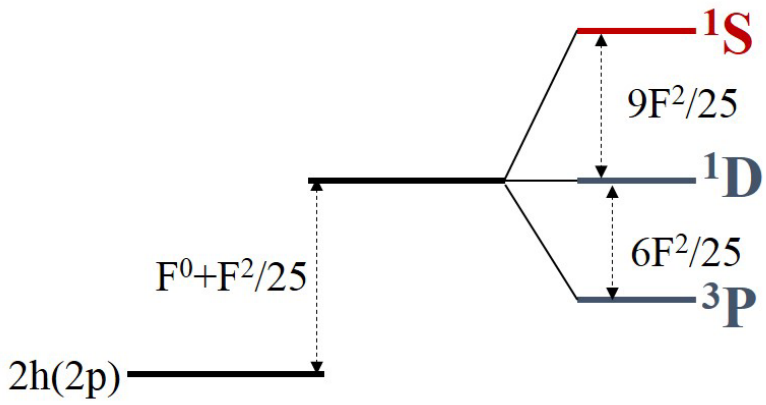


Figure 2.4: Energy diagram of multiplet energy splitting for $2p$ orbital

## 2.3 The interactions between crystalline electric field and rare-earth compounds

The charge distributions for a free single atom/ion have a spherical shape. On the other hand, when the atoms are ionized in solid, since the ions inside of compounds receive the electric field from the neighboring charged ions, the charge distributions become not spherical shape and the phenomena originated from these anisotropic charge distributions can be observed in compounds. The crystalline electric field (CEF) effect is the phenomena which the neighboring atoms (ligands) occur a certain amount of electric potential that determine the symmetry of charge distribution at the center atom. Therefore, the Hamiltonian about the center atoms consists of Hamiltonian for free ions and that by the CEF potential $V_{CEF}$. So that,

$$\mathcal{H} = \mathcal{H}_{\text{free ion}} + \mathcal{H}_{\text{CEF}}. \tag{2.39}$$

Since the $V_{\text{CEF}}$ is the electric potential, this problem can be treated as a part of Stark effect. The scale of the CEF potential depend on the kind of element at the center position and can be compared with other interactions. The Hamiltonian is circumstantially written as:

$$\mathcal{H} = \underbrace{-\frac{\hbar^2}{2m}\sum_i \nabla_i^2 - \sum_i \frac{Ze^2}{r_i}}_{=\mathcal{H}_0} + \frac{1}{2}\sum_{i\neq j}\frac{e^2}{r_{ij}} + \sum \zeta_i(r)\, \boldsymbol{l}_i \cdot \boldsymbol{s}_i + \mathcal{H}_{CEF}, \tag{2.40}$$

where $\zeta_i(r)\, \boldsymbol{l}_i \cdot \boldsymbol{s}_i$ stands for relative spin-orbit interaction and $\frac{e^2}{r_{ij}}$ denotes Coulomb interactions between $4f$ electrons, and the two terms at first (defined as $\mathcal{H}_0$) are unperturbed terms. The comparison between the CEF potential and other interactions is shown below. In $4f$ electron system, the scales of these three interactions have different order. The energy scale of Coulomb interaction is the largest about several eV, and that of CEF splitting is the smallest about $\sim 10^{-2}$ eV. Considering the narrower radial distribution of $4f$ orbital, it can be intuitively understood that the Coulomb interaction is the strongest. The difference between rare-earth compounds and transition metal oxide derive from the different scale of spin-orbit

| | |
|---|---|
| $V_{CEF} < \zeta_i(r)\,\mathbf{l_i}\cdot\mathbf{s_i} < \frac{e^2}{r_{ij}}$ | rare-earth compound |
| $\zeta_i(r)\,\mathbf{l_i}\cdot\mathbf{s_i} < V_{CEF} < \frac{e^2}{r_{ij}}$ | transition metal oxide |
| $V_{CEF} > \frac{e^2}{r_{ij}}$ | organic compound |

interaction due to the atomic number.
To treat these problem by quantum mechanics, the suitable quantum number must be chosen, that the operators can reflect the symmetry of the system accurately and convert into Hamiltonian. For understanding of these interaction, we consider in the order corresponding to Coulomb interactions inside of atoms, spin-orbit interaction, CEF potential.
The operators for Coulomb interactions can convert into orbital angular momentum $\boldsymbol{L}$ and spin angular momentum $\boldsymbol{S}$. Therefore the Coulomb interactions occur the multiplet structure expressed by quantum number $\boldsymbol{L}$,$\boldsymbol{S}$. Since the scale of spin-orbit interaction in rare-earth ion is enough smaller (about $10^{-1}$ – 1 eV) than that of Coulomb potential $\frac{e^2}{r_{ij}}$, the spin-orbit interaction also can be expressed by LS combination. Spin-orbit interaction can convert into total angular momentum $\boldsymbol{J} = \boldsymbol{L} + \boldsymbol{S}$. Considering only Coulomb interaction and spin-orbit interaction, the quantum number $\boldsymbol{L}$,$\boldsymbol{S}$,$\boldsymbol{J}$ become good quantum number and the ground state for rare-earth ion in spherical symmetry is expressed by Fund's rules. However, when the CEF potential is introduced, the total angular momentum $\boldsymbol{J}$ becomes not good quantum number exactly due to the anisotropic charge distribution. On the other hand, for most of case, the CEF splitting in rare-earth compounds can be approximated as enough smaller than spin-orbit interaction. So that the off-diagonal terms of CEF operators for ground-state $\boldsymbol{J}$ can be ignored. As a consequence, the total angular momentum $\boldsymbol{J}$ in $4f$ electrons system can be treated as good quantum number.

## 2.4 Expression for crystalline electric field in rare-earth compounds

### 2.4.1 General solution

As mentioned earlier, the influence by the neighboring ligands can be treated as the CEF potentials, and that occurs anisotropic $4f$ charge distributions. On the other hand, in case of considering only unperturbed Hamiltonian $\mathcal{H}_0$, the $4f$ charge distribution is spherical shape. $\mathcal{H}_0$ is written as:

$$\mathcal{H}_0 = -\frac{\hbar^2}{2m}\nabla^2 - \frac{Ze^2}{r}. \tag{2.41}$$

The CEF potential $V_{CEF}$ can be separated into radial components and angular components, as follows:

$$V_{CEF}(r,\theta,\phi) = \sum_{k=0}^{\infty}\sum_{m=-k}^{k} C_k^m(\theta,\phi)\cdot A_{km}\cdot r^k. \tag{2.42}$$

The normalized spherical surface harmonics for angular components $C_k^m(\theta, \phi)$ is given by:

$$C_k^m(\theta, \phi) = \sqrt{\frac{4\pi}{2k+1}} Y_k^m(\theta, \phi). \tag{2.43}$$

The above expansion is called multipole expansion. For the applicable multipole expansion, since $V_{CEF}$ needs to be converted depending on the symmetry of the system, it is necessary to know the symmetry of the neighboring ligands for the center atom.
In multipole expansion, though Eq. 2.42 is expansed for any $k$ and $m$, the term is the zero-order term ($k = 0$), that the contributions from macro phenomena such as lattice energy and heat is large. However, this term has little influence on electric character and transition of electrons.
The CEF parameters $A_{km}$ is generally written by notation of Stevens[22] or Lea Leask Wolf[23]. In this thesis, we use Stevens's notation.

### 2.4.2 Stevens' operators for rare-earth compounds

When the CEF splitting energy is small, eigenvalues for all $J$ subspaces can be calculated by Stevens' CEF operator. Since the hybridization between different $J$ multiplet terms can be ignored for most of rare-earth compounds, the assumption by Stevens come into existence. On the other hand, in the case where the scale of the spin orbit interaction is as large as that of the CEF splitting as in $Eu^{3+}$ or the case where a hybridization of the $J$ multiplet is observed due to the larger CEF splitting than the splitting between $J = 5/2$ and $J = 7/2$ as $CeRh_3B_2$, this method cannot be appropriate exceptionally. So that this method confines all the CEF calculations to the minimum $J$ multiplet term, therefore the dimension of the diagonal matrix required for the calculation can be drastically reduced [22]. It is especially beneficial in the $4f$ electron system, since very large amounts of CEF calculation are required. For example, considering the $f^3$ configuration, since three orbitals of the 14 orbitals are occupied by electrons, there are $\binom{14}{3} = \frac{14 \cdot 13 \cdot 12}{2 \cdot 3} = 364$ wave functions and the matrix for CEF calculation is also very large. As increasing of this number of electrons, thousands of matrix calculations must be required. Recently it is not difficult to calculate thousands of determinants, but still approximate Stevens is convenient to easily understand the information of the CEF. This Stevens ' method is called Stevens' calculation method [22].
In Stevens' calculation method, the CEF potential is expressed by the Stevens' operator.

$$V_{CEF} = \sum_{k,m} B_{km} O_{km} \tag{2.44}$$

In this method, it is the most important that the operators in Eq. 2.42 and Eq. 2.44 are corresponding on one-on-one. In general, the components of full-angular momentum $J_x$,$J_y$,$J_z$ are the simplest operators to define the multiplet terms with L, S, J. So that we should find the operators which can be represented by a combination of $J_x$, $J_y$ and $J_z$ and which are commutative for all symmetric operations, such as the potential of the CEF Hamiltonian.
Firstly, as shown in Fig. 2.5, we consider the case where six ions (charge $q$) are placed in (±a, 0,0), (0, ±b, 0), (0,0, ±c). Considering until the sixth order term, the CEF potential

$V_{CEF}$ created by these ions at the position $\boldsymbol{r}$ is given by [24]:

$$
\begin{aligned}
V_{CEF}(\boldsymbol{r}) &= q\left(\frac{1}{\{(x-a)^2+y^2+z^2\}^{1/2}}+\frac{1}{\{(x+a)^2+y^2+z^2\}^{1/2}}+\frac{1}{\{x^2+(y-b)^2+z^2\}^{1/2}}\right.\\
&\left.+\frac{1}{\{x^2+(y+b)^2+z^2\}^{1/2}}+\frac{1}{\{x^2+y^2+(z-c)^2\}^{1/2}}+\frac{1}{\{x^2+y^2+(z+c)^2\}^{1/2}}\right)\\
&\simeq q\left[\frac{2}{a}+\frac{2}{b}+\frac{2}{c}+(\frac{2}{a^3}-\frac{1}{b^3}-\frac{1}{c^3})x^2+(\frac{2}{b^3}-\frac{1}{c^3}-\frac{1}{a^3})y^2+(\frac{2}{c^3}-\frac{1}{a^3}-\frac{1}{b^3})z^2\right.\\
&+\frac{1}{4}\left\{(\frac{8}{a^5}+\frac{3}{b^5}+\frac{3}{c^5})x^4+(\frac{8}{b^5}+\frac{3}{c^5}+\frac{3}{a^5})y^4+(\frac{8}{c^5}+\frac{3}{a^5}+\frac{3}{b^5})z^4\right\}\\
&-\frac{3}{2}(\frac{4}{a^5}+\frac{4}{b^5}-\frac{1}{c^5})x^2y^2-\frac{3}{2}(\frac{4}{b^5}+\frac{4}{c^5}-\frac{1}{a^5})y^2z^2-\frac{3}{2}(\frac{4}{c^5}+\frac{4}{a^5}-\frac{1}{b^5})z^2x^2\\
&+\frac{1}{8}\left\{(\frac{16}{a^7}-\frac{5}{b^7}-\frac{5}{c^7})x^6+(\frac{16}{b^7}-\frac{5}{c^7}-\frac{5}{a^7})y^6+(\frac{16}{c^7}-\frac{5}{a^7}-\frac{5}{b^7})z^6\right\}\\
&+\frac{15}{8}\left\{(\frac{6}{a^7}-\frac{8}{b^7}-\frac{1}{c^7})x^2y^4+(\frac{6}{a^7}-\frac{8}{c^7}-\frac{1}{b^7})x^2z^4+(\frac{6}{b^7}-\frac{8}{a^7}-\frac{1}{c^7})y^2x^4\right.\\
&\left.+(\frac{6}{b^7}-\frac{8}{c^7}-\frac{1}{a^7})y^2z^4+(\frac{6}{c^7}-\frac{8}{a^7}-\frac{1}{b^7})z^2x^4+(\frac{6}{c^7}-\frac{8}{b^7}-\frac{1}{a^7})z^2y^4\right\}\\
&\left.+\frac{45}{2}(\frac{1}{a^7}+\frac{1}{b^7}+\frac{1}{c^7})x^2y^2z^2)\right]. \qquad (2.45)
\end{aligned}
$$

Also the electrostatic interaction energy of electrons at the position $\boldsymbol{r}$ is given by:

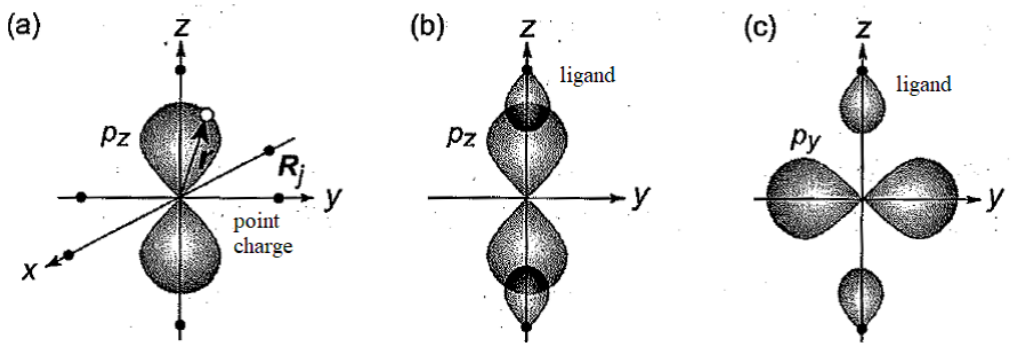


Figure 2.5: Point charge model in considering the CEF effect[24]

$$\mathcal{H}_{CEF} = -|e|V_{CEF}(\boldsymbol{r}). \qquad (2.46)$$

In a tetragonal symmetry a=b≠c, whereas a=b=c in a cubic symmetry. The constant term in the CEF Hamiltonian in tetragonal symmetry is removed, and taking into account until the second order term,

$$
\begin{aligned}
\mathcal{H}_{CEF} &= A(3z^2-r^2)\\
(A &= |e|q(\frac{1}{a^3}-\frac{1}{c^3})). \qquad (2.47)
\end{aligned}
$$

The average of the polynomial about the coordinates in a certain of subspace with constant total angular momentum by charge distributions is equivalent to the polynomial of the angular momentum operators in Wigner · Eckert's theorem of quantum mechanics. For example, the following conversion from spatial coordinates to angular momentum is established.

$$\mathcal{H}_{CEF} = A(3z^2 - r^2) \quad \rightarrow \quad \mathcal{H}_{CEF} = B_{20}(3l_z^2 - l(l+1)) = B_{20}O_{20} \tag{2.48}$$

Therefore $O_{20} = 3l_z^2 - l(l+1)$ can be obtained. Considering the CEF Hamiltonian in cubic symmetry, from Eq. 2.45, it becomes

$$\begin{aligned}
\mathcal{H}_{CEF} &= C\left\{(x^4+y^4+z^4) - \frac{3}{5}r^4\right\} + D\left\{(x^6+y^6+z^6\right. \\
&\quad \left. + \frac{15}{4}(x^2y^4 + x^2z^4 + y^2x^4 + y^2z^4 + z^2x^4 + z^2y^4) - \frac{15}{14}r^6\right\} \\
&\quad \left(C = \frac{35|e|q}{4a^5},\ \ D = -\frac{21|e|q}{2a^7}\right)
\end{aligned} \tag{2.49}$$

and the second order term disappears. In particular, paying attention to the fourth order term, it becomes

$$C\left\{(x^4+y^4+z^4) - \frac{3}{5}r^4\right\} = \frac{C}{20}\left\{\underbrace{(35z^4 - 30r^2z^2 + 3r^4)}_{O_{40}} + 5\underbrace{(x^4 - 6x^2y^2 + y^4)}_{O_{44}}\right\} \tag{2.50}$$

$$\rightarrow \quad B_{40}(O_{40} + 5O_{44}), \tag{2.51}$$

and $O_{40}$ and $O_{44}$ can be obtained. Similarly, when we calculate up to the sixth order term, we can obtain the relations as:

$$O_{60} = 231z^6 - 315z^4r^2 + 105z^2r^4 - 5r^6, \tag{2.52}$$

$$O_{64} = (11z^2 - r^2)(x^4 - 6x^2y^2 + y^4). \tag{2.53}$$

Also it can be noticed that the relations of $B_{20} = 0$, $B_{44} = 5B_{40}$, $B_{64} = -21B_{60}$ are satisfied in cubic symmetry ($O_h$). When the total angular momentum $\boldsymbol{J}$ takes a good quantum number like a rare earth compound, the orbital angular momentum $l$ can be replaced to the total angular momentum $J$, and $O_{20}$,$O_{40}$,$O_{44}$,$O_{60}$,$O_{64}$ can be expressed as follows.

$$O_{20} = 3J_z^2 - J(J+1), \tag{2.54}$$

$$O_{40} = 35J_z^4 - \left[30J(J+1) - 25\right]J_z^2 - 6J(J+1) + 3J^2(J+1)^2, \tag{2.55}$$

$$O_{44} = \frac{1}{2}\left(J_+^4 + J_-^4\right), \tag{2.56}$$

$$\begin{aligned}
O_{60} &= 231J_z^6 - 105\left[3J(J+1) - 7\right]J_z^4, \\
&\quad + \left[105J^2(J+1)^2 - 525J(J+1) + 294\right]J_z^2, \\
&\quad -5J^3(J+1)^3 + 40J^2(J+1)^2 - 60J(J+1),
\end{aligned} \tag{2.57}$$

$$\begin{aligned}
O_{64} &= \frac{1}{4}\left[\left(11J_z^2 - J(J+1) - 38\right)\left(J_+^4 + J_-^4\right)\right. \\
&\quad \left. + \left(J_+^4 + J_-^4\right)\left(11J_z^2 - J(J+1) - 38\right)\right].
\end{aligned} \tag{2.58}$$

Since the ladder operators are defined by

$$J_{\pm}|J, J_z\rangle = \sqrt{(J \mp J_z)(J \pm J_z + 1)}|J, J_z \pm 1\rangle, \tag{2.59}$$

$J_+$ and $J_-$ have components at a position shifted by one from the diagonal term. Since $O_{44}$ and $O_{64}$ are obtained by quadruplicate $J_+$ and $J_-$, they have components at positions shifted by 4 from the diagonal terms. Therefore, when we calculate the CEF potential given by Eq. 2.44 with the basis of $J_z$, its matrix has components at diagonal terms and 4-positions-shifted terms from the diagonal and $J_z$ in its eigenfunctions definitely changed by ±4.
The operators which equivalent quantity with the CEF represented by the full-angle momentum are summarized by Stevens, and they are called Stevens's equivalent operator. However, it should be noted that the combinations of $J_x$, $J_y$ and $J_z$ are represented by spherical harmonic functions only when considering the LSJ multiplet terms. So that Stevens' s equivalent method can be applied only when $L$, $S$ and $J$ have good quantum numbers, and hybridization between different LSJ multiplet terms can be neglected.
This Stevens' s equivalent calculation method is used in a wide range of fields. In addition, since the forms expressed by the spherical harmonic function are more general notations, it is necessary to understand the excited state in the x-ray absorption and photoemission process. Therefore, it is important to know the conversion between Stevens operators $B_{km}$ and the parameters for complete theory of CEF $\alpha A_{km}$.

### 2.4.3 Expansion of CEF Hamiltonian

As mentioned preceding section, the CEF Hamiltonian can be expanded with spherical surface harmonics. Since the CEF Hamiltonian can be variable separated into a radial component and an angular component, it can be transformed to

$$\begin{aligned}
\mathcal{H}_{i,j}^{CEF} &= \langle R_{n_i}^{l_i}(r) Y_{l_i}^{m_i}(\theta,\ \phi)| \sum_{k=0}^{\infty} \sum_{m=-k}^{k} A_{km} r^k C_k^m(\theta,\ \phi)|R_{n_j}^{l_j}(r) Y_{l_j}^{m_j}(\theta,\ \phi)\rangle \\
&= \sum_{k=0}^{\infty} \sum_{m=-k}^{k} A_{km} \langle Y_{l_i}^{m_i}(\theta,\ \phi)|C_k^m(\theta,\ \phi)|Y_{l_j}^{m_j}(\theta,\ \phi)\rangle \langle R_{n_i}^{l_i}(r)|r^k|R_{n_j}^{l_j}(r)\rangle
\end{aligned} \tag{2.60}$$

from Eq. 2.42. The value of integral for angle component can be obtained analytically. The crystal field parameter $A_{km}$ can be also obtained by the method described later. On the other hand, the radial component can be calculated by atomic Hatree - Fock calculation. However, the radial component for the ions in compounds sometimes is not equivalent to the calculation in the atomic model. Therefore, we treat $A_{km}$ of the CEF together with the radial component as follows:

$$\tilde{A}_{km} = A_{km} \langle R_{n_i}^{l_i}(r)|r^k|R_{n_i}^{l_i}(r)\rangle. \tag{2.61}$$

$\tilde{A}_{km}$ can be obtained by local density approximate (LDA) calculation that approximates the potential as only a function of the density of the focusing coordinates. In actual, $\tilde{A}_{km}$ are often treated as a fitting parameters in experiments. To calculate $\tilde{A}_{km}$, it is necessary to consider the following conditional expressions.

- Hamiltonian is the Hermitian operator.

$$\mathcal{H}_{i,j}^{CF} = (\mathcal{H}_{i,j}^{CF})^* \quad \rightarrow \quad A_{km} = (-1)^m A_{k-m}^* \tag{2.62}$$

- Orbital angular momentum $L$ satisfies the conditional expression of triangle relation by $3j$-symbol. [25]。

$$|l_i - l_j| \leq k \leq l_i + l_j \tag{2.63}$$

- Since the values of integral for the odd function in the whole space become equivalent to 0, for finite value of $\langle Y^{m_i l_i}(\theta,\phi)|C_k^m(\theta,\phi)|Y^{m_j l_j}(\theta,\phi)\rangle$, it is necessary to satisfy the following relation.

$$k + l_i + l_j = even \tag{2.64}$$

- Considering the symmetry of the crystal, we can reduce the calculation amount of $A_{km}$. With $p$ times symmetry around the $z$ axis, since the CEF potential are expanded with spherical surface harmonics,

$$V_{CF}(\theta,\phi) = V_{CF}(\theta,\phi + \frac{\pi}{p}). \tag{2.65}$$

  and the relation as $V_{CEF} \propto C_k^m \propto e^{im\phi}$ is satisfied. In addition,

$$e^{im\phi} = e^{im(\phi+\frac{\pi}{p})}. \tag{2.66}$$

  In quantum mechanics, $m$ is written as $m = -l, -l+1, \ldots, l$. In this case the variable $m$ can be decreased to

$$|m| = n \cdot p, n \in Z(integer) \tag{2.67}$$

  by using the integer $n$.

### 2.4.4 Relation between CEF potential and Stevens operator

From Eq. 2.42, with the charge of the ligand $q_{km}$, the CEF Hamiltonian is given by:

$$\begin{aligned}
\mathcal{H}_{CEF} &= \sum_{k=0}^{\infty}\sum_{m=-k}^{k}\left\{q_{km}\int r^{k+2}R_{nl_1}(r)\,R_{nl_2}(r)\,dr\right\} \\
&\quad \cdot\left\{\sqrt{\frac{4\pi}{2k+1}}\int Y_{l_1m_1}^*(\theta,\varphi)\,Y_{km}(\theta,\varphi)\,Y_{l_2m_2}(\theta,\varphi)\,\sin\theta d\theta d\varphi\right\} \\
&= \sum_{k=|l_1-l_2|}^{l_1+l_2} A_{k,m}c^k(l_1m_1,l_2m_2).
\end{aligned} \tag{2.68}$$

Since Eq. 2.68 is correspoding to the Hamiltonian with Stevens operator $V_{CF} = \sum_{k,m} B_{km}O_{km}$, the following relation can be obtained.

$$\mathcal{H}_{CEF} = \sum_{km} A_{km}c^k(l_1m_1,l_2m_2) = \sum_{km} A_{km}\langle J||\theta^k||J\rangle O_{km}(J) = \sum_{km} B_{km}O_{km}(J) \tag{2.69}$$

$\theta^k$ stands for $k$ order tensor matrix. From this, we can obtain the relations between $A_{km}$ and $B_{km}$ by the reduction matrix elements $\langle J||\theta^k||J\rangle$. To calculate them particularly, we start to rewrite spherical surface harmonics for $c^k(l_1m_1, l_2m_2)$.

$$\begin{aligned}&\int Y_{l_1m_1}(\theta,\varphi)Y_{l_2m_2}(\theta,\varphi)Y_{l_3m_3}(\theta,\varphi)\sin\theta\, d\theta\, d\varphi\\ =\ &\sqrt{\frac{(2l_1+1)(2l_2+1)(2l_3+1)}{4\pi}}\begin{pmatrix} l_1 & l_2 & l_3\\ 0 & 0 & 0\end{pmatrix}\begin{pmatrix} l_1 & l_2 & l_3\\ m_1 & m_2 & m_3\end{pmatrix}\end{aligned} \tag{2.70}$$

$3\,j$-symbol is written by Clebsch-Gordan coefficient as:

$$\begin{pmatrix} l_1 & l_2 & l_3\\ m_1 & m_2 & m_3\end{pmatrix} = \frac{(-1)^{l_1-l_2-m_3}}{\sqrt{2l_3+1}}\langle l_1m_1l_2m_2|l_3-m_3\rangle. \tag{2.71}$$

So that the spherical surface harmonics can be written as:

$$\begin{aligned}&\int Y_{l_1m_1}(\theta,\varphi)Y_{l_2m_2}(\theta,\varphi)Y_{l_3m_3}(\theta,\varphi)\sin\theta\, d\theta\, d\varphi\\ =\ &\sqrt{\frac{(2l_1+1)(2l_2+1)(2l_3+1)}{4\pi}}\frac{(-1)^{l_1-l_2}}{\sqrt{2l_3+1}}\langle l_1,0l_2,0|l_3,0\rangle\frac{(-1)^{l_1-l_2-m_3}}{\sqrt{2l_3+1}}\langle l_1m_1l_2m_2|l_3-m_3\rangle.\end{aligned} \tag{2.72}$$

Therefore,

$$c^k(l_1m_1,l_2m_2) = \sqrt{\frac{4\pi}{2k+1}}\int Y^*_{l_1m_1}(\mathbf{r})\ Y_{km}(\theta,\varphi)\ Y_{l_2m_2}(\mathbf{r})\, d\mathbf{r} \tag{2.73}$$

$$\begin{aligned}&= \sqrt{\frac{4\pi}{2k+1}}\sqrt{\frac{(2l_1+1)(2k+1)(2l_2+1)}{4\pi}}\\ &\quad\cdot\frac{(-1)^{l_1-k}}{\sqrt{2l_2+1}}\langle l_1,0k,0|l_2,0\rangle\frac{(-1)^{l_1-k-m_2}}{\sqrt{2l_2+1}}\langle l_1m_1km|l_2-m_2\rangle.\end{aligned} \tag{2.74}$$

Especially when $l_1 = l_2 = l$,

$$c^k(lm_1,lm_2) = \langle l,0k,0|l,0\rangle\langle lm_1km|l-m_2\rangle \tag{2.75}$$

Generally, the reduction matrix elements $J||\theta^k||J\rangle$ are expressed as $\alpha_J$ with $k=2$, $\beta_J$ with $k=4$, and $\gamma_J$ with $k=6$. With $k=2$, the concrete relation is given by [26]:

$$\alpha_J = \frac{2(2l+1-4S)}{(2l-1)(2l+3)(2L-1)}\times\begin{cases}\frac{(L+1)(2L+3)}{J+1}2J+3 & if\ J=L-S\ (lightRE)\\ \frac{L(2L-1)}{J(2J-1)} & if\ J=L+S\ (heavyRE).\end{cases} \tag{2.76}$$

The list of Stevens' factors $\alpha_J$, $\beta_J$, $\gamma_J$ for the trivalent rare earth ions [26] is shown in Table 2.1.

Considering the concrete term of the CEF potencial with $k=2, m=0$, the following relation

is obtained.

$$\begin{aligned} A_{20}\sqrt{\frac{4\pi}{5}}Y_{20}(\Omega) &= A_{20}\sqrt{\frac{4\pi}{5}}\frac{\sqrt{5}}{2\sqrt{2}}(3\cos^2\theta-1)\times\frac{1}{\sqrt{2\pi}} \\ &= A_{20}\frac{1}{2}\alpha_J(3\cos^2\theta-1) = A_{20}\frac{1}{2}\alpha_J O_{20} = B_{20}O_{20} \end{aligned} \tag{2.77}$$

Therefore,

$$B_{20} = \frac{\alpha_J}{2}A_{20}.$$

Also, by using the relation $A_{km} = (-)^m A_{k,-m}$, the following relations can be obtained.

$$\begin{aligned} B_{22} &= \frac{\sqrt{6}}{2}\alpha_J A_{22} \\ B_{40} &= \frac{1}{8}\beta_J A_{40} \\ B_{42} &= \frac{\sqrt{10}}{4}\beta_J A_{42} \\ B_{43} &= -\frac{\sqrt{35}}{2}\beta_J A_{43} \\ B_{44} &= \frac{\sqrt{70}}{8}\beta_J A_{44} \\ B_{60} &= \frac{1}{16}\gamma_J A_{60} \\ B_{63} &= -\frac{\sqrt{3\cdot 5\cdot 7}}{8}\gamma_J A_{63} \\ B_{64} &= \frac{3\sqrt{14}}{16}\gamma_J A_{64} \\ B_{66} &= \frac{\sqrt{231}}{16}\gamma_J A_{66} \end{aligned} \tag{2.78}$$

Table 2.1: List of Steven's factors $\alpha_J$, $\beta_J$, $\gamma_J$ for the trivalent rare earth ions [26]

| Ion | | | $\alpha_J$ | $\beta_J$ | $\gamma_J$ |
|---|---|---|---|---|---|
| $Ce^{3+}$ | $(4f)^1$ | ${}^2F_{5/2}$ | $\frac{-2}{5\cdot 7}$ | $\frac{2}{5\cdot 7\cdot 9}$ | 0 |
| $Pr^{3+}$ | $(4f)^2$ | ${}^3H_4$ | $\frac{-13\cdot 2^2}{11\cdot 5^2\cdot 3^2}$ | $\frac{-2^2}{11^2\cdot 5\cdot 3^2}$ | $\frac{17\cdot 2^4}{13\cdot 11^2\cdot 7\cdot 5\cdot 3^4}$ |
| $Nd^{3+}$ | $(4f)^3$ | ${}^4I_{9/2}$ | $\frac{-7}{11^2\cdot 3^2}$ | $\frac{-2^3\cdot 17}{13\cdot 11^3\cdot 3^3}$ | $\frac{-19\cdot 17\cdot 5}{13^2\cdot 11^3\cdot 7\cdot 3^3}$ |
| $Pm^{3+}$ | $(4f)^4$ | ${}^5I_4$ | $\frac{2\cdot 7}{11^2\cdot 5\cdot 3}$ | $\frac{8\cdot 7\cdot 17}{13\cdot 11^3\cdot 5\cdot 3^3}$ | $\frac{19\cdot 17\cdot 2^3}{13^2\cdot 11^2\cdot 7\cdot 3^3}$ |
| $Sm^{3+}$ | $(4f)^5$ | ${}^6H_{5/2}$ | $\frac{13}{7\cdot 5\cdot 3^2}$ | $\frac{2\cdot 13}{11\cdot 7\cdot 5\cdot 3^3}$ | 0 |
| $Eu^{3+}$ | $(4f)^6$ | ${}^7F_0$ | 0 | 0 | 0 |
| $Gd^{3+}$ | $(4f)^7$ | ${}^8S_{7/2}$ | 0 | 0 | 0 |
| $Tb^{3+}$ | $(4f)^8$ | ${}^7F_6$ | $\frac{-1}{11\cdot 3^2}$ | $\frac{2}{11^2\cdot 5\cdot 3^3}$ | $\frac{-1}{13\cdot 11^2\cdot 7\cdot 3^4}$ |
| $Dy^{3+}$ | $(4f)^9$ | ${}^6H_{15/2}$ | $\frac{-2}{7\cdot 5\cdot 3^2}$ | $\frac{-8}{13\cdot 11\cdot 7\cdot 5\cdot 3^3}$ | $\frac{2^2}{13^2\cdot 11^2\cdot 7\cdot 5\cdot 3^3}$ |
| $Ho^{3+}$ | $(4f)^{10}$ | ${}^5I_8$ | $\frac{-1}{5^2\cdot 3^2\cdot 2}$ | $\frac{-1}{13\cdot 11\cdot 7\cdot 5\cdot 3\cdot 2}$ | $\frac{-5}{13^2\cdot 11^2\cdot 7\cdot 3^3}$ |
| $Er^{3+}$ | $(4f)^{11}$ | ${}^4I_{15/2}$ | $\frac{2^2}{7\cdot 5^2\cdot 3^2}$ | $\frac{2}{13\cdot 11\cdot 7\cdot 5\cdot 3^2}$ | $\frac{2^3}{13^2\cdot 11^2\cdot 7\cdot 3^3}$ |
| $Tm^{3+}$ | $(4f)^{12}$ | ${}^3H_6$ | $\frac{1}{11\cdot 3^2}$ | $\frac{2^3}{11^2\cdot 5\cdot 3^4}$ | $\frac{-5}{13\cdot 11^2\cdot 7\cdot 3^4}$ |
| $Yb^{3+}$ | $(4f)^{13}$ | ${}^2F_{7/2}$ | $\frac{2}{7\cdot 3^2}$ | $\frac{-2}{11\cdot 7\cdot 5\cdot 3}$ | $\frac{2^2}{13\cdot 11\cdot 7\cdot 3^3}$ |

## 2.5 Crystalline electric field in cubic symmetry

The CEF Hamiltonian can be written by $J_x$, $J_y$, $J_z$ owing to Stevens operators. The matrix operators in this section are defined by $J_z$ as basis, and the eigenfunctions are expressed by the linear combination of $J_z$ states. Since the orbital quantum number of both $Ce^{3+}$ with $4f^1$ configuration and $Yb^{3+}$ with $4f^{13}$ is 3, $0 \leq k \leq 6$ is only considered. In addition, the CEF effect except for the even number of $k$ disappears. Therefore, the CEF potential should be considered about $k = 0, 2, 4, 6$. In cubic symmetry ($O_h$), the CEF have fourfold symmetry and $m$ is equivalent to the integral multiple of 4 ($m = 4, 8, 12$). Following the relation as $m = -k, -k+1, \ldots, k$, only the case of $|m| = 0, 4$ should be considered. Using the relations in cubic symmetry given by $B_{44} = 5B_{40}$, $B_{64} = -21B_{60}$, the CEF Hamiltonian is written as:

$$H_{CEF} = B_{40}(O_{40} + 5O_{44}) + B_{60}(O_{60} - 21O_{64}). \tag{2.79}$$

In this section, the CEF Hamiltonians with $J = 5/2$ and $J = 7/2$ ground-state multiplet are picked up.

### 2.5.1 In the case of $J = 5/2$ ground-state multiplet

Since the sixth term of the CEF Hamiltonian with $J = 5/2$ can be ignored by Eq. 2.63, the Eq. 2.79 is described as

$$H_{CEF} = B_{40}(O_{40} + 5O_{44}). \tag{2.80}$$

With the basis of $|J_z\rangle$, $J_+$ and $J_-$ are written as:

$$J_+ = \begin{array}{c} \\ \langle J_z = +\frac{5}{2}| \\ \langle +\frac{3}{2}| \\ \langle +\frac{1}{2}| \\ \langle -\frac{1}{2}| \\ \langle -\frac{3}{2}| \\ \langle -\frac{5}{2}| \end{array} \begin{array}{c} \begin{array}{cccccc} |J_z = +\frac{5}{2}\rangle & |+\frac{3}{2}\rangle & |+\frac{1}{2}\rangle & |-\frac{1}{2}\rangle & |-\frac{3}{2}\rangle & |-\frac{5}{2}\rangle \end{array} \\ \begin{pmatrix} 0 & \sqrt{5} & 0 & 0 & 0 & 0 \\ 0 & 0 & 2\sqrt{2} & 0 & 0 & 0 \\ 0 & 0 & 0 & 3 & 0 & 0 \\ 0 & 0 & 0 & 0 & 2\sqrt{2} & 0 \\ 0 & 0 & 0 & 0 & 0 & \sqrt{5} \\ 0 & 0 & 0 & 0 & 0 & 0 \end{pmatrix} \end{array} \tag{2.81}$$

$$J_- = \begin{pmatrix} 0 & 0 & 0 & 0 & 0 & 0 \\ \sqrt{5} & 0 & 0 & 0 & 0 & 0 \\ 0 & 2\sqrt{2} & 0 & 0 & 0 & 0 \\ 0 & 0 & 3 & 0 & 0 & 0 \\ 0 & 0 & 0 & 2\sqrt{2} & 0 & 0 \\ 0 & 0 & 0 & 0 & \sqrt{5} & 0 \end{pmatrix}. \tag{2.82}$$

Also $O_{40}$ and $O_{44}$ are written as:

$$O_{40} = \begin{pmatrix} 60 & 0 & 0 & 0 & 0 & 0 \\ 0 & -180 & 0 & 0 & 0 & 0 \\ 0 & 0 & 120 & 0 & 0 & 0 \\ 0 & 0 & 0 & 120 & 0 & 0 \\ 0 & 0 & 0 & 0 & -180 & 0 \\ 0 & 0 & 0 & 0 & 0 & 60 \end{pmatrix} \tag{2.83}$$

$$O_{44} = \begin{pmatrix} 0 & 0 & 0 & 0 & 12\sqrt{5} & 0 \\ 0 & 0 & 0 & 0 & 0 & 12\sqrt{5} \\ 0 & 0 & 0 & 0 & 0 & 0 \\ 0 & 0 & 0 & 0 & 0 & 0 \\ 12\sqrt{5} & 0 & 0 & 0 & 0 & 0 \\ 0 & 12\sqrt{5} & 0 & 0 & 0 & 0 \end{pmatrix}. \tag{2.84}$$

Therefore, the CEF Hamiltonian with $J = 5/2$ is given by:

$$H_{CEF} = \begin{pmatrix} 60B_{40} & 0 & 0 & 0 & 60\sqrt{5}B_{40} & 0 \\ 0 & -180B_{40} & 0 & 0 & 0 & 60\sqrt{5}B_{40} \\ 0 & 0 & 120B_{40} & 0 & 0 & 0 \\ 0 & 0 & 0 & 120B_{40} & 0 & 0 \\ 60\sqrt{5}B_{40} & 0 & 0 & 0 & -180B_{40} & 0 \\ 0 & 60\sqrt{5}B_{40} & 0 & 0 & 0 & 60B_{40} \end{pmatrix} \tag{2.85}$$

The eigen equation $|H_{CEF} - \lambda I| = 0$ is written as:

$$|H_{CEF} - \lambda I| = -(120B_{40} - \lambda)^4(240B_{40} + \lambda)^2 = 0. \tag{2.86}$$

From this eigen equation, the eigenvalues $\lambda$ are obtained as:

$$\lambda = -240B_{40}, 120B_{40}. \tag{2.87}$$

So that the six-fold degenerated state in $J = 5/2$ split into a doublet with energy eigenvalue of $E_1 = -240B_{40}$ and a quartet with energy eigenvalue of $E_2 = 120B_{40}$.
To require the eigen function with energy eigenvalue of $E_1 = -240B_{40}$, when we define the eigen vector as:

$$\begin{matrix} \langle J_z = +\frac{5}{2}| \\ \langle +\frac{3}{2}| \\ \langle +\frac{1}{2}| \\ \langle -\frac{1}{2}| \\ \langle -\frac{3}{2}| \\ \langle -\frac{5}{2}| \end{matrix} \begin{pmatrix} a_1 \\ b_1 \\ c_1 \\ d_1 \\ e_1 \\ f_1 \end{pmatrix}. \tag{2.88}$$

When the eigenvalue of $E_1 = -240B_{40}$ is assigned to $\lambda$, the equation is written as:

$$\begin{pmatrix} 300B_{40} & 0 & 0 & 0 & 60\sqrt{5}B_{40} & 0 \\ 0 & 60B_{40} & 0 & 0 & 0 & 60\sqrt{5}B_{40} \\ 0 & 0 & 360B_{40} & 0 & 0 & 0 \\ 0 & 0 & 0 & 360B_{40} & 0 & 0 \\ 60\sqrt{5}B_{40} & 0 & 0 & 0 & 60B_{40} & 0 \\ 0 & 60\sqrt{5}B_{40} & 0 & 0 & 0 & 300B_{40} \end{pmatrix} \begin{pmatrix} a_1 \\ b_1 \\ c_1 \\ d_1 \\ e_1 \\ f_1 \end{pmatrix} = 0. \quad (2.89)$$

From this equation, the following relations come into existence.

$$\begin{aligned} -\sqrt{5}a_1 &= e_1 \\ b_1 &= -\sqrt{5}f_1 \\ c_1 &= 0 \\ d_1 &= 0 \end{aligned} \quad (2.90)$$

So that the following normalized eigen function can be obtained.

$$|\Gamma_7\rangle = \sqrt{\frac{1}{6}}|\pm\frac{5}{2}\rangle - \sqrt{\frac{5}{6}}|\mp\frac{3}{2}\rangle \quad (2.91)$$

Similarly, in case of considering eigenvalue of $E_2 = 120B_{40}$, the equation is written as:

$$\begin{pmatrix} -60B_{40} & 0 & 0 & 0 & 60\sqrt{5}B_{40} & 0 \\ 0 & -300B_{40} & 0 & 0 & 0 & 60\sqrt{5}B_{40} \\ 0 & 0 & 0 & 0 & 0 & 0 \\ 0 & 0 & 0 & 0 & 0 & 0 \\ 60\sqrt{5}B_{40} & 0 & 0 & 0 & -300B_{40} & 0 \\ 0 & 60\sqrt{5}B_{40} & 0 & 0 & 0 & -60B_{40} \end{pmatrix} \begin{pmatrix} a_2 \\ b_2 \\ c_2 \\ d_2 \\ e_2 \\ f_2 \end{pmatrix} = 0. \quad (2.92)$$

The following relations as:

$$\begin{aligned} a_2 &= \sqrt{5}e_2 \\ \sqrt{5}b_2 &= f_2 \end{aligned} \quad (2.93)$$

and

$$\begin{aligned} c_2 &= Const(\neq 0) \\ d_2 &= Const(\neq 0) \end{aligned} \quad (2.94)$$

come into existence.
So that the following normalized eigen function given by:

$$|\Gamma_8\rangle = \begin{cases} |\pm\frac{1}{2}\rangle \\ \sqrt{\frac{5}{6}}|\pm\frac{5}{2}\rangle + \sqrt{\frac{1}{6}}|\mp\frac{3}{2}\rangle \end{cases} \quad (2.95)$$

can be obtained.
By using the energy eigenvalues $E_1$ and $E_2$, from the table 2.1, $B_{40}$ and $B_{44}$ are described as:

$$B_{40} = \frac{E_2 - E_1}{360} \tag{2.96}$$

$$B_{44} = \frac{E_2 - E_1}{72}. \tag{2.97}$$

Especially, in case of considering $Ce^{3+}$, the following relations are obtained.

$$A_{40} = \frac{7(E_1 - E_2)}{2} \tag{2.98}$$

$$A_{44} = \frac{\sqrt{70}(E_1 - E_2)}{4} \tag{2.99}$$

### 2.5.2 In the case of $J = 7/2$ ground-state multiplet

Considered the case of considering $J = 7/2$ ground-state multiplet, Eq. 2.79 is described as:

$$H_{CEF} = B_{40}(O_{40} + 5O_{44}) + B_{60}(O_{60} - 21O_{64}).$$

With the basis of $|J_z\rangle$, $J_+$ and $J_-$ with $J = 7/2$ are written as:

$$J_+ = \begin{array}{c} \\ \langle J_z = +\frac{7}{2}| \\ \langle +\frac{5}{2}| \\ \langle +\frac{3}{2}| \\ \langle +\frac{1}{2}| \\ \langle -\frac{1}{2}| \\ \langle -\frac{3}{2}| \\ \langle -\frac{5}{2}| \\ \langle -\frac{7}{2}| \end{array} \begin{array}{c} \begin{array}{cccccccc} |J_z = +\frac{7}{2}\rangle & |+\frac{5}{2}\rangle & |+\frac{3}{2}\rangle & |+\frac{1}{2}\rangle & |-\frac{1}{2}\rangle & |-\frac{3}{2}\rangle & |-\frac{5}{2}\rangle & |-\frac{7}{2}\rangle \end{array} \\ \begin{pmatrix} 0 & \sqrt{7} & 0 & 0 & 0 & 0 & 0 & 0 \\ 0 & 0 & 2\sqrt{3} & 0 & 0 & 0 & 0 & 0 \\ 0 & 0 & 0 & \sqrt{15} & 0 & 0 & 0 & 0 \\ 0 & 0 & 0 & 0 & 4 & 0 & 0 & 0 \\ 0 & 0 & 0 & 0 & 0 & \sqrt{15} & 0 & 0 \\ 0 & 0 & 0 & 0 & 0 & 0 & 2\sqrt{3} & 0 \\ 0 & 0 & 0 & 0 & 0 & 0 & 0 & \sqrt{7} \\ 0 & 0 & 0 & 0 & 0 & 0 & 0 & 0 \end{pmatrix} \end{array} \tag{2.100}$$

$$J_- = \begin{pmatrix} 0 & 0 & 0 & 0 & 0 & 0 & 0 & 0 \\ \sqrt{7} & 0 & 0 & 0 & 0 & 0 & 0 & 0 \\ 0 & 2\sqrt{3} & 0 & 0 & 0 & 0 & 0 & 0 \\ 0 & 0 & \sqrt{15} & 0 & 0 & 0 & 0 & 0 \\ 0 & 0 & 0 & 4 & 0 & 0 & 0 & 0 \\ 0 & 0 & 0 & 0 & \sqrt{15} & 0 & 0 & 0 \\ 0 & 0 & 0 & 0 & 0 & 2\sqrt{3} & 0 & 0 \\ 0 & 0 & 0 & 0 & 0 & 0 & \sqrt{7} & 0 \end{pmatrix}. \tag{2.101}$$

From above formulas, $O_{40}$,$O_{44}$,$O_{60}$,$O_{64}$ are given by:

$$O_{40} = \begin{pmatrix} 420 & 0 & 0 & 0 & 0 & 0 & 0 & 0 \\ 0 & -780 & 0 & 0 & 0 & 0 & 0 & 0 \\ 0 & 0 & -180 & 0 & 0 & 0 & 0 & 0 \\ 0 & 0 & 0 & 540 & 0 & 0 & 0 & 0 \\ 0 & 0 & 0 & 0 & 540 & 0 & 0 & 0 \\ 0 & 0 & 0 & 0 & 0 & -180 & 0 & 0 \\ 0 & 0 & 0 & 0 & 0 & 0 & -780 & 0 \\ 0 & 0 & 0 & 0 & 0 & 0 & 0 & 420 \end{pmatrix} \tag{2.102}$$

$$O_{44} = \begin{pmatrix} 0 & 0 & 0 & 0 & 12\sqrt{35} & 0 & 0 & 0 \\ 0 & 0 & 0 & 0 & 0 & 60\sqrt{3} & 0 & 0 \\ 0 & 0 & 0 & 0 & 0 & 0 & 60\sqrt{3} & 0 \\ 0 & 0 & 0 & 0 & 0 & 0 & 0 & 12\sqrt{35} \\ 12\sqrt{35} & 0 & 0 & 0 & 0 & 0 & 0 & 0 \\ 0 & 60\sqrt{3} & 0 & 0 & 0 & 0 & 0 & 0 \\ 0 & 0 & 60\sqrt{3} & 0 & 0 & 0 & 0 & 0 \\ 0 & 0 & 0 & 12\sqrt{35} & 0 & 0 & 0 & 0 \end{pmatrix} \tag{2.103}$$

$$O_{60} = \begin{pmatrix} 1260 & 0 & 0 & 0 & 0 & 0 & 0 & 0 \\ 0 & -6300 & 0 & 0 & 0 & 0 & 0 & 0 \\ 0 & 0 & 11340 & 0 & 0 & 0 & 0 & 0 \\ 0 & 0 & 0 & -6300 & 0 & 0 & 0 & 0 \\ 0 & 0 & 0 & 0 & -6300 & 0 & 0 & 0 \\ 0 & 0 & 0 & 0 & 0 & 11340 & 0 & 0 \\ 0 & 0 & 0 & 0 & 0 & 0 & -6300 & 0 \\ 0 & 0 & 0 & 0 & 0 & 0 & 0 & 1260 \end{pmatrix} \tag{2.104}$$

$$O_{64} = \begin{pmatrix} 0 & 0 & 0 & 0 & 180\sqrt{35} & 0 & 0 & 0 \\ 0 & 0 & 0 & 0 & 0 & -420\sqrt{3} & 0 & 0 \\ 0 & 0 & 0 & 0 & 0 & 0 & -420\sqrt{3} & 0 \\ 0 & 0 & 0 & 0 & 0 & 0 & 0 & 180\sqrt{35} \\ 180\sqrt{35} & 0 & 0 & 0 & 0 & 0 & 0 & 0 \\ 0 & -420\sqrt{3} & 0 & 0 & 0 & 0 & 0 & 0 \\ 0 & 0 & -420\sqrt{3} & 0 & 0 & 0 & 0 & 0 \\ 0 & 0 & 0 & 180\sqrt{35} & 0 & 0 & 0 & 0 \end{pmatrix}. \tag{2.105}$$

From Eq. 2.79, the CEF Hamiltonian with $J = 7/2$ is written as Eq. 2.110 in next page.

The eigen function is given by:

$$\begin{aligned} |H_{CEF} - \lambda I| &= -(120B_{40} - 20160B_{60} + \lambda)^4 \\ &\quad (840B_{40} - 25200B_{60} - \lambda)^2(1080B_{40} + 15120B_{60} + \lambda)^2 = 0. \quad (2.106) \end{aligned}$$

From this eigen equation, the eigenvalues $\lambda$ are obtained as:

$$\lambda = 840(B_{40} - 30B_{60}) \quad (= E_1), \quad (2.107)$$

$$-1080(B_{40} + 14B_{60}) \quad (= E_2), \quad (2.108)$$

$$120(B_{40} + 168B_{60}) \quad (= E_3) \quad (2.109)$$

So that the eightfold degenerated state in $J = 7/2$ split into two doublet with each energy eigenvalue of $E_1$ and $E_2$, and a quartet with energy eigenvalue of $E_3$.

$$H_{CEF} = \begin{pmatrix} 420B_{40} + 1260B_{60} & 0 & 0 & 0 & 60\sqrt{35}B_{40} - 3780\sqrt{35}B_{60} & 0 & 0 & 0 \\ 0 & -780B_{40} - 6300B_{60} & 0 & 0 & 0 & 300\sqrt{3}B_{40} + 8820\sqrt{3}B_{60} & 0 & 0 \\ 0 & 0 & -180B_{40} + 11340B_{60} & 0 & 0 & 0 & 300\sqrt{3}B_{40} + 8820\sqrt{3}B_{60} & 0 \\ 0 & 0 & 0 & 540B_{40} - 6300B_{60} & 0 & 0 & 0 & 60sqrt35B_{40} - 3780\sqrt{35}B_{60} \\ 60\sqrt{35}B_{40} - 3780\sqrt{35}B_{60} & 0 & 0 & 0 & 540B_{40} - 6300B_{60} & 0 & 0 & 0 \\ 0 & 300\sqrt{3}B_{40} + 8820\sqrt{3}B_{60} & 0 & 0 & 0 & -180B_{40} + 11340B_{60} & 0 & 0 \\ 0 & 0 & 300\sqrt{3}B_{40} + 8820\sqrt{3}B_{60} & 0 & 0 & 0 & -780B_{40} - 6300B_{60} & 0 \\ 0 & 0 & 0 & 60\sqrt{35}B_{40} - 3780\sqrt{35}B_{60} & 0 & 0 & 0 & 420B_{40} + 1260B_{60} \end{pmatrix}$$

(2.110)

To require the eigenfunction with energy eigenvalue of $E_1 = 840(B_{40} - 30B_{60})$, the eigen vector is defined as:

$$\begin{matrix} \langle J_z = +\frac{7}{2}| \\ \langle +\frac{5}{2}| \\ \langle +\frac{3}{2}| \\ \langle +\frac{1}{2}| \\ \langle -\frac{1}{2}| \\ \langle -\frac{3}{2}| \\ \langle -\frac{5}{2}| \\ \langle -\frac{7}{2}| \end{matrix} \begin{pmatrix} a_1 \\ b_1 \\ c_1 \\ d_1 \\ e_1 \\ f_1 \\ g_1 \\ h_1 \end{pmatrix}.$$

As a result, the following relations come into existence.

$$\begin{aligned} a_1 &= \sqrt{\frac{5}{7}} e_1 \\ d_1 &= \sqrt{\frac{7}{5}} h_1 \\ b_1 &= c_1 = f_1 = g_1 = 0 \end{aligned} \tag{2.111}$$

So that the following normalized eigenfunction can be obtained.

$$|\Gamma_6\rangle = \sqrt{\frac{5}{12}}|\pm\frac{7}{2}\rangle + \sqrt{\frac{7}{12}}|\mp\frac{1}{2}\rangle \tag{2.112}$$

Similarly, the eigen vectors with energy eigenvalue of $E_2 = -1080(B_{40} + 14B_{60})$ and $E_3 = 120(B_{40} + 168B_{60})$ are respectively defined as:

$$\begin{pmatrix} a_2 \\ b_2 \\ c_2 \\ d_2 \\ e_2 \\ f_2 \\ g_2 \\ h_2 \end{pmatrix}, \qquad \begin{pmatrix} a_3 \\ b_3 \\ c_3 \\ d_3 \\ e_3 \\ f_3 \\ g_3 \\ h_3 \end{pmatrix}.$$

So that the following relations and normalized eigenfunction are obtained.

$$\begin{aligned} b_2 &= -\sqrt{3} g_2 \\ c_2 &= -\sqrt{\frac{1}{3}} f_2 \\ a_2 &= d_2 = e_2 = h_2 = 0 \end{aligned} \tag{2.113}$$

$$|\Gamma_7\rangle = -\frac{\sqrt{3}}{2}|\pm\frac{5}{2}\rangle + \frac{1}{2}|\mp\frac{3}{2}\rangle \tag{2.114}$$

Also the following relations come into existence.

$$\begin{aligned} a_3 &= -\sqrt{\frac{7}{5}}e_3 \\ d_3 &= -\sqrt{\frac{5}{7}}h_3 \end{aligned} \tag{2.115}$$

and

$$\begin{aligned} b_3 &= \sqrt{\frac{1}{3}}g_3 \\ c_3 &= \sqrt{3}f_3 \end{aligned} \tag{2.116}$$

Finally, the quartet normalized eigen function following as

$$|\Gamma_8\rangle = \begin{cases} -\sqrt{\frac{7}{12}}|\pm\frac{7}{2}\rangle + \sqrt{\frac{5}{12}}|\mp\frac{1}{2}\rangle \\ \frac{1}{2}|\pm\frac{5}{2}\rangle + \frac{\sqrt{3}}{2}|\mp\frac{3}{2}\rangle \end{cases} \tag{2.117}$$

can be obtained.

By using the energy eigenvalues $E_1$, $E_2$ and $E_3$, $B_{40}$,$B_{44}$,$B_{60}$,$B_{64}$ are described as:

$$B_{40} = \frac{2695}{2}(7E_1 - 9E_2 + 2E_3) \tag{2.118}$$

$$B_{44} = \frac{13475}{2}(7E_1 - 9E_2 + 2E_3) \tag{2.119}$$

$$B_{60} = \frac{351351}{10}(5E_1 + 3E_2 - 8E_3) \tag{2.120}$$

$$B_{64} = \frac{737837}{10}(5E_1 + 3E_2 - 8E_3). \tag{2.121}$$

Especially, in case of considering $Yb^{3+}$, the following relations are obtained.

$$A_{40} = \frac{7}{24}(7E_1 - 9E_2 + 2E_3) \tag{2.122}$$

$$A_{44} = \frac{7\sqrt{5}}{24\sqrt{14}}(7E_1 - 9E_2 + 2E_3) \tag{2.123}$$

$$A_{60} = \frac{13}{40}(5E_1 + 3E_2 - 8E_3) \tag{2.124}$$

$$A_{64} = -\frac{13\sqrt{7}}{40\sqrt{2}}(5E_1 + 3E_2 - 8E_3) \tag{2.125}$$

## 2.6 Crystalline electric field in tetragonal symmetry

In this section, the CEF Hamiltonians in tetragonal symmetry with $J = 5/2$ and $J = 7/2$ ground-state multiplets are briefly shown.

### 2.6.1 In the case of $J = 5/2$ ground-state multiplet

Since the sixth term of the CEF Hamiltonian with $J = 5/2$ can be ignored as is the case with cubic symmetry, the CEF Hamiltonian is described as:

$$H_{CEF} = B_{20}O_{20} + B_{40}O_{40} + B_{44}O_{44}. \tag{2.126}$$

So that the CEF Hamiltonian matrix is given by:

$$H_{CEF} = \begin{pmatrix} 10B_{20}+60B_{40} & 0 & 0 & 0 & 12\sqrt{5}B_{44} & 0 \\ 0 & -2B_{20}-180B_{40} & 0 & 0 & 0 & 12\sqrt{5}B_{44} \\ 0 & 0 & -8B_{20}+120B_{40} & 0 & 0 & 0 \\ 0 & 0 & 0 & -8B_{20}+120B_{40} & 0 & 0 \\ 12\sqrt{5}B_{44} & 0 & 0 & 0 & -2B_{20}-180B_{40} & 0 \\ 0 & 12\sqrt{5}B_{44} & 0 & 0 & 0 & 10B_{20}+60B_{40} \end{pmatrix}. \tag{2.127}$$

From the eigen equation for this Hamiltonian, the following normalized eigenfunctions can be obtained.

$$|\Gamma_6\rangle = |\pm\frac{1}{2}\rangle \tag{2.128}$$

$$|\Gamma_7^1\rangle = a|\pm\frac{5}{2}\rangle - \sqrt{1-a^2}|\mp\frac{3}{2}\rangle \tag{2.129}$$

$$|\Gamma_7^2\rangle = \sqrt{1-a^2}|\pm\frac{5}{2}\rangle + a|\mp\frac{3}{2}\rangle \tag{2.130}$$

$$(0 \le a \le 1) \tag{2.131}$$

By using the energy eigenvalues $E_1$ corresponding to $\Gamma_7^1$, $E_2$ corresponding to $\Gamma_6$, $E_3$ corresponding to $\Gamma_7^2$,$B_{20}$, $B_{40}$ and $B_{44}$ are described as:

$$B_{20} = \frac{1}{84}(-E_1 + 6a^2E_1 - 4E_2 + 5E_3 - 6a^2E_3) \tag{2.132}$$

$$B_{40} = \frac{1}{840}(-3E_1 + 4a^2E_1 + 2E_2 + E_3 - 4a^2E_3) \tag{2.133}$$

$$B_{44} = \frac{a\sqrt{1-a^2}}{12\sqrt{5}}(E_3 - E_1). \tag{2.134}$$

Especially, in case of considering $Sm^{3+}$, the following relations are obtained.

$$A_{20} = \frac{15}{26}(-E_1 + 6a^2E_1 - 4E_2 + 5E_3 - 6a^2E_3) \quad (2.135)$$

$$A_{40} = \frac{99}{26}(-3E_1 + 4a^2E_1 + 2E_2 + E_3 - 4a^2E_3) \quad (2.136)$$

$$A_{44} = \frac{99\sqrt{7}}{13\sqrt{2}}a\sqrt{1-a^2}(E_3 - E_1) \quad (2.137)$$

### 2.6.2 In the case of $J = 7/2$ ground-state multiplet

The CEF Hamiltonian with $J = 7/2$ is written as:

$$H_{CEF} = B_{20}O_{20} + B_{40}O_{40} + B_{44}O_{44} + B_{60}O_{60} + B_{64}O_{64}. \quad (2.138)$$

From the eigen equation for the CEF Hamiltonian with $J = 7/2$, the following normalized eigenfunctions can be obtained.

$$|\Gamma_6^1\rangle = a|\pm\frac{1}{2}\rangle + \sqrt{1-a^2}|\mp\frac{7}{2}\rangle \quad (2.139)$$

$$|\Gamma_6^2\rangle = \sqrt{1-a^2}|\pm\frac{1}{2}\rangle - a|\mp\frac{7}{2}\rangle \quad (2.140)$$

$$|\Gamma_7^1\rangle = b|\pm\frac{5}{2}\rangle + \sqrt{1-b^2}|\mp\frac{3}{2}\rangle \quad (2.141)$$

$$|\Gamma_7^2\rangle = \sqrt{1-b^2}|\pm\frac{5}{2}\rangle - b|\mp\frac{3}{2}\rangle \quad (2.142)$$

$$(0 \le a \le 1, 0 \le b \le 1) \quad (2.143)$$

In case of considering $Yb^{3+}$, by using the energy eigenvalues $E_1$ corresponding to $\Gamma_7^1$, $E_2$ corresponding to $\Gamma_7^2$, $E_3$ corresponding to $\Gamma_6^1$, and $E_4$ corresponding to $\Gamma_6^2$, $A_{20}$, $A_{40}$, $A_{44}$, $A_{60}$, and $A_{64}$ are described as:

$$A_{20} = \frac{1}{4}\left(3E_1 - 4b^2E_1 - E_2 + 4b^2E_2 - 7E_3 + 12a^2E_3 + 5E_4 - 12a^2E_4\right) \quad (2.144)$$

$$A_{40} = \frac{1}{4}\left(-3E_1 - 10b^2E_1 - 13E_2 + 10b^2E_2 + 7E_3 + 2a^2E_3 + 9E_4 - 2a^2E_4\right) \quad (2.145)$$

$$A_{44} = \frac{1}{4}\sqrt{\frac{7}{3}}\left(3\sqrt{10}b\sqrt{1-b^2}(E_1 - E_2) + \sqrt{42}a\sqrt{1-a^2}(E_3 - E_4)\right) \quad (2.146)$$

$$A_{60} = \frac{13}{20}\left(-9E_1 + 14b^2E_1 + 5E_2 - 14b^2E_2 - E_3 + 6a^2E_3 + 5E_4 - 6a^2E_4\right) \quad (2.147)$$

$$A_{64} = \frac{13}{20}\left(\sqrt{42}b\sqrt{1-b^2}(E_1 - E_2) + 3\sqrt{10}a\sqrt{1-a^2}(-E_3 + E_4)\right). \quad (2.148)$$

## 2.7 Recently developed method for determination of CEF parameters

The CEF parameters have been determined by several methods [27] such as inelastic neutron scattering, magnetic susceptibility. Although these method have been performed for many

years, the information which can obtained by these experiments are often insufficient to determine detailed crystal field parameters.Therefore, the new CEF determination methods have been developed in recent years.

### 2.7.1 Determination of $4f$ orbital symmetry by linear dichroism in x-ray absorption spectra

Recently, the determination of $4f$ ground-state symmetry for tetragonal Ce compounds by linear dichroism (LD) in Ce $3d-4f$ x-ray absorption spectroscopy (XAS) has been reported [10, 11, 12, 13].
In this method, since the dipole selection rules given by:

$$E \perp c \rightarrow \Delta m = \pm 1 \tag{2.149}$$

$$E \parallel c \rightarrow \Delta m = \pm 0 \tag{2.150}$$

work in transition process, LD in multiplet structures in Ce $3d-4f$ XAS spectra reflected $4f$ orbital symmetry can be obtained as shown in Fig. 2.6. The CEF-split ground states have determined by the ion-model calculations which reproduce the experimental LDs. For tetragonal symmetry, this method is so powerful, but it cannot be applicable for cubic crystal because there is no anisotropic axis. In addition, it is difficult to apply this technique to probe $Yb^{3+}$ states since there is only a single-peak structure ($3d^9 4f^{14}$ final state) at the $M_5$ absorption edge as shown in Fig. 2.7, in contrast to that of $Ce^{3+}$ with clear multiplet structures. Furthermore, $4f$ charge spatial distribution can be obtained, but the rotational symmetry around $z$ axis cannot be distinguished by LD in XAS.

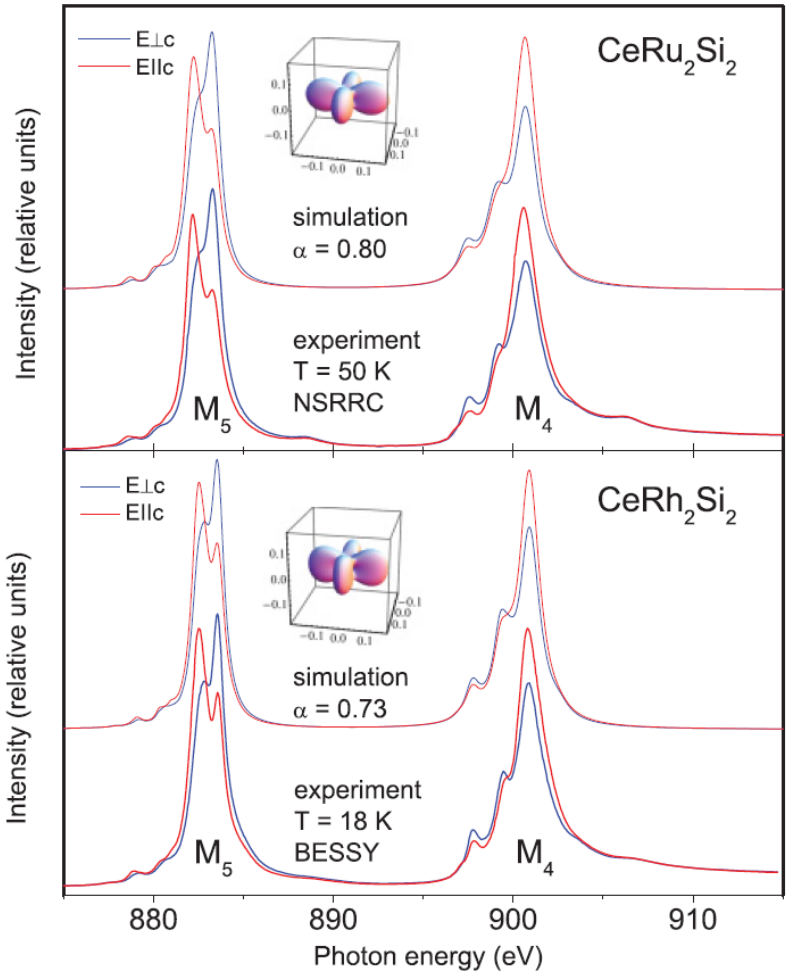


Figure 2.6: Determination of $4f$ ground-state symmetry for tetragonal $CeRu_2Si_2$ by linear dichroism in Ce $3d-4f$ XAS [13]

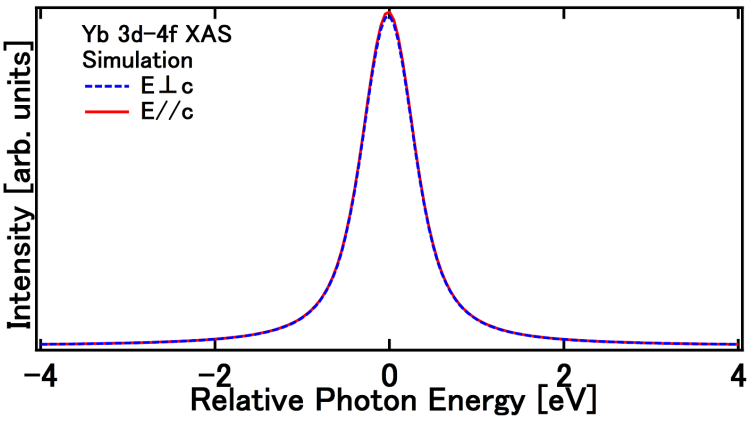


Figure 2.7: Simulated Yb $3d-4f$ XAS spectra for $Yb^{3+}$

### 2.7.2 Determination of $4f$ orbital symmetry by linear dichroism in hard x-ray core-level photoemission spectra

Recently we have reported the determination of $4f$ CEF ground-state symmetry by linear dichroism in hard x-ray photoemission spectroscopy (LD-HAXPES) [14, 15, 16, 17]. Since the selection rules also work in photoemission while the excited electron energy is much higher than that in absorption, the $4f$ orbital symmetry also reflects in LD-HAXPES. In addition, there is another controllable measurement parameter in photoemission called as the photoelectron detection direction relative to the single-crystalline axis in addition to the polarization direction of the excitation light. Therefore, the $4f$ charge distribution for cubic crystals and more detailed information of $4f$ orbital symmetry including the rotation symmetry around $z$ axis can be obtained.

In this technique, we perform the ionic calculation with CEF theory for core-level photoemission spectra by using Xtls ver. 9.0 [19], and we compare the LD in experiment with simulations. Generally, the ground-state symmetry can be obtained by the experimental spectra measured at enough lower temperature than first excited-state energy level. (The information of CEF energy splitting is often referred from inelastic neutron scattering.) The angle-resolved polarization-dependent $Yb^{3+}$ $3d_{5/2}$ HAXPES spectra of $YbCu_2Si_2$ and simulated ones are shown in Fig. 2.8. There are clear LDs in multiplet structures of $Yb^{3+}$ $3d_{5/2}$ PES spectra. The experimental LDs are reproduced by simulated ones assuming the $\Gamma_7^2$ ground state.

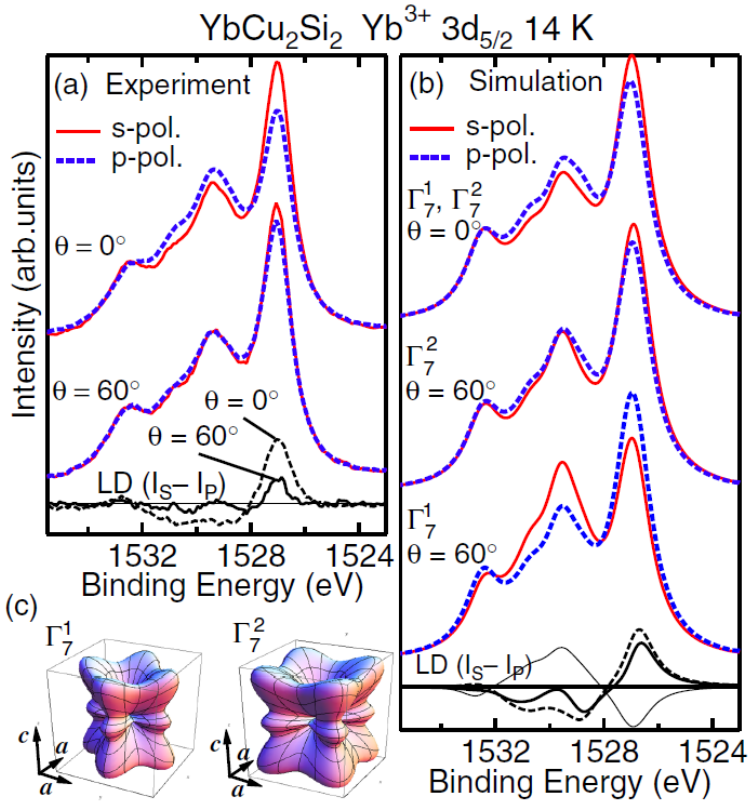


Figure 2.8: Determination of $4f$ ground-state symmetry for tetragonal $YbCu_2Si_2$ by linear dichroism in Yb $3d$ HAXPES [14]

# Chapter 3

# The theory of photoemission spectroscopy

## 3.1 Photoemission spectroscopy

Photoemission spectroscopy is a powerful method to directly observe the electronic states. Its application field extends not only in condensed material physics, solid physics but also in a wide range of fields such as chemistry, surface science and material science. Recently, this method had become a powerful tool to get detailed information in electronic occupied state with the development of synchrotron radiation and the performance of vacuum technique and the electronic energy analyzer.
Since one-electron approximation without considering electron-electron interaction is too simple to interpret photoelectron spectra, the analysis of experimental results is complicated. On the other hand, the analysis clearly considering interactions between electrons makes possible to obtain quantitative information for interactions between electrons. Photoemission spectroscopy can be a powerful means to investigate the electronic correlation within a substance for this reason. In this chapter, the theoretical framework of photoemission spectroscopy used in our experiments and polarization dependence of photoelectron spectrum, photoelectron spectra in strongly-correlated materials, and the ionic calculations of photoemission spectra considering crystalline electric field are explained [30, 31, 32, 33].

### 3.1.1 Principle of photoelectron spectroscopy

Photoemission spectroscopy (PES, particularly in using x-ray, X-ray Photoemission Spectroscopy: XPS) is the experimental method to investigate the electronic states in compounds by observing the electrons (photoelectrons) emitted due to the external photoelectric effect occurred by incidence of monochromated x-ray to the materials. Since the energy conservation law holds in the excitation process of photoelectron emitting, the relation between the energy *h nu* of incident light and the binding energy E $_B$ of photoelectrons is expressed as:

$$E_B = h\nu - \phi - E_K. \tag{3.1}$$

$h\nu$:Incident photon energy
$E_K$:Kinetic Energy of photoelectrons emitted from the sample
$E_B$:Binding energy of emitted electrons under the sample compound

$\phi$:Work function for the sample

The incident photon energy is fixed in experiments and the work function takes a constant value (several eV). From the above relation, it is necessary to set the incident photon energy as $h\nu \geq \phi + E_B$. In practical photoelectron experiment, since the work function $\phi$ is not equivalent to that of measuring sample but that of the photoelectron spectrometer which located in infinite distance and electrically connected to the sample, it is unnecessary to determine the work function for each individual samples. The value obtained from a reference sample (usually a vapor-deposited Au film) can be used as the work function for all measurement samples. The kinetic energy of photoelectron at the Fermi level $E_{K\_EF}$ is obtained by fitting of the measuring photoemission spectrum of Fermi edge by using Au as a reference sample, which electrically connected to the sample in actual measurements. The conceptual diagram of photoelectron emission process is shown in Fig. 3.1.

In Fig. 3.1(b), the vertical axis represents energy scale in compounds and the horizontal axis represents electrons density of states. Also the vertical axis represents kinetic energy of photoelectrons, and the horizontal axis represents photoemission intensity in Fig 3.1(c). The photoelectron spectrum is obtained by analysis of photoemission intensity on each kinetic energy $E_{Kin}$. Since the electron binding energy $E_B$ is based on the Fermi energy $E_F$, the value of $E_B$ at the Fermi level is equivalent to 0.

So that the following relation consists and the electrons binding energy in compounds which is equivalent to the energy distribution of electrons can be obtained.

$$E_B = E_{K\_EF} - E_K \tag{3.2}$$

### 3.1.2 Photoemission process

The Hamiltonian for interactions between electrons is expressed as:

$$\begin{aligned} \mathcal{H}_{int} &= \frac{1}{2m}(\boldsymbol{p}_{j'} + e\boldsymbol{A})^2 - \frac{1}{2m}\boldsymbol{p}_{j'}^2 \\ &= \frac{e}{2m}(\boldsymbol{p}\cdot\boldsymbol{A} + \boldsymbol{A}\cdot\boldsymbol{p}) + \frac{e^2}{2m}\boldsymbol{A}^2, \end{aligned} \tag{3.3}$$

where $\boldsymbol{p}_{j'}$ is momentum operator for the j'-th electron to be excited. $\boldsymbol{A}$ is the quantized vector potential of the incident photons given by:

$$\boldsymbol{A} \propto \boldsymbol{e}(exp(i\boldsymbol{q}\cdot\boldsymbol{r}_{j'}a_\nu + exp(-i\boldsymbol{q}\cdot\boldsymbol{r}_{j'}a_\nu^\dagger) \tag{3.4}$$

in SI units. $\boldsymbol{e}$, $\boldsymbol{q}$, $\boldsymbol{r}_{j'}$ stand for the unit vector of light polarization, the phonon wave vector, and the position vector of the j'-th electron excited, respectively. $a_\nu^\dagger$ and $a_\nu$ represent the creation and annihilation operators of the incident photon. By the exchange relation, $\boldsymbol{p}\cdot\boldsymbol{A}$ is equivalent to $\boldsymbol{A}\cdot\boldsymbol{p} - i\hbar\nabla\cdot\boldsymbol{A}$. When Coulomb gauge $\nabla\cdot\boldsymbol{A} = 0$ is introduced, by the relation following as $\boldsymbol{A}\cdot\boldsymbol{p} + \boldsymbol{p}\cdot\boldsymbol{A} = 2\boldsymbol{A}\cdot\boldsymbol{p}$, fomula 3.3 is rewritten as:

$$\mathcal{H}_{int} = \frac{e}{m}\boldsymbol{A}\cdot\boldsymbol{p} + \frac{e^2}{2m}\boldsymbol{A}^2. \tag{3.5}$$

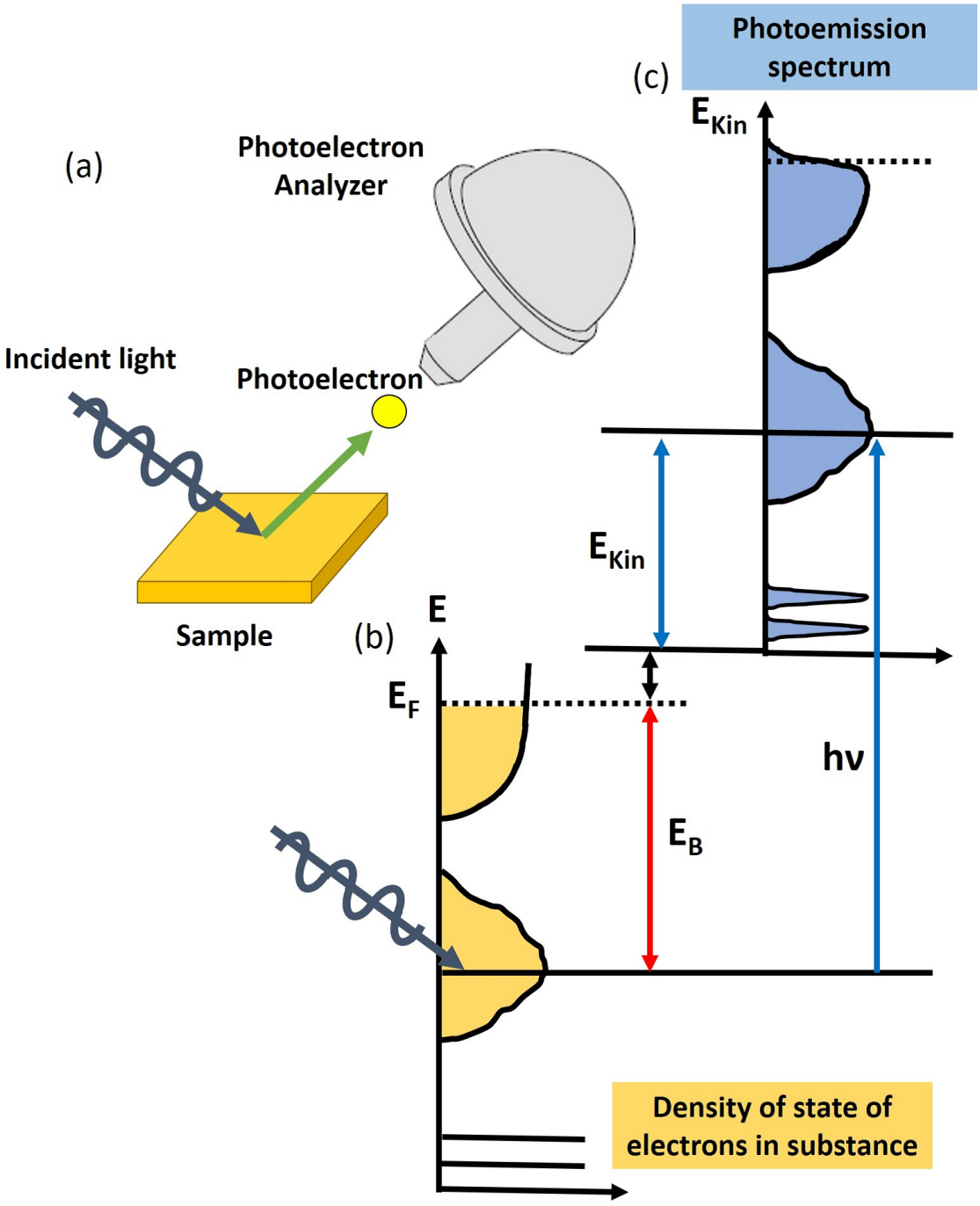


Figure 3.1: Conceptual diagram of photoelectron emission process

The first term in Eq.3.6 represents the emission and absorption of one photon, and the second term $\boldsymbol{A}^2$ represents the two-photon process. In case of not considering multiphoton process, $\mathcal{H}_{int}$ is written as:

$$\mathcal{H}_{int} = \boldsymbol{A} \cdot \frac{e}{m}\mathbf{p} \tag{3.6}$$

When the initial (final) state of $N$ electrons with the photon field $|i\rangle$ ($\langle f|$) is represented by the direct product of the $N$-electron initial (final, including the excited photoelectron) state with the total electron energy of $E_i(N)$ ($E_f(N)$) and initial (final) photon state $|n_{h\nu}\rangle$ ($|n_{h\nu}-1\rangle$) with the photon number of $n_{h\nu}$ ($n_{h\nu}$-1) as

$$|i\rangle = |E_i(N)\rangle|n_\nu\rangle, |f\rangle = |E_f(N)\rangle|n_\nu - 1\rangle. \tag{3.7}$$

Then transition (photoexcitation) probability $w_{fj'}$ is obtained by the time-dependent pertubation theory in quantum mechanics as:

$$\begin{aligned} w_{fj'} &= \frac{2t}{\hbar^2}\pi|\langle f|H_{int}|i\rangle|^2\delta(E_f(N) - E_i(N) - h\nu) && (3.8)\\ &\propto \frac{n_\nu t}{h\nu}|\langle E_f(N)|e^{i\boldsymbol{q}\cdot\boldsymbol{r}_{j'}}\boldsymbol{e}\cdot\boldsymbol{p}_{j'}|E_i(N)\rangle|^2\delta(E_f(N) - E_i(N) - h\nu) && (3.9)\end{aligned}$$

which is called Fermi's golden rule. This formula tells that the photoelectron intensity is proportional to the total photon flux $n_{h\nu}t$. The probability of photoexcitation of electron inside the solid $P(E_{\boldsymbol{K}}, h\nu)$ is given by

$$\begin{aligned} P(E_{\boldsymbol{K},h\nu}) &= \sum_{f,j'} w_{fj'} \\ &\propto \sum_{fj'} |E_f(N)|e^{i\boldsymbol{q}\cdot\boldsymbol{r}_{j'}}\boldsymbol{e}\cdot\boldsymbol{p}_{j'}|E_i\rangle|^2\delta(E_f(N) - E_i(N) - h\nu). && (3.10)\end{aligned}$$

Since the photoexcited electron energy is much larger than each one-electron energy in the remaining (N-1)-electron system, it is reasonable to assume that the photoexcited electron does not interact with the N-1 electrons. This assumption is equivalent to the situation that the time scale of the photoexcitation is much shorter than that of the electron interactions and thus the photoelectron is instantaneously created by the electron-photon interaction. This is called as "sudden approximation", which is applicable at least to the high-energy photoelectron limit.
Under the sudden approximation, the total $N$-electron energies $E_f(N)$ in the photoexcited (final) states are expressed as:

$$E_f(N) = \epsilon_f + E_f(N-1), \tag{3.11}$$

where $\epsilon_f$ stands for the one-electron. Since Coulomb interactions between excited electron and the remaining N-1 electrons are switched off in the approximation, $\epsilon_f$ can be obtained from the equation

$$(-\frac{\hbar^2}{2m}\nabla^2 + V_{eff}(\boldsymbol{r}))\phi_f(\boldsymbol{r}) = \epsilon_f\phi_f(\boldsymbol{r}), \tag{3.12}$$

where $\phi_f(\boldsymbol{r})$ is one-electron wavefunction of the excited electron and $V_{eff}(\boldsymbol{r})$ stands for the effective potential for the excited electron in solid. Considering the situation that the photoelectron energy is conserved until the emission into vacuum,

$$\epsilon_f = E_{\boldsymbol{K}} + \phi \tag{3.13}$$

is satisfied, where $\phi$ stands for the work function of the solid. Then, $E_f(N)$ is rewritten as:

$$E_f(N) = E_{\boldsymbol{K}} + \phi + E_f(N-1). \tag{3.14}$$

The $N$-electron (photoexcited) final states $|E_f(N)\rangle$ are represented by the direct product of the states in the subspaces of the photoelectron and the remaining $N-1$ electrons as

$$|E_f(N)\rangle = |E_{\boldsymbol{K}}\rangle|E_f(N-1)\rangle. \tag{3.15}$$

By the same way, the $N$-electron initial states $|E_i(N)\rangle$ are represented by:

$$|E_i(N)\rangle = |0_{PE}\rangle|E_i(N)\rangle, \tag{3.16}$$

where $|0_{PE}\rangle$ denotes the vacuum state in the photoelectron subspace. By using the second quantization formalism, $P(E_{\boldsymbol{K}}, h\nu)$ is rewritten as:

$$\begin{aligned} P(E_{\boldsymbol{K}}, h\nu) &\propto \sum_{f,j} |\langle E_f(N-1)|\langle E_{\boldsymbol{K}}|M_{fj}a^\dagger_{\boldsymbol{K}}a_j|0_{PE}\rangle|E_i(N)\rangle|^2\delta(E_f(N)-E_i(N)-h\nu) \\ &= \sum_{f,j} |M_{f,j}\langle E_f(N-1)|a_j|E_i(N)\rangle|^2\delta(E_f(N-1)-E_i(N)+E_{\boldsymbol{K}}+\phi-h\nu), \end{aligned} \tag{3.17}$$

$$M_{fj} = \int\int\int \phi^*_f(\boldsymbol{r})e^{i\boldsymbol{q}\cdot\boldsymbol{r}}(\boldsymbol{e}\cdot\boldsymbol{p})\phi_j(\boldsymbol{r})dV, \tag{3.18}$$

where $a^\dagger_{\boldsymbol{K}}$ and $a_j$ stand for the photoelectron creation operator and annihilation operator of the electron in the j-th occupied state, respectively, and $\phi_j(\boldsymbol{r})$ is the one-electron wavefunction for the j-th occupied state. $M_{fj}$ is called as matrix element representing the one-electron photoexcitation process. The kinetic energy of photoelectrons is given by its conservation law as:

$$E_{\boldsymbol{K}} = h\nu - [E_f(N-1) - E_i(N)] - \phi. \tag{3.19}$$

This means that the energy distribution of electrons obtained by photoemission spectroscopy in the multi electron system shows the energy difference between the final- and the initial-states.

### 3.1.3 Electric dipole transition

Focusing on electrons in crystals, in photoemission process, the electrons in ground state (state m) optically transit to the excited state (state n) by receiving the energy from incident light. Electric dipole transition can be thought as an imaginary electric dipole appearing with transition from state m to state n. There are selection rules for electric dipole transi-

tion, which can be explained by considering the quantum transition matrix. As understood from Fermi's golden law 3.9, the photoemission intensity is proportional to the square of the transition matrix. This transition matrix can be written as $\langle \Psi_f | \boldsymbol{er} | \Psi_i \rangle$ for an electric dipole transition and the parity of the dipole operator $\boldsymbol{er}$ is odd.（Changing the signs for space reversal operation x → - x, y → - y, z → - z.）Therefore, when the parity of the initial state and the final state are same, the transition matrix becomes 0 and forbidden. The selection rules for transitions between intra-atomic electron orbitals are defined by the azimuthal quantum number $l$ and the magnetic quantum number $m$, which specifies the wave function spread directionof the wave as follows: For the light with the parallel electric field vector to z axis,

$$\Delta l = \pm 1, \ \Delta m = 0 \tag{3.20}$$

For the light with the perpendicular electric field vector to z axis,

$$\Delta l = \pm 1, \ \Delta m = \pm 1 \tag{3.21}$$

Only transitions between states following these rules are allowed.
In the case of the $s \rightarrow p$ transition, the $p$ state ($l = 1$) has three independent states corresponding to $m = +1, 0, -1$, and it is represented by a linear combination of $Y_1^0, Y_1^1, Y_1^{-1}$.

$$Y_{px} = \frac{1}{\sqrt{2}}(Y_1^1 + Y_1^{-1}) \tag{3.22}$$

$$Y_{py} = \frac{1}{\sqrt{2}}(Y_1^1 - Y_1^{-1}) \tag{3.23}$$

$$Y_{pz} = Y_1^0 \tag{3.24}$$

For the light with the parallel electric field vector to z axis, only the transition to the $P_z$ state is a permissive transition, and conversely for the light with the perpendicular electric field vector to z axis, the transition to the $P_z$ state bocomes forbidden. Even the prohibited transition, the prohibition only means that no electric dipole transition occurs, so the transition probability is not completely equivalent to 0. Although the transition probability is small, the transition due to the interaction between the magnetic field component of the light and the magnetic moment of the particle system (magnetic-dipole transition), the transition due to the interaction between the electric field component and the electric-dipole moment of the particle system (electric-quadrupole transition) causes transitions between forbidden orbitals.

### 3.1.4 Photoionization cross section

The photoionization cross is one of the parameters for determining the photoemission intensity [32]. Assuming that the intensity of incident light as $I_0$, the number of atoms A per unit area as N, and the photoelectron generating shell of atom A as $nl$, the photoelectron M (per unit time and unit area) is expressed as follows:

$$M = I_0 N \sigma_{nl}. \tag{3.25}$$

$\sigma_{nl}$ is called as the photoionization cross section. In the case that ionization of solids by x-ray can be expressed by electric dipole approximation, differential ionization cross section

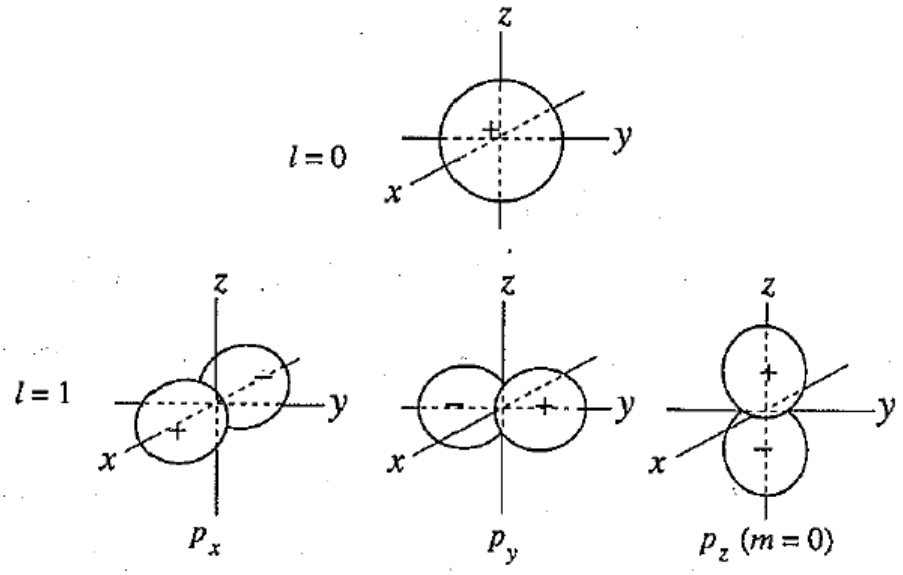


Figure 3.2: Absolute part of angular dependent components of wave functions for $s$ orbital and $p$ orbital[34]

$\frac{d\sigma_{nl}}{d\Omega}$ is given by:

$$\frac{d\sigma_{nl}}{d\Omega} = \frac{C}{g_i}(\frac{1}{h\nu})\sum_{i,f}|e\langle\Psi_f(N)|\sum_{l=1}^{M}\nabla_i|\Psi_l(N)\rangle|^2, \tag{3.26}$$

where $C$ is a constant value, $e$ is a unit vector parallel to electric field vector, $i, f$ indicate initial and final states of the system, $g_i$ is the degeneracy in initial state. The matrix elements of the transition probabilities for $i \to f$ have three notations:

$$\begin{aligned}\langle\Psi_f(N)|\sum_{l=1}^{M}\nabla_i|\Psi_l(N)\rangle &= \frac{1}{\hbar}\langle\Psi_f(N)|\sum_{l=1}^{M}p_i|\Psi_l(N)\rangle \\ &= \frac{mh\nu}{\hbar^2}\langle\Psi_f(N)|\sum_{l=1}^{M}r_i|\Psi_l(N)\rangle \\ &= \frac{1}{\hbar\nu}\langle\Psi_f(N)|\sum_{l=1}^{M}\nabla_i V|\Psi_l(N)\rangle. \end{aligned}\tag{3.27}$$

. The first formula shows the display by the velocity, the second and third formulas are the display by the distance and the acceleration respectively. These formulas gives the same result if we use accurate wave function. The photoionization cross section $\sigma_{nl}$ with unpolarized light is given by:

$$\sigma_{nl} = \frac{4\pi\alpha_0 a_0^2}{3}(h\nu)[lR_{l-1}^2(\epsilon_{kin}) + (l+1)R_{l+1}^2(\epsilon_{kin})]. \tag{3.28}$$

$\alpha_0$ stands for the microstructure constant, $a_0$ denotes the Bohr radius and $R$ under condition of $\epsilon_{kin} = h\nu - E_{nl}$ is a dipole matrix element can be written as:

$$R_{l\pm1} = \int_0^\infty R_{nl}(r) r R_{l\pm1}(r) r^2 dr, \tag{3.29}$$

where $R_{nl}$ and $R_{l\pm1}$ indicate respectively the radial parts of the electrons wave function before and after photoionization.

### 3.1.5 Angular dependence of photoelectrons

Angular dependence of photoelectron emitting probability in the photoemission process is expressed as

$$f = \frac{\sigma_i}{4\pi}[1 + \beta P_2(\cos\theta)] \tag{3.30}$$

$$P_2(\cos\theta) = \frac{3\cos^2\theta - 1}{2} \tag{3.31}$$

by using electric dipole approximation [35]. $P_n$ is the term of the n-th order of Legendre polynomial, $\theta$ is the angle between the observed photoelectron direction and the incident polarized light direction, and $\sigma_i$ is the photoionization cross section. Considering the parameter $\gamma$, which represent the term corresponding to the interference between the electric dipole and the quadrupole, and $\delta$ which is the term corresponding to the magnetic dipole,

$$f = \frac{\sigma_i}{4\pi}[1 + \beta P_2(\cos\theta) + (\delta + \gamma\cos^2\theta)\sin\theta\cos\phi] \text{ [36].} \tag{3.32}$$

The relationship between $\theta$ and $\phi$ is shown in Fig. 3.3.
The MB Scientific A1-HE analyzer used in HAXPES at BL19LXU in SPring-8 is set with the angle of 60 ° between the optical axis of synchrotron radiatio. In case of using horizontal polarized excitation light in HAXPES, $\theta = 30°$ and $\phi = 180°$, and in the case of using vertical polarized excitation light, they are $\theta = 90°$ and $\phi = 120°$.
In case of using horizontally polarized light（$\theta = 30°$,$\phi = 180°$,

$$f_{Hori} = \frac{\sigma_i}{4\pi}[1 - \frac{5}{8}\beta - \frac{1}{2}(\delta + \frac{3}{4}\gamma)]. \tag{3.33}$$

In case of using vertically polarized light（$\theta = 90°$,$\phi = 120°$,

$$f_{Vert} = \frac{\sigma_i}{4\pi}(1 - \frac{\beta}{2} - \frac{\delta}{2}). \tag{3.34}$$

In $s$ orbital exciting, since $\beta \sim 2$ and $\gamma \sim 0$ come into existence [37], so it becomes

$$f_{Vert} \sim 0. \tag{3.35}$$

As seen above, with vertically polarized excitation light, the $s$ orbital is remarkably suppressed as compared with the $p$, $d$ orbitals as shown in Fig. 3.4.
Furthermore, the Eq. 3.32 can be transformed to

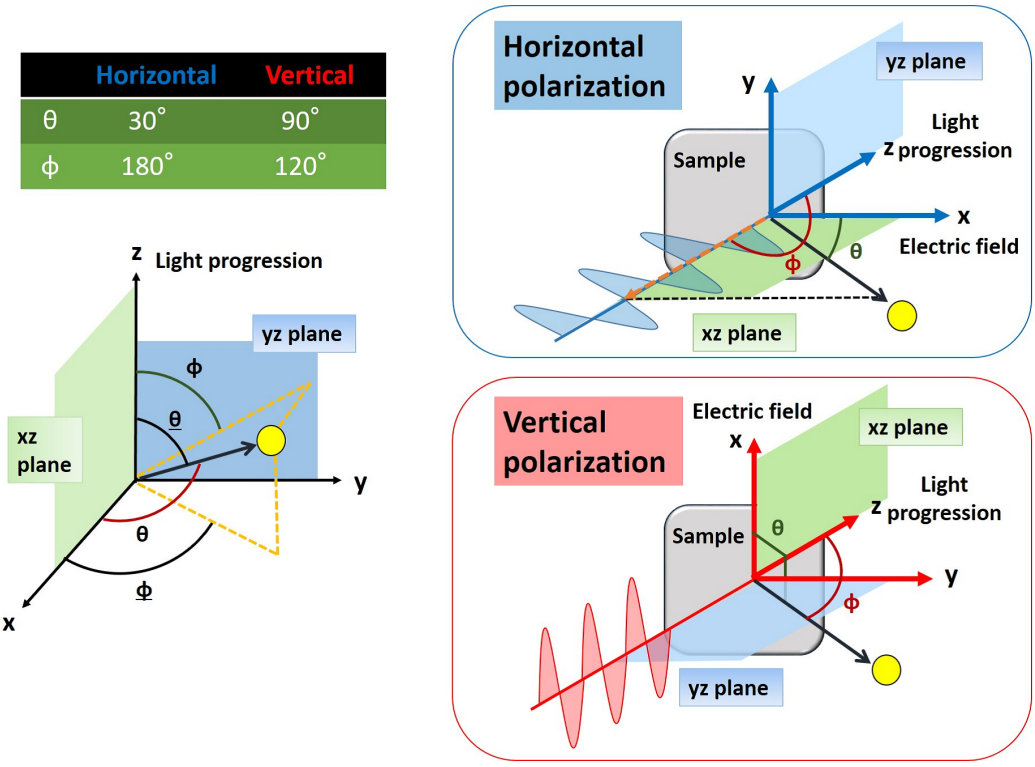


Figure 3.3: Relationship between photoemission detection direction and polarized excitation light

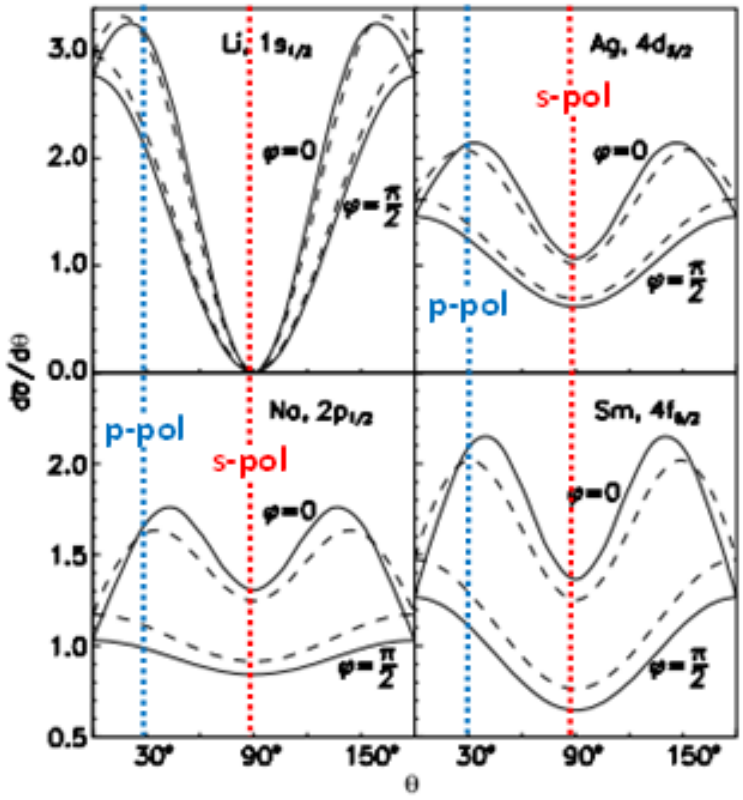


Figure 3.4: Angular dependence of photoelectrons for orbital [37]

$$
\begin{aligned}
f &= \frac{\sigma_i}{4\pi}[1 + (\beta + \Delta\beta_{lp})P_2(\cos\theta) + (\delta + \gamma\cos^2\theta)\sin\theta\cos\phi \\
&\quad +\eta P_2(\cos\theta)\cos 2\phi + \mu\cos 2\phi + \xi(1 + \cos 2\phi)P_4(\cos\theta) \\
&= \frac{\sigma_i}{4\pi}[1 + \frac{\beta + \Delta\beta_{lp}}{2}(3\cos^2\theta - 1) + (\delta + \gamma\cos^2\theta)\sin\theta\cos\phi \\
&\quad +\frac{\eta}{2}(3\cos^2\theta - 1)\cos 2\phi + \mu\cos 2\phi \\
&\quad +\frac{\xi}{8}(1 + \cos 2\phi)(35\cos^4\theta - 30\cos^2\theta + 3)] \qquad (3.36)
\end{aligned}
$$

by considering the second order term of the electric dipole approximation $\Delta\beta_{lp}$ and the angle dependent parameter $\eta, \mu, \xi$ of the second order term [37].
Therefore, in case of horizontal polarization($\theta = 30°$,$\phi = 180°$),

$$
f_{Hori} = \frac{\sigma_i}{4\pi}[1 + \frac{5}{8}(\beta + \Delta\beta_{lp}) - \frac{1}{2}(\delta + \frac{3}{4}\gamma) + \frac{5}{8}\eta + \mu + \frac{3}{64}\xi]. \qquad (3.37)
$$

In case of vertical polarization ($\theta = 90°$,$\phi = 120°$),

$$
f_{Vert} = \frac{\sigma_i}{4\pi}[1 - \frac{1}{2}\beta - \frac{1}{2}\delta + \frac{1}{4}\eta - \frac{1}{2}\mu + \frac{3}{16}\xi]. \qquad (3.38)
$$

### 3.1.6 Polarization dependence in core-level photoemission spectra

In the core-level photoemission process, one inner-core electron is excited by the incident photon with an energy $h\nu$ from the strongly correlated sites, and this photoelectron with a kinetic energy $E_K^*$ is detected in its final state. The intensity of core-level photoemission spectra of strongly correlated electron systems has so far been expressed using an angle and polarization integrated form [39, 40, 41] as a function of $\omega \equiv E_K^* - h\nu$

$$
\rho_{n_c l_c}(\omega) = \sum_{f, m_c, s_c} |\langle E_f | a_{\lambda_c} | E_i \rangle|^2 \delta(\omega + E_f - E_i), \qquad (3.39)
$$

where $E_i$ stands for the initial-state energy and $E_f$ denotes the eigenenergy of the final state $f$ with a core hole in a solid.
To deal with LD in the angle-resolved core-level photoemission spectra of a single crystal, we need to start from the form in which the transition matrix elements $M_{\gamma_c}$ are explicitly taken into account, as follows:

$$
\rho_{n_c l_c}(\omega, \boldsymbol{e}, \theta_k, \varphi_k) = \sum_{f, s_c} |\sum_{m_c} M_{\gamma_c} \langle E_f | a_{\lambda_c} | E_i \rangle|^2 \delta(\omega + E_f - E_i), \qquad (3.40)
$$

where $\boldsymbol{e}$ is the unit vector indicating the electric field direction of the incident light, and $\theta_k$ and $\varphi_k$ denote the polar and azimuthal angles of the observed photoelectrons, respectively. Here, another joint index $\gamma_c \equiv (n_c, l_c, m_c)$ [thus $\lambda_c = (\gamma_c, s_c)$] is introduced. $M_{\gamma_c}$ is represented as

$$
M_{\gamma_c} = \int\int\int \phi_{\boldsymbol{k}}^*(\boldsymbol{r}) e^{i\boldsymbol{q}\cdot\boldsymbol{r}} \boldsymbol{e}\cdot\boldsymbol{p}) \phi_{\gamma_c}(\boldsymbol{r}) dV, \qquad (3.41)
$$

where $\phi_{\gamma_c}(\boldsymbol{r})$ and $\phi_{\boldsymbol{k}}(\boldsymbol{r})$ denote the one-electron wave function of the core level with $\gamma_c$ and that of the excited photoelectron with a momentum $\boldsymbol{k}$ ($E_K^* = \hbar^2 k^2/2m$), respectively; $\boldsymbol{q}$ is the photon momentum and $\boldsymbol{p} = -\hbar\nabla$. For simplicity, let us discuss the core-level photoemission process for a single ion in the CEF within the electric dipole transitions, i.e., $\exp i\boldsymbol{q}\cdot\boldsymbol{r} \simeq 1$. By using the partial wave expansion[42, 43, 44, 45], the photoelectron wave function excited from the inner core state $\lambda_c$ with the atomic-like one-electron wave function

$$\phi_{\gamma_c}(\boldsymbol{r}) = R_{n_c l_c}(r) Y_{l_c}^{m_c}(\theta,\varphi) \tag{3.42}$$

can be expressed as

$$\phi_{\boldsymbol{k}}(\boldsymbol{r}) = 4\pi \sum_{l'm'} i^{l'} e^{-i\delta_{l'}} Y_{l'}^{m'*}(\theta_k,\varphi_k) R_{kl'}(r) Y_{l'}^{m'}(\theta,\varphi), \tag{3.43}$$

where $\delta_{l'}$ stands for the phase shift and $R_{kl'}(r)$ denotes the radial function of the continuum state. By inserting Eqs. 3.42 and 3.43 into Eq. 3.41, the transition matrix elements are rewritten within the electric dipole approximation as

$$\begin{aligned} M_{\gamma_c} &= 4\pi \sum_{l'=l_c\pm1,m'} (-i)^{l'} e^{i\delta_{l'}} Y_{l'}^{m'}(\theta_k,\varphi_k) P(n_c l_c \to kl') \\ &\quad \times \int\int Y_{l'}^{m'*}(\theta,\varphi)(\boldsymbol{e}\cdot\hat{\boldsymbol{r}}) Y_{l_c}^{m_c}(\theta,\varphi) d\Omega, \qquad (3.44) \\ P(n_c l_c \to kl') &\propto \int R_{kl'}(r) R_{n_c l_c}(r) r^3 dr, \qquad (3.45) \end{aligned}$$

where $d\Omega = \sin\theta d\theta d\phi$ and $\hat{\boldsymbol{r}}$ is the unit radial vector. We further assume that the $l_c \to l_c + 1$ transitions are predominant over the $l_c \to l_c - 1$ transitions [19, 43] and therefore the interference effects between the outgoing $l_c+1$ and $l_c-1$ photoelectron waves are negligible. Indeed, with this assumption, the experimental polarization-dependent angleresolved core-level photoemission spectra have been well reproduced by spectral simulations [14, 15, 17, 16]. By substituting Eq. 3.44 into Eq. 3.40 and omitting the $l_c \to l_c - 1$ transitions, we finally obtain

$$\rho_{n_c l_c}(\omega,\boldsymbol{e},\theta_k,\varphi_k) \propto \sum_{f,s_c} \Big| \sum_{m',m_c} Y_{l_c+1}^{m'}(\theta_k,\varphi_k) A_{l_c m_c}^{m'}(\boldsymbol{e}) \langle E_f | a_{\lambda_c} | E_i \rangle \Big|^2 \delta(\omega + E_f - E_i), \tag{3.46}$$

where

$$A_{l_c m_c}^{m'}(\boldsymbol{e}) = \int\int Y_{l_c+1}^{m'*}(\theta,\varphi)(\boldsymbol{e}\cdot\boldsymbol{r}) Y_{l_c}^{m_c}(\theta,\varphi) d\Omega. \tag{3.47}$$

Here, the term $P(n_c l_c \to kl')$ in Eq. 3.46 is omitted since it is independent of $\boldsymbol{e}$, $theta_k$, and $\varphi_k$. Comparing Eq. 3.46 with Eq. 3.39, one can recognize that the spectral weights of the multiplet-split peaks are modulated from those in the isotropic spectral function by the light polarization $A_{l_c m_c}^{m'}(\boldsymbol{e})$ and photoelectron angular $Y_{l_c+1}^{m'}(\theta_k,\varphi_k)$ factors in the polarization-dependent angle-resolved core-level photoemission spectra. Therefore, the multiplet line shape can show the polarization and angular dependence in the CEF, where the coordination axes for the electrons cannot be arbitrarily chosen.

### 3.1.7 Inelastic mean free path

In the strongly correlated electronic material, the electronic state of the surface and the inside (bulk) are drastically different. Therefore, bulk sensitive photoemission spectroscopy measurement is required to measure the bulk electronic state. The choice of high energy light with a long mean free path is one such means. Generally, for the excitation light energy （10eV≤ $h\nu$ ≤several keV） used in photoelectron spectroscopy, the photoelectrons escape depth is sufficiently shorter than the light penetration depth (several hundred ÃĔ). The detection depth in photoemission spectroscopy is generally approximated by the mean free path of photoelectrons. Some electrons undergo inelastic scattering in solids by other electrons or electrons collective excitation or phonons in the process of photoemission. The mean free path $\lambda$ that can move without such inelastic scattering effect is computationally required as shown in Fig. 3.6. Tanuma, Powell and Penn proposed the general formula TPP-2M of mean free path $\lambda$ as shown below [46].

$$\lambda = \frac{E}{E_p^2[\beta \ln(\gamma E) - \frac{C}{E} + \frac{D}{E^2}]} \tag{3.48}$$

$$E_p = 28.8\sqrt{\frac{N_V\rho}{M}} \tag{3.49}$$

$$\beta = -0.10 + \frac{0.944}{(E_p^2 + E_g^e)^{\frac{1}{2}}} + 0.069\rho^{0.1} \tag{3.50}$$

$$\gamma = 0.191\rho^{-0.5} \tag{3.51}$$

$$C = 1.97 - 0.91U \tag{3.52}$$

$$D = 53.4 - 20.8U \tag{3.53}$$

$$U = \frac{N_V\rho}{M} = \frac{E_p^2}{829.4} \tag{3.54}$$

$$\begin{aligned} E(eV) &: \textit{Kinetic energy of electrons} \\ E_p &: \textit{Plasmon energy} \\ E_g &: \textit{Band gap energy in nonconductor} \\ \rho(g \cdot cm^{-3}) &: \textit{Density of solids} \\ N_V &: \textit{Number of valence electrons per atom or molecule} \\ M &: \textit{Weight of atom or molecular} \end{aligned} \tag{3.55}$$

In the vicinity of the electron kinetic energy of 50 eV, $\lambda$ is several Å. In such case, photoemission spectroscopy is surface sensitive measurement. The electrons which transit to lower energy states due to inelastic scattering lose information of the initial state and form a broad background in the photoemission spectrum as secondary electrons.

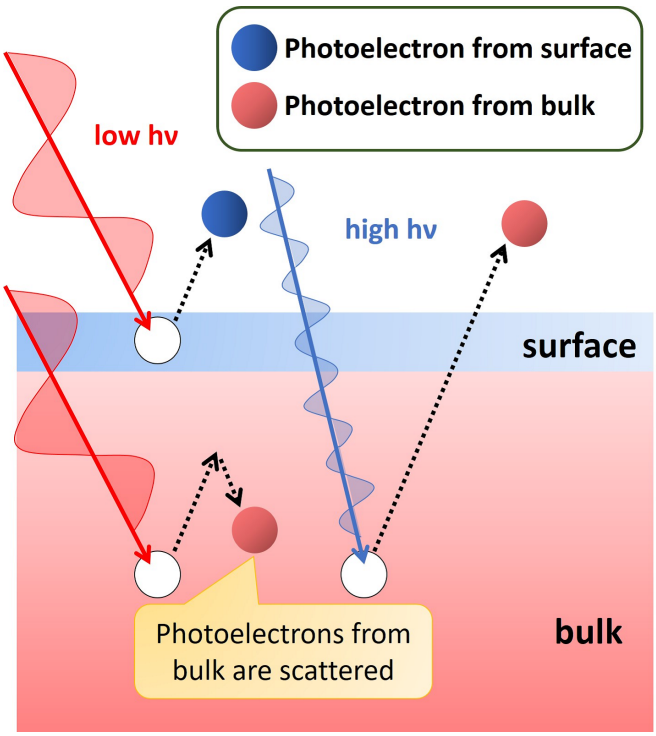


Figure 3.5: Schematic diagram showing the relationship between incident light energy and bulk sensitivity

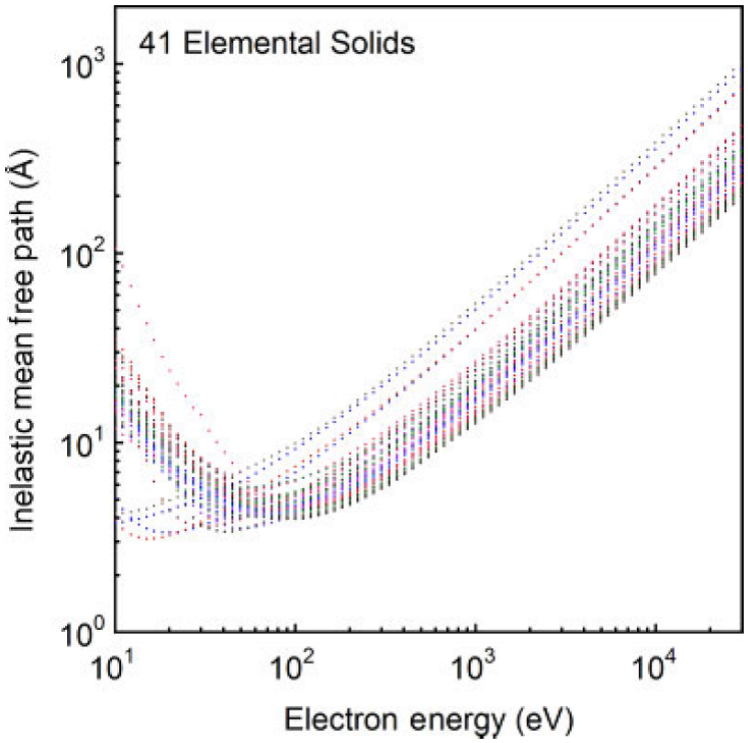


Figure 3.6: Relationship between photoelectron mean free path and kinetic energy [46]

For bulk sensitive measurements, it is necessary to use high energy excitation light. However, as mentioned above, the photoionization cross section of photoexcitation becomes smaller as the energy becomes higher [38], the high resolution photoemission experiment is difficult at high energy light over hard x-ray region in the past. In recent years, since bright hard x-ray radiation can be obtained owing to the construction of a large synchrotron radiation facility such as SPring-8, the small photoionization cross section at high photon energy region bocomes to be overcome. has resulted in the brightness of light which compensates for the low ionization cross section.

### 3.1.8 Background generation and Shirley method

#### Background in photoemission spectroscopy

In photoemission spectroscopy, there are generally two kinds of back ground. One is peak background due to the presence of peak, and one is other matrix background (secondary electron etc.) [30]. In general, matrix background does not matter in XPS. On the other hand, the peak background is originated from photoelectrons which undergo inelastic scattering many times and is released from the surface into vacuum, and that becomes a considerably large background in general.
Assuming that the generated true peak as $I(E_0)$, the measured photoelectron peak $J(E)$ is expressed by [47]:

$$J(E) = \int_E^\infty I(E_0)h(E - E_0)dE_0, \tag{3.56}$$

where h represents the probability that photoelectrons with energy $E_0$ lose the energy and appear at the position of $E$. Therefore, h is considered as a response function. As just described, the background of XPS is caused by multiple inelastic scattering of the photoelectron peak and has information inside of the solid. That is, if the form of h is clear, it is possible to obtain a true spectrum from the above formula, and information on the depth direction of the detected element is obtained from background information.
The response function h of Eq. 3.56 becomes a very strong peak at the free electron plasmon energy position in free-electronic substances such as alkali metals and aluminum. Therefore, in this case, a sharp peak called as a plasmon satellite peak is observed. Free electron plasmon energy is denoted by:

$$E_p = 28.8\sqrt{\frac{N_V\rho}{M}} \quad (eV), \tag{3.57}$$

where $N_V$ is the number of valence electrons per atom or molecule, $M$ denotes atom or molecular weight, $\rho$ stands for density ($g \cdot cm^{-3}$).

#### Shirley method

It is the first step in quantitative analysis to remove peak backgrounds in photoemission spectroscopy. The typical method for subtracting backgrounds are listed below.

- Straight line method

- Shirley method
- Tougaard method

In this thesis, we use Shirley method [48] for subtracting photoemission background. Fig 3.7 shows a conceptual diagram of the background for Shirley method. The shaded area represents the total background, and $l_1$ denotes the background of the peak (b), $l_2$ denotes the background of the peak (a), $l_3$ denotes the whole background $l_1 + l_2$. As is clear from above, the most of character in Shirley method is that the number of inelastic scattering electrons is proportional to the intensity of peak, but it is independent of energy loss. There are several algorithms for Shirley method, this thesis introduce Proctor-Sherwood's method [49].
Fig. 3.8 shows conceptual diagram of Proctor-Sherwood's method. The basic flame of ap-

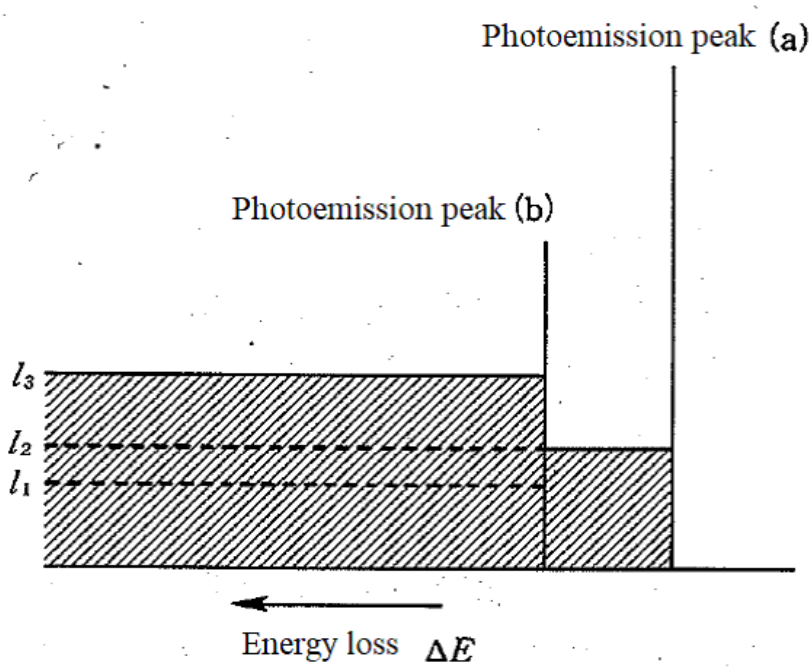


Figure 3.7: Conceptual diagram of the background in the Shirley method [30]

proaching is that the background intensity with no existence of peak becomes to be $b$ (end point), and the background intensity with all peaks existence becomes to be $a$, the background between from the point $x$ to $k$ depends on the ratio of the peak component to total. Expressed as a formula, the background intensity at the point $x$ is given by:

$$B(x) = \frac{(a-b)Q(x;k)}{T} + b, \tag{3.58}$$

where $T$ is the total peak intensity, which is total area above $B(x)$. $Q(x;k)$ is the peak intensity from the interval $x$ to the end point $k$ and is expressed as:

$$Q(x;k) = \int_x^k [J(t) - B(t)]dt \tag{3.59}$$

, where $J(t)$ denotes the photoelectron intensity. The total peak intensity $T$ becomes to be equivalent to $Q(1;k)$.

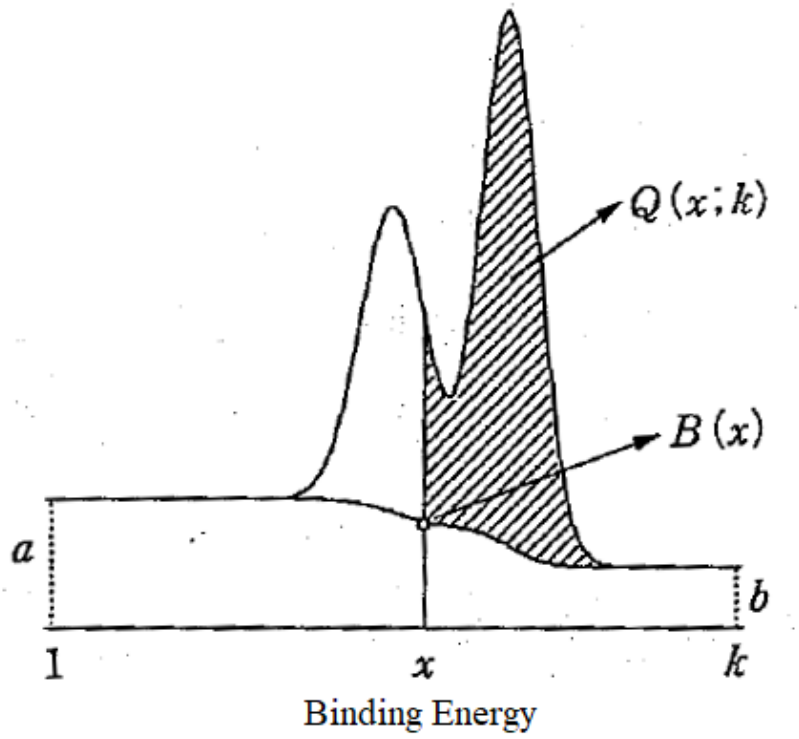


Figure 3.8: Background subtraction by the Proctor-Sherwood method [30]

In this method, the selection of the end point of the background on the higher energy side is important, and when peak intensity almost stay constant with changing this end point, it becomes good background subtracting. However, it is difficult to apply this method for the case when there is a large difference in the background intensity between the higher and lower energy sides, there is a satellite peak. In general, there is little problem for using the same background range for a standard sample and an unknown sample, but extreme caution is required for taking the background area.

## 3.2 Energy levels in 3*d* core-level photoemission spectroscopy

Since the core hole is generated in the final state for photoemission process, the energy level states in the initial state and the final state are different. We explain the energy levels in the Ce and Yb 3*d* core-level photoemission process.

### 3.2.1 Energy level in initial and final state for Ce 3*d* core-level photoemission process

The possible configurations in the Ce system are $|4f^0\rangle$, $|4f^1\rangle$ and $|4f^2\rangle$. Firstly, we consider the energy levels in the initial state. Assuming that the energy level of $|4f^0\rangle$ is equivalent to 0 (base state), the energy levels for $|4f^0\rangle$, $|4f^1\rangle$ and $|4f^2\rangle$ configurations in initial state are

given by:

$$E^{(i)}(f^0) = 0 \tag{3.60}$$
$$E^{(i)}(f^1) = -\epsilon_f \tag{3.61}$$
$$E^{(i)}(f^2) = -2\epsilon_f + U_{ff}. \tag{3.62}$$

$\epsilon_f$ denotes the energy required to bring one electron from Fermi level to 4 $f$ level, $U_{ff}$ stands for Coulomb energy between 4 $f$ electrons.
In the final state, these energy levels lower by $\epsilon_{3d}$ due to the $3d$ core hole generated in photoemission process. As $\epsilon_{3d}$ is a constant, it may sometimes be ignored. When the Coulomb interaction between the $3d$ core hole and the $4f$ electrons is stood by $U_{fc}$, the energy levels in the final state are respectively,

$$E^{(f)}(f^0) = -\epsilon_{3d} \tag{3.63}$$
$$E^{(f)}(f^1) = -\epsilon_{3d} + \epsilon_f - U_{fc} \tag{3.64}$$
$$E^{(f)}(f^2) = -\epsilon_{3d} + 2\epsilon_f + U_{ff} - 2U_{fc}. \tag{3.65}$$

So that in the final state $|4f^2\rangle$ state becomes the most stable. Similar energy levels are also obtained in the final state for $4d$ core-level photoemission process, and $|4^2\rangle$ becomes stable in final state.
The schematic diagram of Energy level in initial and final state for Ce $3d$ core-level photoemission process is shown in the Fig. 3.9.

### 3.2.2 Energy level in initial and final state for Yb $3d$ core-level photoemission process

The possible configurations in the Yb system are $|4f^{14}\rangle$ and $|4f^{13}\rangle$. The approachment for the Yb system is almost the same as that of the Ce system, but we consider as one $4f$ hole exist for Yb system. As is the case with the Ce system, assuming that the energy of $|4f^0\rangle$ is equivalent to 0 (base state), the energy levels for $|4f^{14}\rangle$ and $|4f^{13}\rangle$ configurations in initial state are given by:

$$E^{(i)}(f^{14}) = 14\epsilon_f + \binom{14}{2} U_{ff} = 14\epsilon_f + 91U_{ff} \tag{3.66}$$
$$E^{(i)}(f^{13}) = 13\epsilon_f + \binom{13}{2} U_{ff} = 13\epsilon_f + 78U_{ff}. \tag{3.67}$$

. Where the energy required to bring one electron from $4f$ level to Fermi level, that is, the energy required to bring one hole from Fermi level to $4f$ level is defined as $\epsilon_f^h$,

$$\epsilon_f^h = E^{(i)}(f^{14}) - E^{(i)}(f^{13}) \tag{3.68}$$
$$= \epsilon_f - 13U_{ff}. \tag{3.69}$$

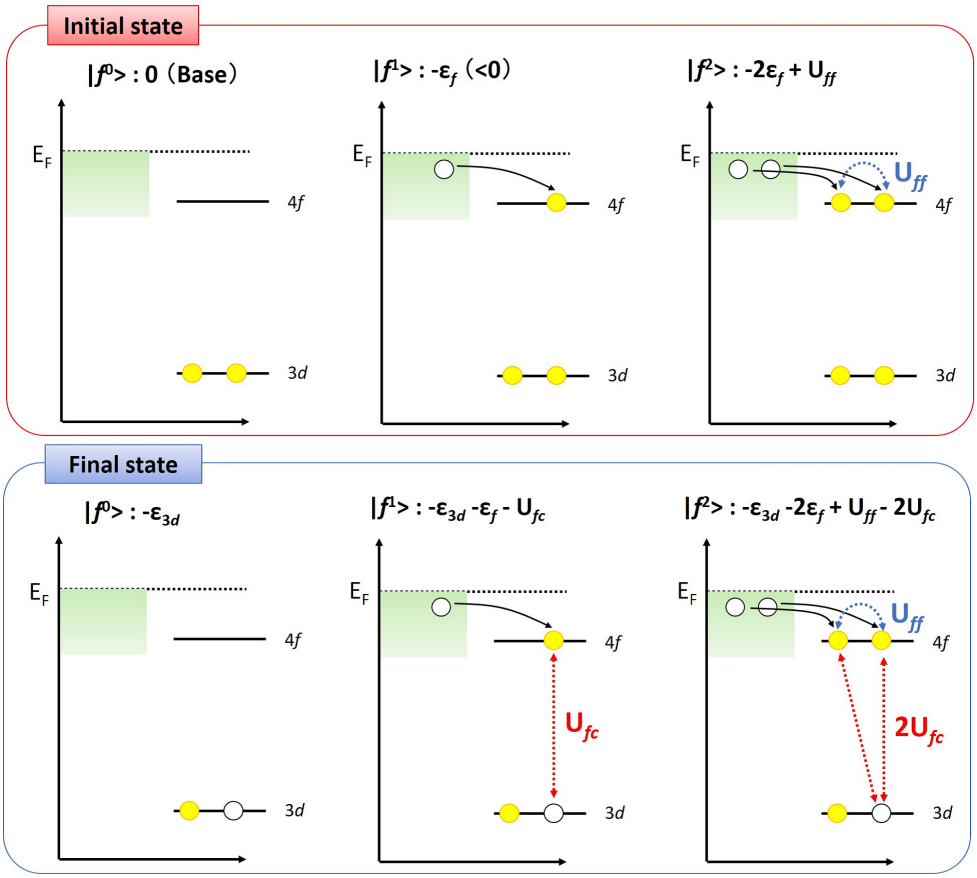


Figure 3.9: Energy diagram of Ce $3d$ core-level photoemission process in initial and final states. $\epsilon_f$ in indicates naked $4f$ level.

When the energy of the $|4f^{14}\rangle$ state is set to 0 (base state), the energy levels in initial state are rewritten with $\epsilon_f^h$, as follows:

$$E^{(i)}(f^{14}) = 0 \tag{3.70}$$
$$E^{(i)}(f^{13}) = -\epsilon_f^h. \tag{3.71}$$

Since the hole is formed in $3d$ core level in final state, the energy level lower by $-\epsilon_{3d}$ from the initial state and Coulomb interaction between $3d$ core hole and $4f$ hole $U_{fc}^h(<0)$ accrues. Therefore, the energy levels in the final state is

$$E^{(f)}(f^{14}) = -\epsilon_{3d} \tag{3.72}$$
$$E^{(f)}(f^{13}) = -\epsilon_{3d} - \epsilon_f^h + U_{fc}^h. \tag{3.73}$$

The basis functions in the initial state with SIAM in Yb compounds are shown below, and the schematic diagram of Energy level in initial and final state for Yb $3d$ core-level photoemission process is shown in the Fig. 3.10.

The schematic energy diagram of $3d$ XPS in Ce and Yb systems is shown in Fig. 3.11. In the Ce system, the $f^2$ configuration state is located in the highest level in the initial state, whereas in the final state it becomes the lowest level. It means that it is necessary to consider the $4f^2$ final state for spectrum analysis.

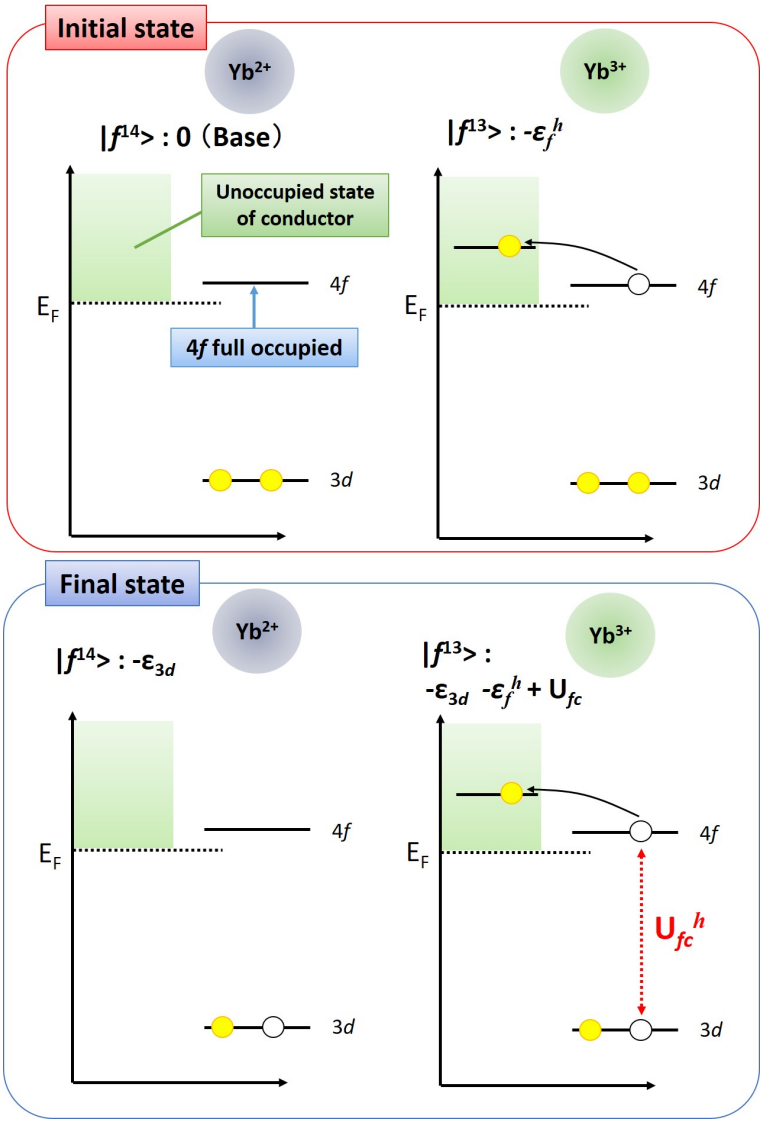


Figure 3.10: Energy diagram of Yb $3d$ core-level photoemission process in initial and final states. $\epsilon_f$ in indicates empty $4f$ level.

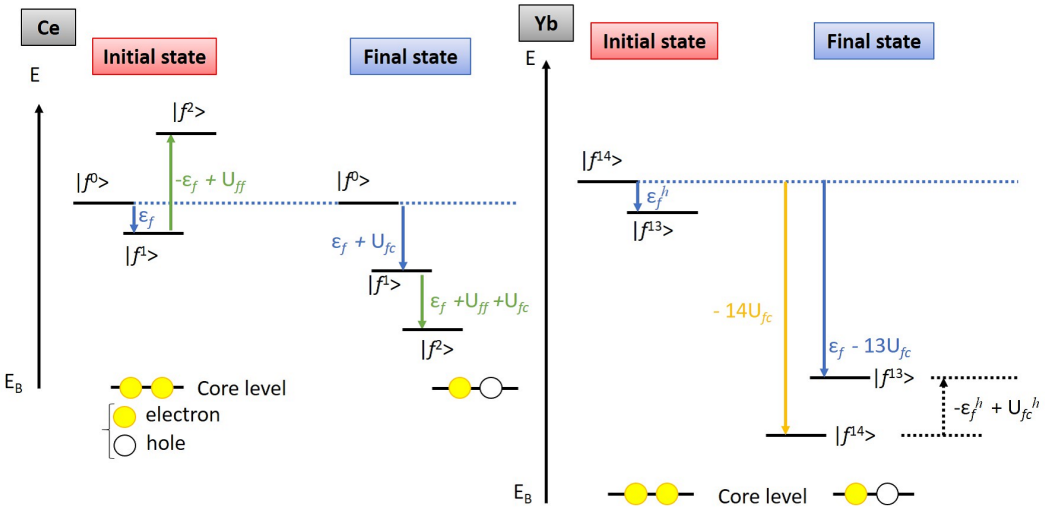


Figure 3.11: Conceptual energy diagram of different $f$ level for Ce and Yb $3d$ XPS. $\epsilon_f$ denotes the naked and empty $4f$ level for Ce and Yb system respectively.

## 3.3 Ion-model calculation of linear dichroism in photoemission spectra

In this thesis, to clarify the origin of LD in the rare-earth core-level and $4f$ photoemission spectra, we have performed ionic calculations including the full multiplets [18] and the local CEF splitting using the XTLS 9.0 program [19]. The advantage of the ion model is that we should consider only the interaction parameter within the atom, the interaction parameter with the ligands is not necessary to consider, since the rare-earth elements in compounds are treated as ions. Also, once interaction parameters within the atom are determined, it can be applied to any compounds containing the same rare-earth ions. All atomic parameters such as the $4f$-$4f$ and $3d$-$4f$ Coulomb and exchange interactions (Slater integrals) and the $3d$ and $4f$ spin-orbit couplings have been obtained using Cowan's code [25] based on the Hartree-Fock method.

# Chapter 4

# Polarized hard x-ray photoemission spectroscopy

## 4.1 Synchrotron radiation light

Synchrotron radiation is the light radiated by the electrons or positrons accelerated to the nearby speed of light due to the magnetic field [50].
The characteristic behavior of this light are shown below.

- Wide range of wavelength from vacuum ultraviolet to x-ray
- Collimation
- Polarization
- Pulse property

The energy of the electrons in storage ring of SPring-8 is the value of 8 GeV, at which therefore we can perform experiments with use of the hard x-ray. Though it had been difficult to perform photoemission spectroscopy with hard x-ray due to the small photoionization cross-section as mentioned in Chapter 3 in the past, the highly brilliant light by the large synchrotron radiation facility has enabled to perform the photoemission experiment with hard x-ray.
In this chapter, we present the instrumental status of BL19LXU in SPring-8 where we have performed the experiments, and our developed polarization-switching technique and the instruments employed for our study.

## 4.2 BL19LXU in SPring-8

We have performed polarized hard-xray photoemission experiments at BL19LXU in SPring-8. In this section, the features of the BL19LXU in SPring-8 are shown [51, 52, 53].

### 4.2.1 Layout of BL19LXU in SPring-8

The schematic layout of the BL19LXU in SPring-8 is shown in Fig. 4.1. The radiated light from the long x-ray undulator are monochromated by double-crystal monochromator

before reach to the experimental hatch. The experimental hatches which we can enter for experiment are experimental hatch 1 (EH1) and EH3.

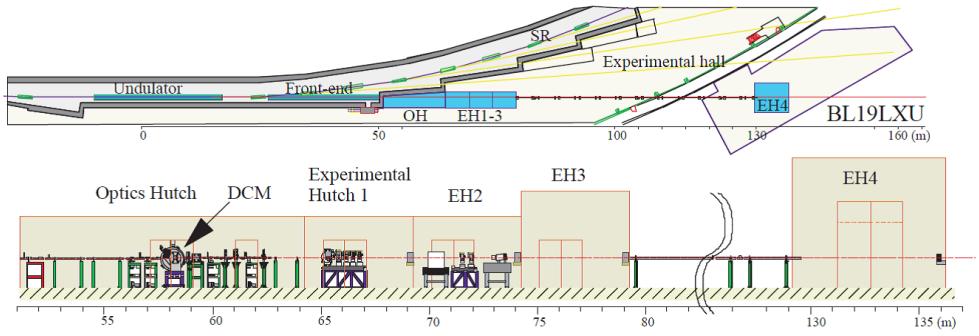


Figure 4.1: Schematic layout of BL19LXU in SPring-8[51]

### 4.2.2 Long x-ray undulator

The long x-ray undulator is used at the BL19LXU in SPring-8（Fig. 4.2). The all length of the magnet of the undulator is 27 m, and the period length of that is 32 mm (781 period) [51]. The undulator consists of the NdFe permanent magnet. The maximum value of its magnetic field is 0.59 T with the minimum undulator gap size of 12 mm [52].

Owing to this undulator, the beamline users can use the horizontally-polarized primary-light

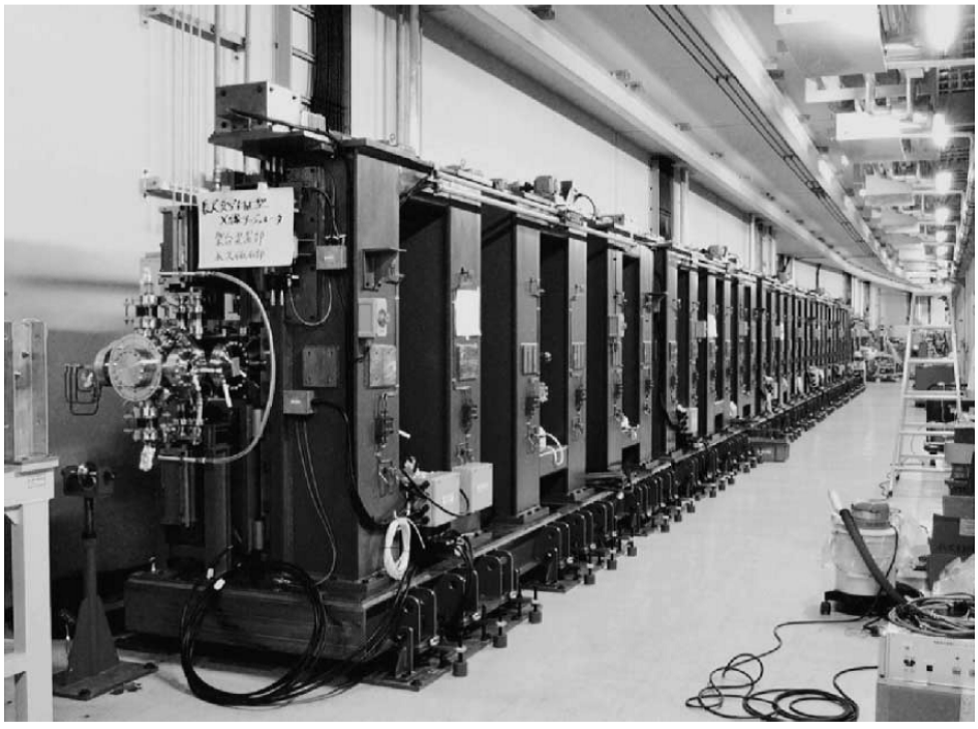

Figure 4.2: The long x-ray undulator at BL19LXU in SPring-8[52]

of which energy range is from 7.4 keV to 18.8 keV [51, 52].

### 4.2.3 Si(111) double-crystal monochromator

The primary-light radiated from the undulator have been firstly monochromated by the Si(111) double-crystal monochromator. The first crystal size of that is 90 × 50 × 35t mm$^3$, and the second of that is 80 × 50 × 35t mm$^3$.

## 4.3 Polarized hard x-ray photoemission system

### 4.3.1 Polarized hard x-ray photoemission system at BL19LXU in SPring-8

Our system for polarized hard x-ray photoemission spectroscopy is shown in Fig. 4.3. We have further monochromate the light monochromated by the Si(111) double-crystal monochromator, and then we have swich the polarization of the light by using two single-crystalline (100) diamonds as phase retarders at the EH1. Finally, we have focused the polarized light using an ellipsoidal Kirkpatrik-Baez mirror before the photoemission process at EH3.

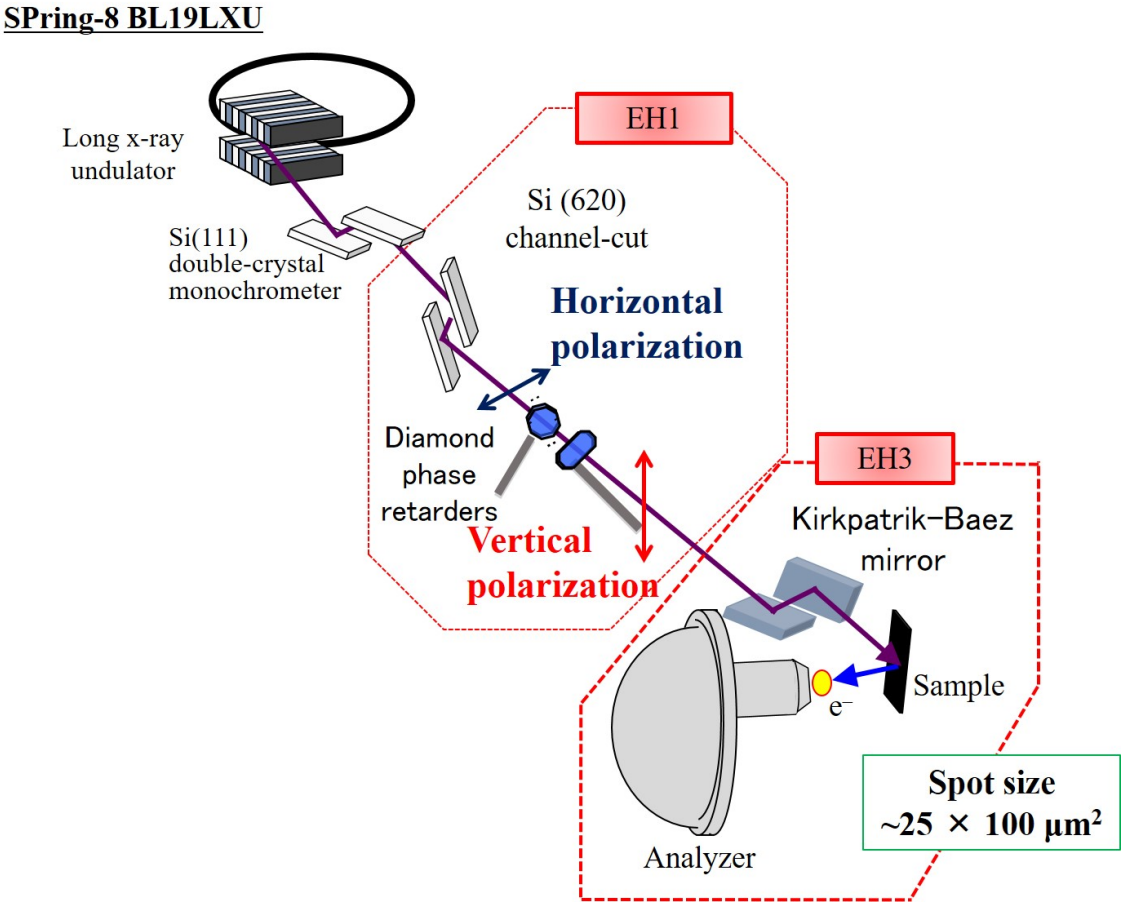


Figure 4.3: Schematic layout of the system for polarized hard x-ray photoemission at BL19LXU in SPring-8

### 4.3.2 Channel-cut crystal

A channel-cut crystal is designed to make Bragg reflection twice with the (+ -) configuration in one crystal and enable us to utilize higher resolution light. There are several channel-cut crystals, for example, using Si(440), Si(620), Si(551) reflections. We utilize the Si(620) channel-cut crystal which obtain the reflection from Si(310) phase.

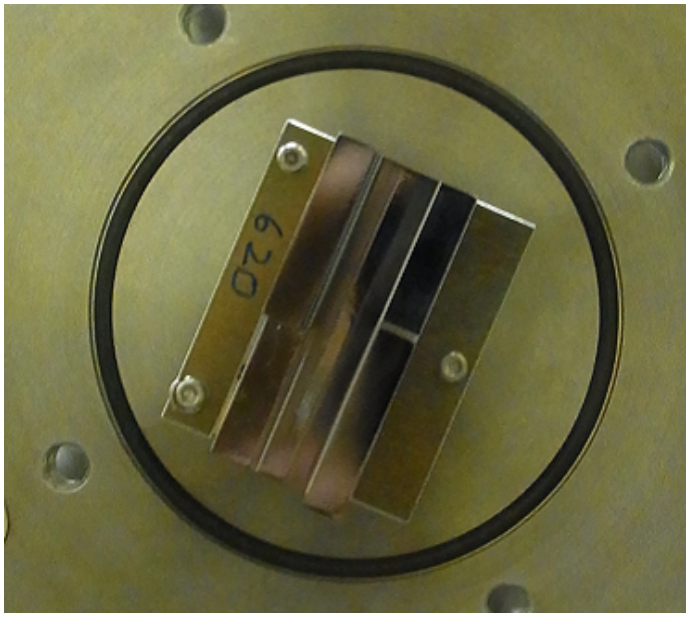


Figure 4.4: The Si(620) channel-cut crystal

### 4.3.3 Diamond phase retarders

We have switched horizontal polarization light to vertical polarization light using by two single-crystalline (100) diamonds as phase retarders. The picture of the diamonds we actually use for experiment is shown in Fig. 4.5. The thickness of each diamond is 0.25 mm. The theory of method to switch the polarization of the light is described later.

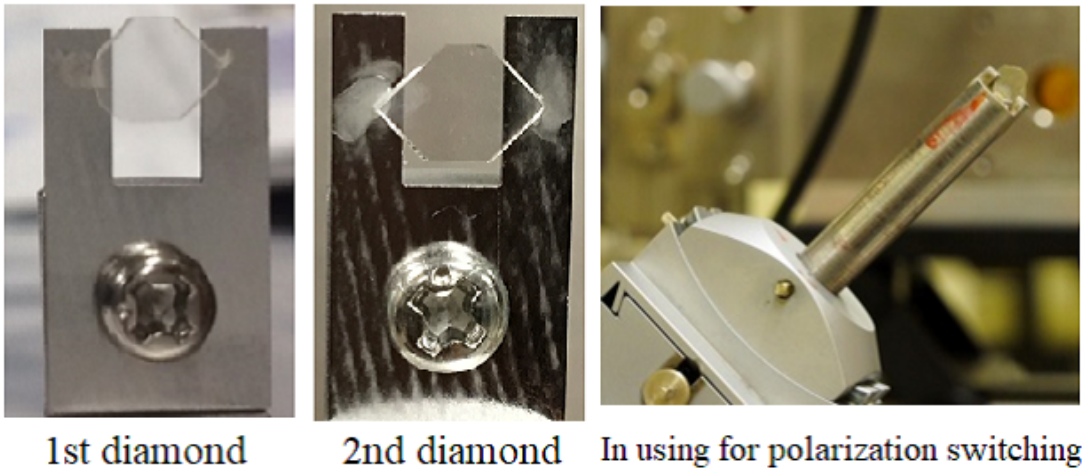


Figure 4.5: The two single-crystalline (100) diamonds for polarization switching

### 4.3.4 Kirkpatrik-Baez (KB) mirror

Since the both horizontal and vertical radiated light width at the mirror point are as small as the value of 1 2 mm, Kirkpatrik-Baez (KB) mirror is often used to focus the light, which consists of two meridian curved mirror. The KB mirror enable to reduce aberration in process of focusing light, as compared with toroidal mirror. We have two-dimensionally (along horizontal direction and vertical direction) focused the light reached to EH3, and the best size of focusing light is 25 $\mu$m × 25 $\mu$m.
In actually, we have focused the excitation light within 30$\mu$m × 100$\mu$m to keep linearity of photoelectron counts by multi-channel plate (MCP) as described later. Since it is necessary to reduce the concentration of photoelectrons for keeping linearity of photoelectron counts, we have released horizontal light focusing. The analyzer slit is horizontally broad, there is little problem to releasing horizontal light focusing.

### 4.3.5 Hemi-spherical photoelectron spectrometer

Schematic representation of the electrostatic hemi-spherical photoelectron spectrometer is shown in Fig 4.7. Hemispherical photoelectron analyzer was used to analysis the energy of the emitted photoelectrons. In the hemispherical photoelectron analyzer, a negative potential was applied outside the hemispherical $-V_P/2$ while a positive potential was applied inside the hemispherical $V_P/2$. Photoelectrons which have a certain amount of kinetic energy are chosen from the electrons entered from a slit A and passed to another slit B. The difference of electronic voltage between outside and inside the hemispherical is applied $V_P$. The kinetic energy of electrons which pass the slit B is described by the outside (R1) and inside hemispherical radius (R2) as:

$$E_P = \frac{eV_P}{\frac{R_2}{R_1} - \frac{R_1}{R_2}}. \tag{4.1}$$


Figure 4.6: The Kirkpatrik-Baez mirror at BL19LXU in SPring-8

The energy resolution ΔE is determined by the width of slit (w) between two hemispherical [54] as:

$$\Delta E = \frac{wE_P}{R_1 + R_2} = \frac{wE_P}{2R_0}. \tag{4.2}$$

Therefore, the ratio between pass energy ($E_P$)$and energy resolution$($\Delta E$) can be expressed as:

$$\frac{E_P}{\Delta E} = \frac{R_1 + R_2}{w}, \tag{4.3}$$

which means this value is depend on only the shape of the analyzer including the slit width (w), but independent with pass energy. The basic value of $E_P/\Delta E$ is about 50∼200. The electrons passed analyzer are amplified and counted by the channeltron. In case of measuring by micro-channel plate (MCP), the counts of photoelectrons are recognized by the image of the screen placed to back of MCP (induced ~3.5 kV) which is imported by CCD camera. Though the photoelectrons essentially intensity should be proportional to the counts obtained from detectors, the linearity between them sometimes have not kept by using MCP, due to the method of photoelectrons counts.
By sweeping pass energy $E_P$, photoemission spectra can be obtained. Since the energy resolution $\Delta E$ for photoelectrons which have high kinetic-energy (low binding-energy) is so large as $\Delta E$∼10eV in soft and hard x-ray region, when the value of $E_P/\Delta E$ is consistent with sweeping $E_P$, the photoelectrons have be deaccelerated in static electric field before passing analyzer. The relation between deaccelerated electronic voltage ($V_R$), photoelectron

kinetic energy ($E_K$), pass energy ($E_P$) and the work function in analyzer ($\phi_A$) can be given as:

$$E_P = E_K - eV_R - \phi_A. \tag{4.4}$$

So that we can obtain photoemission spectra with keeping small pass energy by sweeping $V_R$.
We have utilized A1-HE analyzer produced by MB Scientific company, and we have measured photoelectrons counts by MCP. To keep the linearity of photoelectrons intensity measured by MCP, we have controlled to make the photoelectron countrate at the p-polarization configuration equivalent to that at the s-polarization configuration by using the attenuator made of aluminum foils.

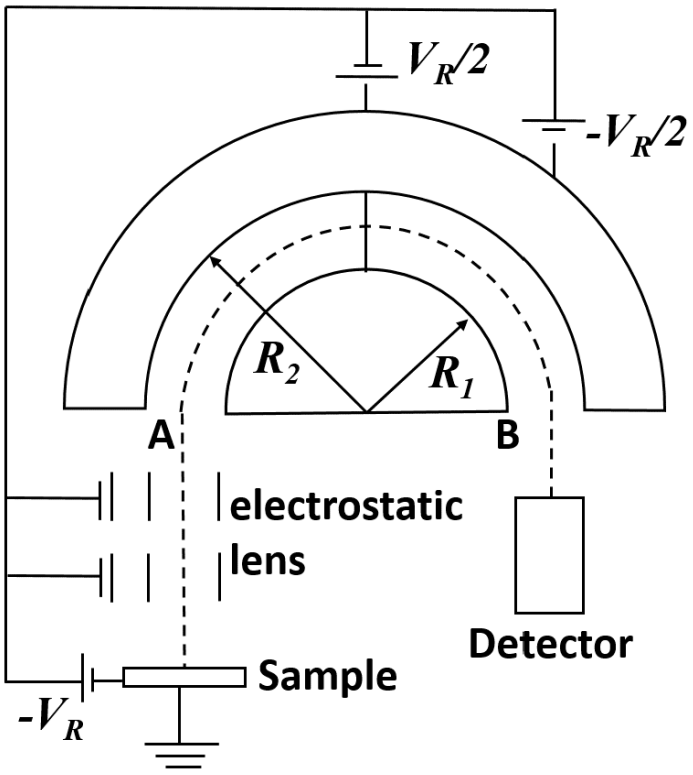


Figure 4.7: Schematic representation of the electrostatic hemi-spherical photoelectron spectrometer

### 4.3.6 Developed low-temperature two-axis manipulator

Our using developed low-temperature two-axis manipulator is shown in Fig 4.8[55], which fix and rotate samples. The low-temperature refrigerator for measuring samples is also shown in Fig 4.9

By using the two-axis manipulator, the experimental geometry was controlled to easily optimize the detection direction of photoelectrons. The rotation feedthrough provides polar rotation $\theta$. The top of the rotation stage gives the azimuthal rotation $\phi$ over a 90° range.

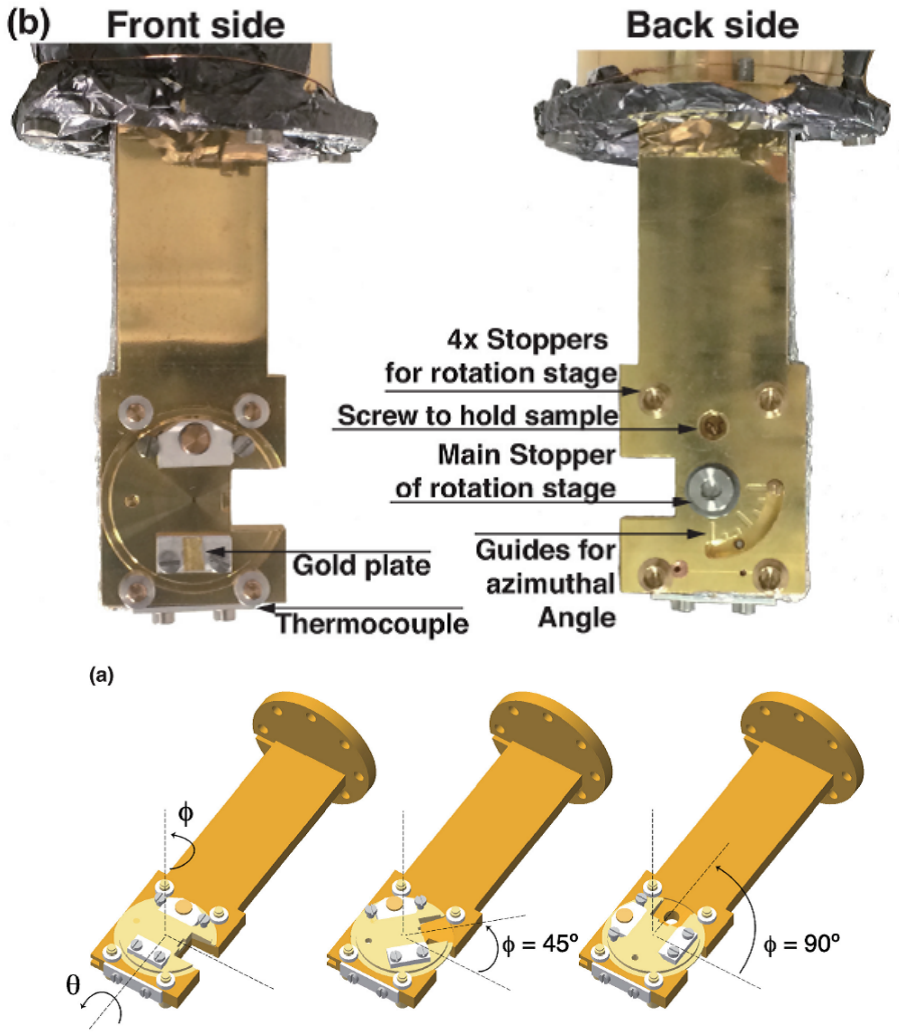


Figure 4.8: Schematic view of developed low-temperature two-axis manipulator[55]

In order to observe the ground-state symmetries of strongly-correlated systems, the measuring environment is required to cool to very low temperature. Using the closed-cycle He refrigerator and the heater for temperature control are enable us to perform photoemission experiment from 5 K to 300 K.

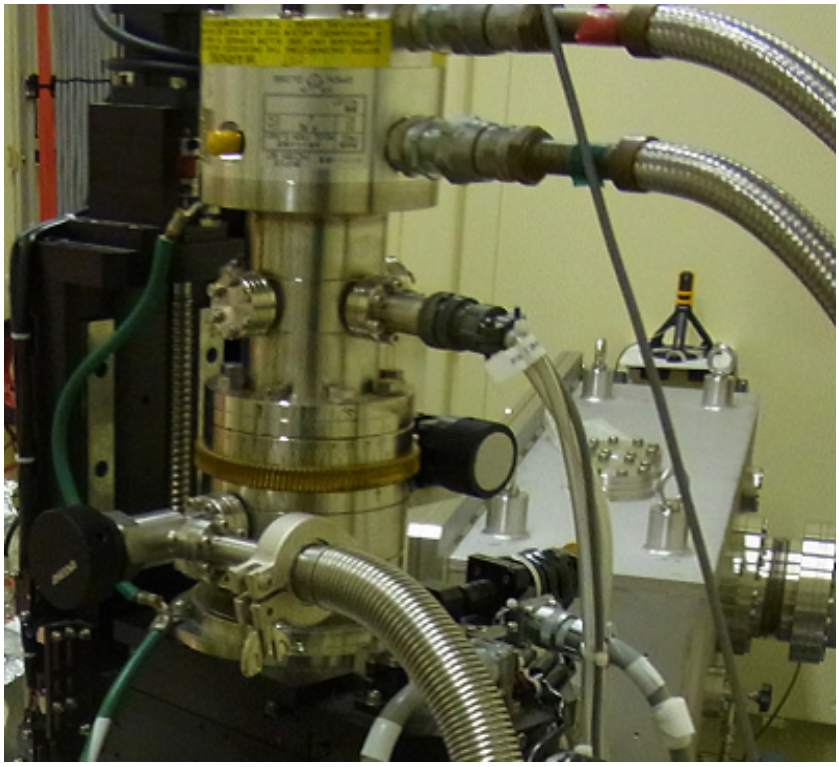

Figure 4.9: Schematic view of closed-cycle He refrigerator at BL19LXU in SPring-8

## 4.4 Hard x-ray polarization switching method

The synchrotron radiated hard x-ray light from basic undulator is almost horizontally polarized. At the soft x-ray or vacuum ultraviolet rays beamline it is difficult to switch the polarization by users. On the other hand, the polarization switching can be performed by users for the hard x-ray in photon energy of 6〜12 keV region (wavelength : 0.1〜0.2 nm) [55, 56, 57]. In this section, the polarization switching method by two single-crystalline diamond phase retarders.

### 4.4.1 Polarization switching by diamond phase retarders

The theory of polarization switching according to dynamic theory of diffraction is shown below [50]. In the x-ray reflection at single-crystal phase, the wave front direction of horizontal component and vertical component shift near Bragg angle, in result, birefringence with a little difference wave number vector occurs. The phase difference between horizontal component and vertical component ($\delta$) is formed with propagating of wave field in crystal. $\delta$ is described as:

$$\delta = -\frac{\pi}{2}[\frac{r_e^2 Re[F_h F_{\bar{h}}]}{\pi^2 V^2} \cdot \frac{\lambda^3 sin2\theta_B}{\Delta\theta}]\Delta t. \tag{4.5}$$

$r_e$:classical electron radius $2.8174 \times 10^{-5}$Å
$V$:unit cell radius
$F_h$:crystal structure factor of Bragg reflection in index number of reflecting

plane (hkl)
$\lambda$:wavelength
$\theta_B$:Bragg angle
$\Delta\theta$:angle shift from Bragg angle (offset angle)
$\Delta t$:effective thin of single-crystalline diamond

The formula 4.5 show that the phase difference is proportional to the effective thin of single-crystalline diamond and inversely proportional to the angle shift from Bragg angle. We have utilized two single-crystalline diamond phase retarders to get higher quality vertically polarized light.
The phase going straight to the traveling direction of light is defined as $x$ axis, and the parallel direction to that is defined as $y$ axis. Considered the shifting of electric field at the observation point of light, the $x$ and $y$ component of electric field vectors are following as:

$$E_x = E_{x0} \cos \omega t \tag{4.6}$$
$$E_y = E_{y0} \cos (\omega t + \delta). \tag{4.7}$$

$\omega$ shows angular frequency and $\omega = 2\pi c/\lambda$, $\lambda$ show wavelength of light, and $c$ is the speed of light. Since in case of linear polarization the ratio between $E_x$ and $E_y$ is consistent for time, the phase difference $\delta$ must be equivalent to 0 or $\pm\pi$. By using the slope angle of electric field vector from horizontal direction $\phi$ and the relations as $E_{x0} = E_0 \cos\phi$, $E_{y0} = E_0 \sin\phi$, the electric field vectors are described as:

$$E_x = E_0 \cos\phi \cos \omega t \tag{4.8}$$
$$E_y = E_0 \sin\phi \cos \omega t. \tag{4.9}$$

The phase difference $\delta$ is treated as 0 in this formula. In case of $\phi = 0°, 90°$, the polarizations of light show horizontal and vertical respectively.
When the diamond phase retarder is set with 45° gradient from horizontally polarized light, the relation as $E_0 \cos\phi = E_0 \sin\phi = E_0/\sqrt{2}$ is given. So that the electric field vectors can be described as

$$E_x = \frac{E_0}{\sqrt{2}} \cos \omega t \tag{4.10}$$
$$E_y = \frac{E_0}{\sqrt{2}} \cos \omega t. \tag{4.11}$$
$$\tag{4.12}$$

In the case of using one diamond phase retarder, since $\sigma$ polarization component is kept and the phase for $\pi$ polarization component shifts half wavelength (equal to 180°), the linearly polarized light of which angle direction shifts 90° from the incident light is obtained. The schematic diagrams of polarization switching by one single-crystalline diamond phase retarder are shown in Figs 4.10,4.11.

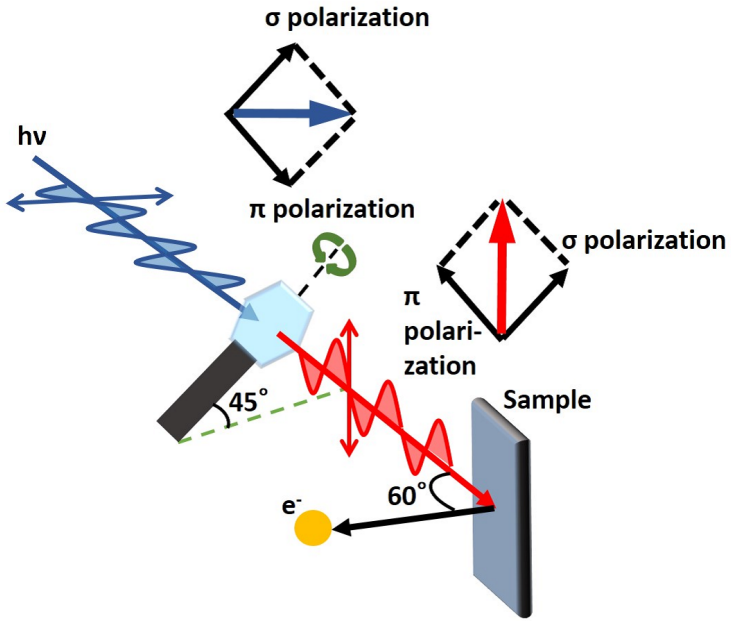


Figure 4.10: Schematic diagram of polarization switching from horizontally polarized light to vertically polarized light by one single-crystalline diamond phase retarder

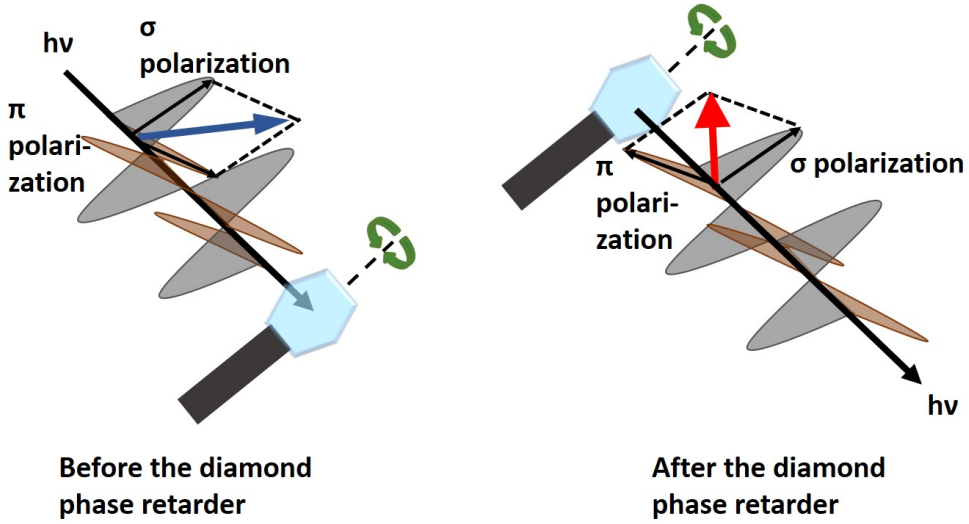


Figure 4.11: Schematic diagram of electric field vector switching by one single-crystalline diamond phase retarder (After passing a diamond phase retarder, the phase for $\pi$ polarization component shifts 180°.)

In case of using two diamond phase retarders, the first diamond is set to keep $\sigma$ polarization component as the case of one diamond, and shift the phase of $\pi$ polarization component to 1/4 of wavelength, which follows that incident horizontally polarized light is switched to circular polarization. The second diamond is set with 45° gradient from horizontally polarized light, alternately facing to the first diamond, for suppressing blurring of phase difference $\delta$ by diffusion of finite light in scattering surface. Since $\pi$ polarization component is kept and the phase for $\sigma$ polarization component shifts -1/4 of wavelength (−90°) by the second diamond, the circular polarized light is switched to vertically polarized light. The schematic diagrams of polarization switching by two single-crystalline diamond phase retarders are shown in Figs. 4.12,4.13.

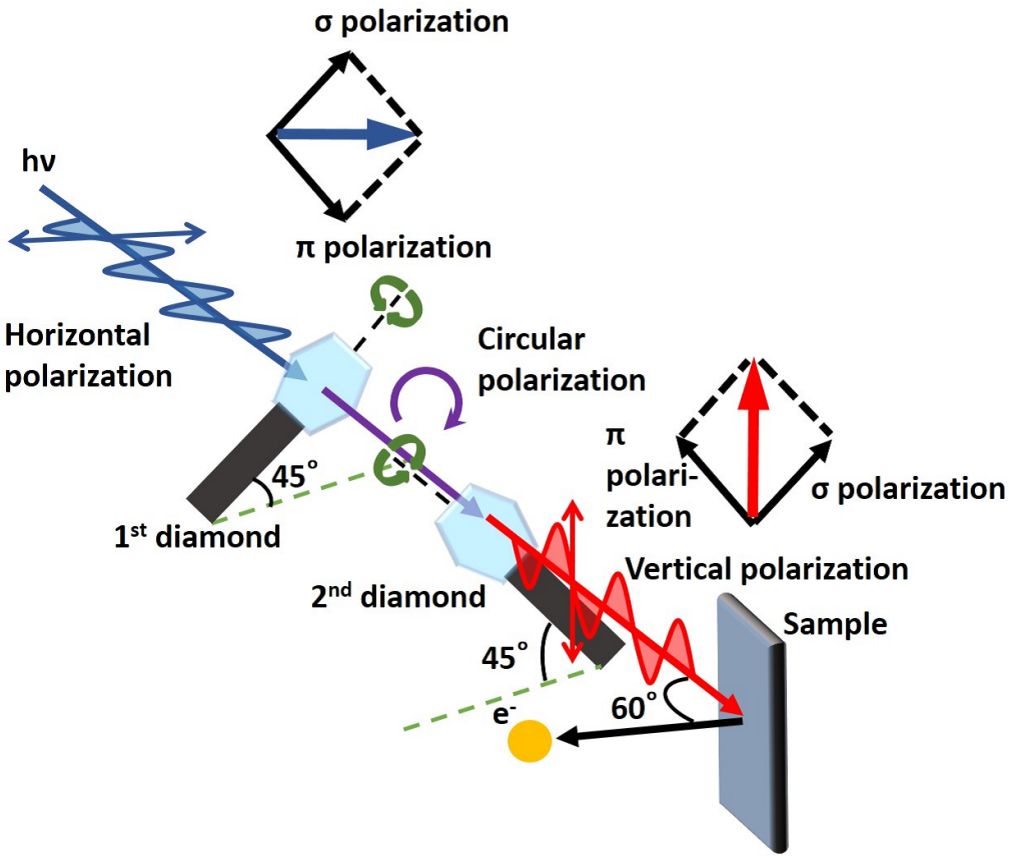


Figure 4.12: Schematic diagram of polarization switching from horizontally polarized light to vertically polarized light by two single-crystalline diamond phase retarders

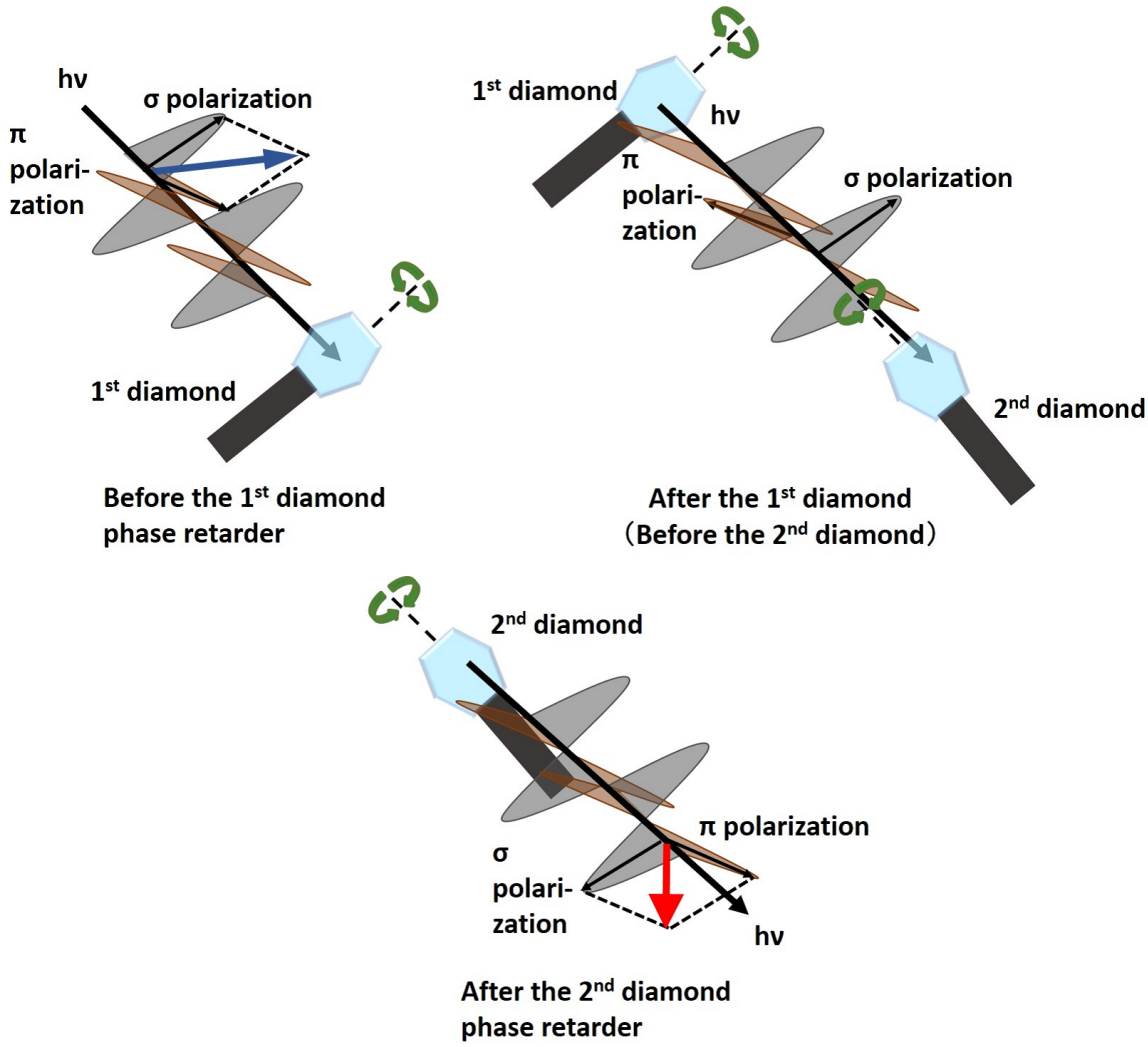


Figure 4.13: Schematic diagram of electric field vector switching by two single-crystalline diamond phase retarders (After passing the first diamond phase retarder the phase for $\pi$ polarization component shifts 90°, and after passing the second diamond phase retarder, the phase for $\sigma$ polarization component shifts -90°.)

### 4.4.2 Observation system for polarization degree and transmittance

We have observed polarization degree by two NaI scintillation counters placed horizontally and vertically downstream of the double diamond phase retarders. The transmittance of the x-ray beam after the double diamond phase retarders has been observed by an ion-chamber which measure relative intensity of light with the phenomena that the gas between electric poles ionized by incident x-ray. We have set up diamond phase retarders and NaI scintillation counters and an ion-chamber as Fig 4.14.
Since the horizontal component is not scattered to horizontal direction (electric field direction) and vertical component is not scattered to vertical direction when a kapton film is set with (111) plane before NaI scintillation counters, the counts for horizontal polarization component have been measured by vertically placed NaI scintillation counter, and reversely The counts for vertical polarization component have been measured by horizontally placed scintillation counter.
In actual experiment, we have used the fluorescent plate and the CCD camera to find the Bragg reflection. We have set the fluorescent plate near diamond phase retarders and monitored emissions of light by diamonds with Bragg angle from outside of experimental hatch. After finding the Bragg angle, we have measured the transformation of polarization degree by scanning along angle direction of the counts obtained from NaI scintillation counters.

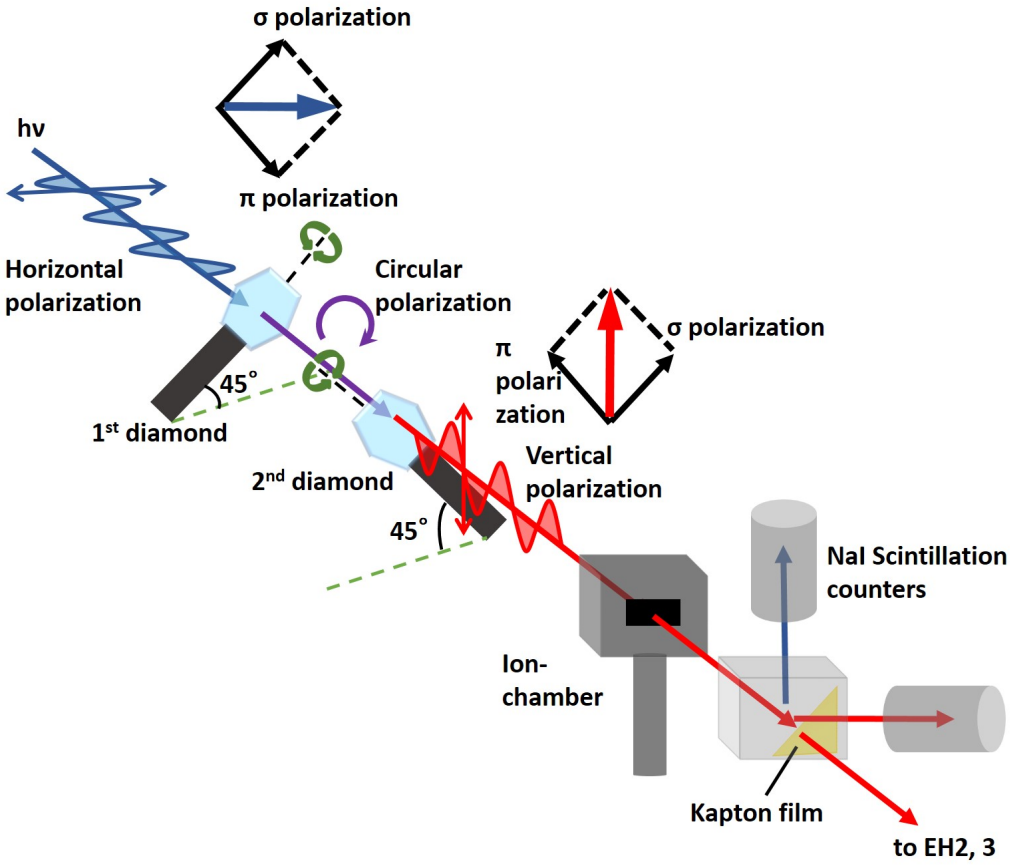


Figure 4.14: Schematic layout of diamond phase retarders and the observation system for polarization degree and transmittance

### 4.4.3 Transmittance of the x-ray beam after the diamond phase retarders

The transmittance of the x-ray beam after the diamond phase retarders is obtained from the intensity of the light measured by an ion-chamber or two NaI scintillation counters. The transmittance of the x-ray beam for two diamond phase retarders with the thickness of 0.25 mm is about 50 % (70 % per one diamond).

### 4.4.4 Degree of linear polarization

The degree of linear polarization $P_L$ is defined as:

$$P_L = \frac{I_H - I_V}{I_H + I_V} \tag{4.13}$$

The angle dependences of the degree of linear polarization $P_L$ for the first and second diamond phase retarder are shown in Figs. 4.15,4.16. The circular polarization which have equivalent horizontal and vertical component is obtained with small offset angle (the angle from Bragg angle) of ±18 arcsecond for the first diamond. After obtained the circular polarization by the first diamond, by using second diamond the minimum value of the degree of linear polarization $P_{Lmin} = -0.93$ is obtained with offset angle of +18 arcsecond for the second diamond. Since the ratio between horizontal component and vertical component is following as $1+P_L$:$1-P_L$, the vertically polarized light component is 96 % when the degree of linear polarization $P_L$ has minimum value.

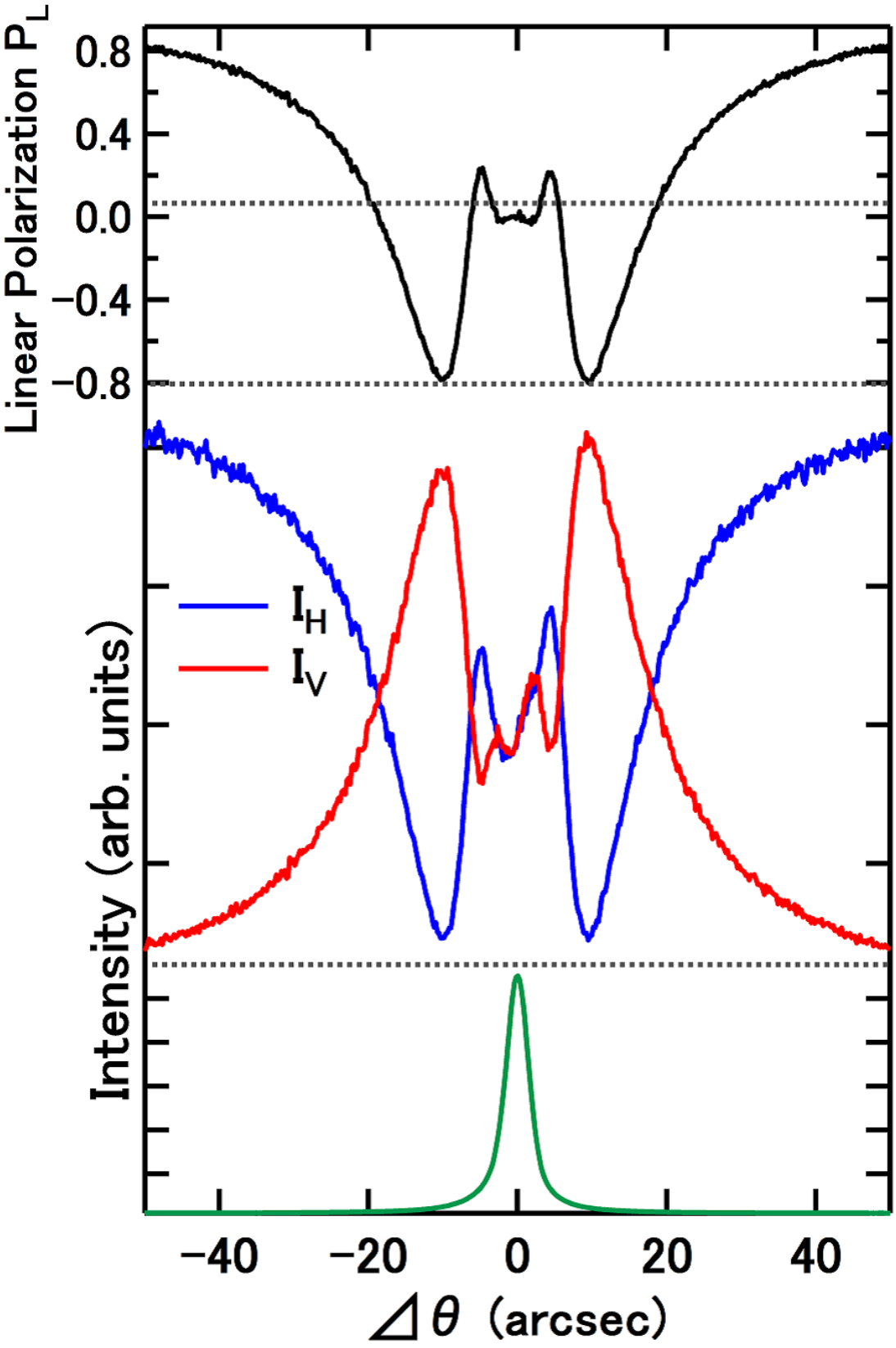


Figure 4.15: The angle dependence of the degree of linear polarization $P_L$, the counts of horizontally and vertically polarized x-ray component, and the intensity of Bragg reflection with the offset angle from Bragg angle for the first diamond phase retarder

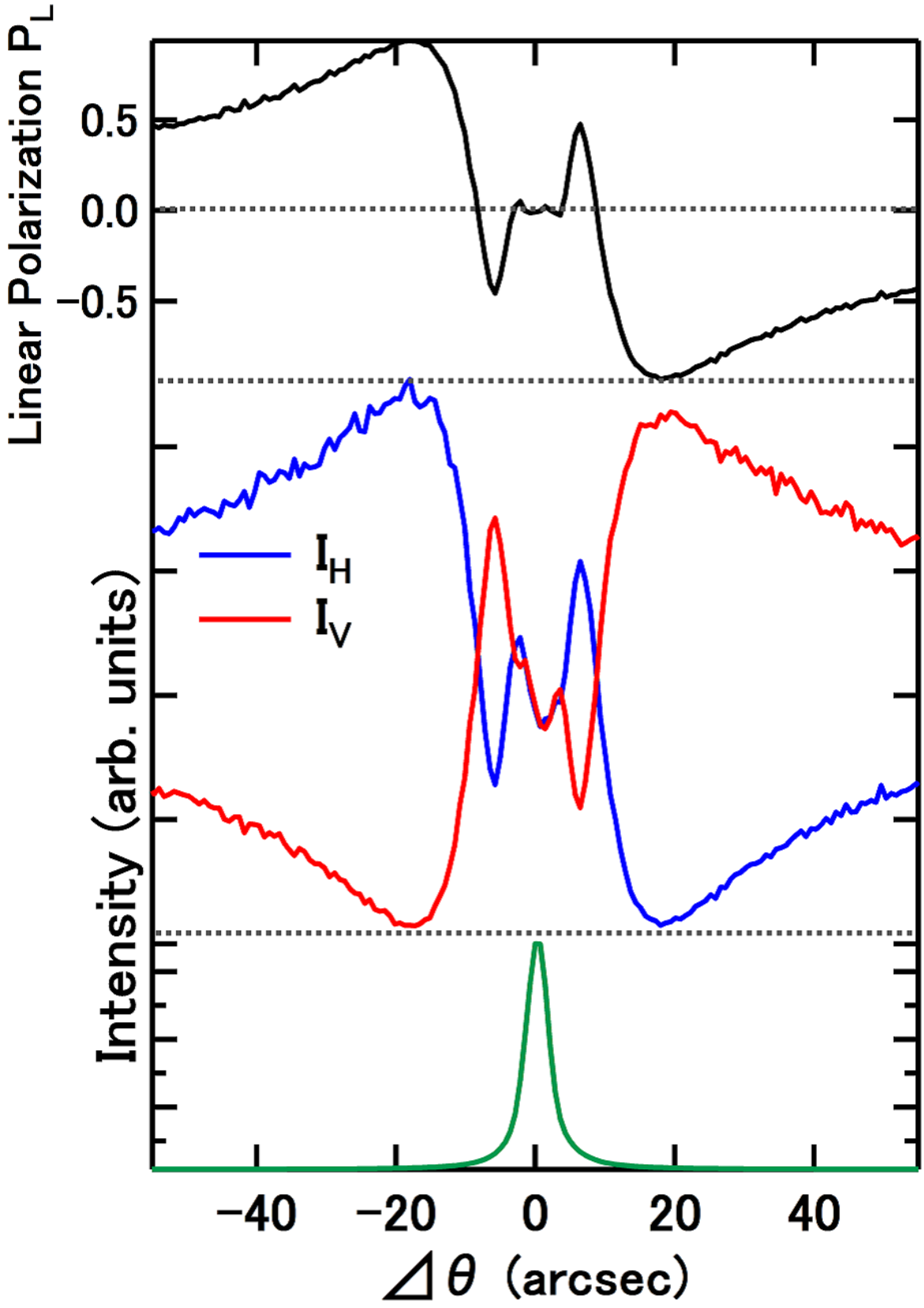


Figure 4.16: The angle dependence of the degree of linear polarization $P_L$, the counts of horizontally and vertically polarized x-ray component, and the intensity of Bragg refrection with the offset angle from Bragg angle for the second diamond phase retarder

# Chapter 5

# Probing $4f$ ground-state symmetry of cubic $YbB_{12}$ by linear dichroism in core-level photoemission

$Yb^{3+}$ has one $4f$ hole (thirteen $4f$ electrons). In this chapter, we discuss the $4f$ ground state for the $Yb^{3+}$-dominated Yb compound by linear dichroism in $Yb^{3+}$ $3d$ core-level photoemission spectra which multiplet structures clearly occurs. Especially we pick up $YbB_{12}$ known as Kondo semiconductor [15].

## 5.1 Energy splitting of $Yb^{3+}$ $4f$ levels in cubic symmetry

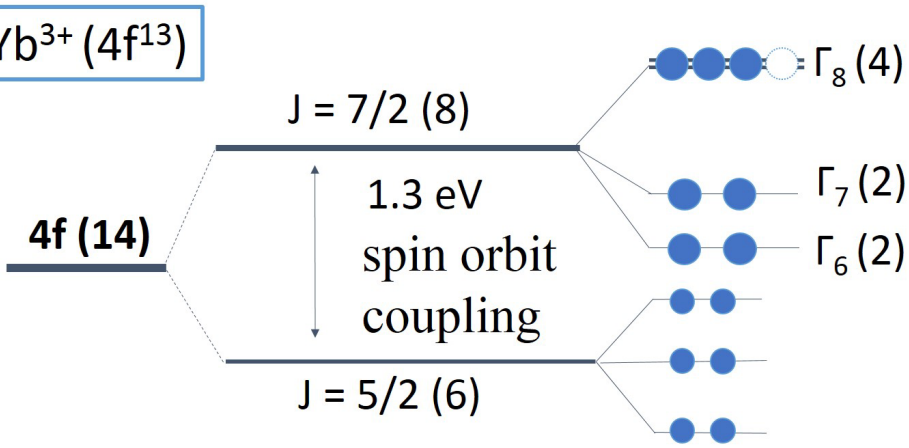


Figure 5.1: Schematic diagram of energy splitting of $Yb^{3+}$ $4f$ levels in cubic symmetry

The energy diagram of $Yb^{3+}$ $4f$ levels in cubic symmetry is shown in Fig. 5.1. Firstly, the $4f$ levels are split by the spin-orbit interaction into sixfold degenerated $J = 5/2$ states and eightfold degenerated $J = 7/2$ states. Since the size of splitting by the spin-orbit interaction is ~1.3 eV, and this value is enough larger than CEF splitting, we may consider only $J = 7/2$ states (assuming hole picture). The eightfold degenerated $J = 7/2$ states are further split due to the CEF. There are three eigenfunctions for $\Gamma_6$ (doublet), $\Gamma_7$ (doublet), and $\Gamma_8$ (quartet)

states as mentioned Chapter2. These three functions are written by the linear combination of $|J_z\rangle$ states as follows:

$$|\Gamma_6\rangle = \sqrt{5/12}|\pm 7/2\rangle + \sqrt{7/12}|\mp 1/2\rangle, \tag{5.1}$$

$$|\Gamma_7\rangle = -\sqrt{3}/2|\pm 5/2\rangle + 1/2|\mp 3/2\rangle, \tag{5.2}$$

$$|\Gamma_8\rangle = \begin{cases} -\sqrt{7/12}|\pm 7/2\rangle + \sqrt{5/12}|\mp 1/2\rangle \\ 1/2|\pm 5/2\rangle + \sqrt{3}/2|\mp 3/2\rangle \end{cases} .. \tag{5.3}$$

Fig. 5.2 shows the $Yb^{3+}$ $4f$ hole charge distributions for each wave functions $\Gamma_6$, $\Gamma_7$, and

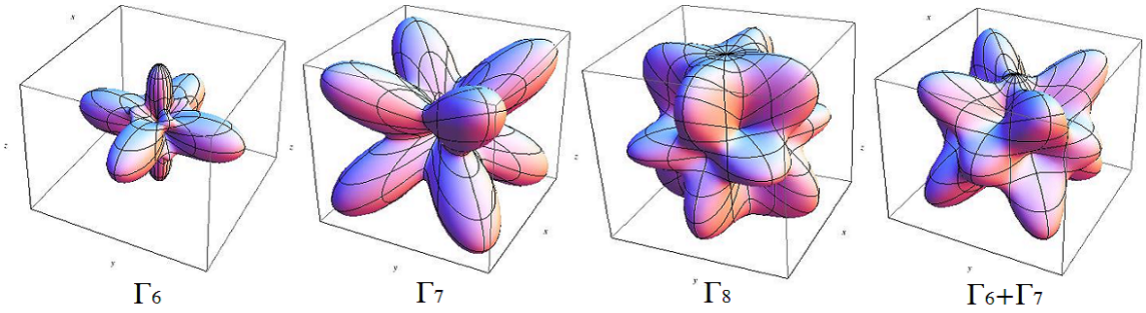


Figure 5.2: $Yb^{3+}$ $4f$ hole charge distributions with CEF in cubic symmetry

$\Gamma_8$. The $\Gamma_6$, $\Gamma_7$, and $\Gamma_8$ $4f$ charge distributions are elongated along the <100>, <111>, and <110> directions, respectively. In the case of $YbB_{12}$, since the accidentally degenerated $\Gamma_6 + \Gamma_7$ states could be a candidate for the ground state [58], the $4f$ hole spatial distribution of the $\Gamma_6 + \Gamma_7$ state are also shown. Fig. 5.1 shows one instance of $4f$ level scheme, and in actual it is not clear which eigenfunction is the lowest state.

## 5.2 Overview of Yb 3*d* core-level photoemission spectrum

The polarization-dependent $Yb^{3+}$ $3d$ HAXPES spectra in the [100] direction of $YbB_{12}$ are shown in Fig. 5.3. Generally there are four peaks originated from $Yb^{2+}$ and $Yb^{3+}$. Single peak at a binding energy of ~1519 eV and 1567 eV are corresponding to $Yb^{2+}$ $3d_{5/2}$ and $Yb^{2+}$ $3d_{3/2}$ respectively, since the $4f$ subshell is fully occupied in the $Yb^{2+}$ sites with a spherically symmetric $4f$ distribution. Multiple peaks ranging from 1524 to 1534 eV and 1570 to 1584 eV are from $Yb^{3+}$ $3d_{5/2}$ and $Yb^{3+}$ $3d_{3/2}$ respectively. In addition the broadly plasmon peaks exist at the 20 eV higher binding energy from the peak originated from $Yb^{3+}$. The substitution of photoemission background is too difficult for $Yb^{3+}$ $3d_{3/2}$ spectral region due to the plasmon peaks located in both higher and lower binding energy side, so that we determine $4f$ orbital symmetry by $Yb^{3+}$ $3d_{5/2}$ photoemission spectra.

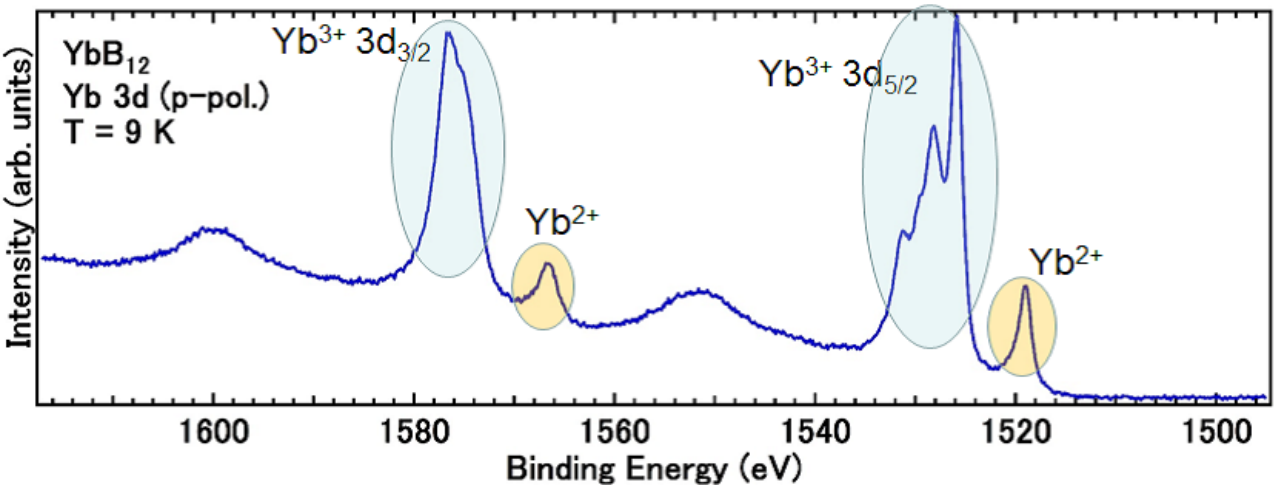


Figure 5.3: Yb 3*d* core-level photoemission spectrum of $YbB_{12}$

## 5.3 Simulated polarization-dependent $Yb^{3+}$ $3d_{5/2}$ photoemission spectra

Simulated polarization-dependent $Yb^{3+}$ $3d_{5/2}$ core-level HAXPES spectra assuming the crystal-field-split ground state in cubic symmetry at 3 photoelectron directions ([100], [111] and [110]) are shown in Fig. 5.4. In the case of $YbB_{12}$, since the accidentally degenerated $\Gamma_6+\Gamma_7$ states could be a candidate for the ground state, the simulations assuming the $\Gamma_6+\Gamma_7$ ground state and its $4f$ hole spatial distribution are also shown. Simulations shown in Figs.5.4(a), (b), (c) is respectively corresponding to assuming photoelectron detection direction along [100], [111], [110]. In Fig. 5.4, the blue lines show the spectra at p-polarization configuration, and the red lines shows that at s-polarization configuration. We have performed these ionic calculations including the full multiplet theory [18] and the local CEF splitting using the XTLS 9.0 program [19]. All atomic parameters such as the $4f$-$4f$ and $3d$-$4f$ Coulomb and exchange interactions (Slater integrals) and the $3d$ and $4f$ spin-orbit couplings have been obtained using Cowan's code [25]. The Slater integrals (spin-orbit couplings) are reduced to 88% (98%) to fit the core-level photoemission spectra [59].

LD defined by the difference in spectral weight between the s- and p-polarization configurations is reversed between the [100] and [111] directions for all states displayed here. LD for the $\Gamma_6$ ground state has the same tendency as that for the $\Gamma_8$ ground state. On the other hand, LD for the $\Gamma_8$ state is the smallest since the $4f$ hole spatial distribution for the $\Gamma_8$ state is the nearest to a spherical shape among these three eigenfunctions. LD assuming the $\Gamma_6+\Gamma_7$ state is reversed to that for the $\Gamma_8$ state. These simulations indicate that the symmetry of the $Yb^{3+}$ state can be determined by LD in the core-level photoemission.

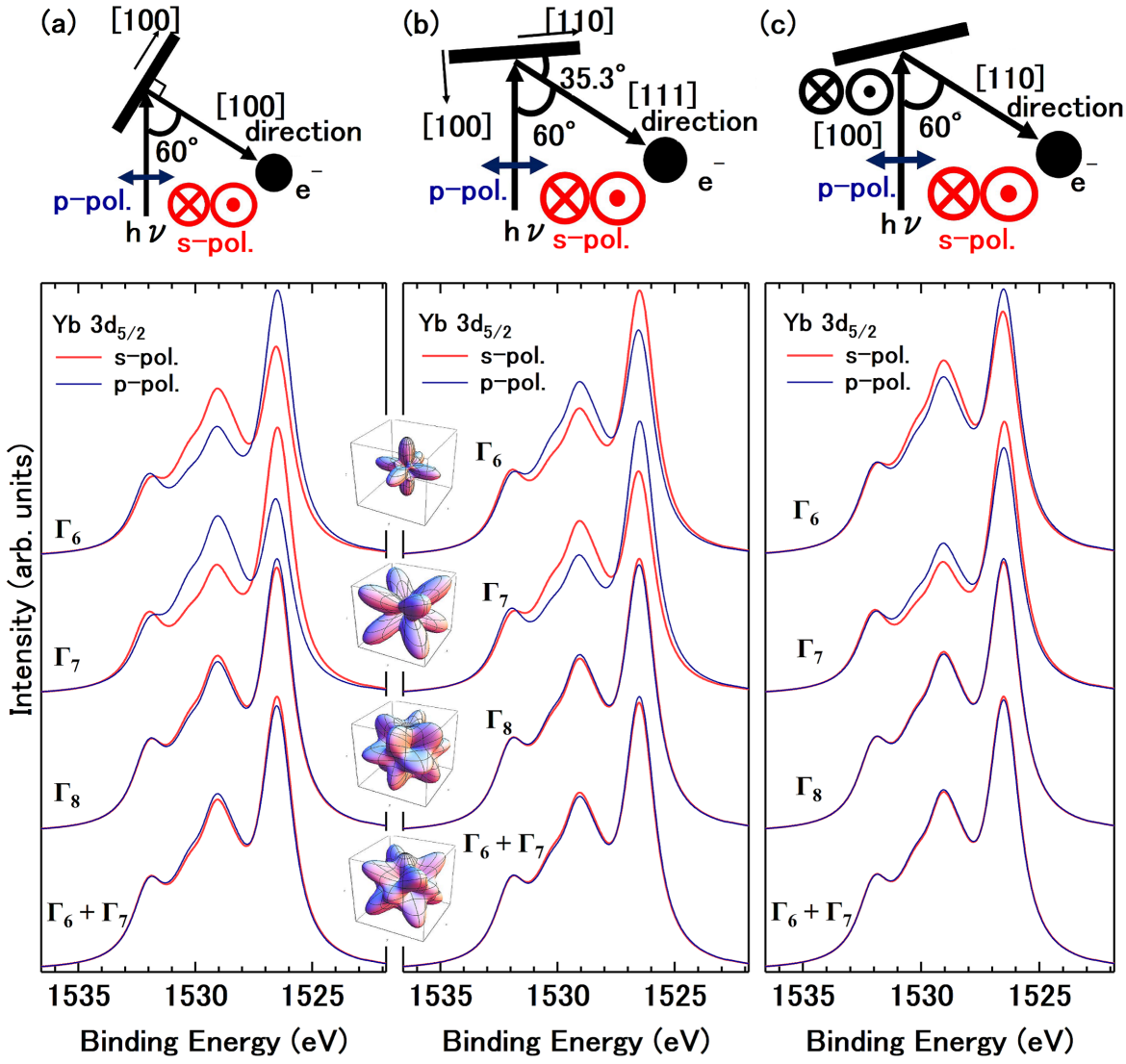


Figure 5.4: Simulated polarization-dependent $3d_{5/2}$ photoemission spectra of $Yb^{3+}$ ions assuming the crystal-field-split ground state in cubic symmetry in the 3 photoelectron detection directions, together with the corresponding experimental geometry. The $4f$-hole spatial distributions for the corresponding states are also shown.

## 5.4 Determination of 4$f$ ground-state symmetry by the linear dichroism in $Yb^{3+}$ 3$d$ core-level photoemission spectra

### 5.4.1 Physical properties of $YbB_{12}$

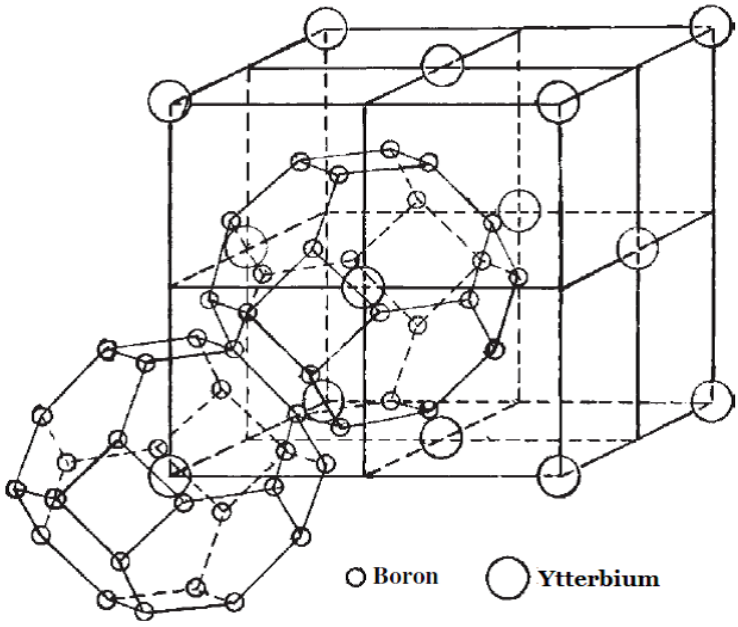


Figure 5.5: Crystal structure of $YbB_{12}$ ($UB_{12}$ cubic structure)[60]

The crystal structure of $YbB_{12}$ is shown in Fig. 5.5. The crystal structure of $YbB_{12}$ is cubic $UB_{12}$ structure [60] that correspond to NaCl structure where $B_{12}$ cluster is treated as one atom. For discussion of the $Yb^{3+}$ 4$f$ ground state, it is simple to understand considering as Borons environ Yb ions.
The temperature dependences of electric resistivity and magnetic susceptibility are shown in Figs. 5.6, 5.7 [61]. The resistivity increases with decreasing temperature below 100 K, and magnetic susceptibility has a peak at 80 K and drop down below this temperature. $YbB_{12}$ is known as a Kondo semiconductor [62, 63, 64, 65, 66], which has been recently recognized as a candidate for topological insulators [67], as intensively discussed for another Kondo semiconductor, $SmB_6$ [68, 69, 70]. The mean valence of $YbB_{12}$ has been estimated as ~2.9+ by bulk-sensitive 3$d$ core-level hard X-ray photoemission (HAXPES) spectroscopy [59]. To discuss the mechanisms of the gap opening at low temperatures [66, 71, 72, 73, 74, 75, 76] and the possibility of a topological insulator, it is essential to verify the ground-state symmetry of the $Yb^{3+}$ [$4f^{13}$ (one hole)] state determined by crystalline-electric-field (CEF) splitting.

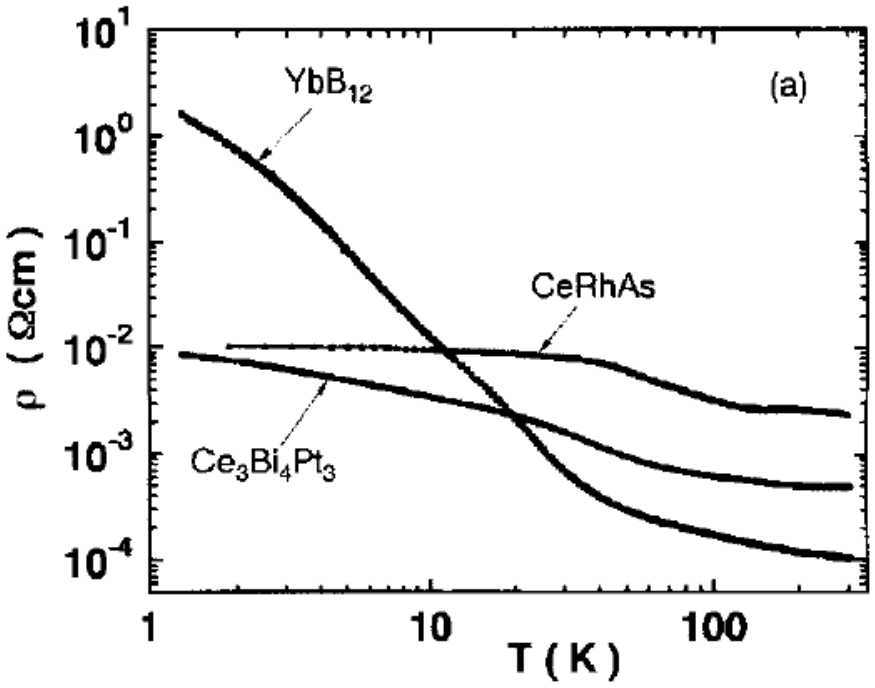


Figure 5.6: Temperature dependence of electric resistivity of $YbB_{12}$[61]

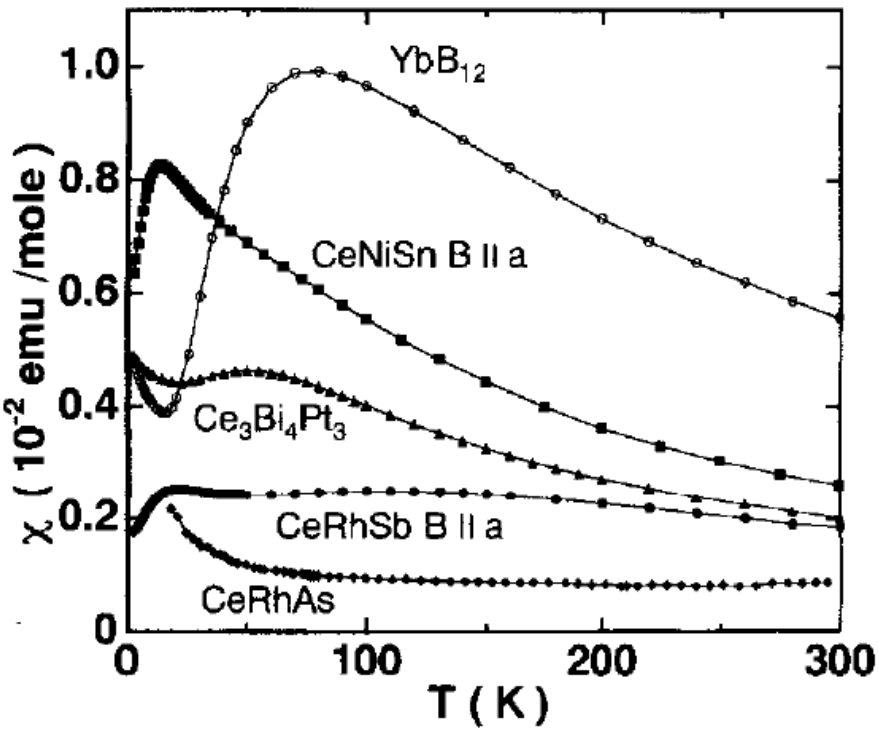


Figure 5.7: Temperature dependence of magnetic susceptibility of $YbB_{12}$[61]

### 5.4.2 CEF splitting of $YbB_{12}$

The Contour plots of imaginary part of RPA dynamical susceptibility of $YbB_{12}$ and the results of polarized neutron scattering for $YbB_{12}$ are shown in Figs. 5.8, 5.9 respectively [58, 77]. The former indicates the eightfold degenerated $4f$ levels in $YbB_{12}$ are split into two quartets by CEF. Some peaks have observed in the latter, the peak named as $M_h$ is only corresponding to the CEF excitation and indicate $\Gamma_8$ ground state. Furthermore, the LDA+U calculation also suggest $\Gamma_8$ ground-state [66]. However, a possible accidentally degenerated $\Gamma_6 + \Gamma_7$ ground state is not completely excluded [58].

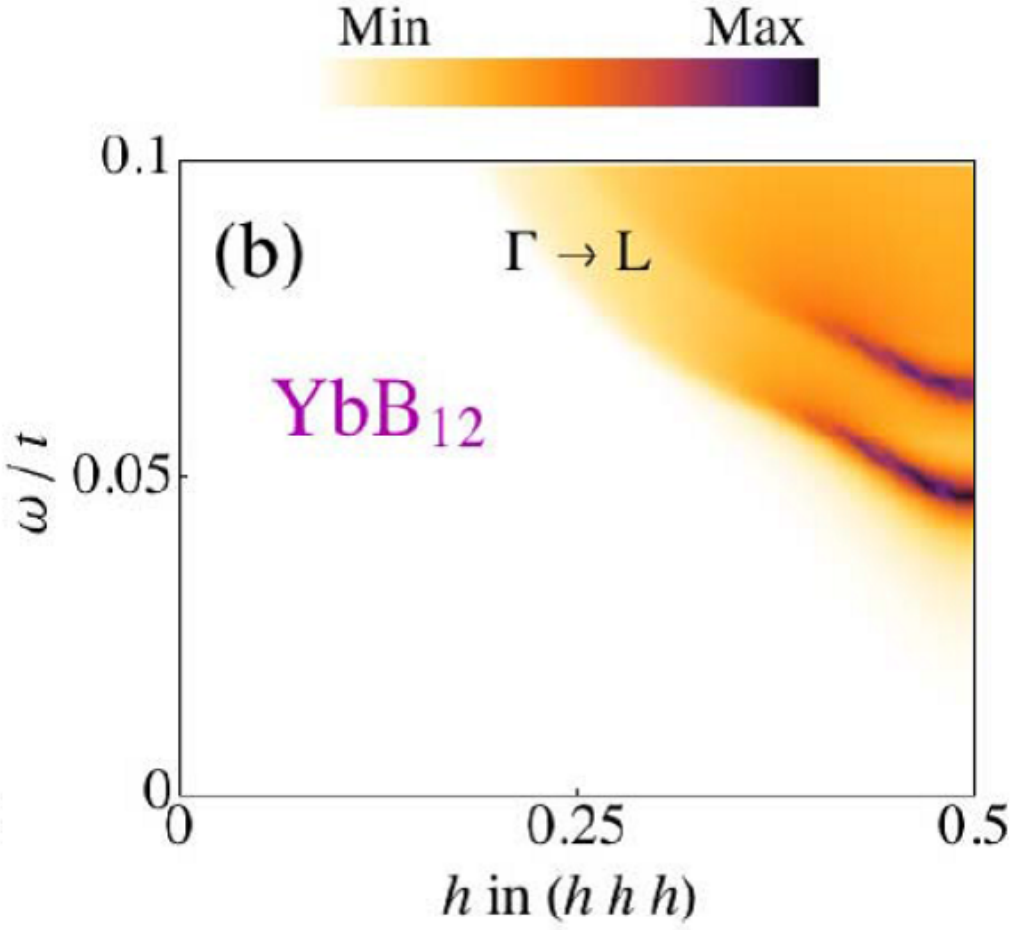


Figure 5.8: Contour plots of imaginary part of RPA dynamical susceptibility of $YbB_{12}$ [58], which indicate the $4f$ levels are split into two quartets by CEF

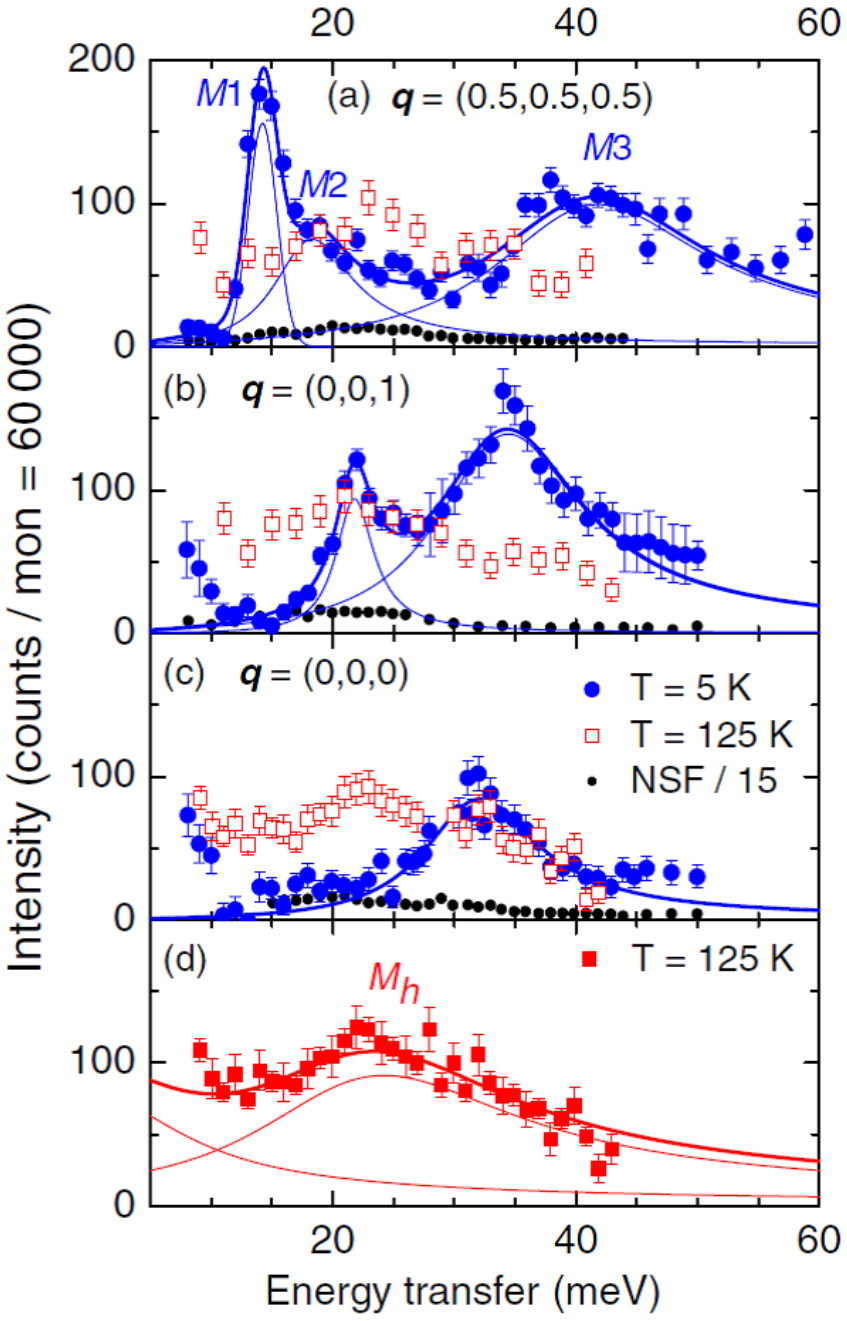


Figure 5.9: Polarized neutron scattering for $YbB_{12}$[77]、$M_h$ correspond to CEF excitation.

### 5.4.3 Experimental conditions

The experimental conditions for $YbB_{12}$ is shown in below table. Single crystals of $YbB_{12}$ synthesized by the traveling-solvent floating-zone method [65, 78] was given by Professor Iga (College of Science, Ibaraki University). The experimental geometry was controlled using a developed two-axis manipulator [55], where the normal emission direction parallel to the [100] direction in Fig. 5.4(a) was changed to the photoelectron detection in the [111] direction in Fig. 5.4(b) by azimuthal rotation of 45° and polar rotation by ~55°.The measuring temperature is 9 K, which is sufficiently lower than the excited state ($\gtrsim$ 250 K) [77].

| Sample | $YbB_{12}$ |
|---|---|
| Light source | SPring-8 BL19LXU |
| Analyzer | MB Scientific A1-HE analyzer |
| Photon energy | 7900 eV |
| Energy resolution | 400 meV |
| Temperature | 9 K |
| Surface | Fractured along (100) plane *in situ* |
| Base pressure | ~$2 \times 10^{-7}$ Pa |
| Photoelectron direction | [100], [111], [110] |

### 5.4.4 Shirley-type background and normalization of $Yb^{3+}$ $3d_{5/2}$ core-level HAXPES spectra of $YbB_{12}$

The polarization-dependent Yb $3d_{5/2}$ HAXPES spectra in the [100] direction of $YbB_{12}$ are shown in Fig. 5.10. Also we show the same raw spectra in the expanded scale ranging from 1524.5 to 1530.5 eV in Fig. 5.10. A slight but intrinsic LD is seen in the highest and second-highest peaks in the raw spectra. The so-called Shirley-type backgrounds are also displayed in Fig. 5.10. We have optimized the backgrounds as follows: After the normalization of the background-subtracted spectra by both $Yb^{2+}$ and $Yb^{3+}$ $3d_{5/2}$ spectral weights, the relative $Yb^{2+}/Yb^{3+}$ contributions and the intensities in the high-binding-energy region of 1534 – 1540 eV become equivalent between the s- and p-polarization configurations. The reference binding energy on the higher side has been set to 1536.2 eV corresponding to the local minimum of the raw spectral weight in the p-polarization. As a result, there are finite spectral weights at ~1536 eV in the background-subtracted spectra. However, these should be intrinsic owing to the overlap of the tails of the lifetime-broadened $Yb^{3+}$ $3d_{5/2}$ main peaks and a plasmonic energy-loss structure at the higher binding energy. Note that we have confirmed the robustness of LD in the 1524 – 1531 eV region regardless of background intensity.

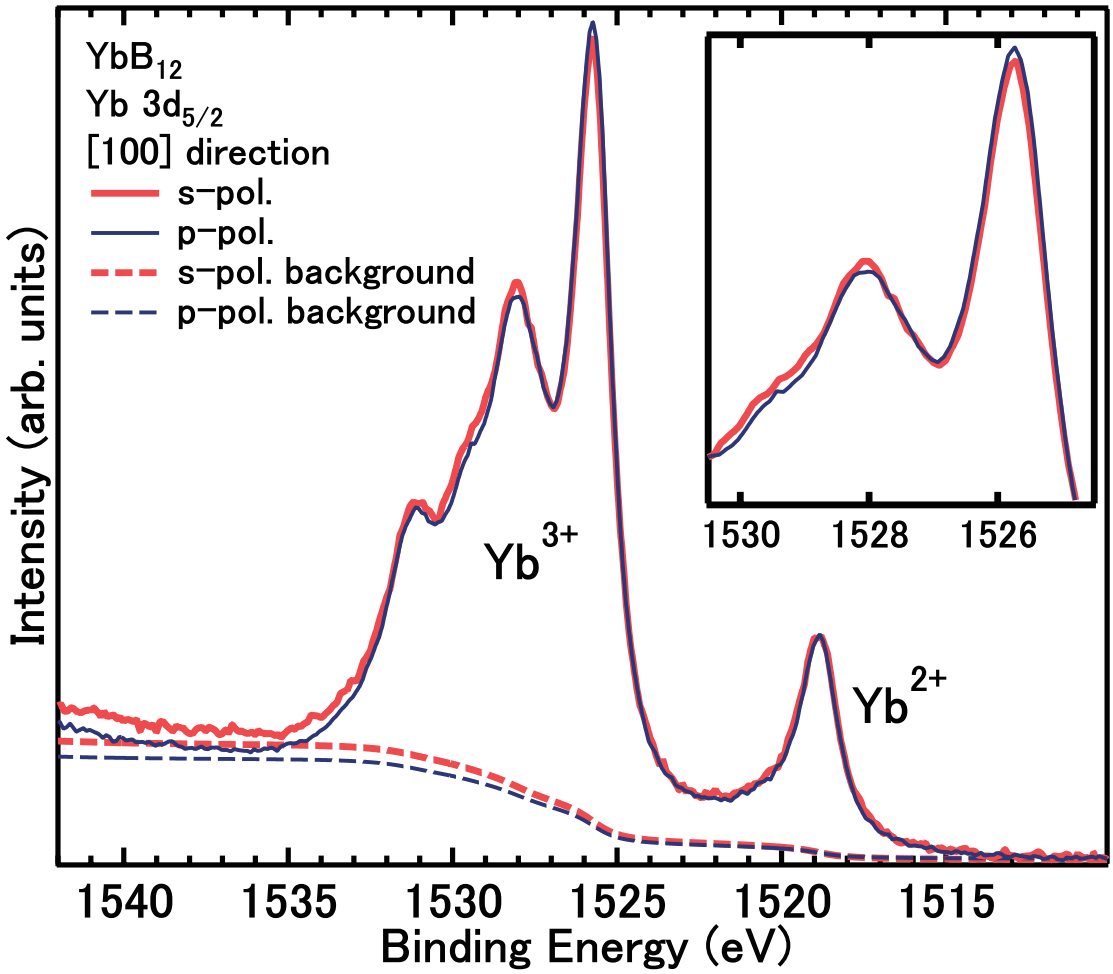


Figure 5.10: Polarization-dependent Yb $3d_{5/2}$ core-level HAXPES raw spectra (solid lines) of $YbB_{12}$ in the [100] direction and optimized Shirley-type backgrounds (dashed lines). The raw spectra have been normalized by the $Yb^{2+}$ spectral weight. The same spectra in the expanded scale are also shown.

### 5.4.5 Linear dichroism in $Yb^{3+}$ $3d_{5/2}$ core-level HAXPES spectra of $YbB_{12}$

A comparison of the polarization-dependent background-subtracted $Yb^{3+}$ $3d_{5/2}$ HAXPES spectra of $YbB_{12}$ and their LD with the photoelectron directions of [100], [111] and [110] with the simulated ones for the $\Gamma_8$ ground state is shown in Fig. 5.11. The highest peak is slightly stronger in the p-polarization configuration (p-pol.) than in the s-polarization one (s-pol.), and the second highest peak is stronger in the s-pol. for both experimental and simulated spectra in the [100] direction. These tendencies are reversed in the data in the [111] direction. The LD in the spectra along the [110] direction is much reduced compared with those along the [100] and [111] directions. As shown in Figs. 5.11, the observed LDs and spectra are quantitatively reproduced by the simulations for the $\Gamma_8$ ground state, for which the $4f$ charge distribution is shown in Fig. 5.12. If the $4f$ ground state of $YbB_{12}$ were in the $\Gamma_6$ symmetry, LD would be much larger than the experimental one. The sign of LD for the $\Gamma_7$ or accidentally degenerated $\Gamma_6 + \Gamma_7$ ground state is completely inconsistent with our experimental results. For the experimental LD along the [110] direction, its sign as a function of binding energy is unclear since the required statistics is much better than that along the [100] and [111] directions according to the simulations. Nevertheless, the observed LD seems to be qualitatively consistent with the simulation for the $\Gamma_8$ ground state rather than that for the accidentally degenerated $\Gamma_6$+$\Gamma_7$ state. At least, our experimental result for the detection angle parallel to the [110] direction is not contradictory to the prediction of the $\Gamma_8$ state. Such a quantitative reproducibility of the observed LD and core-level spectra by the simulations surely indicates the $Yb^{3+}$ ($4f^{13}$) ions in the $\Gamma_8$ symmetry mixed with a small quantity ($\sim$ 10%) of the $Yb^{2+}$ ($4f^{14}$) component [59] in the ground state of $YbB_{12}$.

### 5.4.6 Discussion

Our finding of the $\Gamma_8$ $4f$ symmetry for the $Yb^{3+}$ sites in the ground state is consistent with the prediction by a band-structure (local density approximation + on-site Coulomb repulsion, LDA+$U$) calculation, where the $\Gamma_6$ and $\Gamma_7$ states are on the occupied side [66]. One might consider that the $\Gamma_6$ and $\Gamma_7$ states are possibly mixed in the ground state due to the hybridization between the $4f$ and valence-band orbitals at low temperatures well below the Kondo temperature ($\sim$ 240 K for $YbB_{12}$ [62, 63, 64, 65]). As widely recognized for the local electronic structures of transition metal oxides, on the other hand, note that the so-called CEF splitting actually seen in realistic materials is a consequence of the anisotropic hybridization effects in addition to static ligand potentials. The latter would be much smaller than the former for $YbB_{12}$ since the ligand-field potential on the Yb sites is to some extent nearer to a spherically symmetric one, being caused by the crystal structure [62, 63, 60] where the Yb ion is surrounded by the truncated octahedron made of 24 boron ions as shown in Fig. 5.12. The $4f$-hole spatial distributions are elongated along the centers of the truncated octahedron faces for the $\Gamma_6$ and $\Gamma_7$ states, whereas they are elongated along the edges of the hexagonal faces for the $\Gamma_8$ state, which leads to the conclusion that the $4f$ holes in the $\Gamma_8$ state are relatively stabilized by the hybridizations compared with those in the $\Gamma_6$ and $\Gamma_7$ states with different symmetries, as suggested by the LDA+$U$ calculation. Then, the possible $\Gamma_6$ and/or $\Gamma_7$ state mixture would be experimentally insignificant in our data.

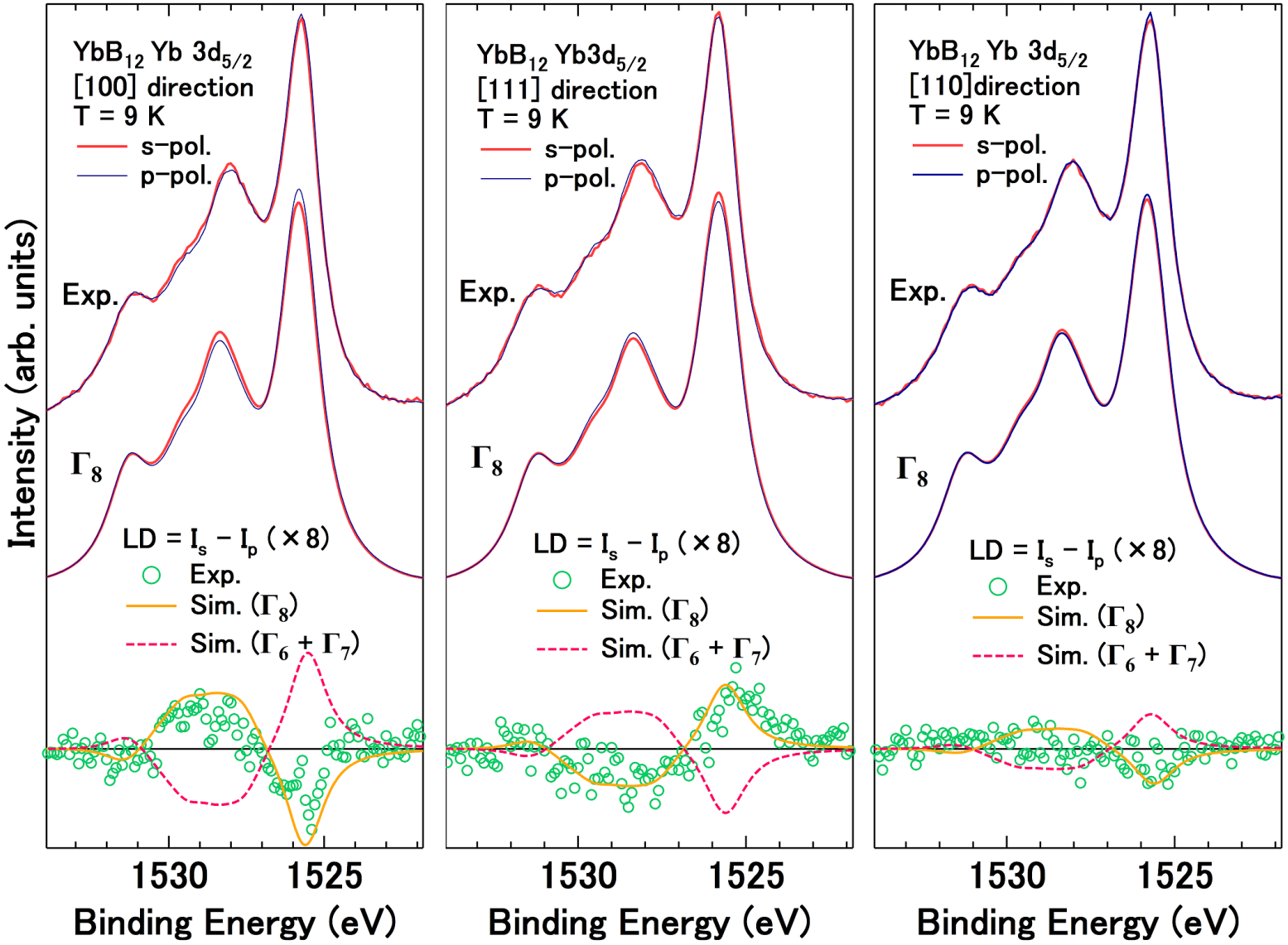


Figure 5.11: Polarization-dependent $Yb^{3+}$ $3d_{5/2}$ core-level HAXPES spectra and LD of $YbB_{12}$ compared with the simulated ones for the $\Gamma_8$ ground state in the 3 photoelectron detection directions. Simulated LD assuming the accidentally degenerated $\Gamma_6+\Gamma_7$ ground state is also shown by the dashed line in the lower panel.

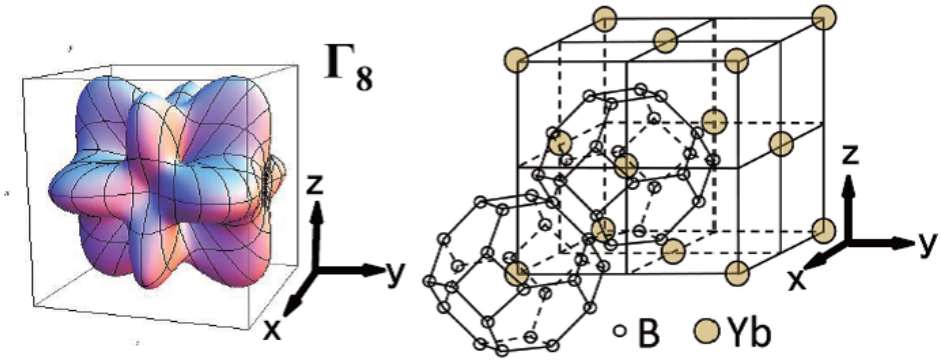


Figure 5.12: $4f$-hole spatial distribution for the $Yb^{3+}$ ion with the $\Gamma_8$ symmetry and crystal structure of $YbB_{12}$ [60]

### 5.4.7 Sample quality

The experimental Laue image is shown in Fig. 5.13. I have pasted the sample to the sample holder with the surface direction along [100] direction (normal photoemission detection direction).

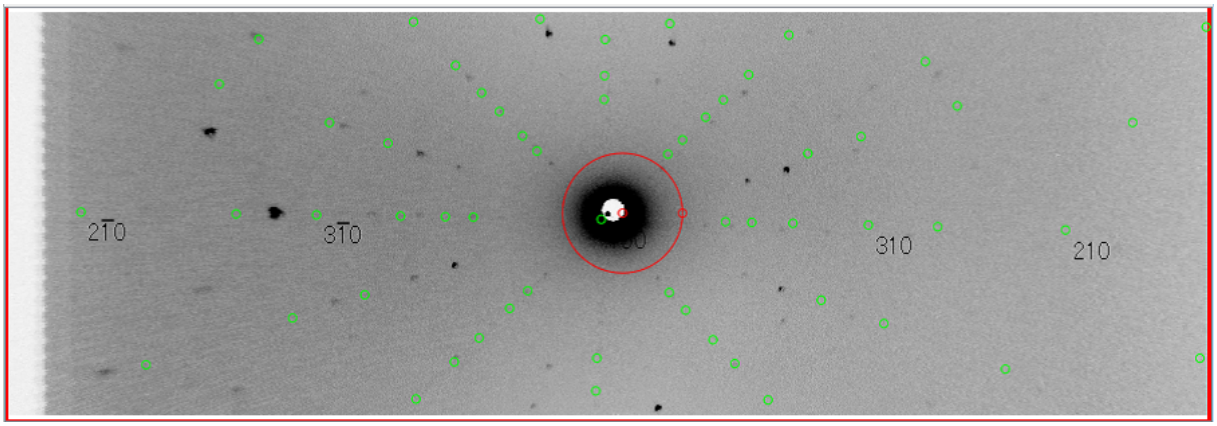


Figure 5.13: Experimental Laue image of $YbB_{12}$

The sample and surface qualities were examined on the basis of the absence of any core-level spectral weight caused by possible impurities including oxygen and carbon as shown below. No peaks from O 1*s* and C 1*s* have observed in spectra of $YbB_{12}$.

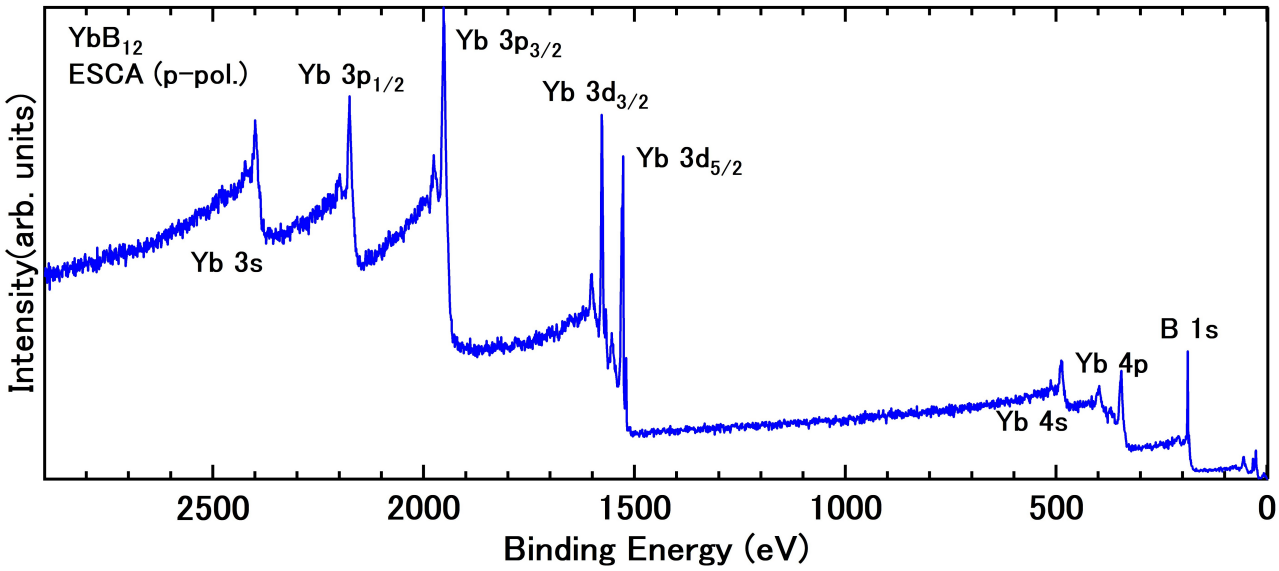


Figure 5.14: Wide energy range HAXPES spectrum of $YbB_{12}$

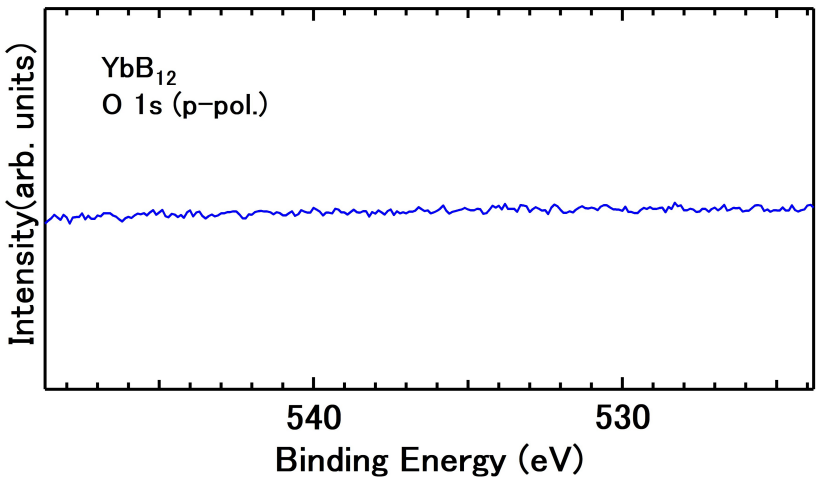


Figure 5.15: The photoemission spectrum of $YbB_{12}$ around the binding energy of O 1*s* peak position

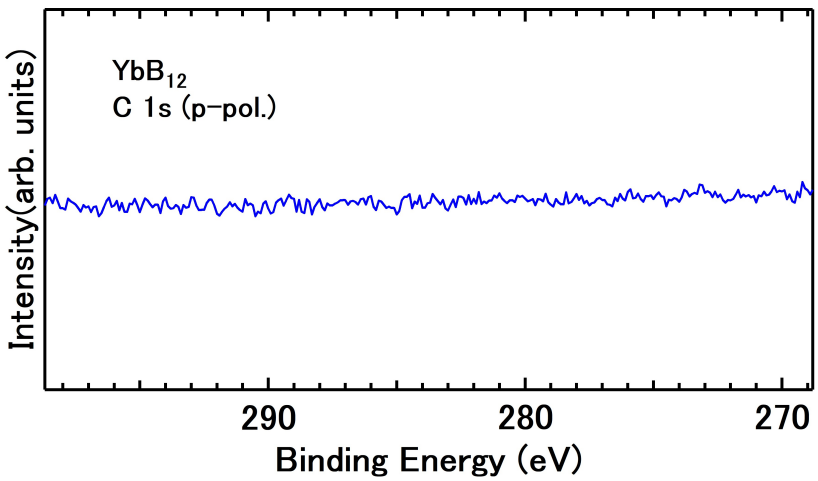


Figure 5.16: The photoemission spectrum of $YbB_{12}$ around the binding energy of C 1*s* peak position

# Chapter 6

# Spectroscopic observations of $4f$ ground-state symmetry by linear dichroism in core-level photoemission in cubic Ce compounds

In $Ce^{3+}$, there is a $4f^1$ configuration. While the $Yb^{3+}$ state ($4f^{13}$ configuration) is rather well separated from the $Yb^{2+}$ state ($4f^{14}$ configuration), in the Ce compounds, the $4f^0$ state and $4f^2$ state are energetically close to the $Ce^{3+}$ state ($4f^1$ final state). Therefore, it is necessary to verify whether the LD in the core-level PES for Ce compounds can be reproduced by the ion-model calculations reflecting their $4f$ charge distribution determined by the CEF theory. Then we have performed LD-HAXPES experiments for $CeB_6$ and $CeAl_2$, of which the CEF-split ground states have already been revealed. The ground state of the former is well known as $\Gamma_8$ ground state originated from quadrupolar ordering, and the physical properties of the latter is explained by $\Gamma_7$ ground state.

## 6.1 Energy splitting of $Ce^{3+}$ $4f$ levels in cubic symmetry

The energy diagram of $Ce^{3+}$ $4f$ levels in cubic symmetry is shown in Fig. 6.1. Firstly, the $4f$ levels are split by the spin-orbit interaction into sixfold degenerated $J = 5/2$ states and eightfold degenerated $J = 7/2$ states. Since the size of splitting by the spin-orbit interaction is ~0.3 eV, and this value is enough larger than CEF splitting (several dozen ~ hundreds meV), we may consider only $J = 5/2$ states (electron picture). The sixfold degenerated $J = 5/2$ states are further split due to the CEF into $\Gamma_7$ doublet and $\Gamma_8$ quartet as mentioned in Chapter 2. These wave functions are written by the linear combination of $|J_z\rangle$ states as follows:

$$|\Gamma_7\rangle = -\sqrt{1/6}|\pm 5/2\rangle + \sqrt{5/6}|\mp 3/2\rangle, \tag{6.1}$$

$$|\Gamma_8\rangle = \begin{cases} |\pm 1/2\rangle \\ \sqrt{5/6}|\pm 5/2\rangle + \sqrt{1/6}|\mp 3/2\rangle \end{cases} \tag{6.2}$$

Fig. 6.2 shows the $Ce^{3+}$ $4f$ hole charge distributions for each wave functions $\Gamma_7$, and $\Gamma_8$. The $\Gamma_7$, and $\Gamma_8$ $4f$ charge distributions are elongated along the <111>, <100> respectively.

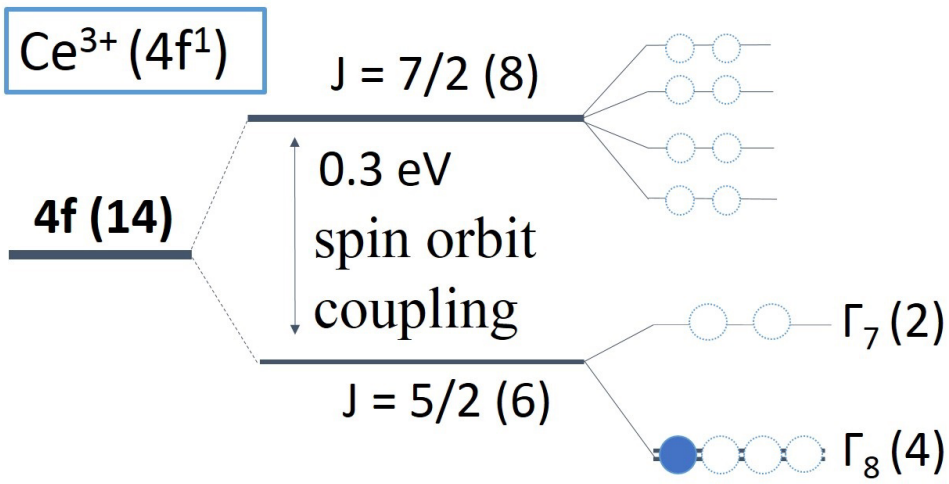


Figure 6.1: Schematic diagram of energy splitting of $Ce^{3+}$ $4f$ levels in cubic symmetry

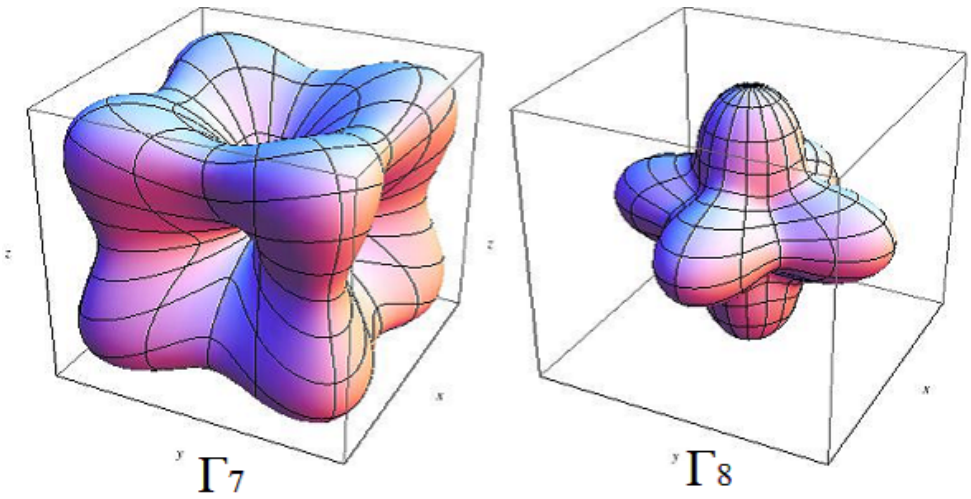


Figure 6.2: $Ce^{3+}$ $4f$ electron charge distributions with CEF in cubic symmetry

## 6.2 Overview of Ce 3*d* core-level photoemission spectrum

The polarization-dependent Ce 3*d* region HAXPES spectra in the [100] direction of $CeB_6$ and $CeAl_2$ are shown in Figs. 6.3, and 6.4. There are three kinds of peaks originated from three configurations $4f^0$, $4f^1$, and $4f^2$ in final state.
Generally the peaks in binding energy ranging from 896 to 920 eV are corresponding to Ce $3d_{3/2}$, and the peaks in binding energy ranging from 876 to 903 eV are corresponding to Ce $3d_{5/2}$ orbital. Especially, the peaks in binding energy ranging from 914 to 918 eV ($3d_{3/2}$) and 900 to 904 eV ($3d_{5/2}$) originate from $4f^0$ configuration, and the peaks in binding energy ranging from 904 to 912 eV ($3d_{3/2}$) and 883 to 892 eV ($3d_{5/2}$) originate from $4f^1$ configuration, and the peaks in binding energy ranging from 896 to 902 eV ($3d_{3/2}$) and 878 to 884 eV ($3d_{5/2}$) originate from $4f^2$ configuration. For discussion of $Ce^{3+}$ $4f$ orbital symmetry, the observed multiplet structures are located in binding energy ranging from 878 to 892 eV (Ce $3d_{5/2}$). In contrast to Yb compounds, since the $4f^0$ state and $4f^2$ state are nearby $Ce^{3+}$ state ($4f^1$ configuration) in Ce compound, it is necessary to pay attention for the analysis of LD in Ce core-level photoemission spectra.

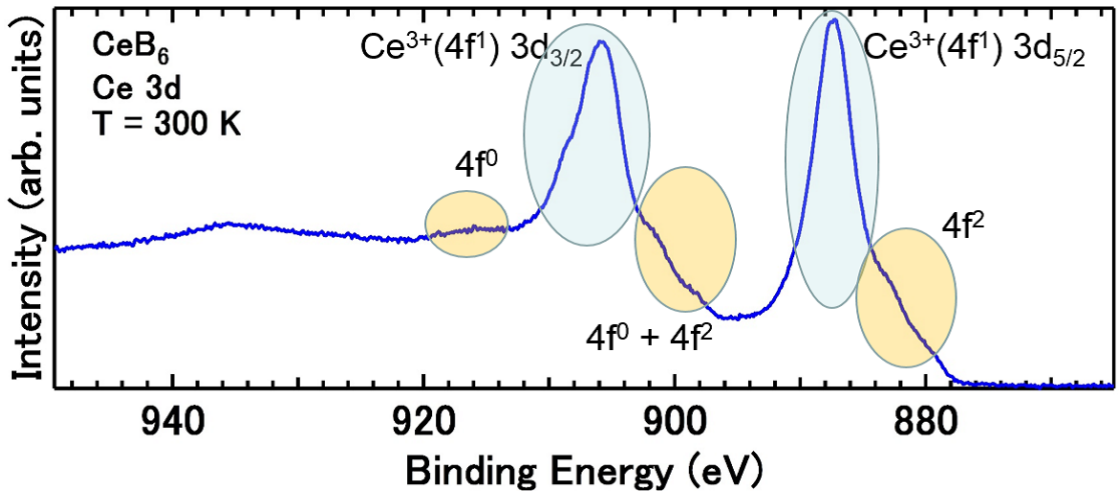


Figure 6.3: Ce 3*d* core-level photoemission spectrum of $CeB_6$

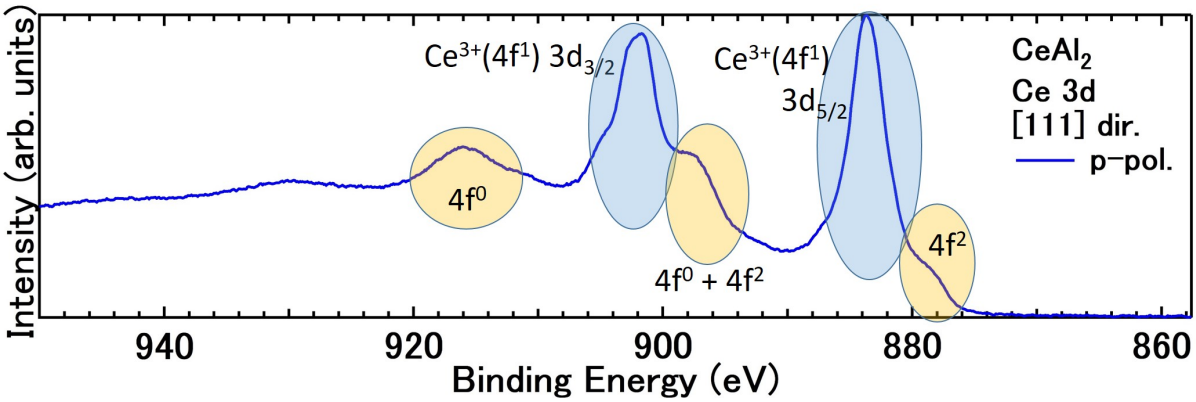


Figure 6.4: Ce 3$d$ core-level photoemission spectrum of $CeAl_2$

## 6.3 Simulated polarization-dependent $Ce^{3+}$ ($4f^1$) $3d_{5/2}$ photoemission spectra

The simulated polarization-dependent $Ce^{3+}$ $3d_{5/2}$ core-level HAXPES spectra in cubic symmetry at two photoelectron directions ([100] and [111]) are shown in Fig. 6.5, the blue lines shows the spectra at p-polarization configuration, and the red lines shows that at s-polarization configuration. We have performed ionic calculations including the full multiplet theory [18] and the local CEF splitting using the XTLS 9.0 program [19] just like Yb ions [15]. All atomic parameters such as the $4f$-$4f$ and $3d$-$4f$ Coulomb and exchange interactions (Slater integrals) and the $3d$ and $4f$ spin-orbit couplings have been obtained using Cowan's code [25] based on the Hartree-Fock method. The Slater integrals (spin-orbit couplings) are reduced to 76% (99%) from the values obtained by Cowan's code to fit the $3d$ core-level photoemission spectra (which values are consistent with ref. [79, 80]).
The tendency of LD for the $\Gamma_7$ ground state is the completely opposite to that for the $\Gamma_8$ ground state. LD defined by the difference in spectral weight between the s- and p-polarization configurations is reversed between the [100] and [111] directions for each states considered in cubic symmetry displayed here. Clear LDs are expected to observe in the top of the main peak around the binding energy of 882.3eV. In addition, it should be noted that we can obtain large LD in the bottom of the peak at the binding energy from 878 to 882 eV and from 885 to 889 eV.

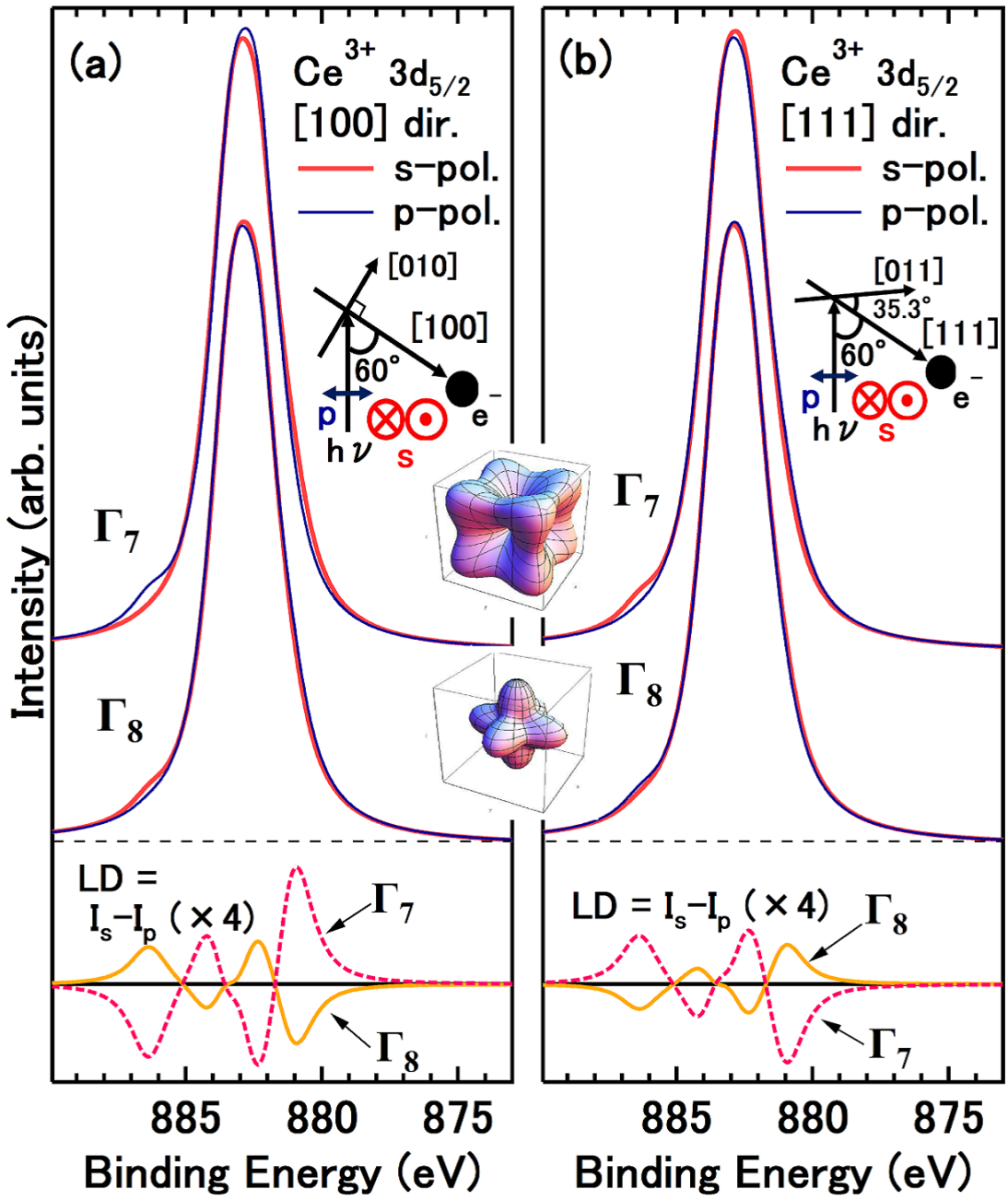


Figure 6.5: (a) Simulated polarization-dependent $3d_{5/2}$ photoemission spectra of $Ce^{3+}$ ions assuming the crystal-field-split ground state in cubic symmetry in the [100] direction, together with the corresponding experimental geometry. (b) Same as (a) but for the photoelectron in the [111] direction. The $4f$-hole spatial distributions for the corresponding states are also shown.

## 6.4 Simulated polarization-dependent $Ce^{3+}$ ($4f^1$) $4d$ photoemission spectra

The simulated polarization-dependent $Ce^{3+}$ $4d$ core-level HAXPES spectra in cubic symmetry at two photoelectron directions ([100] and [111]) are shown in Fig. 6.6, the blue lines shows the spectra at p-polarization configuration, and the red lines shows that at s-polarization configuration. The Slater integrals (the spin orbit couplings) are reduced to 80% from the values obtained by Cowans code to fit the experimental spectra. The values of these parameter are shown in Table. 6.1.
There is advantage in $4d$ spectra, the clear LD can be obtained compared with $3d$ spectra owing to the distinctly multiplet structures. However, the peaks originated from other elements often exist in same binding energy region. As is the case with $3d$ core-level spectra, the tendency of LD for the $\Gamma_7$ ground state is the completely opposite to that for the $\Gamma_8$ ground state, and LD is reversed between the [100] and [111] directions for each ground states in cubic symmetry.

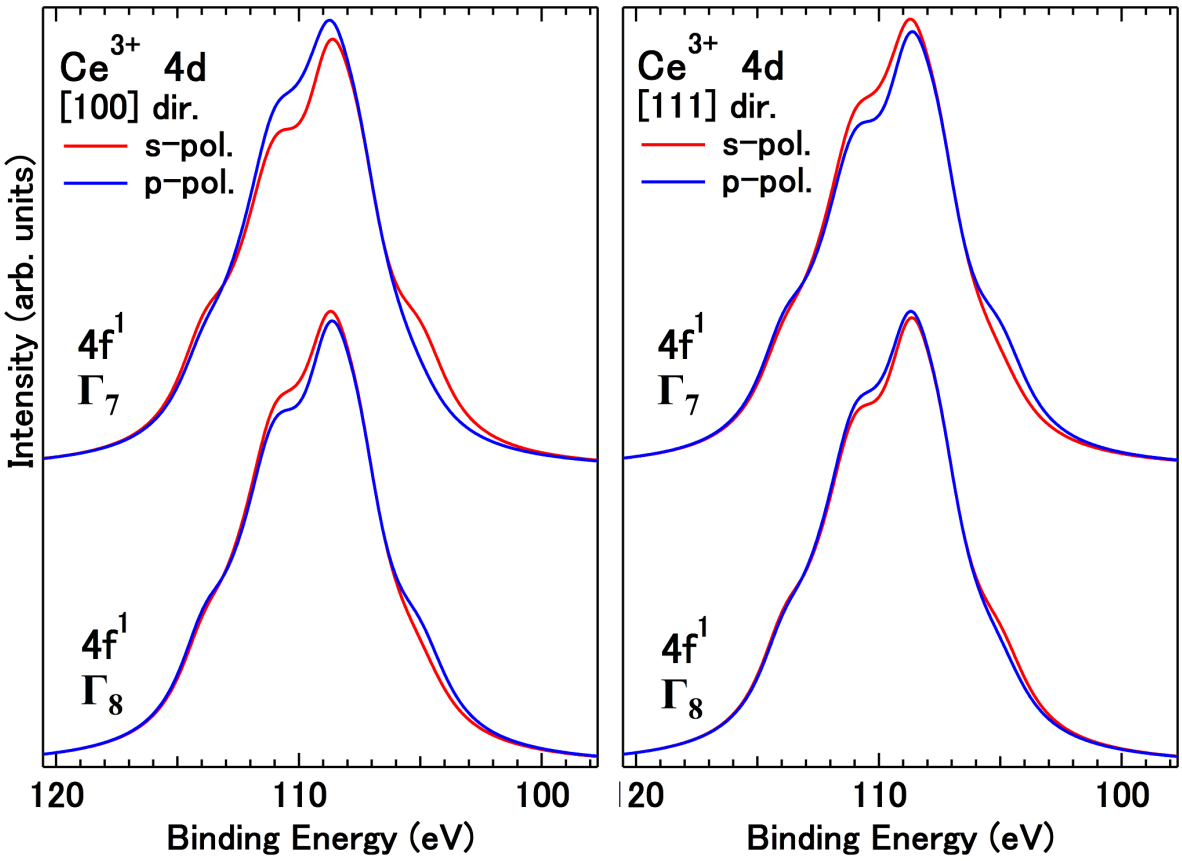


Figure 6.6: simulated polarization-dependent $Ce^{3+}$ $4d$ core-level HAXPES spectra in cubic symmetry at two photoelectron directions ([100] and [111])

| | | | $Ce^{3+}$ $(4d^9 4f^1)$ | | | |
|---|---|---|---|---|---|---|
| $F^2_{(4d4f)}$ | $F^4_{(4d4f)}$ | $G^1_{(4d4f)}$ | $G^3_{(4d4f)}$ | $G^5_{(4d4f)}$ | $\zeta_{4d}$ | $\zeta_{4f}$ |
| 11.55 | 7.41 | 13.72 | 8.62 | 6.10 | 1.20 | 0.10 |

Table 6.1: The values of the Slater integrals and spin orbit couplings used for simulations. These values have reduced to 80% from the values obtained by Cowan's code. The value of spin orbit coupling for 4d orbital corresponds to ref. [79, 96]

## 6.5 Determination of 4*f* ground-state symmetry by the linear dichroism in Ce 3*d* and 4*d* core-level photoemission spectra

### 6.5.1 Physical properties of $CeB_6$

The crystal structure of $CeB_6$ is shown in Fig. 6.7. The crystal structure of $CeB_6$ is cubic $CaB_6$ structure [81]. The $B_6$ clusters locate in <111> direction from Ce atoms. Antiferromagnetic ordering at Néel temperature $T_N$ =2.3 K for $CeB_6$ is observed by neutron scattering, NMR, elastic x-ray scattering. $\Gamma_7$ $4f$ ground state was considered natural for $CeB_6$ by its crystal structure [82, 83, 84], $\Gamma_8$ ground state for $CeB_6$ due to the quadrupolar ordering have been revealed.

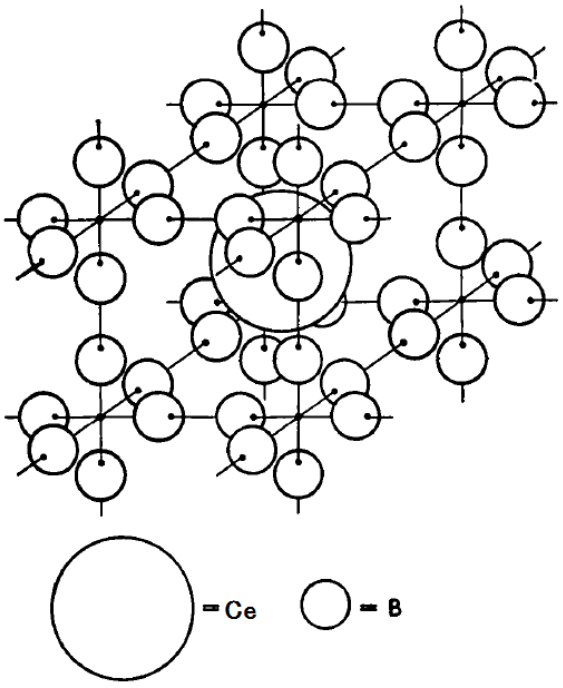


Figure 6.7: Crystal structure of $CeB_6$ ($CaB_6$ cubic structure) [81]

### 6.5.2 Quadrupolar ordering and CEF of $CeB_6$

The temperature dependence of the "elastic constant" indicating the elastic energy stored per unit volume can generally be understood as the quadrupole susceptibility [85]. The quadrupole susceptibility means the electronic dipole moment induced per unit strain. When the ground state is degenerate to the quadrupole, a decrease of the elastic constant proportional to the inverse temperature of $1/T$ occurs at low temperature. The quadrupole operator classified by the irreducible representation of the cubic $O$ group is shown in the Table 6.2, and the corresponding five components of the electronic quadrupole are shown in Fig. 6.8. There are three independent elastic constants in cubic symmetry, $C_{11}$ ,$C_{12}$ and $C_{44}$. The quadrupole susceptibility corresponding to the $\Gamma_3$ symmetry distortion is the response of the quadrupole $O_2^2$, and corresponds to the transverse wave elastic constant $(C_{11} - C_{12})/2$. The quadrupole susceptibility corresponding to the $\Gamma_5$ symmetry distortion denotes the response of the quadrupole $O_{xy}$,$O_{yz}$,$O_{zx}$, and corresponds to the transverse wave elastic constant $C_{44}$. As already mentioned, the $Ce^{3+}$ $4f$ levels are split into $\Gamma_7$ and $\Gamma_8$ by CEF. $\Gamma_7$ is a Klamath doublet which splits by the magnetic field, but the splitting by the strain field does not occur. On the other hand, the $\Gamma_8$ quartet has $4 \times 4 = 16$ degree of freedom for not only magnetic dipole but also electronic quadrupole and magnetic octupole, since it is the degenerated two Klamath doublets. Therefore, for Ce compounds with $\Gamma_8$ ground state, quadrupole or octupole can become ordered variables.

Fig. 6.9 shows the result of inelastic neutron scattering of $CeB_6$ [86]. In this result, the

Table 6.2: Quadrupole operator expressed in irreducible form for cubic $O$ group [85]

| Symmetry | quadrupole operator |
|---|---|
| $\Gamma_3$ | $O_2^0 = \frac{1}{2}(2J_z^2 - J_x^2 - J_y^2)$ |
| | $O_2^2 = \frac{\sqrt{3}}{2}(J_x^2 - J_y^2)$ |
| $\Gamma_5$ | $O_{xy} = \frac{\sqrt{3}}{2}(J_xJ_y + J_yJ_x)$ |
| | $O_{yz} = \frac{\sqrt{3}}{2}(J_yJ_z + J_zJ_y)$ |
| | $O_{zx} = \frac{\sqrt{3}}{2}(J_zJ_x + J_xJ_z)$ |

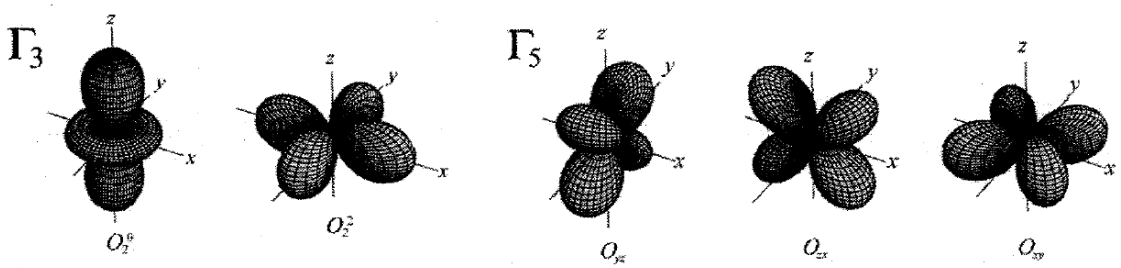


Figure 6.8: Five components of electric dipole by cubic symmetric expression [85]

peak due to the CEF excitation is observed at 46 meV (~530 K), the $\Gamma_8$ ground state and the

$\Gamma_7$ excited state for $CeB_6$ and the CEF energy splitting of 545 K are indicated. In addition, the temperature dependence of elastic constants of $CeB_6$ are shown in Fig. 6.11 [87]. The two kinds of elastic constants $(C_{11} - C_{12})/2$ and $C_{44}$ decrease in proportion to $1/T$ at low temperature. Also the Fig. 6.10 shows the extended low temperature part of temperature dependence of elastic constant $C_{44}$ of $CeB_6$ [87]. It can be seen from this figure that antiferro quadrupolar ordering occurs at $T_Q$ = 3.3 K. The $\Gamma_8$ quartet ground state is split into two Klamath's doublets by the quadrupole-strain interaction of the antiferro quadrupolar order. As a result, the proportional decrease to $1/T$ of $C_{44}$ stops at $T_Q$, and it slowly rises at low temperature. The bending of the elastic constant observed at 2.3 K corresponds to the antiferromagnetic transition. At low temperature, elasticity anomalies due to quadrupolar ordering is observed, but quadrupole interaction should not work at a sufficiently higher temperature (ex. room temperature) than $T_Q$. It is natural that the ground state of $CeB_6$ is in the $\Gamma_7$ ground-state symmetry in terms of crystal structure, specific heat, magnetic susceptibility [82, 83, 84, 88]. Therefore, it is suggested that the exchange of states of active $\Gamma_8$ and inactive $\Gamma_7$ for quadrupoles may occur at high temperatures at which quadrupole order interaction does not work[88].

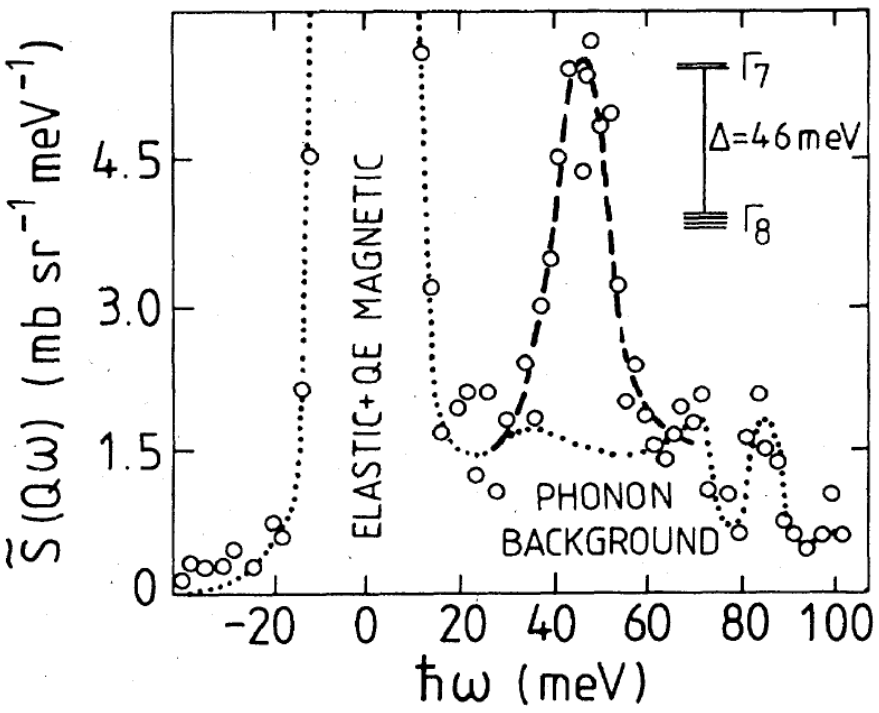


Figure 6.9: Inelestic neutron scattering for $CeB_6$[86]

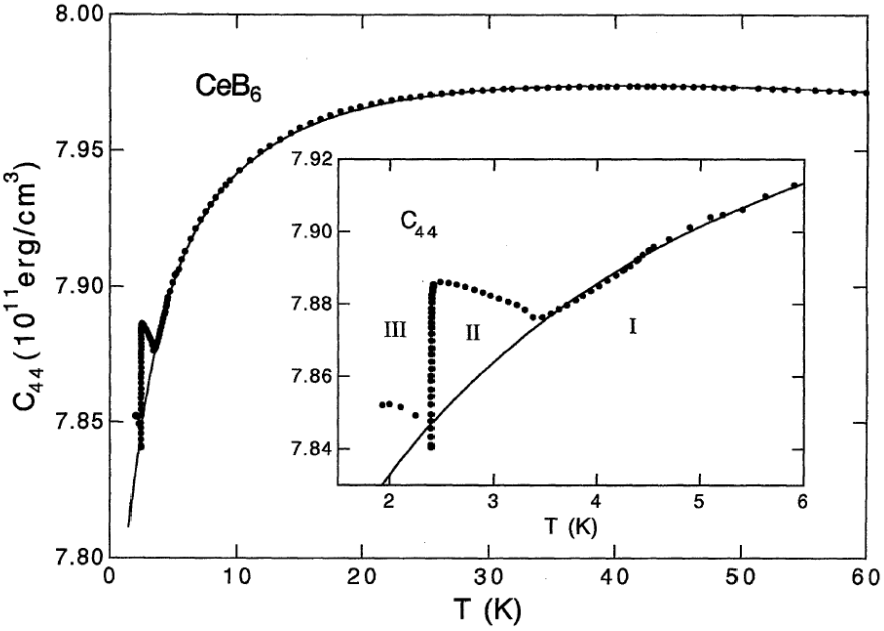


Figure 6.10: Extended low temperature part of temperature dependence of elastic constant $C_{44}$ of $CeB_6$ [87]

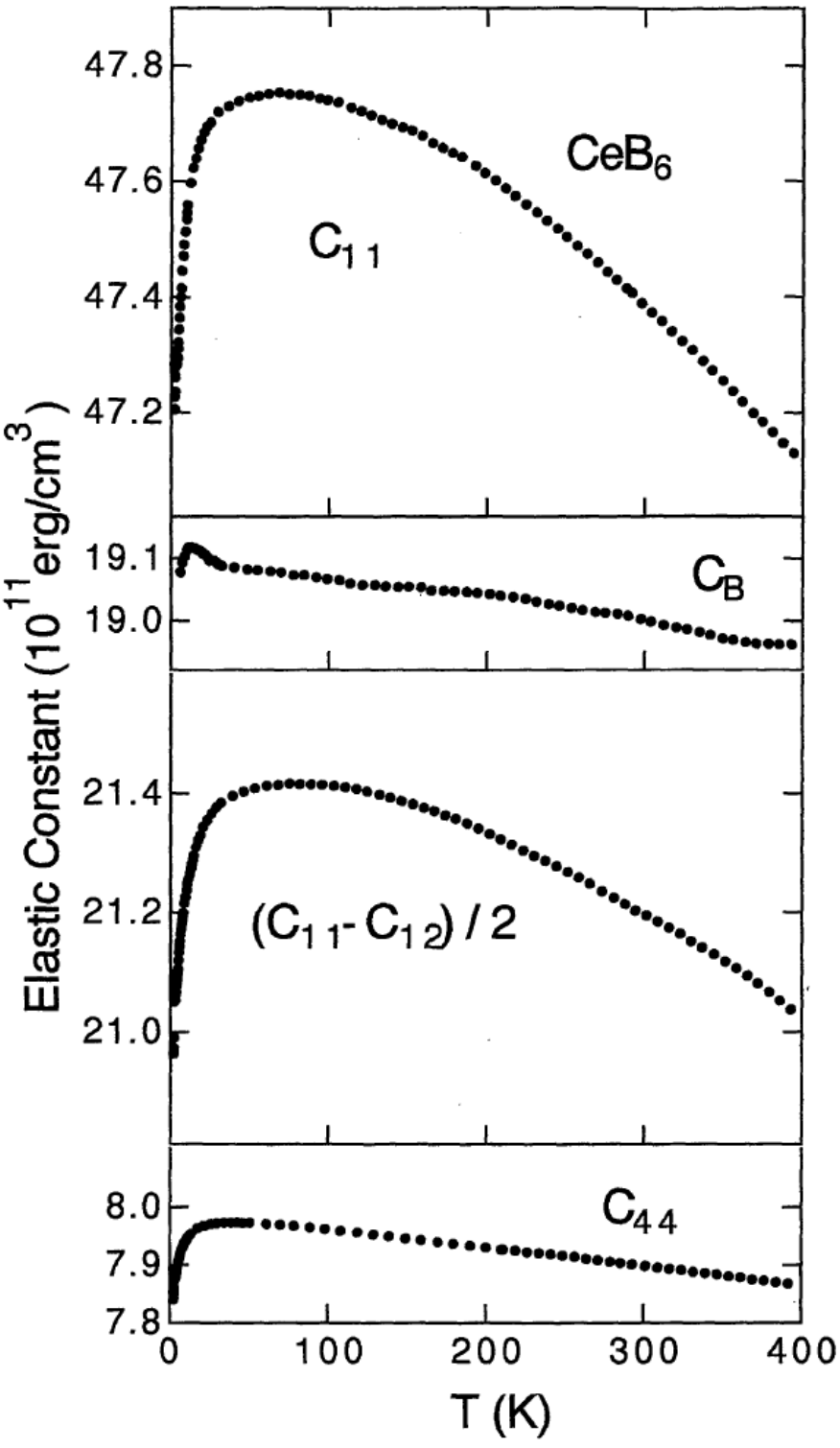


Figure 6.11: Temperature dependence of elastic constants of $CeB_6$ [87]

### 6.5.3 Physical properties of $CeAl_2$

The crystal structure of $CeAl_2$ is shown in Fig. 6.12. The crystal structure of $CeAl_2$ have Laves phase [89]. The squared temperature dependence of specific heat of $CeAl_2$ is shown in Fig. 6.13 [90]. Antiferromagnetic ordering occurs at N*é*el temperature $T_N$ =3.8 K for $CeAl_2$. The magnetic behavior for $CeAl_2$ is well explained by the $\Gamma_7$ ground state and $\Gamma_8$ excited state [91].

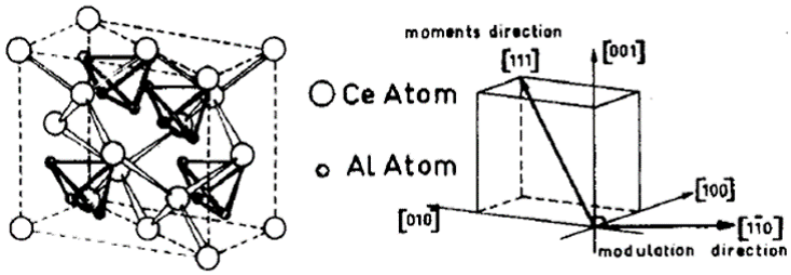


Figure 6.12: Crystal structure of $CeAl_2$（Laves phase) [89]

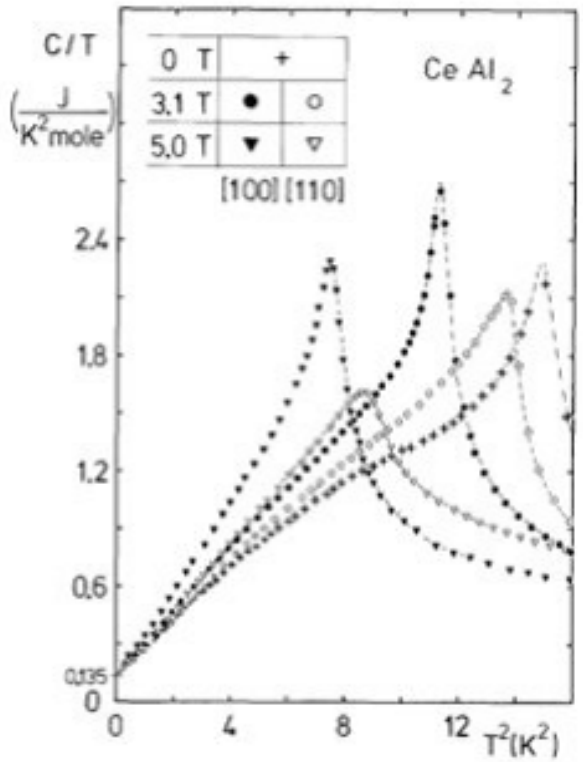


Figure 6.13: Squared temperature dependence of specific heat of $CeAl_2$[61]

### 6.5.4 CEF splitting of $CeAl_2$

The results of inelastic neutron scattering for $CeAl_2$ are shown in Figs. 6.14 [94]. There are two peaks in results, it indicates two excited states, it is uncommon in cubic symmetry, for $CeAl_2$. It is considered that phonon softening in $CeAl_2$ causes the split of a quartet $\Gamma_8$ excited state [92, 93].

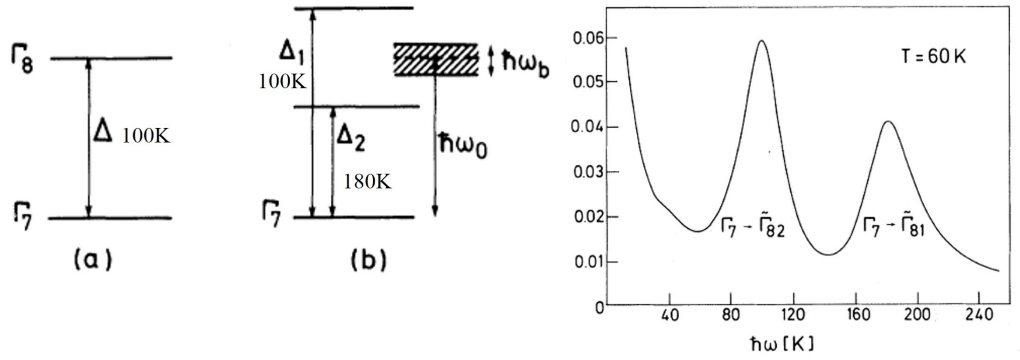


Figure 6.14: Inelastic neutron scattering for $CeAl_2$[92]

### 6.5.5 Experimental conditions

The experimental conditions for $CeB_6$ and $CeAl_2$ are shown in below table. Single crystals of $CeAl_2$ (given by Professor Takao Ebihara (Department of Physics, Shizuoka University)) synthesized by Czochralski pulling method and $CeB_6$ (given by Professor Fumitoshi Iga(College of Science, Ibaraki University)) synthesized by the traveling-solvent floating-zone method [97] were fractured along the (100) or (110) plane *in situ*, where the base pressure was $\sim 1\times10^{-7}$ Pa. The experimental geometry was controlled using a two-axis manipulator [55], where the normal emission direction parallel to the [110] direction was changed to the photoelectron detection in the [100] direction in Fig. 6.5(a) by azimuthal rotation of 0° and polar rotation by ~45° in the [111] direction in Fig. 6.5(b) by azimuthal rotation of 90° and polar rotation by ~35°. The measuring temperature is 5 K, which is sufficiently lower than the excited state (~ 100 K for $CeAl_2$ [94, 95] and ~ 530 K for $CeB_6$ [86]).

| **Sample** | **$CeAl_2$** | **$CeB_6$** | | |
|---|---|---|---|---|
| Core-level | Ce $3d_{5/2}$ | | | Ce 4d |
| Light Source | SPring-8 BL19LXU | | | |
| Analyzer | MB Scientific A1-HE analyzer | | | |
| Photon Energy | 7900 eV | | | |
| Energy Resolution | 480 meV | 400 meV | 480 meV | |
| Temperature | 5 K | | | |
| Base pressure | ~ $1 \times 10^{-7}$ Pa | | | |
| Photoelectron direction | [100], [111] | [100] | [111] | [111], [100] |

### 6.5.6 Shirley-type background and normalization of Ce $3d_{5/2}$ and $4d$ core-level HAXPES spectra

The polarization-dependent Ce $3d_{5/2}$ core-level HAXPES raw spectra (solid lines) of $CeAl_2$ in the [100] direction and optimized Shirley-type backgrounds, which we have subtracted from the raw spectra (dashed lines) is shown in Fig. 6.15. Strong peak with binding energy ~882.5 eV is assigned to the $3d_{5/2}$ peaks with a $4f^1$ final state. The sholder structure approximately 4 eV to lower binding energy are attiributed to the $3d_{5/2}$ peak with a $4f^2$ final state, which is consistent with privious work [98]. We show the same raw spectra in the expanded scale ranging from 879.5 to 883.5 eV in Fig. 6.15. The peak is stronger in the p-polarization configuration (p-pol.) than the s-polarization configuration (s-pol.) around the binding energy of 882.5 eV, in contrast, the bottom of peak is stronger in s-pol. than p-pol. around the binding energy of 880.5 eV. Therefore, there is slight but intrinsic LD in

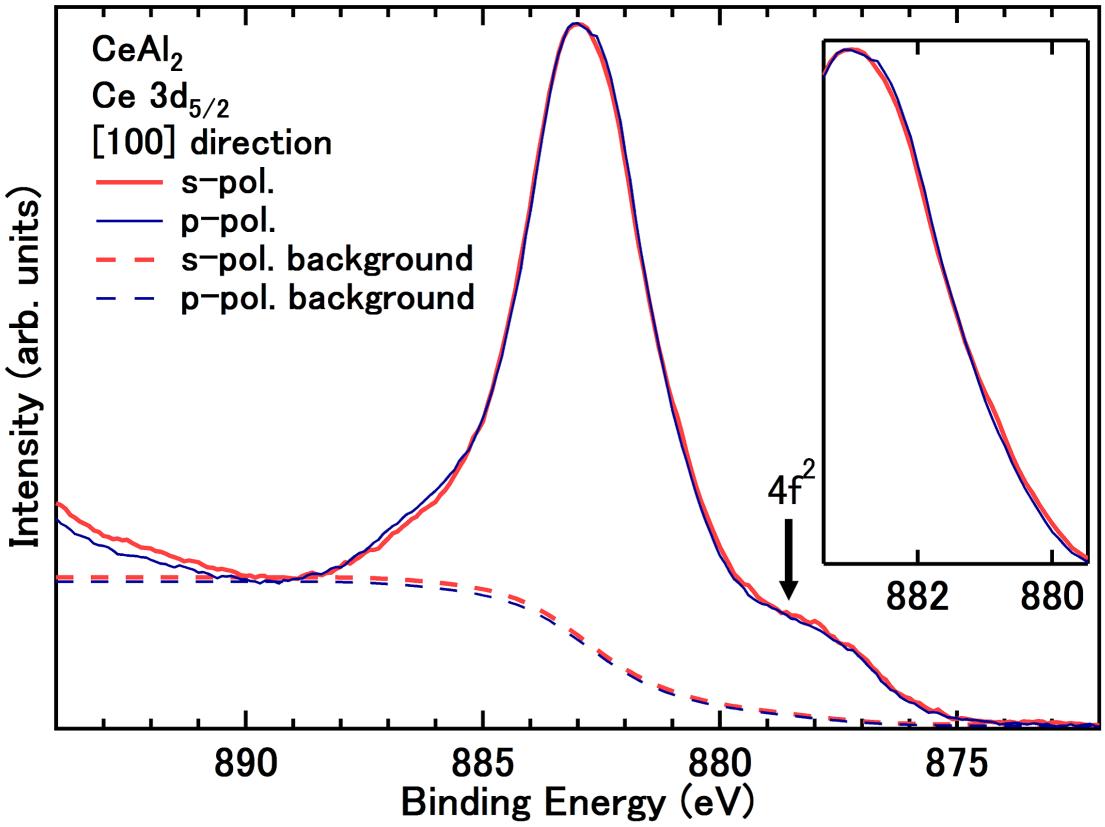


Figure 6.15: Polarization-dependent Ce $3d_{5/2}$ core-level HAXPES raw spectra (solid lines) of $CeAl_2$ in the [100] direction and optimized Shirley-type backgrounds, which we have subtracted from the raw spectra (dashed lines). The raw spectra have been normalized by the height of the main peak. The same spectra in the expanded scale are also shown.

the main peak originated from $4f^1$ final state. We set the binding energy on the higher side to 889.4 eV corresponding to the local minimum of the raw spectral weight in the s-pol. After background subtracting, we normalize Ce $3d_{5/2}$ spectra by both $Ce^{3+}$ $3d_{5/2}$ spectral weights from the binding energy of 879.4 eV to 889.4 eV (even though there are some spectral weights originated from $4f^2$ final state in the normalized region).
The polarization-dependent Ce $3d_{5/2}$ core-level HAXPES raw spectra (solid lines) of $CeB_6$ in the [100] direction and optimized Shirley-type backgrounds, which we have subtracted from the raw spectra (dashed lines) is also shown in Fig. 6.16. The backgrounds are subtracted by the same manner as Ce $3d_{5/2}$ spectra, and then the spectra are normalized by both Ce $4d$ overall spectral weights including the both peaks originated from $4f^1$ and $4f^2$ final states, since the peaks from $4f^2$ final state is very nearby to the peaks from $4f^1$ final state.

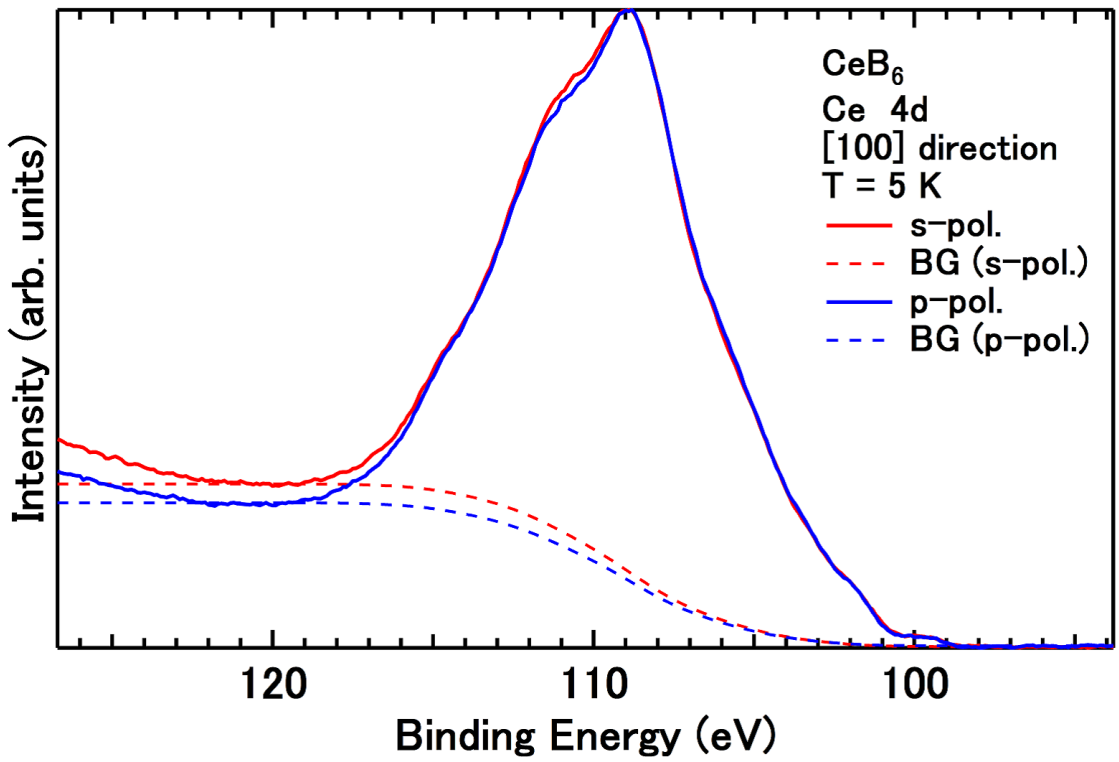


Figure 6.16: Polarization-dependent Ce 4*d* core-level HAXPES raw spectra (solid lines) of $CeAl_2$ in the [100] direction and optimized Shirley-type backgrounds, which we have subtracted from the raw spectra (dashed lines).

### 6.5.7 Linear dichroism in Ce $3d_{5/2}$ core-level HAXPES spectra of $CeB_6$ and $CeAl_2$

The polarization-dependent background-subtracted Ce $3d_{5/2}$ HAXPES spectra of $CeAl_2$ and $CeB_6$ and their LD with the photoelectron directions of [100] and [111] are shown in Fig. 6.17. The sholder structures at the binding energy from 875 to 879.5 eV exist in both experimental spectra of $CeAl_2$ and $CeB_6$ which originate from $4f^2$ final state. These structures are larger in $CeAl_2$ than in $CeB_6$. These spectral shapes as well as the intensity of the peaks due to the $4f^2$ final state are respectively simular to the previous work [79, 99]. The shape for the LD in the spectra of $CeAl_2$ has different feature from that of $CeB_6$ in the [100] directions, such the sign of the LD in [100] direction for $CeAl_2$ changes from plus to minus with getting higher binding energy but the that for $CeB_6$ changes minus to plus. The LD for $CeAl_2$ compared with the simulated ones for the $\Gamma_7$ ground state and the LD for $CeB_6$ compared with the simulated ones for the $\Gamma_8$ ground state are also shown in Fig. 6.17. The features of LD for $CeAl_2$ is corresponding to the simulated LD for the $\Gamma_7$ ground state, and that for $CeB_6$ is near to the simulated LD for the $\Gamma_8$ ground state with the photoelectron directions of the [100] direction. Also the shape for the LD in the spectra of $CeAl_2$ is different from that of $CeB_6$ in the [111] direction, in addition, the former is near to the simulated LD for $\Gamma_7$ ground state and the latter is corresponding to the simulated LD for $\Gamma_8$ ground state. Therefore, there are little effects from $4f^2$ final state for LDs in the Ce $3d_{5/2}$ spectra in the case that we have to discriminate the ground state for Ce compounds in cubic symmetry.

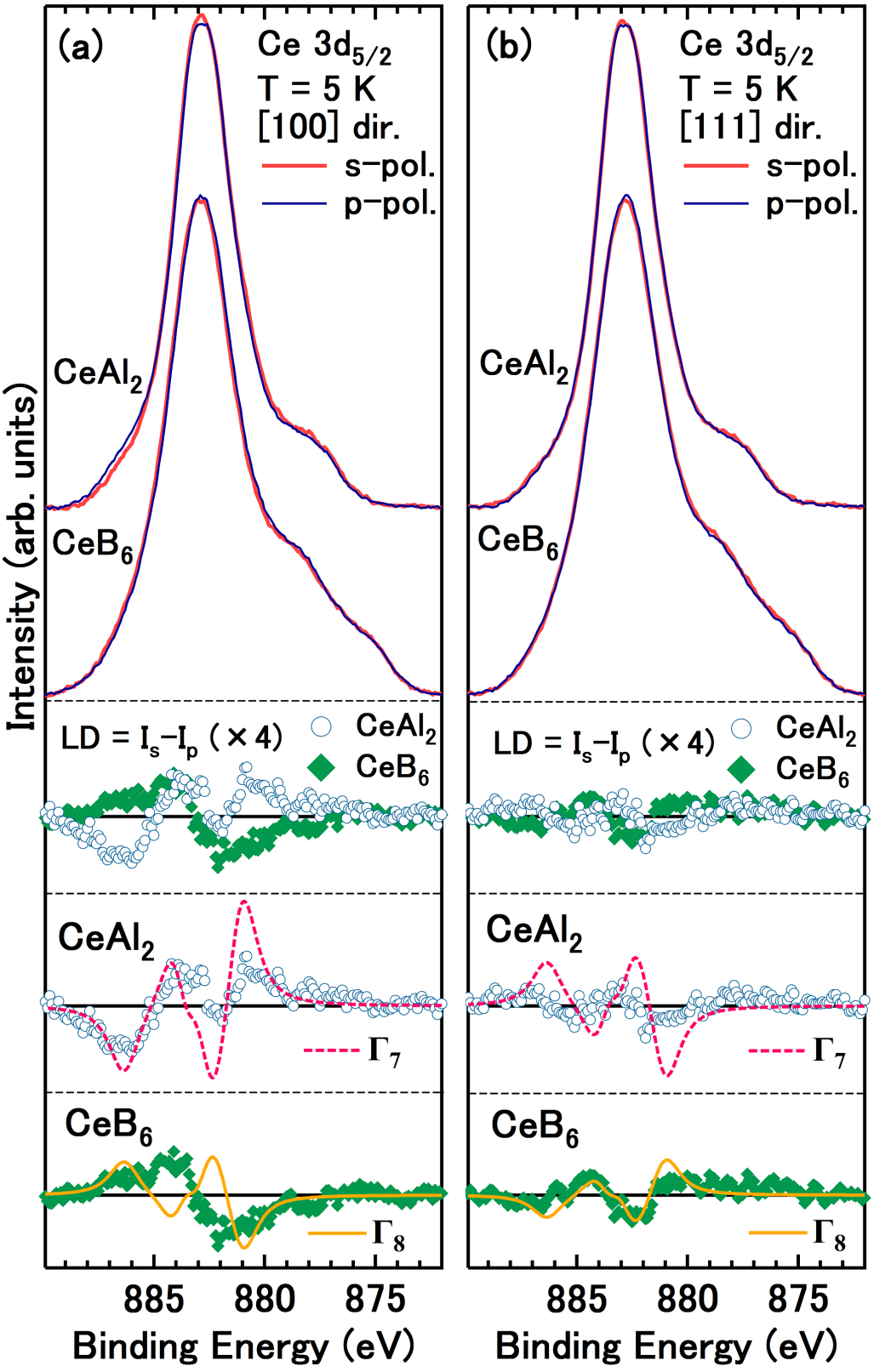


Figure 6.17: (a) Polarization-dependent Ce $3d_{5/2}$ core-level HAXPES spectra and LD of $CeAl_2$ and $CeB_6$ in the [100] direction. The LD for $CeAl_2$ compared with the simulated ones for the $\Gamma_7$ ground state and the LD for $CeB_6$ compared with the simulated ones for the $\Gamma_8$ ground state are also shown. (b) Same as (a) but data in the [111] direction.

### 6.5.8 Linear dichroism in Ce 4*d* core-level HAXPES spectra of $CeB_6$

The polarization-dependent background-subtracted Ce 4*d* HAXPES spectra of $CeB_6$ and their LD with the photoelectron directions of [100] and [111] are shown in Fig. 6.18. Simulated polarization-dependent $Ce^{3+}$ 4*d* core-level HAXPES spectra in cubic symmetry with the photoelectron directions of [100] and [111] are also shown in Fig. 6.18. The tendency for the LD in almost overall Ce 4*d* spectra is corresponding to the LD of simulations assuming $\Gamma_8$ ground state in both photoelectron directions of [100] and [111], except at the binding energy from 99 to 106 eV of [100] direction. For example, the spectra at the binding energy from 109 to 114 eV is slightly stronger in the s-pol. than in the p-pol. one, and the spectra at the binding energy from 114 to 121 eV is stronger in the p-pol. for both experimental and simulated spectra for $\Gamma_8$ ground state in the [100] direction. In contrast, the spectra at the binding energy from 109 to 117 eV is slightly stronger in the p-pol. than in the s-pol. one, and the spectra at the binding energy from 101 to 109 eV is stronger in the s-pol. in the [111] direction. Thus, since the LDs in Ce 4*d* spectra of $CeB_6$ in both two photoelectron directions are near to simulated ones for $\Gamma_8$, the contributions from $4f^2$ final state for LDs in the Ce 4*d* spectra are almost negligible for the discussion of the ground state for Ce compounds in cubic symmetry.

### 6.5.9 Discussion

The LDs in core-level photoemission spectra appears stronger in 4*d* spectra than in $3d_{5/2}$ spectra. One reason for these results are regared as the non-dividing 4*d* spectra due to the small value of spin orbit coupling for 4*d* orbital. In addition, we suggest another reason. The values of Coulomb and exchange interactions $F^n$ and $G^n$ are larger in 4*d*-4*f* than in 3*d*-4*f* [80]. Since the multiplet structures in core-level photoemission spectra are represented by the linear combinations of these $F^n$ and $G^n$ values, LDs in these multiple structures are obtained more clearly in the orbit which the Slater integrals between core-level and 4*f* orbital have large values.

### 6.5.10 Sample quality

The experimental Laue image is shown in Fig. 6.5.10, 6.19. I have pasted the samples to the sample holder with the surface direction along [100] and [110] direction (normal photoemission detection direction).

The sample and surface qualities were examined on the basis of the absence of any core-level spectral weight caused by possible impurities including oxygen and carbon as shown below. Though there is a little peak from O 1*s* in Figs. 6.21 (2015.12) and 6.24, the influence of oxidation is negligible for measuring HAXPES spectra. The peaks from other impurities including carbon have not been observed.

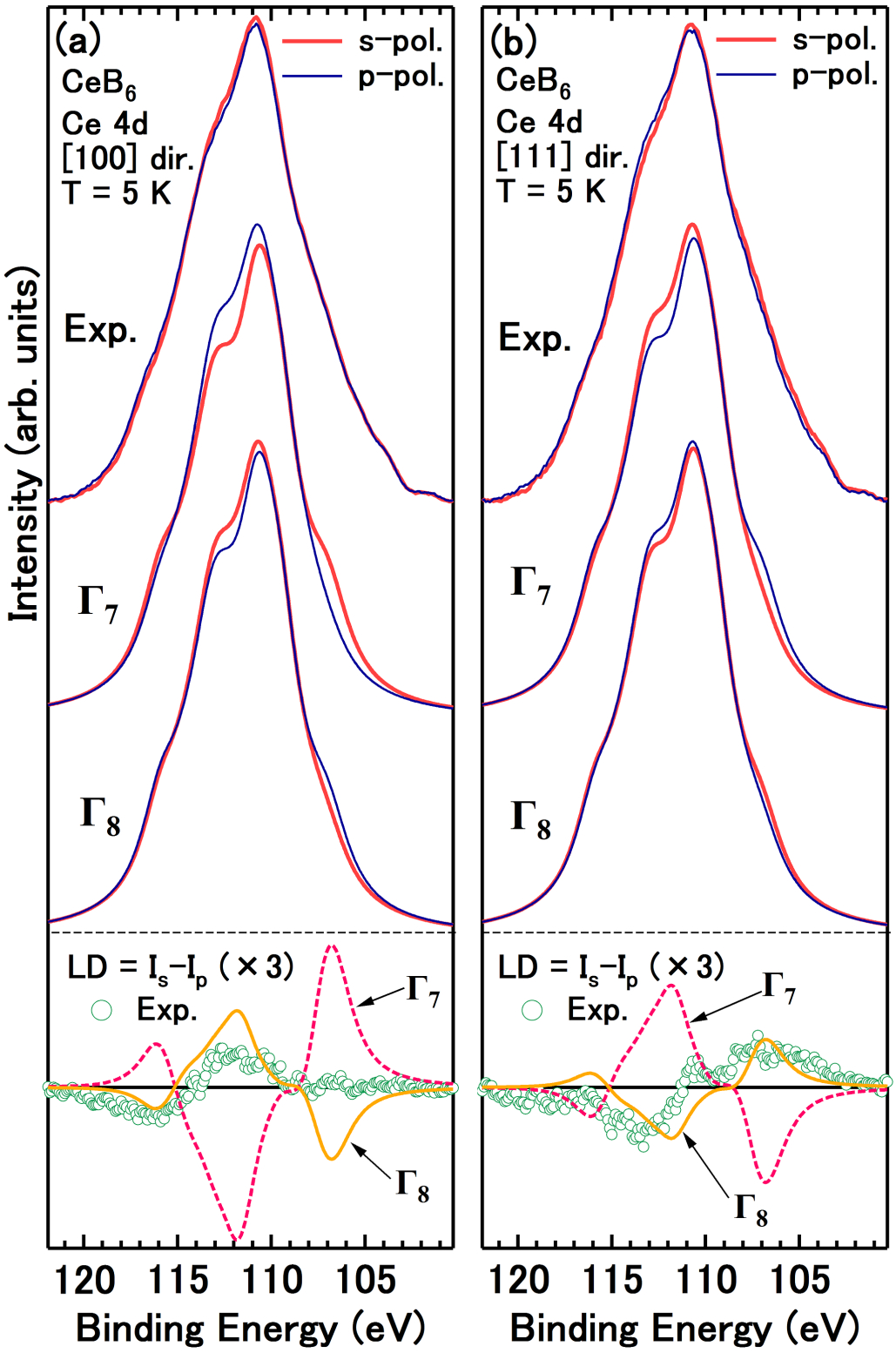


Figure 6.18: (a) Polarization-dependent Ce 4*d* core-level HAXPES spectra and LD of $CeB_6$ and the simulated ones in the cubic symmetry in the [100] direction. (b) Same as (a) but data in the [111] direction. The Shirley-type background has been subtracted from the raw spectra.

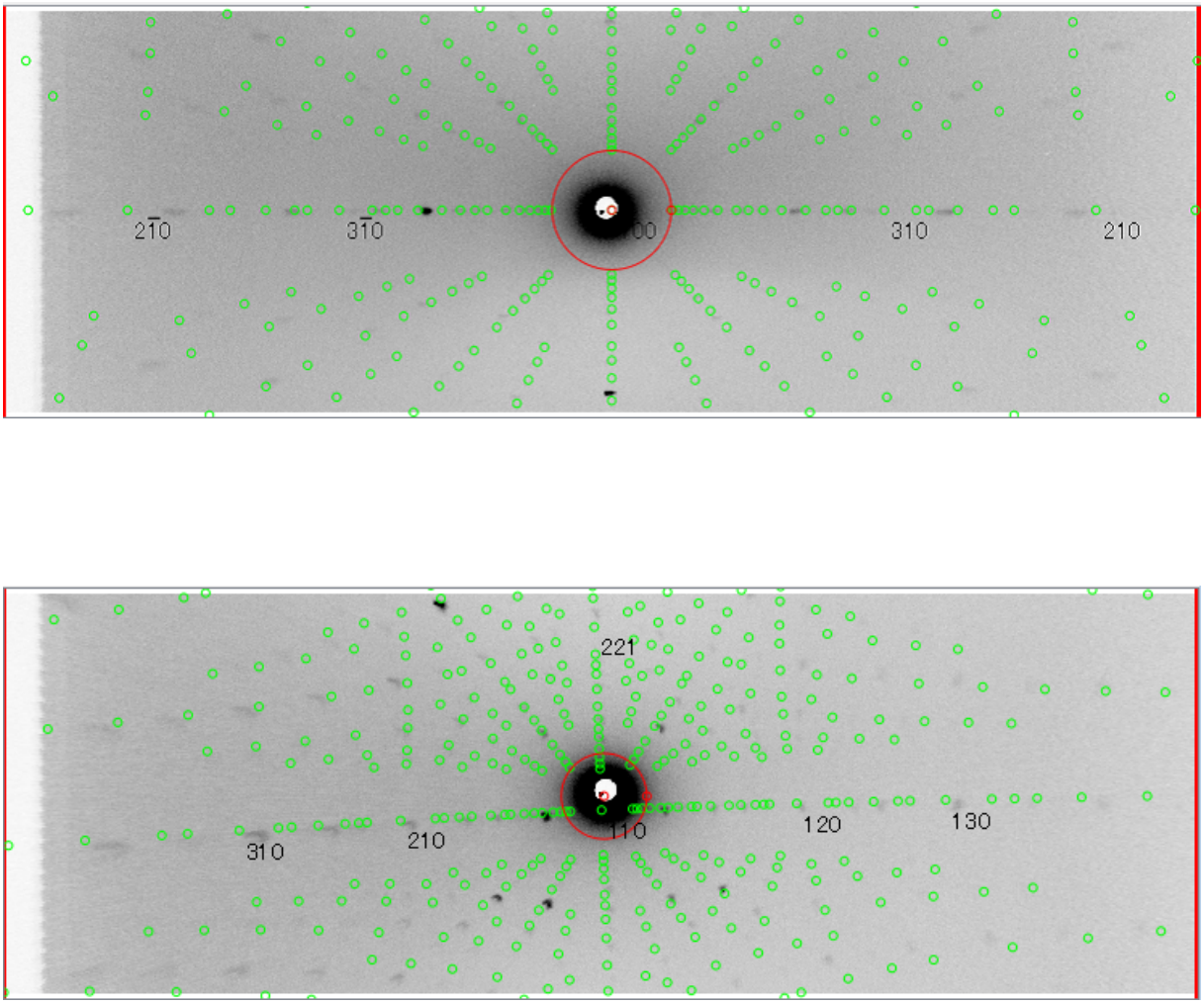


Figure 6.19: Experimental Laue image of $CeB_6$

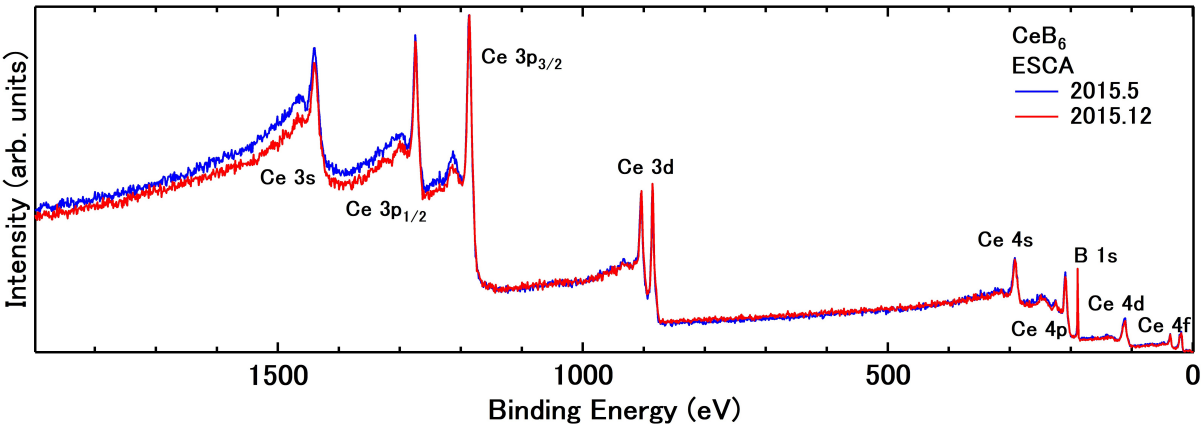


Figure 6.20: Wide energy range HAXPES spectrum of $CeB_6$

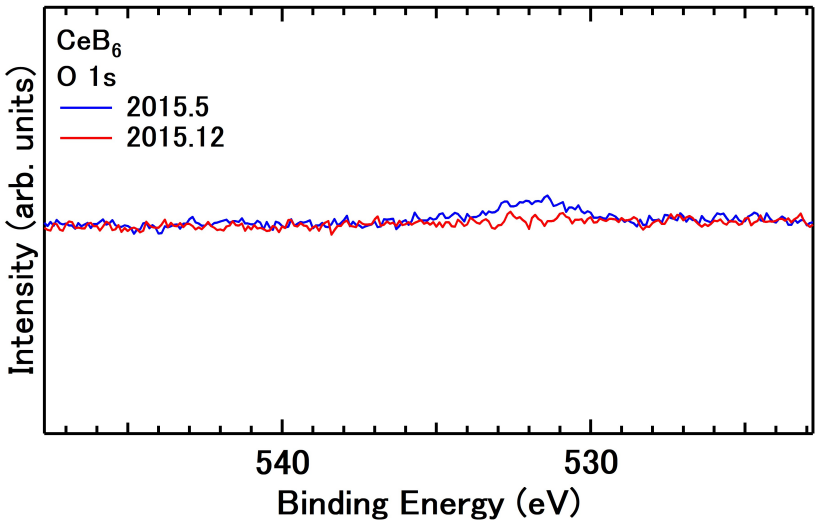


Figure 6.21: The photoemission spectrum of $CeB_6$ around the binding energy of O 1*s* peak position

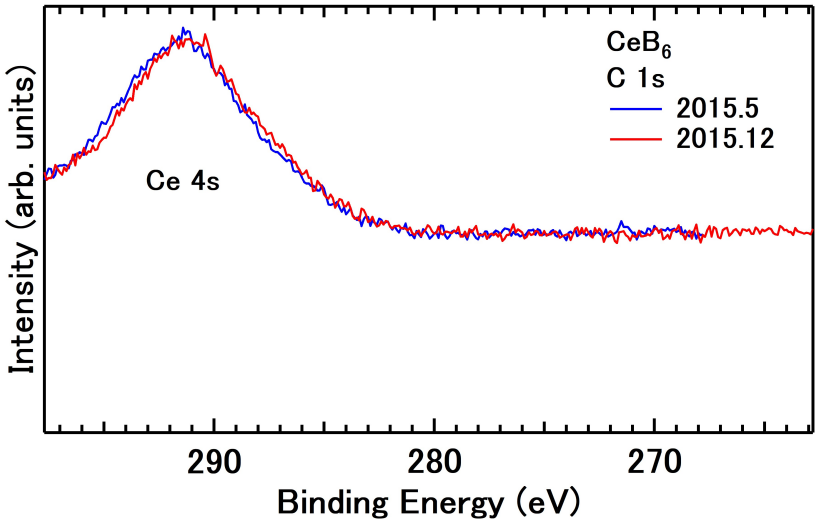


Figure 6.22: The photoemission spectrum of $CeB_6$ around the binding energy of C 1*s* peak position

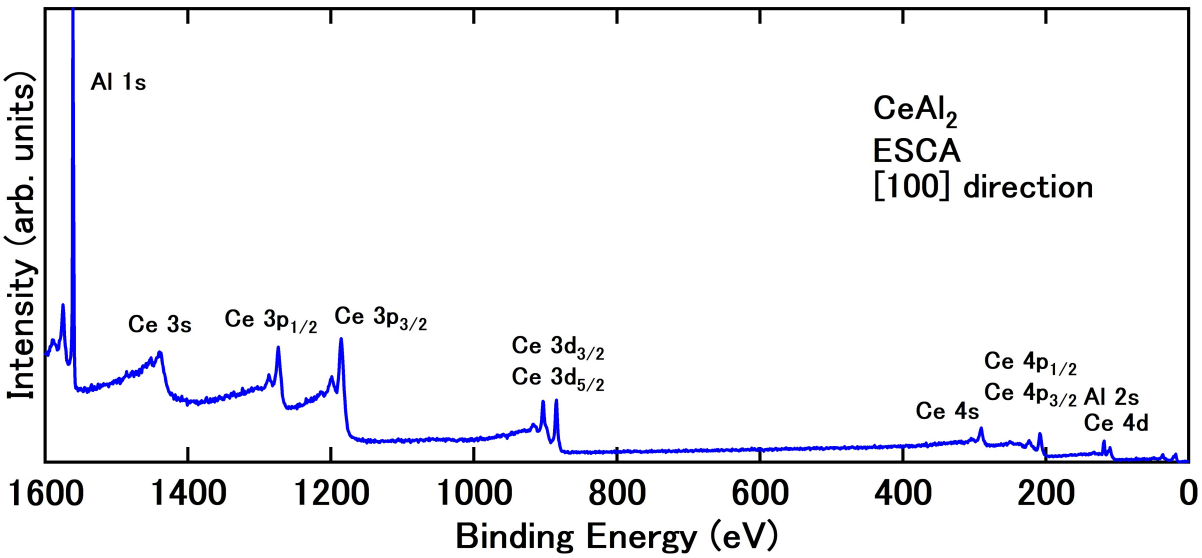


Figure 6.23: Wide energy range HAXPES spectrum of $CeAl_2$

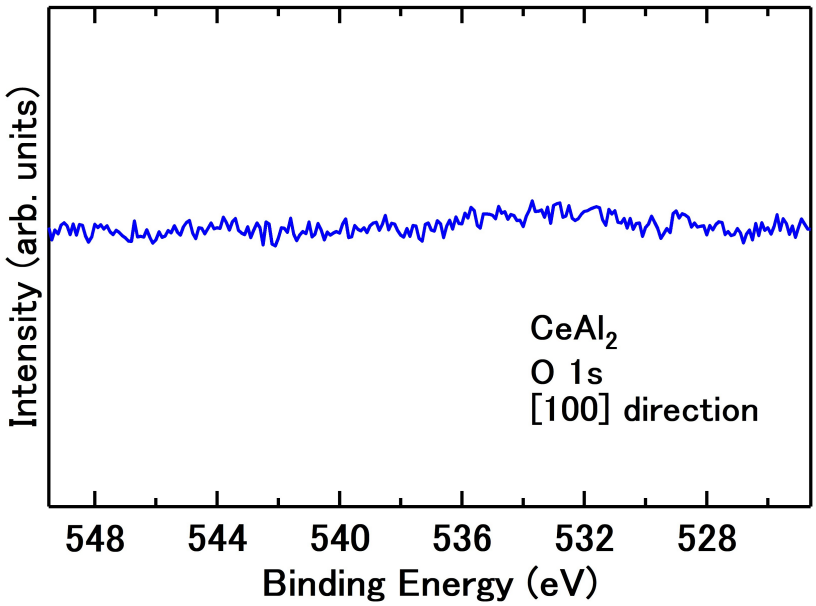


Figure 6.24: The photoemission spectrum of $CeAl_2$ around the binding energy of O 1*s* peak position

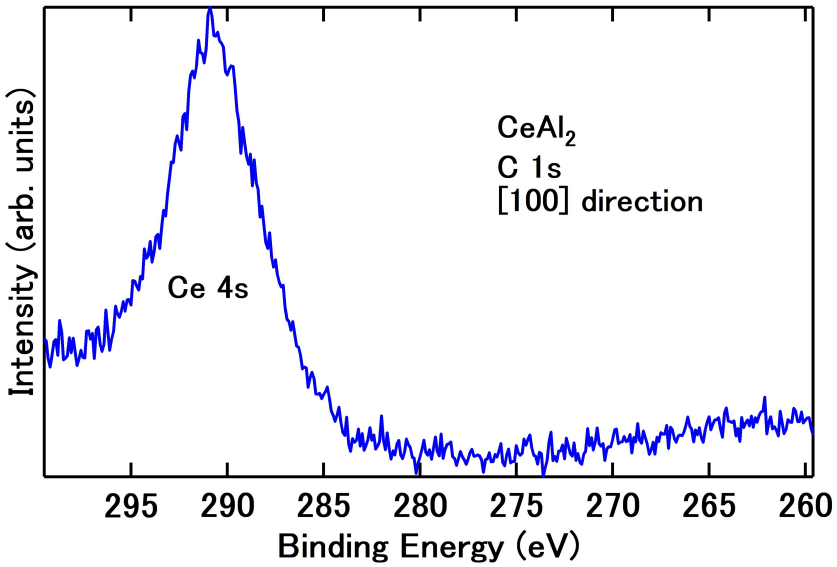


Figure 6.25: The photoemission spectrum of $CeAl_2$ around the binding energy of C 1*s* peak position

# Chapter 7

# Determination of $4f$ orbital symmetry of tetragonal $SmCu_2Si_2$ by linear dichroism in core-level photoemission

In the crystalline solids, Sm ions have two state as trivalent ($4f^5$ electrons) and divalent ($4f^6$), which leads to interesting phenomena such as valence fluctuation and Kondo (or topological) semiconducting states. Photoemission experiment for Sm compounds have been performed long years. However, the applicability of LD in the core-level PES for probing the orbital symmetry has been completely unclear. So that $Sm^{3+}$-dominated compounds should be tested for the determination of $4f$ orbital symmetry by LD-HAXPES with the ion-model calculation. In this chapter, we show the study of tetragonal $SmCu_2Si_2$, in which the Sm ions exist as trivalent state.

## 7.1 Energy splitting of $Sm^{3+}$ $4f$ levels in tetragonal symmetry

The energy diagram of $Sm^{3+}$ $4f$ levels in tetragonal symmetry is shown in Fig. 7.1. Firstly the sixty-sixth-fold degenerated $4f$ levels are split by the spin-orbit interaction into six $J$ multiplets $J = 15/2, 13/2, 11/2, 9/2, 7/2, 5/2$ states. With electron picture, we should consider the lowest $J$ multiplet state. Since the size of splitting by the spin-orbit interaction is ~0.15 eV, and this value is enough larger than CEF splitting (several dozen ~ hundreds meV), we may consider only sixfold degenerated $J = 5/2$ states. The sixfold degenerated $J = 5/2$ states are further split due to the CEF into three doublets as $\Gamma_6$ and $\Gamma_7^1$, and $\Gamma_7^2$, as mentioned in Chapter 2. These wave functions are written by the linear combination of $|J_z\rangle$ states as follows:

$$|\Gamma_6\rangle = |\pm\frac{1}{2}\rangle \tag{7.1}$$

$$|\Gamma_7^1\rangle = a|\pm\frac{5}{2}\rangle - \sqrt{1-a^2}|\mp\frac{3}{2}\rangle \tag{7.2}$$

$$|\Gamma_7^2\rangle = \sqrt{1-a^2}|\pm\frac{5}{2}\rangle + a|\mp\frac{3}{2}\rangle \tag{7.3}$$

$$(0 \le a \le 1). \tag{7.4}$$

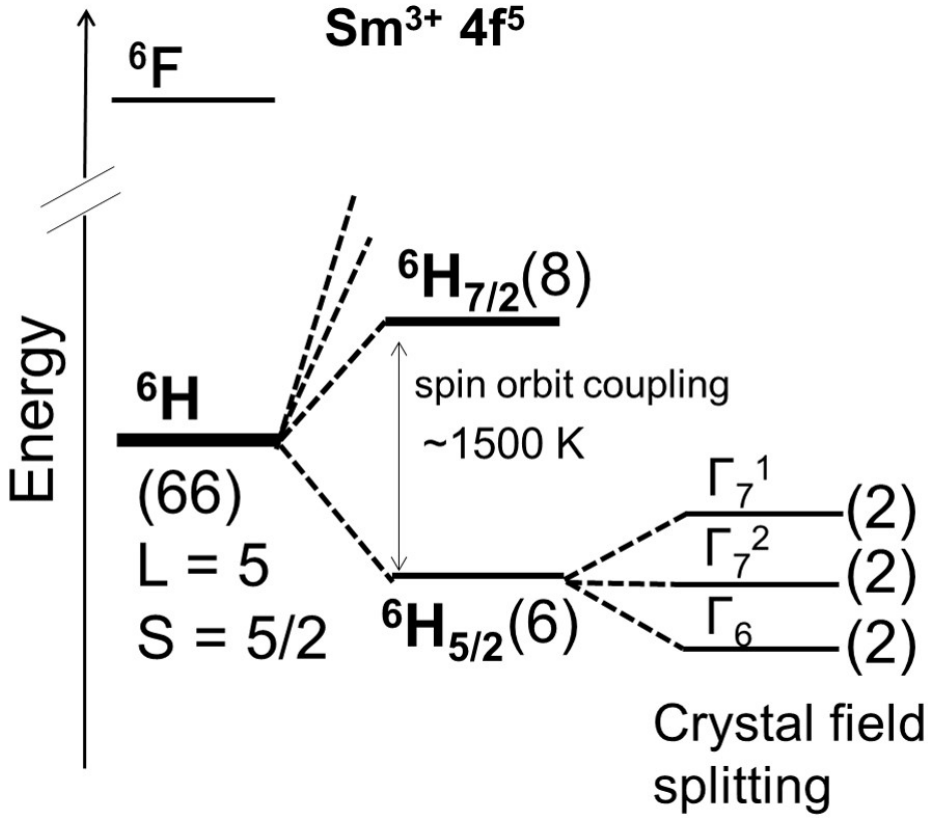


Figure 7.1: Schematic diagram of energy splitting of $Sm^{3+}$ 4$f$ levels in cubic symmetry

Fig. 7.2 shows the $Sm^{3+}$ $4f$ electrons charge distributions with pure $|J_z\rangle$ states. $\Gamma_6$ is pure

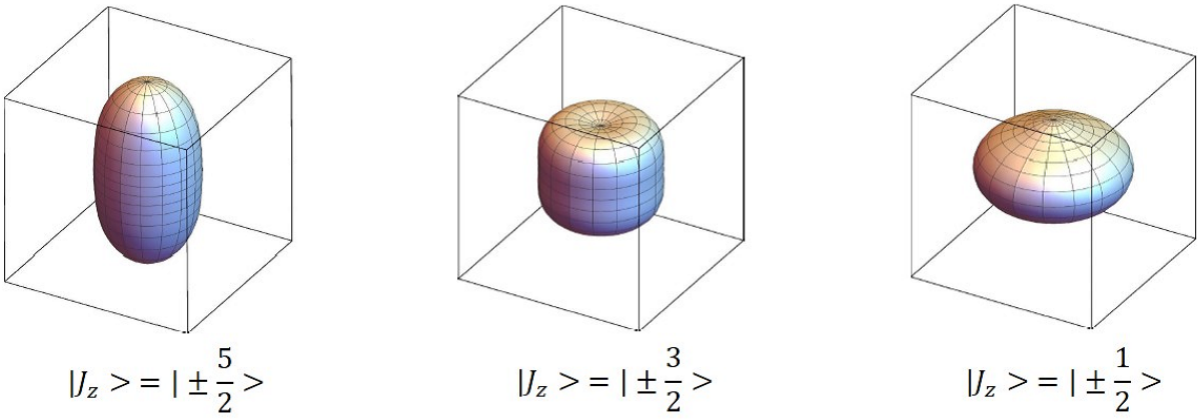


Figure 7.2: $Sm^{3+}$ $4f$ electrons charge distributions with pure $|J_z\rangle$ states

$|J_z\rangle = |\pm 1/2\rangle$ state, and $\Gamma_7$ two consists of linear combinations of $|J_z\rangle = |\pm 5/2\rangle$ state and $|J_z\rangle = |\mp 3/2\rangle$ state. The difference of charge distribution between $\Gamma_7^1$ state and $\Gamma_7^2$ state is occurred in rotation around c axis by 45°. It is noticed that the charge distributions for all pure $|J_z\rangle$ states are close to spherical shape due to the larger number of $Sm^{3+}$ $4f$ electrons compared with the number of $Ce^{3+}$ $4f$ electron and $Yb^{3+}$ $4f$ hole.

## 7.2 Overview of Sm 3*d* core-level photoemission spectrum

The polarization-dependent Sm $3d$ region HAXPES spectra in the [100] direction of $SmCu_2Si_2$ are shown in Fig. 7.3. A multiple peak ranging from 1076 to 1090 eV originate from $Sm^{3+}$ $3d_{5/2}$, and that ranging from 1102 to 1120 eV is from $Sm^{3+}$ $3d_{3/2}$. In addition, a single peak originated from Cu $2s$ orbital is observed at binding energy ranging 1090 to 1102 eV for $SmCu_2Si_2$ especially. Since the substitution of photoemission background is too difficult for $Sm^{3+}$ $3d_{3/2}$ spectral region due to the peak from Cu $2s$ in lower binding energy side and the plasmon peaks in higher binding energy side, we determine $4f$ orbital symmetry by $Sm^{3+}$ $3d_{5/2}$ photoemission spectra.

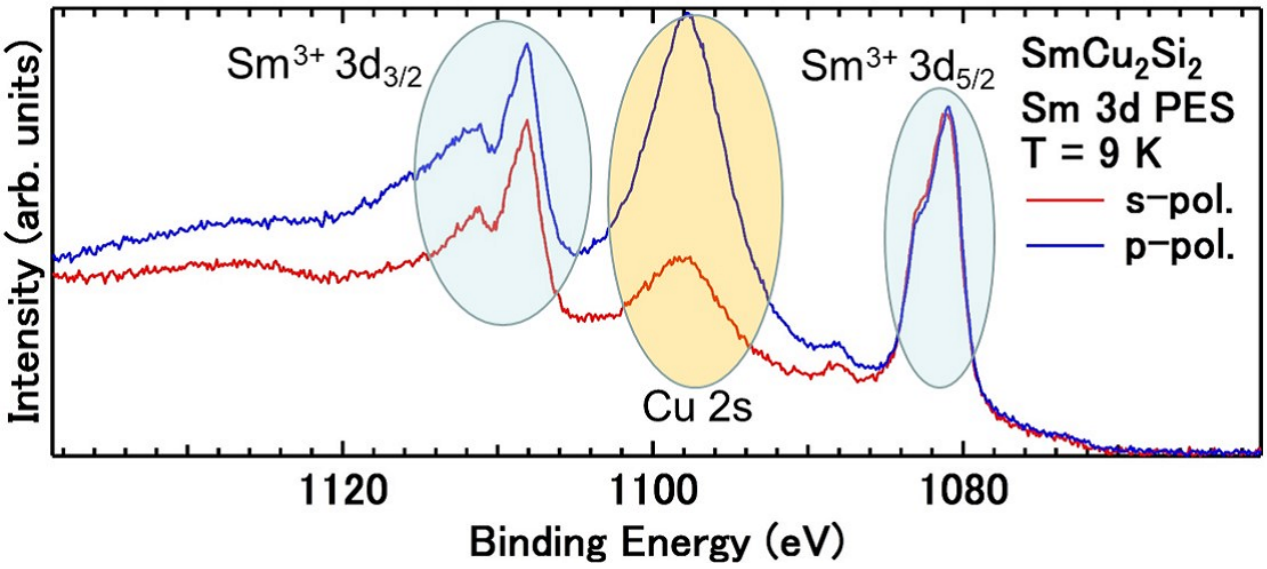


Figure 7.3: Sm $3d$ and Cu $2s$ core-level photoemission spectra of $SmCu_2Si_2$

## 7.3 Simulated polarization-dependent $Sm^{3+}$ $3d_{5/2}$ photoemission spectra

Simulated polarization-dependent $Sm^{3+}$ $3d_{5/2}$ core-level HAXPES spectra assuming pure $|J_z\rangle$ ground states in experimental geometry with $\theta = 60°$ (photoelectron detection direction in along [001] direction) is shown in Fig. 7.4, together with the corresponding $4f$ charge distributions. In Fig. 7.4, the blue lines show the spectra at p-polarization configuration, and the red lines shows that at s-polarization configuration. We performed the ionic calculations including the full multiplet theory [18] and the local CEF splitting for $4f$ photoemission spectra by using the XTLS 9.0 program [19] as is the case with $3d$ core-level photoemission. All atomic parameters such as the $4f$-$4f$ Coulomb and exchange interactions (Slater integrals) and the $4f$ spin orbit couplings have been obtained using Cowan ' s code [25] based on the Hartree-Fock method. The $3d$-$4f$ Slater integrals are reduced to 87% and the ratios of the $4f$-$4f$ Slater integrals $F^2$, $F^4$ and $F^6$ have been chosen as $F^4/F^2 = 0.726$ and $F^6/F^2 = 0.5726$ as in the same manner as in Ref. [100], where $F^2$ is reduced to 68% from the value obtained using the Cowan ' s code. The spin orbit coupling is reduced to 98%.

As shown in Fig. 7.4, the $Sm^{3+}$ $3d_{5/2}$ spectra for $|J_z\rangle = |\pm 1/2\rangle$ ground state has sloping shape, on the other hand that for $|J_z\rangle = |\pm 5/2\rangle$ has sharp peak structure around binding energy of 1080.5 eV. Since $\Gamma_6$ is pure $|J_z\rangle = |\pm 1/2\rangle$ state, and $\Gamma_7$ two consists of linear combinations of $|J_z\rangle = |\pm 5/2\rangle$ state and $|J_z\rangle = |\mp 3/2\rangle$ state, these ground states can be distinguished by the visual of $Sm^{3+}$ $3d_{5/2}$ spectra. For the Sm compound which $4f$ ground state is in $\Gamma_6$ symmetry, observed the $Sm^{3+}$ $3d_{5/2}$ spectra become sloping shape, with higher s-polarization spectrum than p-polarization one around binding energy of 1080.8 eV and higher p-polarization spectrum than s-polarization one around binding energy of 1083 eV. In contrast, For the Sm compound which $4f$ ground state is in $\Gamma_7$ symmetry, the $Sm^{3+}$ $3d_{5/2}$ spectra become sharp, with higher p-polarization peak than s-polarization one around binding energy of 1081 eV. Since the photoelectron detection direction is along [001] direction

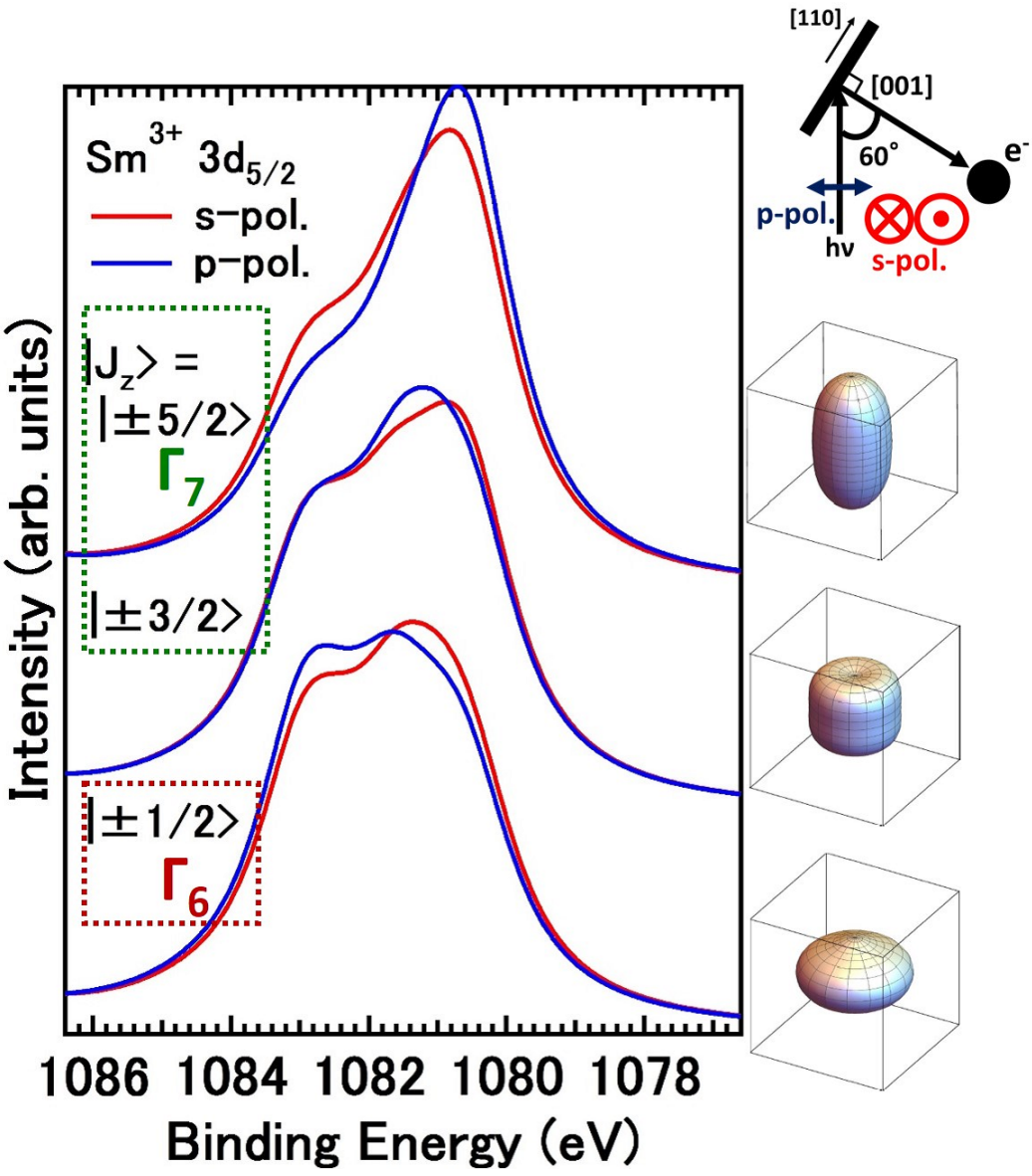


Figure 7.4: Simulated polarization-dependent $3d_{5/2}$ photoemission spectra of $Sm^{3+}$ ions assuming pure $|J_z\rangle$ ground states at photoemission detection direction [001] direction, together with the experimental geometry. The $4f$-hole spatial distributions for the corresponding states are also shown.

(c axis), it is impossible to distinguish $\Gamma_7^1$ and $\Gamma_7^2$ symmetry in this experimental geometry. Therefore, it is essential to change experimental geometry.

## 7.4 Determination of 4*f* ground-state symmetry by the linear dichroism in $Sm^{3+}$ 3*d* core-level photoemission spectra

### 7.4.1 Physical properties of $SmCu_2Si_2$

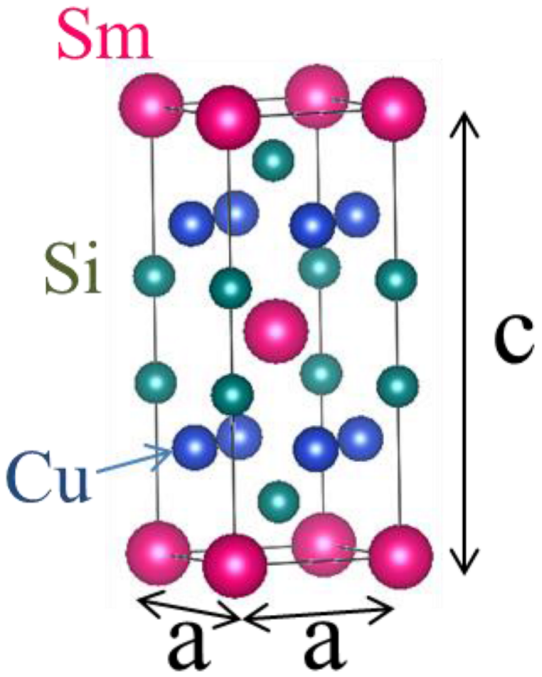


Figure 7.5: Crystal structure of $SmCu_2Si_2$ ($ThCr_2Si_2$ tetragonal structure)

The crystal structure of $SmCu_2Si_2$ is shown in Fig. 7.5. The crystal structure of $SmCu_2Si_2$ is tetragonal $ThCr_2Si_2$ structure as same as $YbCu_2Si_2$ and $YbRh_2Si_2$ that we firstly reported determination of 4*f* ground state by LD-HAXPES [14].
The temperature dependences of magnetic susceptibility is shown in Fig. 7.6 [102]. The magnetic susceptibilities have a peak and the inverses of that ($1/\chi$) have a cusp structure at Néel temperature $T_N$ = 9 K. The temperature dependences of specific heat (a), magnetic specific heat (b), and magnetic entropy (c) of $SmCu_2Si_2$ are shown in Fig. 7.7 [101]. The magnetic specific heat in Fig. 7.7(b) was obtained by subtracting specific heat of $LaCu_2Si_2$ from total specific heat of $SmCu_2Si_2$ (Fig 7.7(a)). As shown in Fig. 7.7(c), magnetic entropy attain to $R \ln 2$ around 40 K and total CEF splitting energy is lower than 100 K.

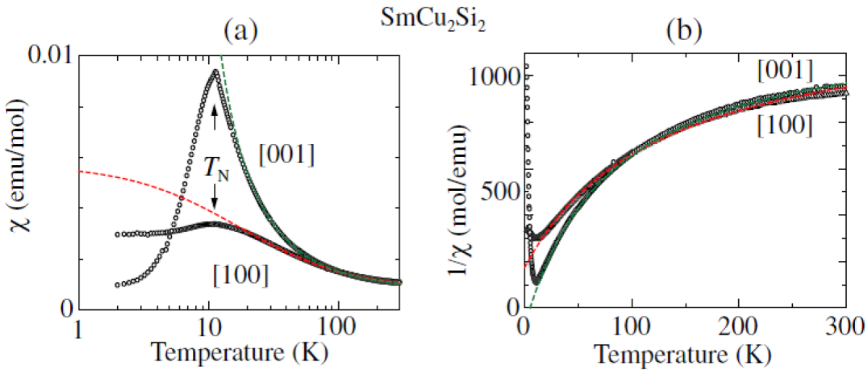


Figure 7.6: Temperature dependence of magnetic susceptibility of $SmCu_2Si_2$ [102]

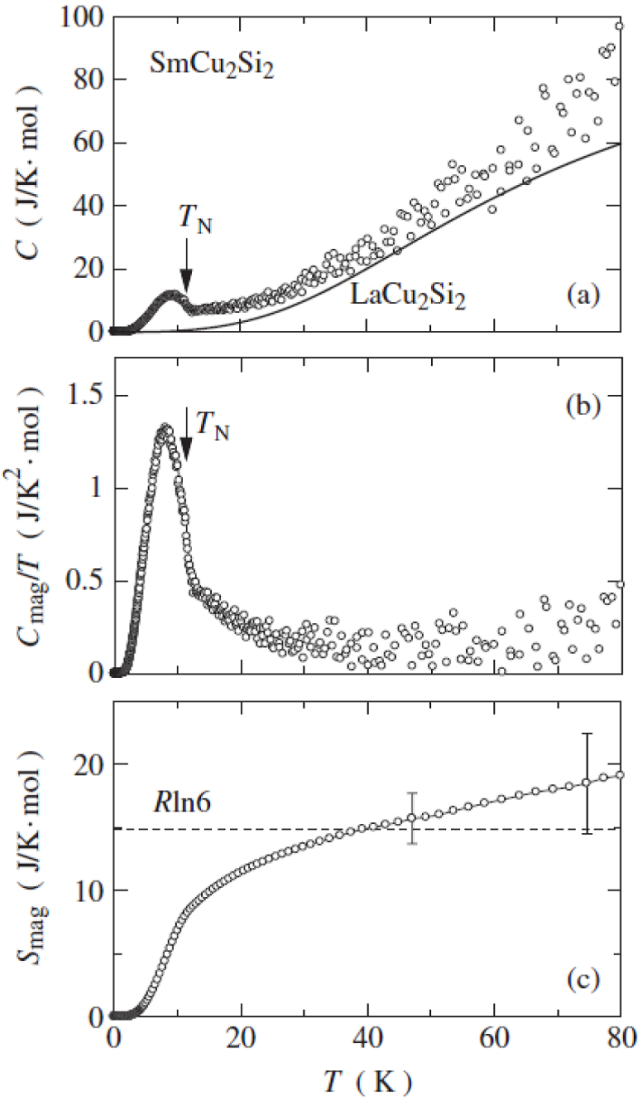


Figure 7.7: The temperature dependences of specific heat (a), magnetic specific heat (b), and magnetic entropy (c) of $SmCu_2Si_2$ [101]

### 7.4.2 Experimental conditions

The experimental conditions for $SmCu_2Si_2$ are shown in below table. Single crystals of $SmCu_2Si_2$ was given by Visiting Professor Yoshitika Onuki (Faculty of Science, University of the Ryukyus). The experimental geometry was controlled using a developed two-axis manipulator [55]. We perfomed LD-HAXPES at three experimetal geometries for the normal emission direction parallel to the [001] direction, and two significantly different photoelectron directions far (~70°) from the c axis (one is a configuration that a axis exist in scattering plane : named as Geometry1, and one is a configuration that a axis not exist in scattering plane, [110] direction exist in the plane : named Geometry2). The measuring temperatures were 10 K for for SmCu2Si2 in the paramagnetic phase [102]

| Sample | $SmCu_2Si_2$ | | |
|---|---|---|---|
| Light Source | SPring-8 BL19LXU | | |
| Analyzer | MB Scientific A1-HE analyzer | | |
| Photon Energy | 7900 eV | | |
| Energy Resolution | 400, 500 meV | | |
| Temperature | 10 K | | |
| Base Pressure | ~1 × $10^{-7}$ Pa | | |
| Experimental Geometry | Normal Emission 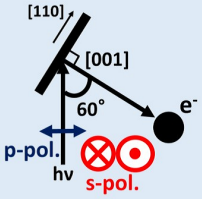  | Geometry1 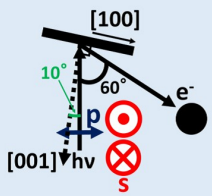  | Geometry2 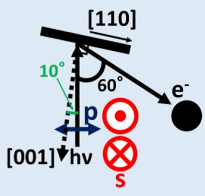  |

### 7.4.3 Shirley-type background and normalization of $Sm^{3+}$ $3d_{5/2}$ core-level HAXPES spectra of $SmCu_2Si_2$

The polarization-dependent $Sm^{3+}$ $3d_{5/2}$ HAXPES spectra (and apart of Cu 2*s* spectra) in the [001] direction of $SmCu_2Si_2$ are shown in Fig. 7.8. A intrinsic LD is seen in the multiplet structures in the $Sm^{3+}$ $3d_{5/2}$ raw spectra. The subtracting Shirley-type backgrounds are also displayed in Fig. 7.8. The reference binding energy on the higher side has been set to 1086.8 eV corresponding to the local minimum of the raw spectral weight in the p-polarization. For $SmCu_2Si_2$, the spectral intensities of Cu 2*s* are drastically different between s-polarization configuration and p-polarization. Since the intensity of Cu 2*s* spectrum is very larger in p-polarization than s-polarization, we subtract Shirley-type background with remaining a little intensity at higher binding energy side for p-polarization configuration.

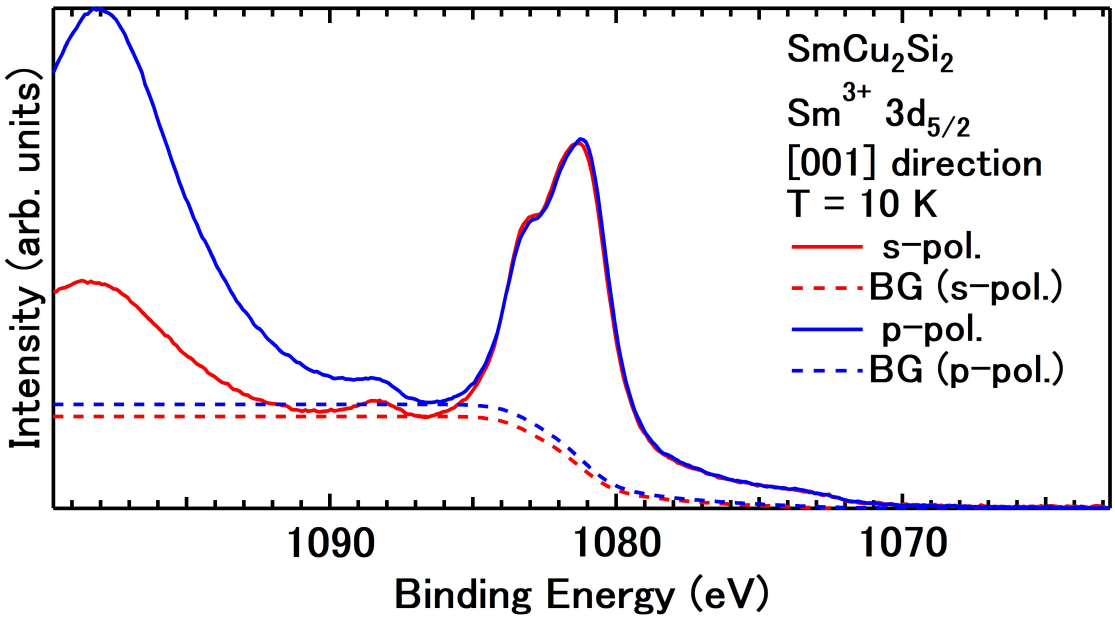


Figure 7.8: Polarization-dependent $Sm^{3+}$ $3d_{5/2}$ core-level HAXPES raw spectra (solid lines) of $SmCu_2Si_2$ in the [001] direction and optimized Shirley-type backgrounds (dashed lines).

### 7.4.4 Linear dichroism in $Sm^{3+}$ $3d_{5/2}$ core-level HAXPES spectra of $SmCu_2Si_2$

The polarization-dependent background-subtracted $Sm^{3+}$ $3d_{5/2}$ HAXPES spectra of $SmCu_2Si_2$ and its LD (defined by the intensity at s-polarization configuration minus the intensity at p-polarization configuration) in the photoelectron detection directions of [001] (normal emission) are shown in Fig. 7.9. The simulation spectra and LD, which reproduce experimental LD, are also shown in Fig. 7.9. The $Sm^{3+}$ $3d_{5/2}$ spectra have sharp peak structure around binding energy of 1081 eV with higher intensity of p-polarization than s-polarization, and shoulder structure around binding energy of 1083 eV with higher intensity of s-polarization than p-polarization. These features of spectrum are completely different from that for $|\Gamma_6\rangle = |\pm 1/2\rangle$ ground state. It means the $Sm^{3+}$ $3d_{5/2}$ HAXPES spectra and its LD in normal emission direction indicate $|\Gamma_7\rangle = a|\pm 5/2\rangle \pm \sqrt{1-a^2}|\mp 3/2\rangle$ ground state. So that we reproduced the experimental spectra and LD with linear combination of $|J_z\rangle = |\pm 5/2\rangle$ and $|J_z\rangle = |\mp 3/2\rangle$ by ionic calculation, and determined the coefficient value of $a$. As determine the value of $a$ to reproduce experimental LD quantitatively, the $4f$ ground state of $SmCu_2Si_2$ are given by:

$$|\Gamma_7\rangle = \sqrt{0.6}|\pm\frac{5}{2}\rangle \pm \sqrt{0.4}|\mp\frac{3}{2}\rangle. \tag{7.5}$$

The $4f$ electron charge distributions corresponding to this determined ground state are also shown in Fig. 7.9. In this experimental geometry the rotation symmetry around c axis cannot be distinguished.

The polarization-dependent background-subtracted $Sm^{3+}$ $3d_{5/2}$ HAXPES spectra of $SmCu_2Si_2$ and simulated ones assuming two ground states, which have been made the candidates by re-

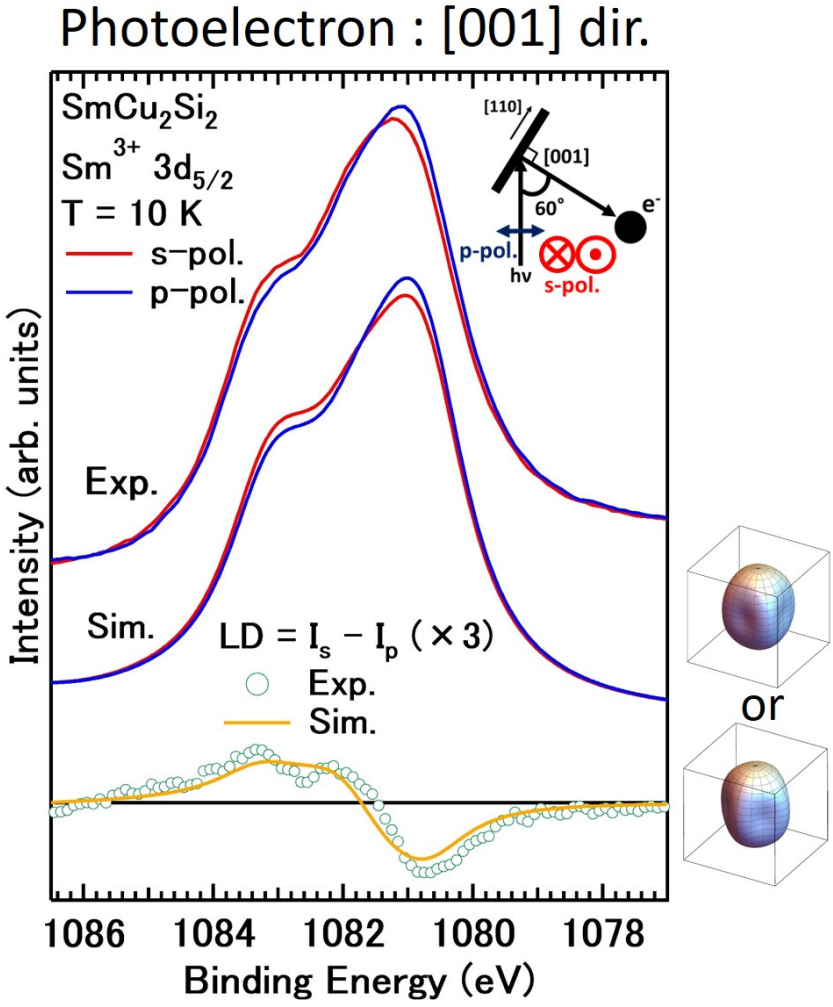


Figure 7.9: Polarization-dependent $Sm^{3+}$ $3d_{5/2}$ core-level HAXPES spectra and LD of $SmCu_2Si_2$ with the simulated ones which reproduce experiment in photoelectron detection direction along [001] direction, together with experimental geometry and $Sm^{3+}$ $4f$ charge distributions corresponding to the ground state assuming in ionic calculation

sults in normal emission direction, at two significantly different photoelectron directions far (~70°) from the c axis named Geometry1 and Geometry2 are shown in Fig. 7.10, together with corresponding $4f$ charge distributions. The feature of experimental spectra in Geometry1 have little difference to that in Geometry2. For perfect determination of $4f$ ground state, A comparisons of LDs in $Sm^{3+}$ $3d_{5/2}$ HAXPES spectra of $SmCu_2Si_2$ and simulated ones assuming nominated two ground states in Geometry1 (green lines) and Geometry2 (blue lines) are shown in Fig 7.11. The total structure LD of $SmCu_2Si_2$ in Geometry1 exists in higher binding energy than that in Geometry2. The feature in experimental LDs is consistent with that in simulated LDs assuming $\Gamma_7^1$ ground state.
So that our finally determined $Sm^{3+}$ $4f$ ground state of $SmCu_2Si_2$ is as follows:

$$|\Gamma_7^1\rangle \quad = \quad \sqrt{0.6}|\pm\frac{5}{2}\rangle - \sqrt{0.4}|\mp\frac{3}{2}\rangle \tag{7.6}$$

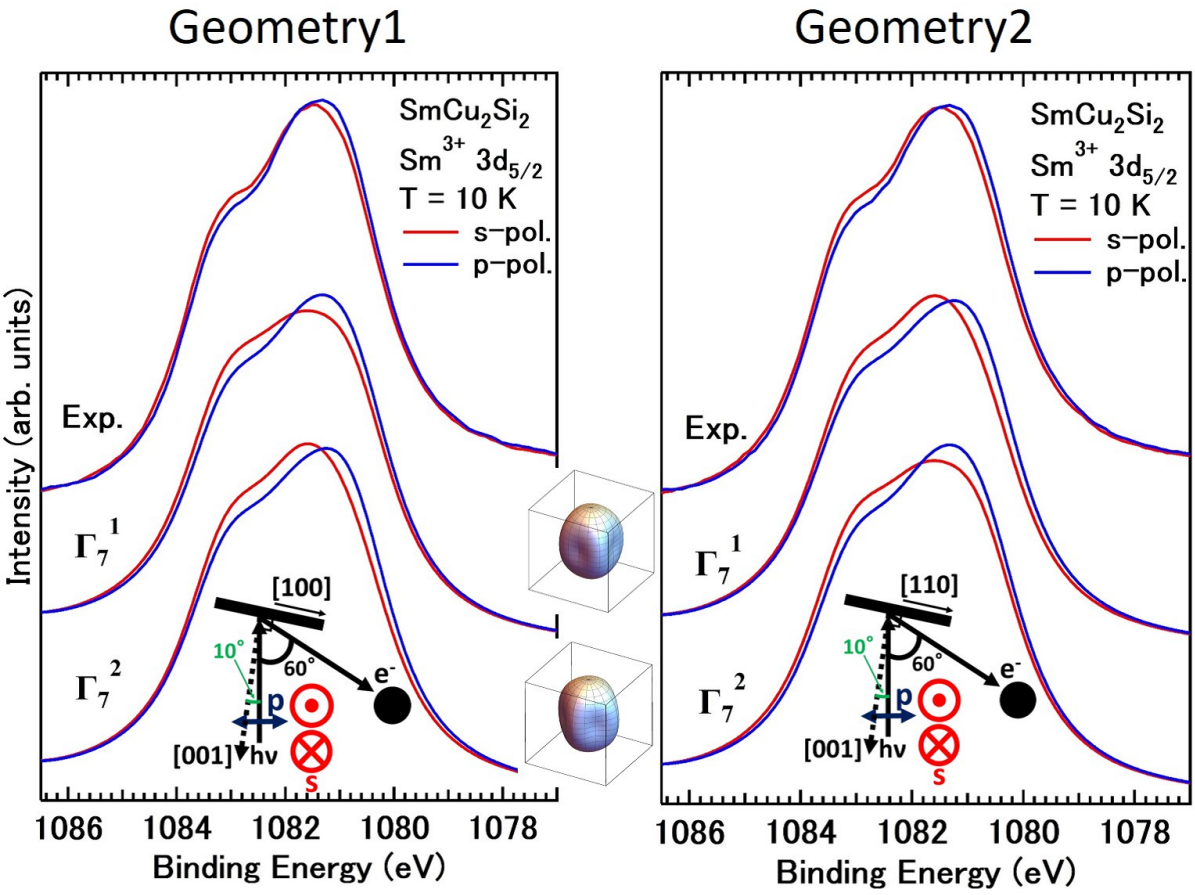


Figure 7.10: Polarization-dependent background-subtracted $Sm^{3+}$ $3d_{5/2}$ HAXPES spectra of $SmCu_2Si_2$ and simulated ones assuming candidate two ground states ($\Gamma_7^1$ and $\Gamma_7^2$) in Geometry1 and Geometry2, together with experimental geometry and corresponding $4f$ charge distributions

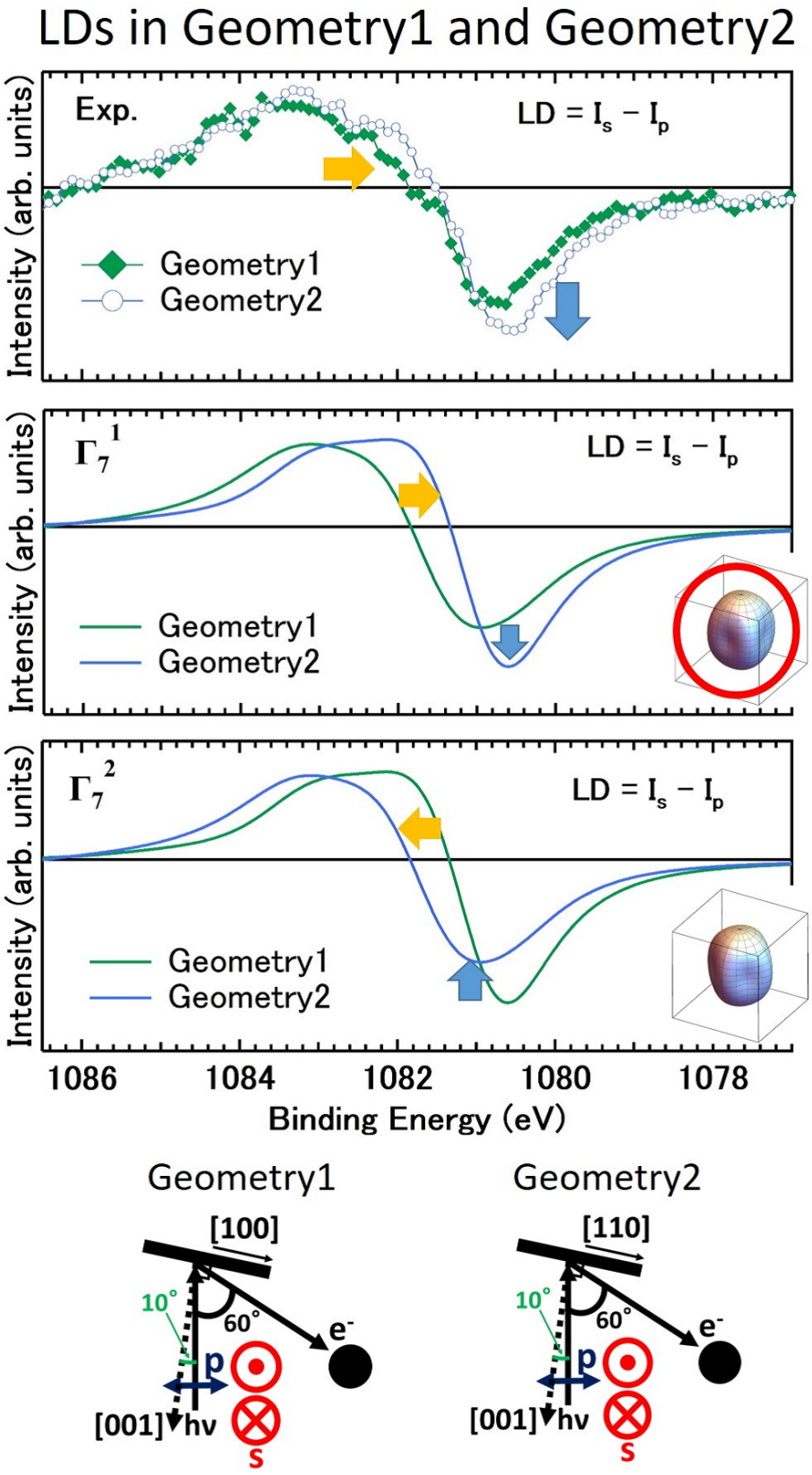


Figure 7.11: Polarization-dependent background-subtracted $Sm^{3+}$ $3d_{5/2}$ HAXPES spectra of $SmCu_2Si_2$ and simulated ones assuming candidate two ground states ($\Gamma_7^1$ and $\Gamma_7^2$) in Geometry1 (green lines) and Geometry2 (blue lines), together with experimental geometry and corresponding $4f$ charge distributions

### 7.4.5 Discussion

The three dimensional view and top view of determined $Sm^{3+}$ $4f$-hole spatial distribution with crystal structure of $SmCu_2Si_2$ are shown in Fig 7.12. The $Sm^{3+}$ $4f$ charge distribution is elongated Si side and this feature is consistent with the $4f$ charge distribution of $YbCu_2Si_2$ [14]. For $RT_2Si_2$ (R:rare-earth, T:transition metal), most of $4f$ CEF ground-state charge distributions have reported to be elongated to Si side, so the hybridization between $4f$ electrons in rare-earth and conduction electrons in Si makes energetically stable state. Thought the coefficient value of $a$ is related to hybridization, for discussion of these relations it is better to know other $4f$ charge distributions of $SmT_2Si_2$ compounds.
Exactly, the $4f$ charge distribution of $Sm^{3+}$ ion is close to spherical shape due to its $4f$ electrons number. So that the features of $4f$ charge distributions are difficult to distinguish. In our experiments, the experimental polarization-dependent $Sm^{3+}$ $3d$ core-level spectra has little difference between Geometry1 and Geometry2. However, from this measurements, we have proved that LD-HAXPES can useful to determine $4f$ CEF ground state even in case $4f$ charge distribution is close to spherical shape.

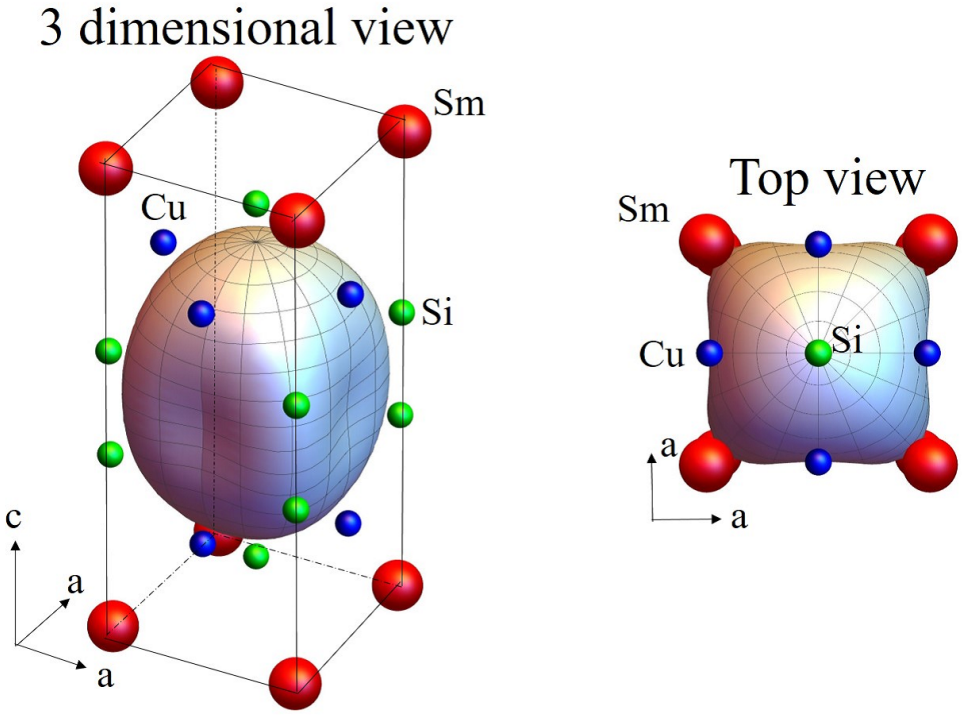


Figure 7.12: Three dimensional view and top view of determined $Sm^{3+}$ $4f$-hole spatial distribution with crystal structure of $SmCu_2Si_2$

### 7.4.6 Linear dichroism in $Sm^{3+}$ $3d_{5/2}$ core-level HAXPES spectra of $SmCu_2Si_2$ at another photoelectron detection directions

The polarization-dependent background-subtracted $Sm^{3+}$ $3d_{5/2}$ HAXPES spectra and LDs of $SmCu_2Si_2$ and simulated ones assuming two candidate ground states in other experimental

geometry (shown in insets of Figure) are shown in Fig 7.13. These results are consistent with $\Gamma_7^1$ ground state for $SmCu_2Si_2$.

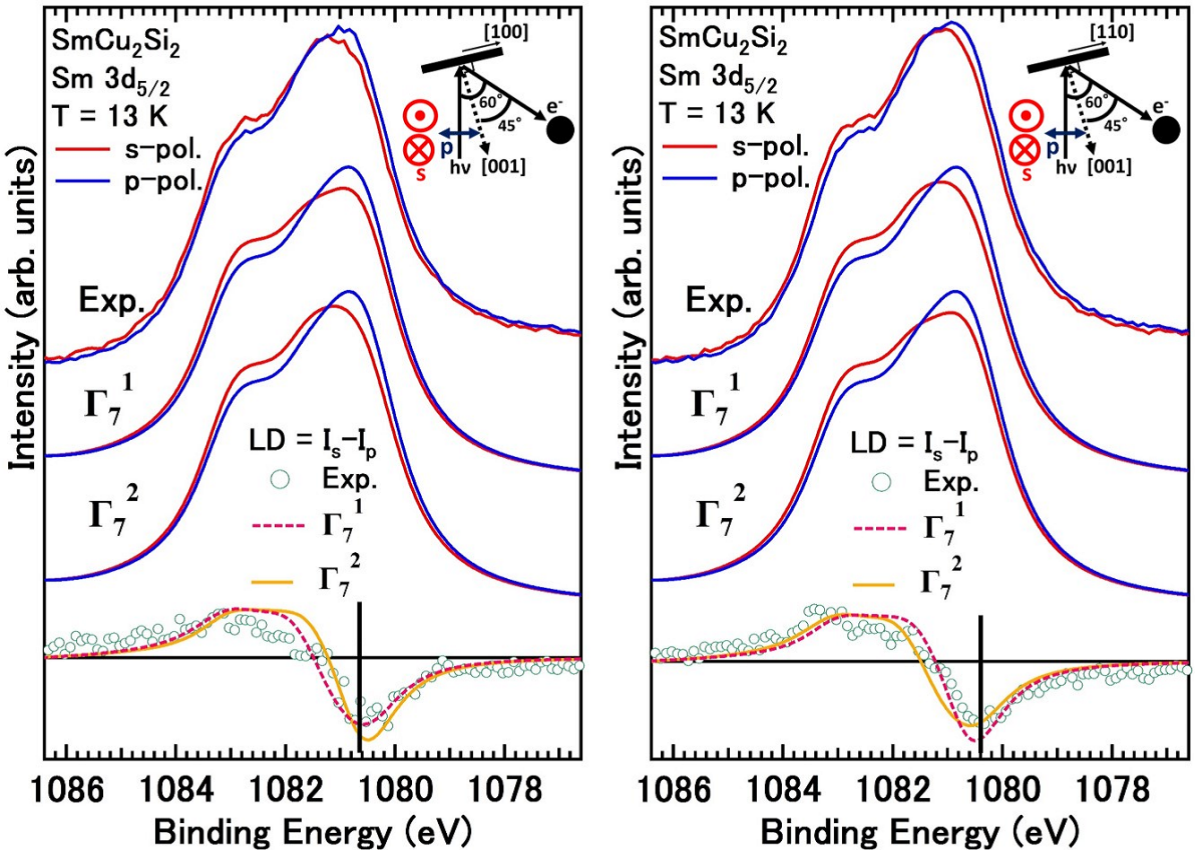


Figure 7.13: Polarization-dependent background-subtracted $Sm^{3+}$ $3d_{5/2}$ HAXPES spectra of $SmCu_2Si_2$ and simulated ones assuming candidated two ground states ($\Gamma_7^1$ and $\Gamma_7^2$) in experimental geometries shown in insets

### 7.4.7 Sample quality

The sample and surface qualities were examined on the basis of the absence of any core-level spectral weight caused by possible impurities including oxygen and carbon as shown below. There is little peaks from O 1*s* and C 1*s* in spectrum of $SmCu_2Si_2$ as shown in Figs. 7.14, and 7.15

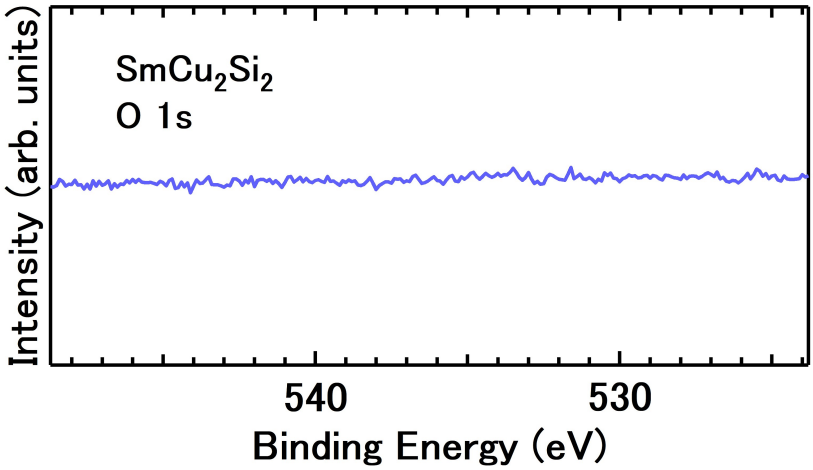


Figure 7.14: The photoemission spectrum of $SmCu_2Si_2$ around the binding energy of O 1*s* peak position

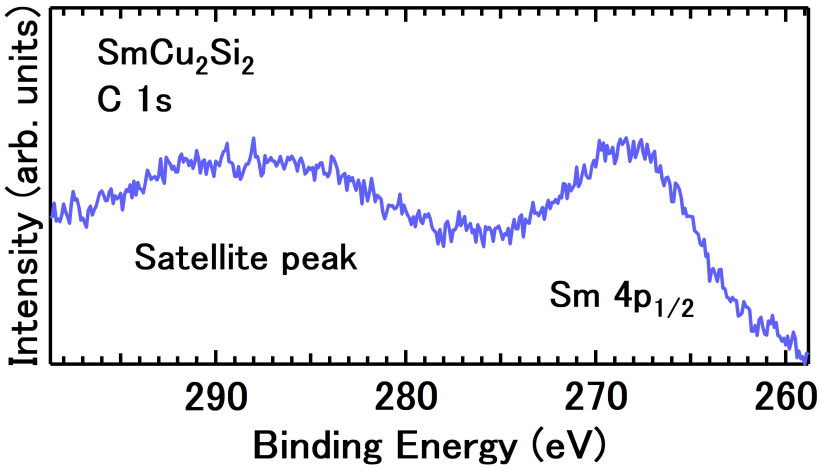


Figure 7.15: The photoemission spectrum of $SmCu_2Si_2$ around the binding energy of C 1*s* peak position

# Chapter 8

# Linear dichroism in $4f$ valence-band photoemission spectra of strongly correlated rare-earth compounds

Since $4f$ photoemission process has the $4f^{12}$ (two $4f$ holes) configuration in the final states, LD in valence-band $4f$ PES spectra have been expected to observe more clearly because of their multiplets structures with many components. Therefore, we have also performed the polarization-dependent valence-band $4f$ PES at BL27SU in SPring-8 [20].

## 8.1 Simulated polarization-dependent $Yb^{3+}$ 4f photoemission spectra

Simulated polarization-dependent $4f$ photoemission spectra of the $Yb^{3+}$ ions assuming the pure $J_z$ ground state and the corresponding $4f$ hole spatial distributions are shown in Fig. 8.1. We performed the ionic calculations including the full multiplet theory [18] and the local CEF splitting for $4f$ photoemission spectra by using the XTLS 9.0 program [19] as is the case with $3d$ core-level photoemission. All atomic parameters such as the $4f$-$4f$ Coulomb and exchange interactions (Slater integrals) and the $4f$ spin orbit couplings have been obtained using Cowan ' s code [25] based on the Hartree-Fock method. The ratios of the $4f$-$4f$ Slater integrals $F^2$, $F^4$ and $F^6$ have been chosen as $F^4/F^2 = 0.726$ and $F^6/F^2 = 0.5726$ as in the same manner as in Ref. [100], where $F^2$ is reduced to 80% from the value obtained using the Cowan ' s code. The spin orbit coupling is reduced to 98%. As shown in Fig. 8.1 LD in $Yb^{3+}$ $4f$ photoemission spectra is clearly predicted for almost pure $J_z$ states. In the case of $Yb^{3+}$ ions in tetragonal symmetry, the eightfold degenerate $J = 7/2$ state splits into four doublets as:

$$|\Gamma_7^1\rangle = c|\pm 5/2\rangle + \sqrt{1-c^2}|\mp 3/2\rangle, \tag{8.1}$$

$$|\Gamma_7^2\rangle = -\sqrt{1-c^2}|\pm 5/2\rangle + c|\mp 3/2\rangle, \tag{8.2}$$

$$|\Gamma_6^1\rangle = b|\pm 1/2\rangle + \sqrt{1-b^2}|\mp 7/2\rangle, \tag{8.3}$$

$$|\Gamma_6^2\rangle = \sqrt{1-b^2}|\pm 1/2\rangle - b|\mp 7/2\rangle, \tag{8.4}$$

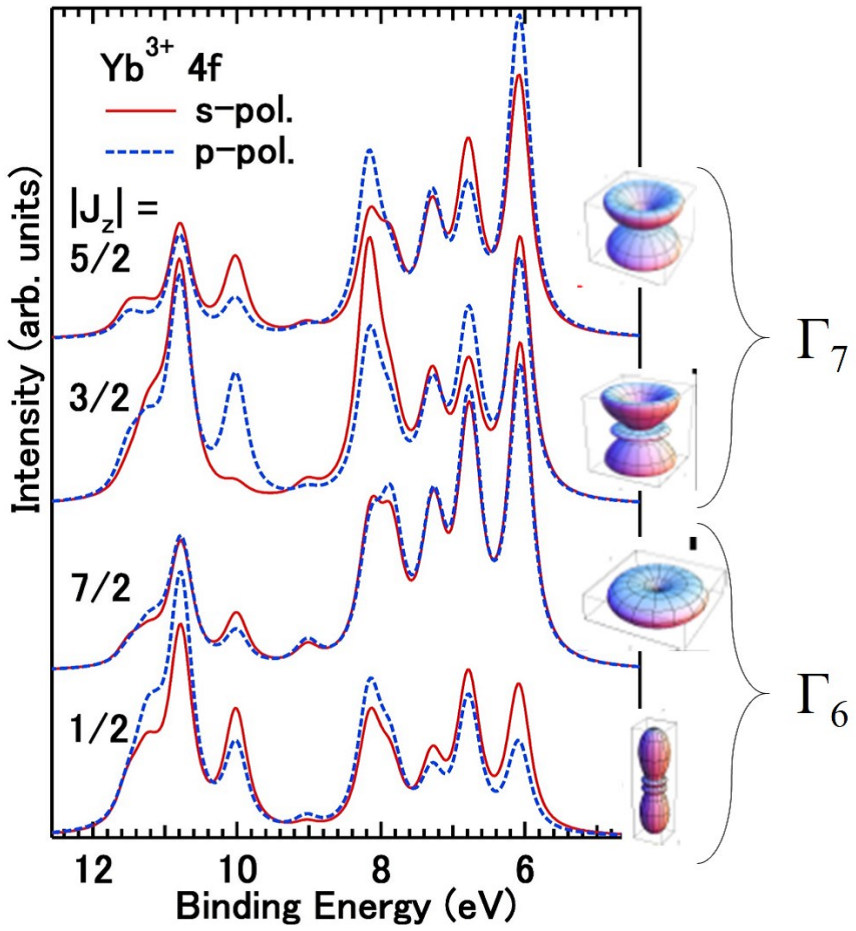


Figure 8.1: Simulated polarization-dependent $4f$ photoemission spectra of the $Yb^{3+}$ ions assuming the pure $J_z$ ground state, together with the corresponding $4f$ hole spatial distributions.

where the coefficients $0 \leq b \leq 1, 0 \leq c \leq 1$. Then large LD in $4f$ PES is expected to be observed especially in tetragonal symmetry.

## 8.2 Experimental linear dichroism in $4f$ valence-band PES of rare-earth compounds

### 8.2.1 Experimantal conditions

We have performed LD in $4f$ valence-band PES at BL27SU of SPring-8 using SPECS PHOIBOS 150 hemispherical photoelectron spectrometer. The excitation light was controlled by the figure-8 undulator [103]. Single crystals of $YbRh_2Si_2$ [104], $YbCu_2Si_2$ [101, 105] and $SmCu_2Si_2$ [102] were cleaved along the (001) plane, and those of $YbIr_2Zn_{20}$ were cleaved along (111) plane in situ, where the base pressure was $\sim 8 \times 10^{-8}$ Pa. The measuring temperatures were 12 K for the Yb compounds and 20 K for $SmCu_2Si_2$ in the paramagnetic phase [102], at which the contributions of the excited $4f$ levels were negligible [14].

| | 4f valence-band PES | | | |
|---|---|---|---|---|
| Sample | $YbRh_2Si_2$ | $YbCu_2Si_2$ | $YbIr_2Zn_{20}$ | $SmCu_2Si_2$ |
| Light source | SPring-8 BL27SU | | | |
| Analyzer | SPECS PHOIBOS 150 | | | |
| Photon energy | 700 eV | | | |
| Energy resolution | 160 meV | | | |
| Temperature | 12 K | | | |
| Base pressure | $\sim 8 \times 10^{-8}$ Pa | | | |

### 8.2.2 Linear dichroism in $4f$ valence-band PES of tetragonal $YbRh_2Si_2$ and $YbCu_2Si_2$

The polarization-dependent $Yb^{3+}$ $4f$ valence-band PES spectra of tetragonal $YbRh_2Si_2$ and $YbCu_2Si_2$ in the two photoelectron directions are shown in Fig. 8.2. The multiple structures exist in the experimental spectra ranging from a binding energy of 5 to 12 eV. These multiplet structures are similar to the $4f$ PES spectra of ionic multiplet calculation [106] and other Yb compounds [107]. Our simulated polarization-dependent $4f$ PES spectra in the two emission directions assuming the crystal-field-split ground state determined by LDs in $Yb^{3+}$ $3d$ core-level PES spectra [14] are also shown in the figure, showing clear detectable LDs. The overall features of LDs in experimental spectra of $YbRh_2Si_2$ are qualitatively consistent with those of simulated spectra in all multiplet $4f$ peaks except for those of the peaks at the binding energy of 6.7 and 7.2 eV with $\theta = 0°$. On the other hand, whereas the experimental LDs are qualitatively consistent with the simulated ones for the peaks at 10.8 and 11.2 eV with $\theta = 0°$ and those at 6.7 and 7.4 eV with $\theta = 45°$, the signs of LDs for many $4f$ multiplet peaks are different between the experiments and simulations for $YbCu_2Si_2$. In addition, LDs in the $4f$ PES spectra of both $YbRh_2Si_2$ and $YbCu_2Si_2$ are much smaller than simulated ones and not quantitatively reproduced.

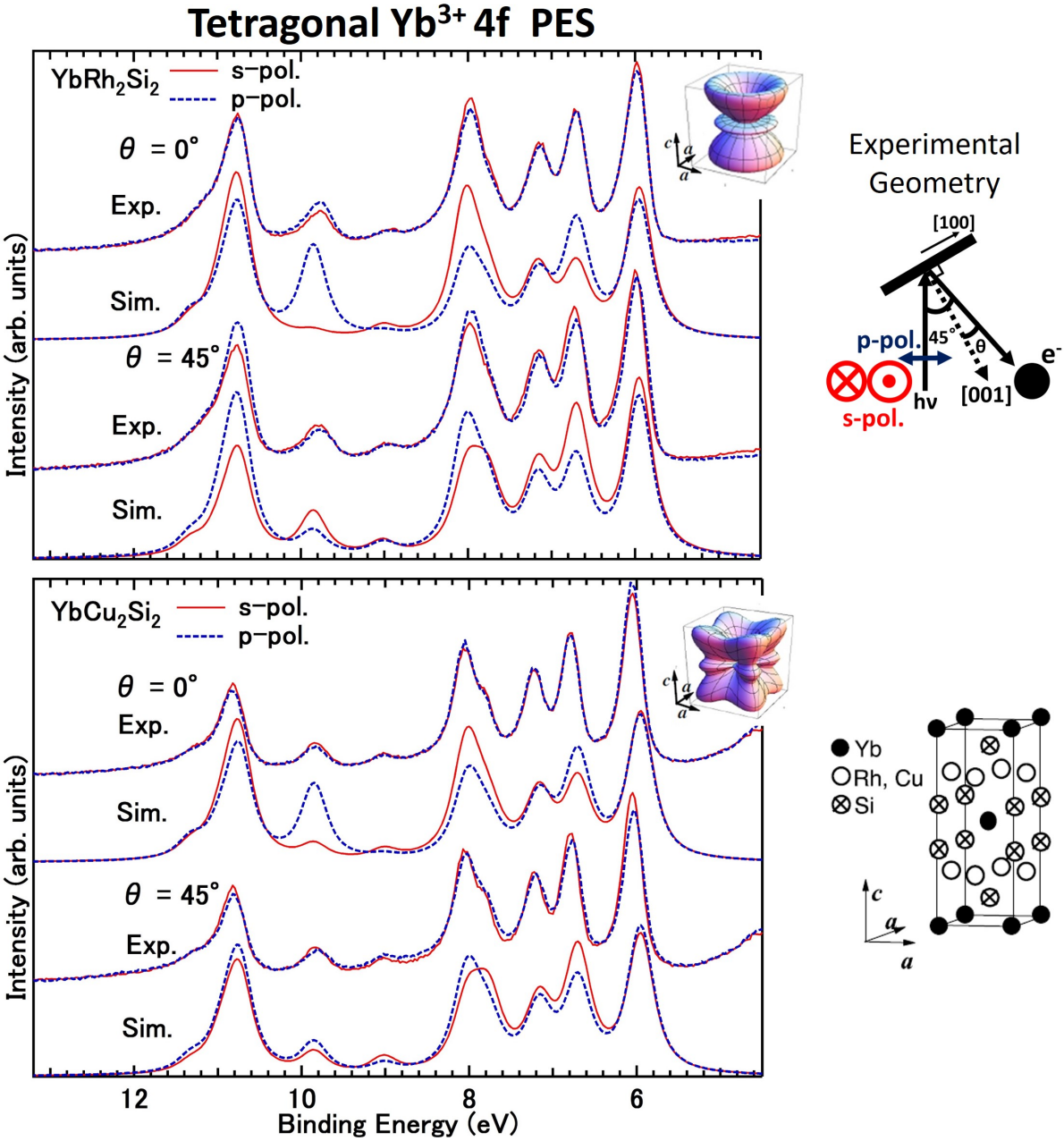


Figure 8.2: Experimental (Exp.) and simulated (Sim.) polarization-dependent $Yb^{3+}$ $4f$ valence-band photoemission spectra of tetragonal YbRh2Si2 YbCu2Si2, where the Shirley-type backgrounds have been subtracted from the raw spectra. Corresponding 4f charge distributions for tetragonal $YbRh_2Si_2$ and $YbCu_2Si_2$ determined by LDs in the $3d$ core-level PES spectra [14] are shown in the inset. Experimental geometry and $ThCr_2Si_2$-type tetragonal crystal structure of $YbRh_2Si_2$ and $YbCu_2Si_2$ are also shown.

### 8.2.3 Linear dichroism in $4f$ valence-band PES of cubic $YbIr_2Zn_{20}$

As mentioned in Chapter5, the $Yb^{3+}$ 4f levels are split into two doublets and a quartet by CEF as follows:

$$|\Gamma_6\rangle = \sqrt{5/12}|\pm 7/2\rangle + \sqrt{7/12}|\mp 1/2\rangle, \tag{8.5}$$

$$|\Gamma_7\rangle = -\sqrt{3}/2|\pm 5/2\rangle + 1/2|\mp 3/2\rangle, \tag{8.6}$$

$$|\Gamma_8\rangle = \begin{cases} -\sqrt{7/12}|\pm 7/2\rangle + \sqrt{5/12}|\mp 1/2\rangle \\ 1/2|\pm 5/2\rangle + \sqrt{3}/2|\mp 3/2\rangle \end{cases} .. \tag{8.7}$$

The polarization-dependent $Yb^{3+}$ $4f$ PES spectra of $YbIr_2Zn_{20}$ and simulated spectra along the [111] photoelectron direction for the CEF-split ground state in cubic symmetry are shown in Fig. 8.3. The multiple peaks in the higher binding energy side than 8.5 eV are overlapped with the strong Zn $3d$ contributions (not shown here). The simulated $4f$ photoemission spectra for the cubic symmetry predict much clear LD even for the $\Gamma_8$ state, for which the LD in the $3d_{5/2}$ core-level PES spectra is much smaller than those for the $\Gamma_6$ and $\Gamma_7$ states as explained by $YbB_{12}$ in Chapter5 [15]. This would be ascribed to the more anisotropic $4f$ charge distributions in the $4f$-photoemission final states with the $4f^{12}$ ($4f^2$ hole) configurations than that in the $\Gamma_8$ initial state with the $4f^1$ hole configuration. On the other hand, the experimental LD in $Yb^{3+}$ $4f$ spectra of cubic $YbIr_2Zn_{20}$ seems to be almost negligible, being inconsistent with the predictions for every ionic $4f$-initial state in cubic symmetry.

### 8.2.4 Linear dichroism in $4f$ valence-band PES of tetragonal $SmCu_2Si_2$

Fig. 8.4 displays the polarization-dependent valence-band PES spectra of $SmCu_2Si_2$. A prominent spectral weight is seen around 4 eV in both spectra, which is ascribed to the almost fully occupied Cu $3d$ bands. The $Sm^{3+}$ $4f$ multiplet structure appears in the binding energy ranging from 5 to 10 eV, which is similar to that for atomic multiplet calculation [106] and so far reported ones of other Sm compounds [109, 110]. Clear LD (or polarization dependence) is seen in the Cu $3d$ band spectral weight rather than the $Sm^{3+}$ $4f$ multiplet structure. For instance, the peak at 3.8 eV in the spectrum in the p-pol. is reduced and seen as a subtle shoulder in that in the s-pol. whereas another peak appears at 4.0 eV in the Cu $3d$ band region. On the other hand, in contrast to the $Sm^{3+}$ $3d_{5/2}$ core-level PES spectra, the LD in the $Sm^{3+}$ $4f$ PES spectra are almost negligible as well as that in $Yb^{3+}$ $4f$ PES spectra of $YbIr_2Zn_{20}$.

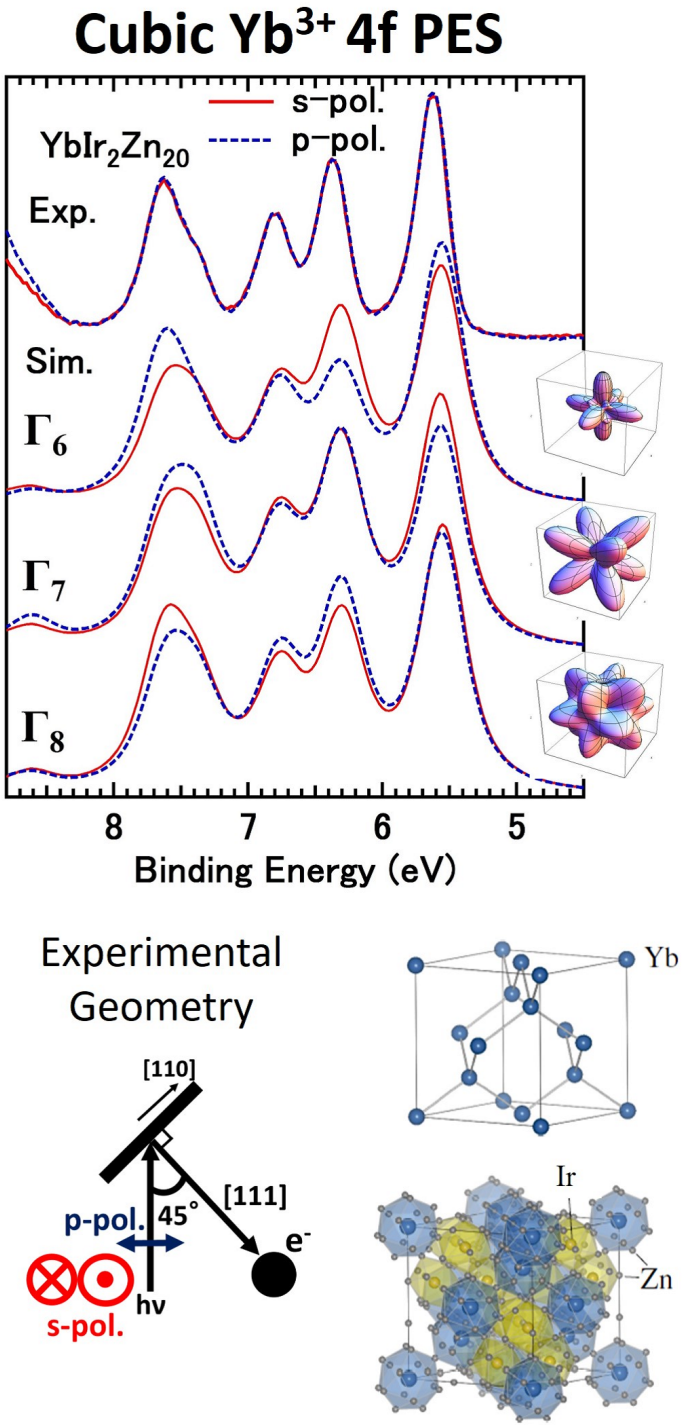


Figure 8.3: Experimental (Exp.) and simulated (Sim.) polarization-dependent $Yb^{3+}$ $4f$ valence-band photoemission spectra of cubic $YbIr_2Zn_{20}$, where the Shirley-type backgrounds have been subtracted from the raw spectra together with $4f$ charge distributions in cubic symmetry. Experimental geometryand $CeCr_2Al_{20}$-type cubic crystal structure of $YbIr_2Zn_{20}$ [108] are also shown.

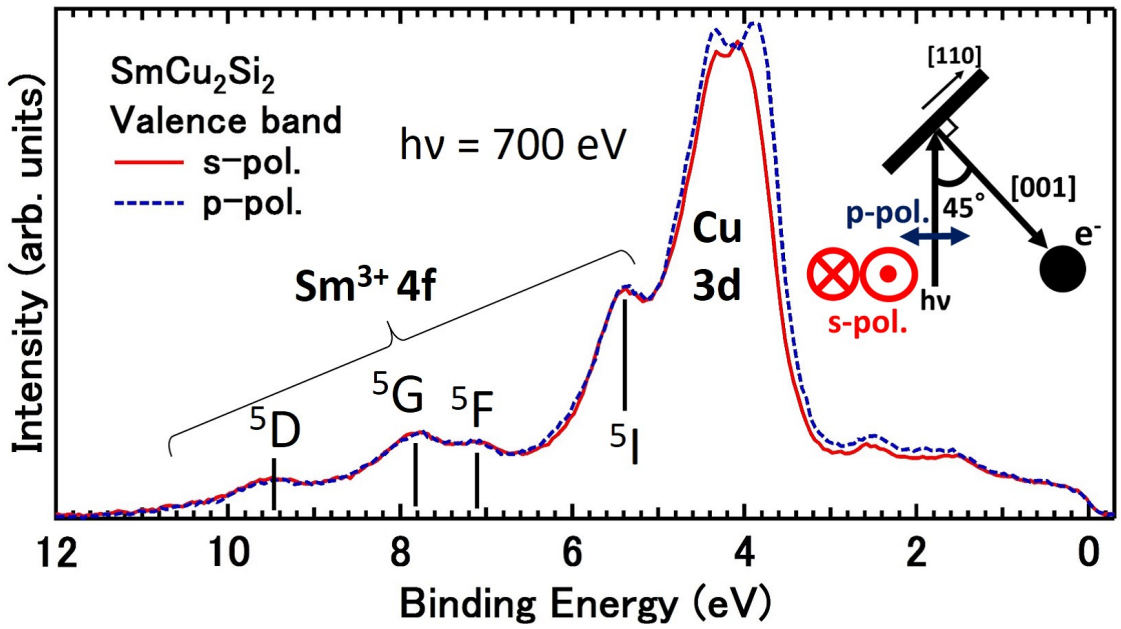


Figure 8.4: Valence-band photoemission spectra of $SmCu_2Si_2$ along the [001] direction. The Shirley-type backgrounds have been subtracted from all raw spectra. The valence-band spectra are normalized to the spectral weight in the binding energy from 5.1 to 12.0 eV in the $Sm^{3+}$ $4f$ region. The assigned $4f$ multiplets based on Ref. [106] are also shown.

### 8.2.5 Discussion

To summarize our results on polarization-dependent valence-band $4f$ PES, the observed LDs are not consistent with the predictions from the ionic model under CEF for the tetragonal and cubic Yb compounds. Furthermore, they are almost negligible for tetragonal $SmCu_2Si_2$ although the clear LD is seen in the $Sm^{3+}$ $3d$ core-level PES spectra as mentioned in Chapter7. Considering the fact that the polarization dependence is clearly observed in the Cu $3d$ valence-band region, we conclude that the suppressions of LDs in the $Sm^{3+}$ and $Yb^{3+}$ $4f$ spectral weight are not caused by extrinsic effects such as relatively high surface sensitivity at the soft x-ray excitation compared with the hard x-ray excitation. On the other hand, it has been well known that the linear polarization dependence of so-called ARPES (k-resolved angle-resolved photoemission) spectra reflects the symmetry of the occupied valence bands in a reciprocal space [111, 112] due to the inter-site hybridizations. Although the observed $Sm^{3+}$ and $Yb^{3+}$ $4f$ spectral line shapes have so far been qualitatively explained by the atomic-like multiplets, the LDs in the $4f$ spectra reflecting the information of the anisotropic $4f$ distributions in a real space would be more or less smeared out by the inter-site effects. In the $3d$ core-level PES final states, on the other hand, the outer trivalent rare-earth $4f$ states are spatially localized by the core-hole interactions $U_{fc} > U$ giving a highly reduced inter-site mixing, and further by the effective “shrink” of the $4f$ orbitals also due to the core-hole interactions leading to the so-called configuration dependence [113]. Therefore, the polarization-dependent core-level PES would be suitable for probing the anisotropic localized $4f$ charge distributions owing to the presence of $U_{fc}$ in the core-level excitations rather than the direct $4f$ PES.

# Chapter 9

# Conclusion

In the preceding chapters, we have discussed the $4f$-orbital symmetry of the strongly correlated rare-earth compounds based on the linear dichroism in core-level and valence-band photoemission, which has shown the power of linear dichroism in angle-resolved core-level photoemission spectroscopy for probing the orbital symmetry.
Firstly, we have successfully determined the $4f$ symmetry of the $Yb^{3+}$ sites in the CEF-split ground state for cubic $YbB_{12}$ as the $\Gamma_8$ symmetry by LD in the $Yb^{3+}$ $3d_{5/2}$ core-level HAXPES at BL19LXU in SPring-8 in two different photoelectron directions. Our result also suggests that the $Yb^{3+}$ ion model under the effective CEF, in which the hybridization effects are implicitly taken into account, is suitable even for the valence-fluctuating system at low temperatures well below the Kondo temperature. The applicability of LD in the core-level HAXPES even to the system in the cubic symmetry (not restricted to systems with lower symmetry) demonstrated here would be promising for revealing the strongly correlated orbital symmetry of the ground state in a partially filled subshell, the charge distribution of which deviates from the spherical symmetry.
Secondly, we have observed LDs which indicate $Ce^{3+}$ $4f$ ground-state symmetry, $\Gamma_7$ for $CeAl_2$ and $\Gamma_8$ for $CeB_6$ in Ce core-level HAXPES spectra. Effective linear dichroism in the $4d$ core-level photoemission with little contributions from $4f^2$ final-state configurations is also found to be useful for the determination of ground-state symmetry of localized cubic Ce system.
Thirdly, we perfectly determine the $Sm^{3+}$ $4f$ ground-state symmetry including the rotation around c-axis of tetragonal $SmCu_2Si_2$ as $|\Gamma_7^1\rangle = \sqrt{0.6}|\pm 5/2\rangle - \sqrt{0.4}|\mp 3/2\rangle$, of which the $4f$ charge distribution is closer to spherical shape than the previously revealed ones for the Ce and Yb systems.
For LD in $4f$ valence-band PES measurement, though the LDs in $4f$ photoemission spectra have also been expected to observe by the theoretical calculations for localized ions, the observed LDs in the $4f$ spectral weights in the valence bands are reduced or suppressed compared with the predicted ones. These phenomena indicate the polarization-dependent core-level PES would be suitable for probing the anisotropic localized $4f$ charge distributions owing to the presence of Coulomb interactions between $4f$ electrons and $d$ core holes in the core-level excitations rather than the direct $4f$ PES.
LD in rare-earth core-level photoemission study should be applicable for all rare-earth compounds and use for determination of $4f$ excited states, not only ground state. So that, we should perform experiment for temperature dependence of LD in the future. Indeed, we should try to verify the applicability of LD in core-level photoemission for the Sm com-

pounds with mixed valence system next time.

# Reference


[1] F. Steglich, J. Aarts, C. D. Bredl, W. Lieke, D. Meshede, W. Franz and H. Shaefer, Phys. Rev. Lek. **43**, 1892 (1979).

[2] S. Nakatsuji, K. Kuga, Y. Machida, T. Tayama, T. Sakakibara, Y. Karaki, H. Ishimoto, S. Yonezawa, Y. Maeno, E. Pearson, G. G. Lonzarich, L. Balicas, H. Lee, and Z. Fisk, Nat. Phys. **4**, 603 (2008).

[3] M. S. Torikachvili, S. Jia, E. D. Mun, S. T. Hannahs, R. C. Black,W. K. Neils, D. Martien, S. L. Bud ' ko, and P. C. Canfield, Proc. Natl. Acad. Sci. U.S.A. **104**, 9960 (2007).

[4] Y. Saiga, K. Matsubayashi, T. Fujiwara, M. Kosaka, S. Katano, M. Hedo, T. Matsumoto, and Y. Uwatoko, J. Phys. Soc. Jpn. **77**, 053710 (2008).

[5] M. Ohta, M. Matsushita, S. Yoshiuchi, T. Takeuchi, F. Honda, R. Settai, T. Tanaka, Y. Kubo, and Y. Onuki, J. Phys. Soc. Jpn. **79**, 083601 (2010).

[6] F. Iga, N. Shimizu, and T. Takabatake, J. Magn. Magn. Mater. **177-181**, 337 (1998).

[7] T. Susaki, Y. Takeda, M. Arita, K. Mamiya, A. Fujimori, K. Shimada, H. Namatame, M. Taniguchi, N. Shimizu, F. Iga, and T. Takabatake, Phys. Rev. Lett. **82**, 992 (1999).

[8] M. Dzero, K. Sun, V. Galitski, and P. Coleman, Phys. Rev. Lett. **104**, 106408 (2010).

[9] O. Trovarelli, C. Geibel, S. Mederle, C. Langhammer, F. M. Grosche, P. Gegenwart, M. Lang, S. Sparn, and F. Steglich, Phys. Rev. Lett. **85**, 626 (2000).

[10] T. Willers, B. Fåk, N. Hollmann, P. O. Körner, Z. Hu, A. Tanaka, D. Schmitz, M. Enderle, G. Lapertot, L. H. Tjeng, and A. Severing, Phys. Rev. B **80**, 115106 (2009).

[11] P. Hansmann, A. Severing, Z. Hu, M. W. Haverkort, C. F. Chang, S. Klein, A. Tanaka, H. H. Hsieh, H.-J. Lin, C. T. Chen, B. Fåk, P. Lejay, and L. H. Tjeng, Phys. Rev. Lett. **100**, 066405 (2008).

[12] T. Willers, Z. Hu, N. Hollmann, P. O. Körner, J. Gergner, T. Burnus, H. Fujiwara, A. Tanaka, D. Schmitz, H. H. Hieh, H.-J. Lin, C. T. Chen, E. D. Bauer, J. L. Sarro, E. Goremychkin, M. Koza, L. H. Tjeng, and A. Severing, Phys. Rev. B **81**, 195114 (2010).

[13] T. Willers, D. T. Adroja, B. D. Rainford, Z. Hu, N. Hollmann, P. O. Körner, Y.-Y. Chin, D. Schmitz, H. H. Hieh, H.-J. Lin, C. T. Chen, E. D. Bauer, J. L. Sarro, K. J. McClellan, D. Byler, C. Geibel, F. Steglich, H. Aoki, P. Lejay, A. Tanaka, L. H. Tjeng, and A. Severing, Phys. Rev. B **85**, 035117 (2012).

[14] T. Mori, S. Kitayama, Y. Kanai, S. Naimen, H. Fujiwara, A. Higashiya, K. Tamasaku, A. Tanaka, K. Terashima, S. Imada, A. Yasui, Y. Saitoh, K. Yamagami, K. Yano, T. Matsumoto, T. Kiss, M. Yabashi, T. Ishikawa, S. Suga, Y. Ōnuki, T. Ebihara, and A. Sekiyama, J. Phys. Soc. Jpn. **83**, 123702 (2014).

[15] Y. Kanai, T. Mori, S. Naimen, K. Yamagami, H. Fujiwara, A. Higashiya, T. Kadono, S. Imada, T. Kiss, A. Tanaka, K. Tamasaku, M. Yabashi, T. Ishikawa, F. Iga, and A. Sekiyama, J. Phys. Soc. Jpn. **84**, 073705 (2015).

[16] S. Hamamoto, S. Fujioka, Y. Kanai, K. Yamagami, T. Nakatani, K. Nakagawa, H. Fujiwara, T. Kiss, A. Higashiya, A. Yamasaki, T. Kadono, S. Imada, A. Tanaka, K. Tamasaku, M. Yabashi, T. Ishikawa, K. T. Matsumoto, T. Onimaru, T. Takabatake, and A. Sekiyama, J. Phys. Soc. Jpn. **86**, 123703 (2017).

[17] H. Aratani, Y. Nakatani, H. Fujiwara, M. Kawada, Y. Kanai, K. Yamagami, S. Fujioka, S. Hamamoto, K. Kuga, T. Kiss, A. Yamasaki, A. Higashiya, T. Kadono, S. Imada, A. Tanaka, K. Tamasaku, M. Yabashi, T. Ishikawa, A. Yasui, Y. Saitoh, Y. Narumi, K. Kindo, T. Ebihara, and A. Sekiyama, Phys. Rev. B **98**, 121113(R) (2018).

[18] B. T. Thole, G. van der Laan, J. C. Fuggle, G. A. Sawatzky, R. C. Karnatak, and J.-M. Esteva, Phys. Rev. B **32**, 5107 (1985).

[19] A. Tanaka, and T. Jo, J. Phys. Soc. Jpn. **63**, 2788 (1994).

[20] Y. Kanai, T. Mori, S. Naimen, K. Yamagami, S. Kitayama, H. Fujiwara, A. Higashiya, T. Kadono, S. Imada, T. Kiss, A. Tanaka, T. Muro, K. Tamasaku, M. Yabashi, T. Ishikawa, F. Iga, T. Ebihara, F. Honda, Y. Onuki, and A. Sekiyama, J. Electron Spectrosc. Relat. Phenom. **220**, 61 (2017).

[21] D. Liberman, J. T. Waber, and Don T. Cromer, Phys. Rev. **137**, A27 (1965).

[22] K. W. H. Stevens, Proc. Phys. Soc. (London) A**65**, 209 (1951).

[23] K. R. Lea, M. J. M. Leask, and W. P. Wolf, J. Phys. Chem. Solids **23**, 1381 (1962).

[24] N. Sato and K. Miyake, "Heavy Fermion Physics : Magnetism and Superconductivity (in Japanese)" The University of Nagoya Press (2013).

[25] R. D. Cowan, Phys. Rev. **163**, 54(1967).

[26] K. Yoshida"Magnetism (in Japanese)" Iwanami Shoten, Publishers (1998).

[27] Michl Loewenhaupt Peter Felde. Magnetic excitations in crystal-field split 4f systems. Advances in Physics, **34**, 589 (1985).

[28] T. Willers, F. Strigari, N. Hiraoka, Y. Q. Cai, M. W. Haverkort, K. D. Tsuei, Y. F. Liao, S. Seiro, C. Geibel, F. Steglich, L. H. Tjeng, and A. Severring, Phys. Rev.Lett. **109**, 046401 (2012).

[29] T. Willers, J. C. Cezar, N. B. Brookes, Z. Hu, F. Strigari, P. Ḱorner, N. Hollmann, D. Schmitz, A. Bianchi, Phys. Rev. Lett. **107**, 236402 (2011). Z. Fisk,6 A. Tanaka,7 L. H. Tjeng,3 and A. Severing1

[30] The Surface Science Society of Japan "X-ray Photoemission Spectroscopy (in Japanese)" Maruzen Publishing (1998).

[31] S. Suga, "Spectroscopy (in Japanese)" Maruzen Publishing (1999).

[32] S. H*ü*fner, "Photoelectron Spectroscopy -3rd edition" Springer-Verlag Berlin (2003).

[33] A. Damascelli, Z. Hussain and Z. -X. Shen, Rev. Mod. Phys. **75**, 473 (2003).

[34] A. Fujimori, "Basic of Strongly Correlated Solids (in Japanese)" Uchida Rokakuho

[35] C. N. Yang, Phys. Rev. **74**, 764 (1948).

[36] J. W. Cooper, Phys. Rev. A **42**, 11 (1990).

[37] M. B. Trzhaskovskaya, V. K. Nikulin, V. I. Nefedov, and V. G. Yarzhemsky, At. Data Nucl. Data Table **92**, 245 (2006).

[38] J. J. Yeh, and I. Lindau, At. Data Nucl. Data Table **32**, 1(1985).

[39] O. Gunnarsson and K. Sch*ö*nhammer, Phys. Rev. B 28, 4315 (1983); O. Gunnarsson and K. Sch*ö*nhammer, Phys. Rev. B **31**, 4815 (1985).

[40] T. Jo and A. Kotani, J. Phys. Soc. Jpn. **55**, 2457 (1986).

[41] 35) S. Imada and T. Jo, J. Phys. Soc. Jpn. 58, 402 (1989); S. Imada and T. Jo, J. Phys. Soc. Jpn. **58**, 2665 (1989).

[42] J. W. Gadzuk, Phys. Rev. B **12**, 5608 (1975).

[43] S. M. Goldberg, C. S. Fadley, and S. Kono, J. Electron Spectrosc. Relat. Phenom. **21**, 285 (1981).

[44] H. Daimon, S. Imada, H. Nishimoto, and S. Suga, J. Electron Spectrosc. Relat. Phenom. **76**, 487 (1995).

[45] H. Nishimoto, T. Nakatani, T. Matsushita, S. Imada, H. Daimon, and S. Suga, J. Phys.: Condens. Matter **8**, 2715 (1996).

[46] S. Tanuma, C. J. Powell and D. R. Penn, Surf. and Interface Anal. **43**, 689 (2011).

[47] H. Yoshikawa and T. Shimizu, J. Vac. Sot. Jpn. **37**, 396 (1994).

[48] A. Jablonski, Surf. and Interface Anal. **23**, 29 (1995).

[49] Y. F. Chen, Surf. Sci. **380**, 199 (1997).

[50] "Introduction of Optics Technique for Synchrotron Radiation Beamline (in Japanese)" The Japanese Society for Synchrotron Radiation Research (2008).

[51] M. Yabashi, T. Mochizuki, H. Yamazaki, S. Goto, H. Ohashi, K. Takeshita, T. Ohata, T. Matsushita, K. Tamasaku, Y. Tanaka, T. Ishikawa, Nucl. Instrm. Methods Phys. Res. A **467-468**, 678 (2001).

[52] H. Kitamura, T. Bizen, T. Hara, X.Maréchal, T. Seike, T. Tanaka, Nucl. Instrm. Methods Phys. Res. A **467-468**, 110 (2001).

[53] S. Takahashi, H. Aoyagi, T. Mochizuki, M. Oura, Y. Sakurai, A. Watanabe, H. Kitamura, Nucl. Instrm. Methods Phys. Res. A **467-468**, 758 (2001).

[54] C. E. Kuyatt and J. A. Simpson, Rev. Sci. Instr. **38**, 103 (1967).

[55] H. Fujiwara, S. Naimen, A. Higashiya, Y. Kanai, H. Yomosa, K. Yamagami, T. Kiss, T. Kadono, S. Imada, A. Yamasaki, K. Takase, S. Otsuka, T. Shimizu, S. Shingubara, S. Suga, M. Yabashi, K. Tamasaku, T. Ishikawa, and A. Sekiyama, J. Synchrotron Rad. **23**, 735 (2016).

[56] A.Sekiyama, J. Yamaguchi, A. Higashiya, M. Obara, H. Sugiyama, M. Y. Kimura, S. Suga, S. Imada, I. A. Nekrasov, M. Yabashi, K. Tamasaku and T. Ishikawa, New J. Phys. **12**, 043045 (2010).

[57] A. Sekiyama, A. Higashiya, S. Imada, J. Electron Spectrosc. Relat. Phenom. **190**, 201 (2013).

[58] A. Akabari and P. Thalmeier, J. Korean Phys. Soc. **62**, 1418 (2012).

[59] J. Yamaguchi, A. Sekiyama, S. Imada, H. Fujiwara, M. Yano, T. Miyamachi, G. Funabashi, M. Obara, A. Higashiya, K. Tamasaku, M. Yabashi, T. Ishikawa, F. Iga, T. Takabatake, and S. Suga, Phys. Rev. B **79**, 125121 (2009).

[60] A. Czopnik, N. Shitsevalova, V. Pluzhnikov, A. Krivchikov, Yu Paderno and Y. Onuki, J.Phys.:Condens. Matter **17**, 5971 (2005).

[61] T. Takabatake, F. Iga, T. Yoshino, Y. Echizen, K. Katoh, K. Kobayashi, M. Higa, N. Shimizu, Y. Bando, G. Nakamoto, H. Fujii, K. Izawa, T. Suzuki, T. Fujita, M. Sera, M. Hiroi, K. Maezawa, S. Mock, H. v. Löhneysen, A. Briickl, K. Neumaier, K. Andres, J. Magn. Magn. Matter **177-181**, 277 (1998).

[62] M. Kasaya, F. Iga, K. Negishi, S. Nakai, and T. Kasuya, J. Magn. Magn. Mater. **31-34**, 437 (1983).

[63] M. Kasaya, F. Iga, M. Takigawa, and T. Kasuya, J. Magn. Magn. Mater. **47-48**, 429 (1985).

[64] F. Iga, N. Shimizu, and T. Takabatake, J. Magn. Magn. Mater. **177-181**, 337 (1998).

[65] T. Susaki, Y. Takeda, M. Arita, K. Mamiya, A. Fujimori, K. Shimada, H. Namatame, M. Taniguchi, N. Shimizu, F. Iga, and T. Takabatake, Phys. Rev. Lett. **82**, 992 (1999).

[66] T. Saso and H. Harima, J. Phys. Soc. Jpn. **72**, 1131 (2003).

[67] H. Weng, J. Zhao, Z. Wang, Z. Fang, and X. Dai, Phys. Rev. Lett. **112**, 016403 (2014).

[68] M. Dzero, K. Sun, V. Galitski, and P. Coleman, Phys. Rev. Lett. **104**, 106408 (2010).

[69] T. Takimoto, J. Phys. Soc. Jpn. **80**, 123710 (2011).

[70] S. Suga, K. Sakamoto, T. Okuda, K. Miyamoto, K. Kuroda, A. Sekiyama, J. Yamaguchi, H. Fujiwara, A. Irizawa, T. Ito, S. Kimura, T. Balashov, W. Wulfhekel, S. Yeo, F. Iga, and S. Imada, J. Phys. Soc. Jpn. **83**, 014705 (2014).

[71] K. A. Kikoin and A. S. Mishchenko, J. Phys.: Condens. Matter **7**, 307 (1995).

[72] P. S. Riseborough, Phys. Rev. B **68**, 235213 (2003).

[73] J. C. Cooley, M. C. Aronson, Z. Fisk, and P. C. Canfield, Phys. Rev. Lett. **74**, 1629 (1995).

[74] V. N. Antonov, B. N. Harmon, and A. N. Yaresko, Phys. Rev. B **66**, 165209 (2002).

[75] P. Thunström, I. Di Marco, A. Grechnev, S. Lebègue, M. I. Katsnelson, A. Svane, and O. Eriksson, Phys. Rev. B **79**, 165104 (2009).

[76] J. Yamaguchi, A. Sekiyama, M. Y. Kimura, H. Sugiyama, Y. Tomida, G. Funabashi, S. Komori, T. Balashov, W. Wulfhekel, T. Ito, S. Kimura, A. Higashiya, K. Tamasaku, M. Yabashi, T. Ishikawa, S. Yeo, S.-I. Lee, F. Iga, T. Takabatake, and S. Suga, New J. Phys. **15**, 043042 (2013).

[77] K. S. Nemkovski, J. -M. Mignot, P. A. Ivanov, E. V. Nefeodova, A. V. Rybina, L. -P. Regnault, F. Iga, and T. Takabatake, Phys. Rev. Lett. **99**, 137204 (2007).

[78] F. Iga, N. Simizu, T. Takabatake, J. Magn. Magn. Mater. **177-181**, 337 (1998).

[79] R. Lässer, J. C. Fuggle, M. Beyss, M. Campagna, F. Steglich and F. Hulliger, Physica B **102**, 360 (1980).

[80] S. Suga, S. Imada, H. Yamada, Y. Saitoh, T. Nanba and S. Kunii, Phys. Rev. B **52**, 1584 (1995).

[81] P. P. Blum, and F. Bertaut, Acta Cryst. **7**, 81 (1954).

[82] T. Fujita, M. Suzuki, T. Komatsubara, S. Kunii, T. Kasuya and T. Ohtsuka, Solid State Commun. **35**, 569 (1980).

[83] M. Kawakami, S. Kunii, T. Komatsubara and T. Kasuya, Solid State Commun. **36**, 435 (1980).

[84] T. Goto, A. Tamaki, S. Kunii, T. Nakajima, T. Fujimura, T. Kasuya, T. Komatsubara and S. B. Woods, J. Magn. Magn. Matter. **31-34**, 419 (1983).

[85] T. Onimaru, "Crystalline-Electric-Field and Freedom Degree of Multipole from Macro Measurement (in Japanese)" Bussei Kenkyu **97(4)**, 764 (2012).

[86] E. Zirngiebl, B. Hillebrands, S. Blumenröder, G. Güntherodt, M. Loewenhaupt, J. M. Carpenter, K. Winzer, Z. Fisk, Phys. Rev. B **30**, 4052 (1984).

[87] S. Nakamura, T. Goto, S. Kunii, K. Iwashita, and A. Tamaki, J. Phys. Soc. Jpn. **63**, 623 (1994).

[88] K. Hanzawa and T. Kasuya, J. Phys. Soc. Jpn. **53**, 1809 (1984).

[89] B. Barbara, M. F. Rossignol, J. X. Boucherle, J. Schweizer, and J. L. Buevoz, J. Appl. Phys. **50**, 2300 (1979).

[90] C.D. Bredl, F. Steglich and K.D. Schotte, Z. Phys. **B29**, 327 (1978).

[91] B. Barbara, M. F. Rossignol, H. G. Purwins and E. Walker, Solid State Commun. **17**, 1525 (1975).

[92] P. Thalmeier and P. Fulde, Phys. Rev. Lett. **49**, 1588 (1982).

[93] P. Thalmeier, J. Phys. C: Solid State Phys. **17**, 4153 (1984).

[94] M. Loewenhaupt and F. Steglich, Physica B **86-88**, 187 (1977).

[95] M. Loewenhaupt and U. Witte, J. Phys. Condens. Matter **15**, S519 (2003).

[96] A. Sekiyama, Y. Fujita, M. Tsunekawa, S. Kasai, A. Shigemoto, S. Imada, D. T. Adroja, T. Yoshino, F. Iga, T. Takabatake, T. Nanba and S. Suga, J. Electron Spectrosc. Relat. Phenom. **144-147**, 655 (2005).

[97] T. Matsumura, T. Yonemura, K. Kunimori, M. Sera, F. Iga, T. Nagao, and J. Igarashi, Phys. Rev. B **85**, 174417 (2012).

[98] M. Campagna, G. K. Wertheim and Y. Baer, in *Photoemission in Solides II*, edited by L. Ley and M. Cardona (Springer-Verlag, Berlin, 1979), p.217.

[99] A. Kakizaki, A. Hirasawa, T. Ishii, T. Kashiwakura, A. Kamata and S. Kunii, J. Phys. Soc. Jpn. **64**, 302 (1995).

[100] W. T. Carnall, P. R. Fields, and K. Rajnak, J. Chem. Phys. **49**, 4424 (1968).

[101] N. D. Dung, Y. Ota, K. Sugiyama, T. D. Matsuda, Y. Haga, K. Kindo, M. Hagiwara, T. Takeuchi, R. Settai, and Y. Onuki, J. Phys. Soc. Jpn. **78**, 024712 (2009).

[102] Y. Takeda, N. D. Dung, Y. Nakano, T. Ishikawa, S. Ikeda, T. D. Matsuda, E. Yamamoto, Y. Haga, T. Takeuchi, R. Settai and Y. Onuki, J. Phys. Soc. Jpn.**77**, 104710 (2008).

[103] T. Tanaka, T. Hara, M. Oura, H. Ohashi, H. Kimura, S. Goto, Y. Suzuki and H. Kitamura, Rev. Sci. Instrum. **70**, 4153 (1999).

[104] O. Trovarelli, C. Geibel, S. Mederle, C. Langhammer, F. M. Grosche, P. Gegenwart, M. Lang, S. Sparn, and F. Steglich, Phys. Rev. Lett. **85**, 626 (2000).

[105] N. D. Dung, T. D. Matsuda, Y. Haga, S. Ikeda, E. Yamamoto, T. Ishikura, T. Endo, S. Tatsuoka, Y. Aoki, H. Sato, T. Takeuchi, R. Settai, H. Harima, and Y. Onuki, J. Phys. Soc. Jpn. **78**, 084711 (2009).

[106] F. Gerken, J. Phys. F: Met. Phys. **13**, 703 (1983).

[107] S. Suga, A. Sekiyama, S. Imada, A. Shigemoto, A. Yamasaki, M. Tsunekawa, C. Dallera, L. Braicovich, T. âĂŞL. Lee, O. Sakai, T. Ebihara, and Y. Onuki, J. Phys. Soc. Jpn. **74**, 2880 (2005).

[108] T. Takeuchi, S. Yasui, M. Toda, M. Matsushita, S. Yoshiuchi, M. Ohya, K. Katayama, Y. Hirose, N. Yoshitani, F. Honda, K. Sugiyama, M. Hagiwara, K. Kindo, E. Yamamoto, Y. Haga, T. Tanaka, Y. Kubo, R. Settai, and Y. Ōnuki, J. Phys. Soc. Jpn. **79**, 064609 (2010).

[109] A. Yamasaki, A. Sekiyama, S. Imada, M. Tsunekawa, C. Dallera, L. Braicovich, T. -L. Lee, A. Ochiai and S. Suga, J. Phys. Soc. Jpn. **74**, 2538 (2005).

[110] A. Yamasaki, S. Imada, H. Higashimichi, H. Fujiwara, T. Saita, T. Miyamachi, A. Sekiyama, H. Sugawara, D. Kikuchi, H. Sato, A. Higashiya, M. Yabashi, K. Tamasaku, D. Miwa, T. Ishikawa, and S. Suga, Phys. Rev. Lett. **98**, 156402 (2007).

[111] H. Iwasawa, Y. Yoshida, I. Hase, S. Koikegami, H. Hayashi, J. Jiang, K. Shimada, H. Namatame, M. Taniguchi and Y. Aiura, Phys. Rev. Lett. **105**, 226406 (2010).

[112] D. V. Vyalikh, S. Danzenbächer, Yu. Kucherenko, K. Kummer, C. Krellner, C. Geibel, M. G. Holder, T. K. Kim, C. Laubchat, M. Shi, L. Patthey, R. Follath and S. L. Molodsov, Phys. Rev. Lett. **105**, 237601 (2010).

[113] O. Gunnarsson and O. Jepsen, Phys. Rev. B **38** 3568 (1988).

# Acknowledgements

I would like to thank Professor Akira Sekiyama who is my supervisor for a lot of helpful suggestions, comments and advice all the time. He has always kindly encouraged me in all things.
I thank the members and grads of Sekiyama group. Professor Takayuki Kiss gave me valuable advice. Assistant Professor Hidenori Fujiwara supported my research empathetically. I thank Dr. Kohei Yamagami, Dr. Yasuhiro Nakatani, Mr. Takeo Mori, Mr. Satoru Hamamoto, Mr. Shuhei Fujioka, Ms. Sayaka Takano, Mr. Moeki Kawada, Mr. Toshiyuki Kashiuchi, Mr. Sho Naimen, Mr. Hiroshi Yomosa, Mr. Yuki Nakata, Mr. Shoichi Tachibana, Mr. Hidekazu Aratani, Mr. Kodai Nagai, Mr. Tatsuhiro Hattori, Mr. Yuichi Aoyama, Mr. Tomohiro Yagi, Mr. Kohei Yano for support and encouragement. Among them, I am grateful to Mr. Satoru Hamamoto and Mr. Shuhei Fujioka for powerful support in the experiment. I am also grateful Ms. Tomoko Imada for support in academic life.
I was supported in experiment at BL19LXU in SPring-8. I thank Professor Shin Imada, Assistant Professor Toshiharu Kadono (Department of Physical Science, Ritsumeikan University), Professor Atsushi Higashiya (Faculty of Science and Engineering, Setsunan University), Professor Atsushi Yamasaki (Faculty of Science and Engineering, Konan university), Dr. Kenji Tamasaku, Dr. Kentaro Kuga (RIKEN SPring-8 Center), and the students of Imada group and Yamasaki group.
I am grateful to Professor Arata Tanaka (Department of Quantum Matter, ADSM, Hiroshima University) for the simulations using the XTLS 9.0 program.
I also thank Dr. Takayuki Muro (JASRI) for support in experiment at BL27SU in SPring-8.
I am grateful to Professor Fumitoshi Iga(College of Science, Ibaraki University), Professor Rikio Settai, Assistant Professor Yusuke Hirose (Department of Physics, Niigata University), Professor Fuminori Honda (Institute for Materials Research, Tohoku University), Professor Takao Ebihara (Department of Physics, Shizuoka University), Visiting Professor Yoshitika Onuki (Faculty of Science, University of the Ryukyus) for providing the excellent single-crystalline samples.
The experiments shown in Chapters 4, 5, 6 and 7 at BL19LXU in SPring-8 were performed under the approval of RIKEN (Proposal Nos. 20130061, 20140038, 20150043, 20160034, 20170043, and 20180026) and that of JASRI (Proposal Nos. 2014A1149, 2014B1305, and 2015A1533). The polarization-dependent soft x-ray photoemission in Chapter 8 at BL27SU in SPring-8 was carried out under the approval of JASRI (Proposal Nos. 2014A1023 and 2014B1299). This work was also supported by a Grant-in-Aid for Scientific Research (JP16H04014) and that on Innovative Area “J-Physics” (JP16H01074 and JP18H04317) from JSPS and MEXT, Japan.
I was supported by the JSPS Research Fellowships for Young Scientists (16J05334).
Finally, I thank my family.

# Achievement List

## Publications

### Main Papers

- “Evidence for $\Gamma_8$ Ground-State Symmetry of Cubic $YbB_{12}$ Probed by Linear Dichroism in Core-Level Photoemission”
  **Yuina Kanai**, T. Mori, S. Naimen, K. Yamagami, H. Fujiwara, A. Higashiya, T. Kadono, S. Imada, T. Kiss, A. Tanaka, K. Tamasaku, M. Yabashi, T. Ishikawa, F. Iga, and A. Sekiyama
  J. Phys. Soc. Jpn. **84**, 073705 (2015).

- “Linear dichroism in 3d core-level and 4f valence-band photoemission spectra of strongly correlated rare-earth compounds”
  **Y. Kanai**, T. Mori, S. Naimen, K. Yamagami, S. Kitayama, H. Fujiwara, A. Higashiya, T. Kadono, S. Imada, T. Kiss, A. Tanaka, T. Muro, K. Tamasaku, M. Yabashi, T. Ishikawa, F. Iga, T. Ebihara, F. Honda, Y. Onuki, and A. Sekiyama
  J. Electron Spectrosc. Relat. Phenom. **220**, 61 (2017).

- “Spectroscopic observations of crystal-field-split ground-state symmetry in cubic Ce compounds”
  **Y. Kanai**, K. Yamagami, S. Fujioka, H. Fujiwara, A. Higashiya, T. Kadono, S. Imada, T. Kiss, A. Tanaka, K. Tamasaku, M. Yabashi, T. Ishikawa, F. Iga, T. Ebihara and A. Sekiyama
  in preparation

- “Probing Strongly Correlated 4f Ground-State Symmetry of Tetragonal $SmCu_2Si_2$ by Linear Dichroism in Angle-Resolved Core-Level Photoemission”
  **Y. Kanai**, S. Hamamoto, K. Yamagami,S. Naimen, S. Fujioka, H. Fujiwara, K. Kuga, A. Higashiya, T. Kadono, S. Imada, T. Kiss, A. Tanaka, K. Tamasaku, M. Yabashi, T. Ishikawa, T. Yamaguchi, H. Kobayashi, Y. Onuki and A. Sekiyama
  in preparation

### Collaborating Papers

- “Probing Strongly Correlated $4f$-Orbital Symmetry of the Ground State in Yb Compounds by Linear Dichroism in Core-Level Photoemission”

T. Mori, S. Kitayama, **Y. Kanai**, S. Naimen, H. Fujiwara, A. Higashiya, K. Tamasaku, A. Tanaka, K. Terashima, S. Imada, A. Yasui, Y. Saitoh, K. Yamagami, K. Yano, T. Matsumoto, T. Kiss, M. Yabashi, T. Ishikawa, S. Suga, Y. Onuki, T. Ebihara, and A. Sekiyama
J. Phys. Soc. Jpn. **83**, 123702 (2014).

- "Polarized Hard X-ray Photoemission System with Micro-positioning Technique for Probing Ground State Symmetry of Strongly Correlated Materials"
H. Fujiwara, S. Naimen, A. Higashiya, **Y. Kanai**, H. Yomosa, K. Yamagami, T. Kiss, T. Kadono, S. Imada, A. Yamasaki, K. Takase, S. Otsuka, T. Shimizu, S. Shingubara, S. Suga, M. Yabashi, K. Tamasaku, T. Ishikawa, and A. Sekiyama
J. Synchrotron Rad. **23**, 735 (2016).

- "Hole doping effect on the electronic structure of layered oxypnictide LaOMnAs"
A. Higashiya, K. Nakagawa, A. Yamasaki, K. Nagai, S. Fujioka, **Y. Kanai**, K. Yamagami, H. Fujiwara, A. Sekiyama, Amina Abozeed, T. Kadono, S. Imada, K. Kuga, M. Yabashi, K. Tamasaku, T. Ishikawa, S. Toyama, and K. Takase
J. Electron Spectrosc. Relat. Phenom. **220**, 58 (2017).

- "Linear Dichroism in angle-resolved core-level photoemission spectra reflecting 4f ground-state symmetry of strongly correlated cubic Pr compounds"
S. Hamamoto, S. Fujioka, **Y. Kanai**, K. Yamagami, Y. Nakatani, K. Nakagawa, H. Fujiwara, T. Kiss, A. Higashiya, A. Yamasaki, T. Kadono, S. Imada, A. Tanaka, K. Tamasaku, M. Yabashi, T. Ishikawa, K. T. Matsumoto, T. Onimaru, T. Takabatake, and A. Sekiyama
J. Phys. Soc. Jpn. **86**, 123703 (2017).

- "Rare-earth Fourth Order Multipole Moment in Cubic ErCo2 Probed by Linear Dichroism in Core-Level Photoemission"
A. A. Abozeed, T. Kadono, A. Sekiyama, H. Fujiwara, A. Higashiya, A. Yamasaki, **Y. Kanai**, K. Yamagami, K. Tamasaku, M. Yabashi, T. Ishikawa, A. V. Andreev, H. Wada, and S. Imada
J. Phys. Soc. Jpn. **87**, 033710 (2018).

- "Polarization-dependent X-ray photoemission spectroscopy for High-Tc cuprate superconductors"
K. Yamagami, **Y. Kanai**, S. Naimen, H. Fujiwara, T. Kiss, A. Tanaka, A. Higashiya, S. Imada, T. Kadono, K. Tamasaku, T. Muro, M. Yabashi, T. Ishikawa, H. Eisaki, S. Miyasaka, S. Tajima, and A. Sekiyama
Physica B **536**, 843 (2018).

- "Revising the 4f symmetry in CeCu2Ge2: Soft x-ray absorption and hard x-ray photoemission spectroscopy"

H. Aratani, Y. Nakatani, H. Fujiwara, M. Kawada, **Y. Kanai**, K. Yamagami, S. Fujioka, S. Hamamoto, K. Kuga, T. Kiss, A. Yamasaki, A. Higashiya, T. Kadono, S. Imada, A. Tanaka, K. Tamasaku, M. Yabashi, T. Ishikawa, A. Yasui, Y. Saitoh, Y. Narumi, K. Kindo, T. Ebihara, and A. Sekiyama
Phys. Rev. B **98**, 121113 (2018).

- “Optical Process of Linear Dichroism in Angle-Resolved Core-Level Photoemission Reflecting Strongly Correlated Anisotropic Orbital Symmetry”
A. Sekiyama, **Y. Kanai**, A. Tanaka, and S. Imada
J. Phys. Soc. Jpn. **88**, 013706 (2019).

## Review

- “Strongly Correlated Ground-State Orbital Symmetry of Tetragonal and Cubic Yb Compounds Probed by Linear Dichroism in Angle-Resolved Core-Level Photoemission”
A. Sekiyama, **Y. Kanai**, and S. Imada
SPring-8 Research Frontiers 2015

## International conference

- “Linear Dichroism in 3d core-level and 4f valence-band photoemission spectra of strongly correlated rare-earth compounds”
**Y. Kanai**, T. Mori, S. Naimen, K. Yamagami, S. Kitayama, H. Fujiwara, A. Higashiya, T. Kadono, S. Imada, T. Kiss, A. Tanaka, T. Muro, K. Tamasaku, M. Yabashi, T. Ishikawa, F. Iga, T. Ebihara, F. Honda, Y. Onuki, and A. Sekiyama
39th International Conference on Vacuum Ultraviolet and X-ray Physics, P-273, ETH Zurich, Switzerland, 3-8 July 2016.

- “Spectroscopic observation of crystal-field-split ground-state symmetry in cubic Ce compounds by high-energy photoemission”
**Y. Kanai**, K. Yamagami, S. Fujioka, H. Fujiwara, A. Higashiya, T. Kadono, S. Imada, T. Kiss, A. Tanaka, K. Tamasaku, M. Yabashi, T. Ishikawa, F. Iga, T. Ebihara, and A. Sekiyama
International Conference on Strongly Correlated Electron Systems 2017, Th-2-13, the Clarion Congress Hotel Prague, Czech, 17-21 July 2016.

- “Observation of the linear dichroism in core-level photoemission reflecting 4f ground-state symmetry of strongly correlated cubic Ce compounds”
**Y. Kanai**, K. Yamagami, S. Fujioka, H. Fujiwara, A. Higashiya, T. Kadono, S. Imada, T. Kiss, A. Tanaka, K. Tamasaku, M. Yabashi, T. Ishikawa, F. Iga, T. Ebihara, and A. Sekiyama

J-Physics 2017 : International Workshop on Multipole Physics and Related Phenomena, P-51, Hachimantai Royal Hotel, Japan, 24-28 September 2017.

- “Ground-state 4f orbital symmetry probed by linear dichroism in x-ray core-level photoemission/absorption spectra of strongly correlated Sm compounds”
  **Y. Kanai**, S. Hamamoto, K. Yamagami, S. Naimen, S. Fujioka, H. Fujiwara, K. Kuga, A. Higashiya, T. Kadono, S. Imada, T. Kiss, A. Tanaka, T. Muro, K. Tamasaku, M. Yabashi, T. Ishikawa, T. Yamaguchi, H. Kobayashi, Y. Onuki and A. Sekiyama
  The Fourteenth International Conference on Electron Spectroscopy and Structure, PB-54, ShanghaiTech University, China, 8-12 October 2018.